Attenuation of Ultrasonic Lamb Waves with Applications to Material Characterization and Condition Monitoring

A Thesis
Presented to
The Academic Faculty

by

Kritsakorn Luangvilai

In Partial Fulfillment
of the Requirements for the Degree
Doctor of Philosophy

School of Civil and Environmental Engineering
Georgia Institute of Technology
August 2007

Attenuation of Ultrasonic Lamb Waves with Applications to Material Characterization and Condition Monitoring

Approved by:

Professor Laurence J. Jacobs, Advisor
School of Civil and Environmental Engineering
Georgia Institute of Technology, Committee Chair

Professor Jianmin Qu, Co-advisor
George W. Woodruff School of Mechanical Engineering
Georgia Institute of Technology

Professor Douglas B. Williams
School of Electrical and Computer Engineering
Georgia Institute of Technology

Professor Reginald DesRoches
School of Civil and Environmental Engineering
Georgia Institute of Technology

Professor Glenn J. Rix
School of Civil and Environmental Engineering
Georgia Institute of Technology

Date Approved: April 25, 2007

To my grandmother, Nilda;

her love to me is indescribable by any words.

ACKNOWLEDGEMENTS

The first person I would like to thank is the late Dr. James Ting-Shun Wang. My interest in Solid Mechanics started when I took his Linear Elasticity course in the first semester of my master's degree. His excellent teaching inspired me to head into this field.

I would like to thank all members of my thesis committee for agreeing to serve on my thesis committee and their useful comments about this research work. My special thanks go to Dr. Jianmin Qu, who is my co-advisor. Discussing researches with him is always a pleasure to me because of his thorough understanding and broad knowledge on the related subjects. I would also like to specially thank Dr. Doug Williams. In the last year and a half, he has been like my third advisor. I really appreciate his willingness to help me in every time I asked for guidance in signal processing. Most importantly, I would like to thank my advisor, Larry—Dr. Laurence Jacobs. It is hard for me to express my gratitude to him, but I can say that he is the one who makes my Ph.D. and thus this thesis possible. He has been both my best friend and best advisor. I do not think I could find a better advisor anywhere else. He is always supportive and understanding. I cannot say enough about what we have been through together.

I have special thanks to Dr. Mike Lowe from Imperial College and Dr. Paul Wilcox from Bristol University. I always learned from them both through direct conversations and via emails. I will never forget hours we spent discussing research results at the QNDE conferences. A part of this research work is inspired by Paul's work.

I would like to thank all my friends around, especially in this NDE group under Larry. To name a few, this group of people includes Marc Dressler, Tobias Kreuzinger, Johannes Maess, Jan Hermann, Florian Kerber, Dr. Wonsiri Punurai and Dr. Guoshuang Shui. They simply make my Ph.D. years eventful and memorable.

I also would like to thank Dr. Jin-Yeon Kim, a researcher in our group for what he has brought to the group and to me personally. I regard him as my friend and teacher.

I have learned very much from his knowledge and experiences in several topics, especially regarding ultrasonic measurements. I have always appreciated those invaluable lessons from him and all conversations with him at coffee times.

Lastly, there are a number of people who indirectly contribute to my thesis. I would like to thank my family—my parents and my sister—for their understandings, supports and encouragements during long years of my Ph.D. study. Their major concerns are always my health and happiness. Special thanks go to Jittrakarn Saiyawat (Jang), who encouraged me during the course of writing this thesis, and to Pimthida Thammajaree (Meen) for her indirect influence on the time frame of this thesis. Finally, I would like to thank Vilasinee Leowarin (Winny) for her immeasurable support to me in which I can always feel. She is probably happier than I when I finish this thesis; I am happy when she is happy.

TABLE OF CONTENTS

LIST OF TABLES

LIST OF FIGURES

SUMMARY

Engineering industries usually require nondestructive evaluation (NDE) methods to ensure quality control, safety, and optimized use of resources. Among potential NDE techniques, ultrasonic wave methods are widely used because of their versatility and affordability. For applications to layered structures, ultrasonic guided waves are naturally excited and detected, so these guided waves are the preferred choice when compared to conventional bulk waves. The main advantage of guided waves over bulk waves for layered structures is that these guided waves can propagate a much farther distance, and thus they enable long range inspection. It is important to note that guided waves are multi-mode, so a preferred mode can be selectively used, although it is sometimes more efficient to use multiple wave modes. The characteristics of guided waves, namely dispersive propagation and attenuation, are directly related to the properties of the system in which they are propagating, so the measurement of these wave characteristics can be used for material characterization and condition monitoring.

Despite a number of successful techniques to experimentally measure propagation characteristics of guided waves, there is a lack of a standard procedure to obtain attenuation characteristics. This research develops such a quantitative and systematic procedure to extract attenuation characteristics from real guided wave time-domain signals. This research considers multiple wave-modes, and focuses on broadband attenuation measurements with laser ultrasonic techniques. The analytical model of guided waves with attenuation is studied in general cases, and a numerical simulation is developed to model the point source/receiver laser measurement system. The attenuation extraction technique is developed using synthetic signals generated by the simulation. Finally, this research demonstrates the use of experimentally-measured attenuation data for material characterization and condition monitoring by developing an inversion scheme to back-calculate material properties for a number of practical cases.

CHAPTER 1

INTRODUCTION

This chapter presents the overview of this research study. The chapter starts with some general background in the field of ultrasonic nondestructive evaluation and testing (NDE and NDT) leading to the motivation of this research. This background is stated to give readers general ideas, so detailed explanations or derivations are not given or shown. Some relevant concepts will be explained and elaborated in later chapters. Literature reviews on the related topic are given in the same section. Next, the objectives and the scope of this research are presented. This chapter ends with the thesis structure and common notions of symbols used throughout this thesis.

1.1 General background, literature reviews and motivation

Nondestructive evaluation and testing for material characterization and condition monitoring is a critical technology for many industries. The accurate characterization of a structural component leads to an accurate prediction of its remaining life, thus enables efficient quality control and maximizes the uses of resources. In some chemical processes (e.g. in the petroleum industry), accurate real-time monitoring is required to ensure the quality of products. For adhesively-bonded structures (which are commonly used in aerospace and automotive industries), the evaluation of the quality of the bond is needed in order to guarantee safety and performance. In those applications, NDE techniques are usually preferred or sometimes even necessary. Because of their well-established theoretical background, ultrasonic wave techniques are particularly effective in accomplishing a number of these tasks [63]. The availability of a number of wave types such as bulk body waves (bulk waves, in short), surface waves, interface waves, guided waves, etc., provides a variety of applicability, and thus, makes ultrasonic wave methods very versatile. Ultrasonic wave techniques usually involve robust, but affordable instrumentation, making these techniques

even more attractive.

In a layered structure—a stack of layers (curved or flat) bonded to each other (this kind of layered structure ranges from a single plate in a vacuum to a multi-layer structure embedded in a solid half-spaces on both sides), guided waves or Lamb waves[1] naturally exist, meaning that they are easily generated (or excited) and detected. As a result, ultrasonic methods involving guided waves have become a primary choice for use in these components. Besides the ease in their generation and detection, guided waves also possess a number of attractive advantages over conventional bulk waves (longitudinal or shear waves). In comparison to bulk waves, guided waves can propagate a much farther distance and hence, in NDE, can be used to cover a larger area with less (testing) time. This benefit results in reduced labor and time to perform a test, and makes long range inspection possible [100, 101]. Moreover, since multiple guided wave modes can be excited depending on frequency and the configuration of excitation and detection, appropriate guided wave modes can be chosen to match the application at hand. Consideration must be taken for the characteristics of the wave mode itself, which is also problem-dependent [95, 17]. This multi-mode nature emphasizes the versatility of using ultrasonic waves, especially guided waves in NDE.

It should be noted that attractive advantages of guided waves are obtained at the expense of having complicated wave signals. Guided wave behavior, which is the main reason for the long range propagation, also causes dispersion, that is, wave velocity varies with mode and frequency. Dispersion makes the received signal complicated because wave packets change their shape while propagating. Comparison of the same guided waves' characteristics extracted from signals measured at different propagation distances are not straightforward. Special care in signal processing is usually required to correctly interpret dispersive signals. The multi-mode nature complicates received signals as well because multiple wave modes can propagate with close velocities in the same frequency range and thus superpose on one another. Single mode generation/detection is often difficult (if not impossible), depending

[1]Strictly speaking, Lamb waves are referred to as waves propagating along a single layer—a plate or a plate connected with a half-space. For a general multi-layer structure, the term "guided" waves are more appropriate to this type of waves. However, since this research deals with Lamb waves and it is acceptable among researchers to use both names interchangeably, this research will use the term "Lamb" waves throughout the rest of the thesis after this section unless the generality of guided waves is emphasized.

on the device and accessibility to the component. As a result, a combination of several propagating modes is probably unavoidable. This multi-mode behavior is magnified when broadband generation/detection is employed because the number of existing guided wave modes increases with the bandwidth of the system. Nevertheless, it is important to make a comment that, in some applications, generation/detection of multi-mode signals may be more efficient especially when the complete characteristics of propagation are preferred.

Another important characteristic of guided waves is attenuation. In general, as they are propagating, guided waves may experience attenuation or reduction in amplitude. This scenario occurs mainly in two situations or a combination of both. First, some of the layers in the structure are made of viscoelastic materials (or of other inelastic types). The molecular structure of materials of this type exhibit a dissipative mechanism which, as a consequence, dissipates some energy of any disturbances [20, 22, 98]. This type of material (viscoelastic) features mechanically a combination of an elastic solid and a viscous fluid. Since polymers and adhesive materials are typically categorized into this group, a study of guided waves in viscoelastic layers can be applied to monitor adhesive bond properties or cure state, or for evaluation of a fiber-reinforced polymer (FRP) repair system.

The other situation where guided waves are attenuated is when the wave energy can leak out of the layered structure. A single solid plate loaded by an infinitely large fluid or a fluid half-space exemplifies this situation. Even though no dissipation is created in the plate (with the assumption that the plate is made of a linearly elastic solid), some energy can leak out of the plate to the fluid because a fluid can support the propagation of elastic waves [18, 9]. Since the fluid is infinite at the other boundary, the energy leaking into it never returns back to the plate, causing attenuation. This situation is clearly representative of guided waves for process monitoring in an oil distillation chamber or a chemical reactor, where, in general, a fluid inside any shell structure can be modelled as a half-space. For all types of attenuative systems, since guided wave behavior changes with frequency and mode, attenuation is also frequency- and mode-dependent.

As for how to generate and detect ultrasonic waves in structural materials, in general, a conventional piezoelectric transducer is widely used due to its availability and sensitivity.

Both narrowband and broadband transducers are available, making them the primary choice in several applications. However, there are some drawbacks associated with the piezoelectric transducers. First of all, being a mechanical device prevents a transducer from responding in an unbiased fashion with frequency. At its resonant frequency, a transducer becomes most sensitive when compared to its other frequencies. Secondly, use of a transducer usually requires a couplant in order to efficiently transmit acoustic energy into a structure. This couplant layer will change the amplitude of a wave produced by a transducer every time a transducer is removed and re-attached. Thus, The entire test becomes unrepeatable from specimen to specimen (or even test to test). This disadvantage can be critical in some applications, especially for those involving amplitude measurements. The last major drawback of a conventional piezoelectric transducer is its finite size. Often times, the size of a transducer cannot be neglected as the size itself is comparable to any of the length parameters of the problem (such as thickness, propagation distance, wavelength, etc.). In such cases, diffraction or a spreading of a wave beam must be taken into account. The theoretical derivation of such corrections may be very involved, even the approximate ones [102, 80, 83]. Other kinds of transducers or other forms of using piezoelectric elements have also been developed to overcome these disadvantages. For example, electro-magnetic acoustic transducers (EMAT) [25, 35] and air-coupled ultrasonic transducers [42, 16, 15] have been developed to create a non-contact system, which eliminates the undesirable variations and effects of coupling. Transducer arrays have also been developed to improve sensitivity and provide focusing/steering capability [103, 23].

Laser techniques can also be used to generate and detect ultrasonic waves; these techniques are more effective when compared to transducers in terms of frequency bandwidth and fidelity (no frequency bias). Commonly, a short-pulse laser is used at the generation side and an interferometer is used at the detection side. A combination of both laser generation and laser detection offers an ideal, non-contact system which is broadband (the bandwidth of the laser system is much broader than that of a broadband transducer system) and also frequency-unbiased (in the frequency range of interest) [86, 3, 13]. Moreover, in contrast to a transducer system, a laser system enables point source/receiver measurements or offers

a spatially broadband system because a laser beam can be focused to a point by an optical lens. Therefore, any size-effect is eliminated. Particularly for layered structures, laser techniques, with a simple configuration, are capable of generating and detecting guided waves, especially (but not necessarily only) in metals [85, 59]. Typical received signals are broadband, multi-mode, and of high signal-to-noise ratio (SNR) [93, 56].

Altogether, laser (generated/detected) ultrasonic guided waves are an effective tool for NDE of layered structures. In material characterization and condition monitoring, material properties (such as stiffnesses) or system parameters (such as a thickness) are of interest. In principle, those properties or parameters can be deduced from the knowledge of guided wave propagation, i.e. guided wave characteristics are directly related to material properties and system parameters. For condition monitoring, continual measuring of guided wave characteristics enables continual monitoring of the layered system. A combination of proper measurement and signal processing techniques makes the aforementioned concept realizable, and therefore constitutes robust NDE methodology.

The characteristics of guided wave propagation can be completely represented by dispersion curves. Dispersion curves are basically loci of roots of the dispersion relation, typically plotted in frequency(ω)-real wavenumber(k) or frequency(ω)-phase velocity (c_p) domain [2]. Each curve, which shows how wave velocity changes with frequency, represents each mode of existing waves. In an attenuative system where guided waves exhibit attenuation, the dispersion relation becomes a complex equation, thus has complex-valued roots in ω-k domain. This situation can be analyzed by keeping the frequency real, and allowing the wavenumber to be complex [96]. In this case, one plot of typical propagation dispersion curves is not enough to describe guided wave propagation; an additional plot of the imaginary part of wavenumber as a function of frequency is required for attenuation information. In this research, dispersion curves in the frequency-real wavenumber (ω-$\Re\{k\}$) domain (or its variations) are referred as *propagation dispersion curves* whereas dispersion curves in the frequency-attenuation (ω-$\Im\{k\}$) domain are called *attenuation dispersion curves*.

Guided waves can be used in a number of ways to nondestructively evaluate a layered system or to monitor a process involving a layered system. A direct approach is to

measure dispersion curves of guided waves and relate them to system parameters. Such approaches are taken for calculation of borehole system parameters by Braunisch et al. [10], and qualitative evaluation of aluminum- and concrete-bonded systems by Heller et al. [41] and Luangvilai et al. [59], respectively. As for other alternatives, indirect approaches use specific behaviors of particular guided wave modes that suit the applications at hand. Guo and Cawley [33, 34] and Tan et al. [90] measure the amplitude of a single guided wave mode to detect a delamination in a composite plate. Gilchrist [29] numerically studies reflection coefficient of the S0 mode by small horizontal defects. A number of researchers study the transmission and reflection of specific types of guided waves across bonded joints and use them to evaluate the quality of those joints. Mal et al. [60] and Nagy and Adler [66] study guided waves leaking into the bond. Rokhlin [81] presents the theoretical formulation of guided waves across two kinds of joints with experimental verification. Lowe et al. [55] investigate reflections and transmissions of different guided wave modes across a perfect lap joint, and discuss each mode's sensitivity. Rose and Ditri [82] apply the reflection and transmission concepts with a scanning technique. The applicability and effectiveness of guided wave techniques for bonded joint application is summarized in the review by Lowe and Cawley [54]. In all of the aforementioned techniques (both direct and indirect approaches), the dispersion curves of guided waves are required. Although some techniques employ only propagation dispersion curves, the attenuation dispersion curves are implicitly required to ensure detectability (thus applicability) in real applications. Therefore, there is a need to be able to measure both propagation and attenuation dispersion curves of guided waves in a layered system.

There are many efficient methods available to experimentally measure propagation dispersion curves, depending on experimental condition and wave types. Ting and Sachse [92] measure the wavelength of standing waves at a given frequency, and deduce a phase velocity as a function of frequency. Their technique employs continuous harmonic waves generated by a transducer. This technique works for single mode bulk waves and requires special care in the calculation of the number of cycles of standing waves in a specimen. Sachse and Pao [84] propose comparing the phase spectrum of a measured signal to that of a reference

signal to calculate a phase velocity as a function of frequency. This technique is simpler than the previous one that uses standing waves, but again, works for only single-mode signals. Pialucha et al. [74] successfully employed only the amplitude spectrum of a recorded signal to calculate phase velocity. This technique is based on the same concept as that of Sachse and Pao's, but it is more robust because the magnitude spectrum is less sensitive to experimental errors as compared to the phase spectrum, and this technique does not involve tricky phase unwrapping considerations. All of the aforementioned techniques are developed (and then experimentally verified) and sometimes applicable only for a one-dimensional case (bulk waves). Schumacher et al. [85] use Sachse and Pao's technique for guided wave signals detected by a laser. However, in Schumacher et al.'s paper, the success of the results relies very much on complete separation between modes since mode identification is required before phase comparison. For multi-mode, guided wave signals, two major techniques to obtain propagation dispersion curves have been proposed. Alleyne and Cawley [4] apply a two-dimensional Fourier transform (2D-FFT) to mulitple signals measured at closely-spaced locations. A three-dimensional result represents spectra of signals in both temporal and spatial frequency domain, which are equivalent to dispersion curves in frequency-real wavenumber domain. The drawback of this technique is the requirement of multiple signals from closely-spaced locations. Multiple measurements are laborious and the closeness between the physical measurements—which, following the sampling theory, is governed by the desired resolution in wavenumber domain—might be difficult to achieve.

The other method to measure propagation dispersion curves of multi-mode guided waves is to use the time-frequency representation (TFR). There are several TFR techniques; a number of common ones are studied particularly for guide wave signals by Niethammer et al. [69]. The TFR techniques overcome the difficulty of the 2D-FFT technique because only a single time-domain signal is required. The TFR captures the non-stationarity of a time-domain signal and present it in a time-frequency domain. This non-stationarity is, in turn, a propagation dispersion curve of each existing wave mode in frequency-energy slowness (sl_e) domain.

While many techniques are successfully applied to time-domain signals to measure propagation dispersion curves, attenuation dispersion curves are comparatively more difficult to measure. All of the techniques for attenuation measurement are developed in a one-dimension configuration, i.e. for bulk waves. A conventional technique is to send a pulse through a thickness of a specimen (by any means) and measure successive pulse echoes of waves traveling back and forth in a specimen. The attenuation is calculated in the frequency domain by comparing two consecutive echoes. This technique is applied successfully to common polymers by Hartmann and Jarzynski [38], and to a number of common materials including some fluids and gases by Selfridge [87]. This technique has been also applied to broadband signals using transducers [73] and laser techniques [7, 76]. He and Zheng [40] slightly modify this same technique to include more pulses in order to improve its robustness. Although this technique is widely used, it has limitations in accuracy when a specimen thickness is too thin in comparison with the wavelength used since the reflected waves are interfered with each other. Kinra and Iyer [46] propose the improvement using both magnitude and phase of the explicit through-transmission transfer function with the knowledge of other relevant quantities (such as density and phase velocity) to measure attenuation. As for guided waves, Bernard et al. [9], without describing the procedure in detail, measure attenuation of some specific modes at some specific frequencies as a part of their study.

1.2 Research objectives and overview

The lack of a standard procedure to measure attenuation dispersion curves of guided waves motivates this study. The main objective of this research is to develop such a technique, i.e. a descriptive technique to obtain the attenuation dispersion curves from measured time-domain signals. The layered systems under consideration are assumed to be low-attenuated. This assumption is reasonable in most applications, for example, a metal plate loaded with an inviscid or low-viscous fluid, or an adhesively-bonded composite system whose adhesive layer is much weaker (stiffness-wise) than other layers. The layered systems are also assumed one-sided accessible to match typical conditions in the field. The goal of this study is to

measure attenuation of Lamb waves in an accessible layer (top layer) of a layered system. This study deals with the most general broadband, multi-mode signals so that the developed technique is also applicable to narrowband or single-mode signals. A numerical simulation of Lamb wave signals will also be developed and used for the verification of the proposed technique before the proposed technique is applied to the real experimentally-measured signals. Finally, this study will develop the inversion scheme for a specific application to demonstrate the use of measured attenuation dispersion curves and its effectiveness.

In summary, the research objectives are

1. to develop an analytical model of Lamb wave propagation with attenuation, in particular Lamb waves in a solid plate connected with a half-space (solid or fluid);

2. to develop a numerical simulation to generate realistic broadband transient responses of Lamb waves, both with and without attenuation;

3. to develop a quantitative and systematic procedure to extract broadband attenuation information from experimentally-measured Lamb wave time-domain signals;

4. to apply this procedure to extract attenuation information for material characterization and condition monitoring in realistic applications.

This research consists of four separate components: analytical model and numerical simulation; signal processing techniques for attenuation measurements; experimental verification; and inversion techniques. The four components are ordered in four research tasks:

Task 1: Develop the analytical model and numerical simulation suitable for the proposed research objectives. The analytical model will be for axisymmetric Lamb waves in an isotropic, elastic plate due to normal excitation. Time-domain responses—the out-of-plane displacement at the surface of the plate—will be generated for all Lamb modes according to characteristics of modes of vibration. To generate attenuated responses, arbitrary attenuation, as a function of frequency, is added to the already-generated responses. Even though these attenuated signals might not be exact, they are sufficient for this study since they capture all important features of the real guided wave signals, and they only serve as known

signals to verify the proposed attenuation measurement technique. However, it is important to note that if needed, the non-attenuative model can be modified to include attenuation to exactly simulate attenuated signals. The simulation is generated by an eigen-expansion technique with characteristics of modes of vibration (dispersion curves) calculated separately (and effectively) by another solver. This technique enables simulation of single-mode or multi-mode signals with any desired number of modes.

Task 2: Develop a technique to extract attenuation information from single-mode attenuated signals. The time-frequency representation (TFR), in particular, the short-time Fourier transform (STFT), will be explored first as a fundamental choice since it also gives additional information about energy localization on propagation dispersion curves. Other signal processing techniques will also be researched. The proposed technique will be finally tested with numerically-simulated, attenuated signals from Task 1. Then, the proposed techniques are extended to apply for multi-mode signals. Some special treatment will need to be imposed when several wave modes interfere with each other. The goal of this task is to obtain a robust technique capable of extracting multi-mode attenuation over significant frequency range (if not all over excitable range). The proposed technique will be tested with numerically-simulated signals.

Task 3: Apply the developed techniques to the actual, experimentally-measured signals. Both narrowband and broadband signals will be tested. The experiment for broadband signals will employ laser techniques both on generation and detection sides for ideal results. The specimen used as an attenuative system consists of an aluminum plate loaded with an ideal (inviscid) fluid such as water. This system generates a low-attenuated system as assumed in the analytical model.

Task 4: Develop an inversion strategy for the use of attenuation dispersion curves for material characterization and condition monitoring. This task will use real attenuation data from Task 3 together with plate properties as input. The output is fluid properties, namely, sound wave speed and density. An inversion for a sound wave velocity in fluid will be demonstrated as an application for material characterization. The inversion tool will be a neural network since the relationship between input and output is multi-dimensional

and too complicated to be explicitly expressible. The reason for using a neural network for such a formidable task is the fact that a well-built and well-trained network can be used as a universal approximation for any Borel measurable function. Another real application is given for condition monitoring. Measured attenuation is used to monitor the change in the level of a fluid inside a closed container. In this case, all material properties are assumed known, and the level of a fluid can be directly related to the measured attenuation.

1.3 Thesis structure

This thesis is presented in seven chapters. Chapter 1 presents an introduction and overview. The purpose is to give a concise scope of this study with overall ideas and rationale. Fundamental backgrounds are given in Chapter 2. The first topic presented is the mechanics of waves in general, developed from fundamental equations in continuum mechanics. Those fundamental equations are stated without proofs or derivations. Guided wave phenomena are derived next after the concept of reflection and transmission of time-harmonic waves are developed. The chapter then switches to basics in signal processing. This topic includes various types of frequency-domain analysis or Fourier transforms in particular. The development starts with the classical continuous-time Fourier transform, and then goes towards the discrete versions which will be employed in real implementations. The final topic in Chapter 2 is a basic understanding of laser ultrasonic techniques. Ultrasonic wave generation and detection by a pulse laser and an interferometer, respectively, are focused since they are used in the experiment. Detailed derivations are omitted because they require some knowledge in electromagnetics and optics, and the laser techniques only play a role in the experiment.

Chapter 3 introduces a concept of attenuation of waves as a direct result from the mathematical analysis of certain wave-propagation problems. The attention is given to attenuation of Lamb waves due to leakage of wave energy into the connected half-space. The dispersion equation is derived for such a case where the system consists of an elastic plate attached with a solid half-space. A special case where the half-space is a fluid is deduced from a general case by a special treatment. This chapter includes the first part of

Task 1 in which the analytical model of attenuated Lamb waves is developed. Chapter 4 concerns the latter part of Task 1. This chapter develops a simulation of a Lamb wave transient response both with and without leakage. The method used to solve the governing equations with non-homogeneous boundary conditions is the eigen-expansion technique. The principle of the method is presented with application to the actual axisymmetric Lamb wave propagation due to a normal point excitation. Derivations and analyses are given with extensive details. The chapter presents verification of the important features of simulated signals such as excitability. A simulated signal is also compared with an experimental signal. In the process, the net source function of a laser system is computed by the deconvolution technique. Relevant derivations are given. Lastly in the chapter, the simulation of Lamb waves without leakage is extended to include attenuation for the leaky case.

Task 2 is presented in Chapter 5. This chapter proposes two methods for attenuation extraction. The first method is a direct product from the short-time Fourier transform. This method is shown to work well with single-mode signals especially when the signals have little dispersion. The other method is developed from applying a series of bandpass filters to the signals to track changes in a wave amplitude at each frequency. This method is shown to work similarly to the first one. Both methods are tested with simulated signals developed in Chapter 4 and then with experimental signals. Discussions over the two proposed techniques are also given at the end of the chapter.

Chapter 6 presents the applicability of the measured attenuation values. Two real applications are given as examples. Those two applications use attenuation measurements of both narrowband and broadband signals, and also represent both forward and inverse problems. The first application is an inverse problem. The goal is to measure a property of a fluid inside a closed container. The attenuation dispersion curve of a particular Lamb mode is measured and used as a tool to extract the property of a fluid, which is a sound wave velocity, in this example. Attenuation measurements of Lamb waves over a broad frequency range is needed to help better inversion so that broadband signals will be used. The inversion scheme is developed using a neural network. A feed-forward, 2-layer network with a backpropagation algorithm is chosen for this task because of its simplicity and

flexibility. Some principles, design and training processes are given for completeness. The inversion result is compared with a reference value. Note that this example can be thought as a representative of applications for material characterization. The second example is the level measurement of a fluid inside a closed container. At different level of a fluid inside, measured attenuation is directly converted into the elevation. In this case, attenuation at a single frequency is sufficient and effective; therefore, narrowband signals will be used. This example represents the application in condition monitoring.

The last chapter—Chapter 7—concludes the entire study. Limitations and shortcomings of the proposed attenuation measurement techniques are discussed. Some ongoing researches are mentioned as a part of continuing work and recommendations.

Besides the above details, this thesis includes five appendices. The purpose of those appendices is mainly to help the readers understand and follow this thesis better. Moreover, they also fill the possible gaps in the thesis contents. Appendix A gives the details which are left out from all derivations throughout the entire thesis. This appendix should make all all mathematical derivations easy to follow and typing errors, if exist, obvious. Appendix B presents conversion of some quantities and equations from the Cartesian coordinates to the cylindrical coordinates. The details of this conversion are rarely found in any textbooks. This appendix chooses to derive those converted expressions by direct transformation to avoid confusion in the technique employing geometry. Appendix C presents derivations of some definite integrals encountered in Chapter 4. These integrals might be straightforward to derive, but they are presented for completeness of the thesis. Appendix D presents the detailed derivation of excitability of Lamb waves in a free plate. This derivation gives readers another traditional way of solving a partial differential equation. The derivation involves a number of crucial mathematical considerations and analyses, some of which have not been explained or presented in any referenced articles. To the author, the demonstration of the problem alone is worth presenting. The last appendix—Appendix E—presents the details of the current research on modal decomposition of a double-mode Lamb wave signal. This topic is an extension to the work presented in this thesis. This appendix provides the direction for future work on the improvements of attenuation extraction techniques.

1.4 General notions and comments

The last note of this chapter is about the notations used and common understanding in the entire thesis. First of all, vector and matrix variables are represented by boldface small and capital letters, respectively. A scalar variable or constant is of regular non-bold, italic type. Sometimes, a vector quantity, instead of a boldface symbol, is written in a component form or an indicial notation. Then, the component of a vector quantity is written as a scalar function with a subscript indicating a direction. For physical quantities, the directions 1, 2 and 3 always correspond to directions x, y and z, respectively, in the Cartesian coordinates. These subscripts of a number (1, 2 or 3) and a letter (x, y or z) will be used interchangeably. If a letter such as i is used for a subscript of a vector quantity, that letter represents a generic direction which can be replaced by any number, 1, 2 or 3. The analogous convention applies for a matrix or a second-order tensor quantity. In this case, two subscripts are required.

A unit vector is not distinguished from a general vector. However, the boldface $\mathbf{e}$ is always used to represent a unit vector in any coordinate system. The type of coordinate system will be clear when $\mathbf{e}$ is written in a component form. For example, (e_x, e_y, e_z) or (e_1, e_2, e_3) represents a unit vector in the Cartesian coordinates whereas (e_r, e_θ, e_z) indicates the use of the cylindrical coordinates. Next, only the notation j will be used throughout the thesis for the imaginary unit, i.e. $j = \sqrt{-1}$. This j will not be used for anything else except as a subscript of a tensor quantity where its meaning is clear.

Lastly, an unknown function which is involved in a differential equation is always assumed to be differentiable up to the order of the highest-order term in the equation. This differentiability is assumed everywhere in the domain. At some stages in the thesis, the order of a double integration or a double summation of a function are interchanged. The integrand (or the term in a double series) is assumed to be absolutely integrable (or summable) with respect to either integration variable (or summation index) so that this operation is legit. With this assumption, order switching is allowed by Fubini's Theorem. This assumption is reasonable because the result of a double integration (or summation) will be a physical quantity of a well-posed problem which should be bounded.

CHAPTER 2

FUNDAMENTAL BACKGROUND

This chapter presents the fundamental theories from which this research has stemmed. Topics presented consist of wave propagation in solids, basic signal processing techniques, and laser ultrasonics. The section of wave propagation theory starts from the development of wave phenomena from fundamental equations in linear elasticity theory. Derivations of those basic equations are not presented; the readers should consult any elasticity or continuum mechanics textbooks such as References [30], [62], [2]. A specific type of waves—Lamb waves—which is of the most interest in this research, is also derived after some paving background in waves in unbounded medium and joined half-spaces. Section 2.2 presents some basic signal processing techniques used in this research. The section starts with the knowledge of the classical, continuous-time Fourier transform, and then links it to its practical counterpart in the discrete domain. This section extends to the more advanced techniques called time-frequency representations. These techniques are more suitable for analyzing non-stationary signals. Among several kinds of time-frequency representations, the short-time Fourier transform is focused. The last section presents relevant concepts in laser ultrasonics. The main objective of this section is to present the nature of laser generation and detection which are used in experiment conducted in this research. The correct understanding of the nature of laser generation and detection leads to a good wave-propagation model which is critical to the success of this study.

2.1 Wave propagation in solids

This section aims to prepare the readers the necessary understanding of the wave phenomena which will be developed further in later chapters. Some topics are included because they pose mathematical tools or techniques which will be used for more complicated problems. This section assumes fundamental concepts and principles in the linear elasticity theory

and continuum mechanics, especially for solids. The objective is to present common types of waves and their physical nature through mathematical formulations.

2.1.1 Basic equations of linear elasticity

This entire study is within the linear-theory framework. To start with, basic equations derived according to linear-elasticity theory's assumptions [30], expressed with the use of indicial notations are the following:

A. **Kinematical relation**

This is a relation between the strain tensor, ε_{ij}, and the displacement field, u_i, where each of i and j ranges from 1 to 3.

$$\varepsilon_{ij} = \frac{1}{2}(u_{i,j} + u_{j,i}). \tag{2.1}$$

In the above equation, the comma convention is used to represent the spatial partial differentiation, i.e. $u_{i,j} = \frac{\partial u_i}{\partial x_j}$.

B. **Constitutive equations**

Materials are assumed to be homogeneous and follow the generalized Hooke's law. Hence, the components of the stress and strain tensors, σ_{ij}'s and ε_{ij}'s, respectively, are linearly related by the material moduli c_{ijkl}'s, which are contained in a fourth-ordered tensor. This relationship is expressed as

$$\sigma_{ij} = c_{ijkl}\varepsilon_{kl}, \tag{2.2}$$

where the Einstein summation convention is assumed for repeated index, i.e. $c_{ijkl}\varepsilon_{kl} = \sum_{k=1}^{3}\sum_{l=1}^{3} c_{ijkl}\varepsilon_{kl}$. In general, this material-stiffness tensor c_{ijkl} consists of 21 distinct constants due to some symmetry of stress and strain components, and thermodynamic principles. For a special case of isotropic materials, c_{ijkl} can be represented by two Lamé constants, λ and μ, and the constitutive equations become

$$\sigma_{ij} = \lambda\varepsilon_{kk}\delta_{ij} + 2\mu\varepsilon_{ij}, \tag{2.3}$$

where again, the Einstein convention is assumed, and δ_{ij} is the Kronecker delta[1].

C. **Balance of linear and angular momenta**

The balance of angular momentum dictates the symmetry of the stress tensor while the balance of linear momentum leads to the governing equation of motion in terms of stress and displacement at every point in the medium volume:

$$\sigma_{ij} = \sigma_{ji} \tag{2.4}$$

$$\sigma_{ji,j} + f_i = \rho \ddot{u}_i, \tag{2.5}$$

where f_i and ρ are body forces per unit volume and density, respectively, and the dot $\dot{}$ indicates the temporal partial differentiation, i.e. $\ddot{u}_i = \frac{\partial^2 u_i}{\partial t^2}$; t is the time variable.

Note that the comma and Einstein conventions will be assumed throughout this thesis unless noted otherwise.

Specifically for isotropic materials, substitution of Equation (2.1) into Equation (2.3) leads the relationship between the stress tensor and the displacement field. Another substitution of that relationship into Equation (2.5) gives the displacement equations of motion or Navier's equations (see details in Appendix A.1.1)

$$(\lambda + \mu) u_{j,ji} + \mu u_{i,jj} + f_i = \rho \ddot{u}_i. \tag{2.6}$$

Equivalently, with the relations: $\nabla(\nabla \cdot \mathbf{u}) = u_{j,ji}$ and $\nabla^2 \mathbf{u} = \nabla(\nabla \cdot \mathbf{u}) - \nabla \times \nabla \times \mathbf{u} = u_{i,jj}$, where boldface symbols represent vector quantities, Equation (2.6) can be rewritten in a vector format as

$$(\lambda + \mu)\nabla(\nabla \cdot \mathbf{u}) + \mu \nabla^2 \mathbf{u} + \mathbf{f} = \rho \ddot{\mathbf{u}}, \tag{2.7}$$

or

$$(\lambda + 2\mu)\nabla(\nabla \cdot \mathbf{u}) - \mu \nabla \times \nabla \times \mathbf{u} + \mathbf{f} = \rho \ddot{\mathbf{u}}. \tag{2.8}$$

[1]The Kronecker delta is defined as

$$\delta_{ij} = \begin{cases} \delta_{ij} = 1, & \text{if } i = j \\ \delta_{ij} = 0, & \text{if } i \neq j. \end{cases}$$

2.1.2 Wave propagation in an unbounded medium

Waves are disturbances (e.g. force or displacement disturbances) that travel in a medium with finite velocities. Of the simplest kind is a plane wave where there exists a plane of uniform disturbance. Motivated by a solution of the one-dimensional wave equation, a plane displacement wave propagating with a phase velocity c can be represented by [2]

$$\mathbf{u} = f(ct - \mathbf{p}\cdot\mathbf{x})\mathbf{d}, \tag{2.9}$$

where $\mathbf{p}$ and $\mathbf{d}$ are unit vectors defining the directions of propagation and motion, respectively; f is an arbitrary, twice-differentiable function; $\mathbf{x}$ is the position vector. From this expression, the planes of uniform displacement (or constant phase) are described by $\mathbf{p}\cdot\mathbf{x} =$ constant. Notice that these planes are normal to the vector $\mathbf{p}$.

Assume that an elastic medium is homogeneous and isotropic. Substitution of the expression (2.9) into the governing equation (2.7) with no body forces gives (see details in Appendix A.1.2)

$$\left[(\lambda+\mu)(\mathbf{p}\cdot\mathbf{d})\mathbf{p} + (\mu - \rho\, c^2)\mathbf{d}\right] f''(ct - \mathbf{p}\cdot\mathbf{x}) = 0,$$

or

$$(\lambda+\mu)(\mathbf{p}\cdot\mathbf{d})\mathbf{p} + (\mu - \rho\, c^2)\mathbf{d} = 0, \tag{2.10}$$

where $'$ represents differentiation with respect to the argument.

Since $\mathbf{p}$ and $\mathbf{d}$ are independent unit vectors, Equation (2.10) can be satisfied by two ways:

- Case 1: $\mathbf{d} = \pm\mathbf{p}$ or $\mathbf{d} \parallel \mathbf{p}$

  This condition leads to $(\mathbf{p}\cdot\mathbf{d})\mathbf{p} = \mathbf{d}$. Thus, Equation (2.10) yields

  $$c = c_L = \sqrt{\frac{\lambda + 2\,\mu}{\rho}}. \tag{2.11}$$

  In this case, the wave is called a *longitudinal wave* or a *P-wave* due to the fact that the wave motion is parallel to the direction of propagation.

- Case 2: $\mathbf{p} \cdot \mathbf{d} = 0$ or $\mathbf{d} \perp \mathbf{p}$

  Equation (2.10) yields

  $$c = c_T = \sqrt{\frac{\mu}{\rho}}. \tag{2.12}$$

  The motion of wave is now perpendicular to the direction of propagation. This wave is called a *transverse wave* or a *shear wave* or an *S-wave*.

The preceding analysis shows that when the medium is unbounded (or infinite), two kinds of waves with different velocities can propagate independently. These waves together are called *bulk waves* due to their nature that they propagate in a volume of a medium.

For a plane wave in an unbounded medium, if a plane, called the problem's plane, is set up such that there are two independent propagating waves—one longitudinal and one shear waves—whose motions are on that plane, this shear wave on the problem's plane is specifically called a vertically-polarized shear wave or an SV-wave. In the same circumstance, there also exists another shear wave propagating in the same direction, with the shear-wave velocity c_T, but its motion is perpendicular to the problem's plane. This wave is called a horizontally-polarized shear wave or a SH-wave. Those two shear waves and one longitudinal wave propagate independently in a medium. This distinction between the two shear waves will become apparent in later sections when plane-strain problems with some boundaries are considered. In such cases, the P- and SV-waves will be coupled with each other due to the boundary whereas the SH-wave remains uncoupled from the other two and can be removed from the analysis as far as the motions on the problem's plane is concerned.

Often times, the study of *time-harmonic* waves simplifies mathematical analysis and manipulations while the important behavior of the wave phenomenon considered is still captured. In this kind of representation, the only function of the time variable, t, is a harmonic function $e^{j\omega t}$; ω is the circular frequency of the wave, and j is the imaginary unit ($j = \sqrt{-1}$). A time-harmonic wave can be thought as a free wave propagating without the origin or the end in time. In such cases, the time variable becomes unimportant whereas the more influential parameter is the wave's frequency ω. As an example, from a general expression in Equation (2.9), a time-harmonic plane wave in an unbounded medium can be

represented by

$$\mathbf{u} = Ae^{jk(ct-\mathbf{p}\cdot\mathbf{x})}\mathbf{d}. \tag{2.13}$$

In this expression, the wave is also assumed harmonic in space. A is a complex amplitude of the wave and k is a parameter called wavenumber. The wavenumber satisfies the relationship $kc = \omega$. The wavenumber can be thought as the spatial frequency of the wave analogous to the temporal frequency ω, i.e. the wavelength $\Lambda = \frac{2\pi}{k}$ (compared to the period $T = \frac{2\pi}{\omega}$). In Equation (2.13), although the displacement $\mathbf{u}$ is expressed as a complex-valued quantity, the actual displacement is understood to be the real or imaginary part of that complex quantity. Note that, as seen at the beginning of this subsection, c can be either c_L or c_T depending on the motion with respect to the direction of propagation. In other words, at a fixed frequency ω, there exist two kinds of time-harmonic waves propagating independently in an unbounded medium with different velocities and wavenumbers.

2.1.3 Reflection and refraction of waves at the interface between two solid half-spaces

This subsection considers the unbounded domain consisting of two half-spaces of different materials. Time-harmonic plane waves are considered. The coordinate system can be arranged such that a plane of constant phase (constant disturbance) lies perpendicular to the xz-plane. With this setup, all field quantities will depend only on x and z. When the boundary—the interface between two half-spaces—is introduced, additional six conditions of continuity across the boundary must be imposed on the solution. Those six conditions are the continuity of three displacement components (u_x, u_y, and u_z) and three stress components on the interface (σ_{zz}, σ_{zx}, σ_{zy}). Since the stress σ_{zy} depends only on u_y ($\sigma_{zy} = \mu u_{y,z}$) while σ_{zx} and σ_{zz} depend on both u_x and u_z but not u_y ($\sigma_{zx} = \mu(u_{x,z} + u_{z,x})$, and $\sigma_{zz} = \lambda u_{x,x} + (\lambda + 2\mu)u_{z,z}$), the disturbance in the y-direction is uncoupled from the disturbance on the xz-plane. In other words, the SH-wave which supports the motion in the y-direction propagate independently (and thus can be analyzed separately) from the SV- and P-waves (each of which supports the motion in both x- and z-directions).

Regardless of the type of the incident wave, at the interface between the two half-spaces, this incident wave will generally be reflected and refracted into both P- and SV-waves in

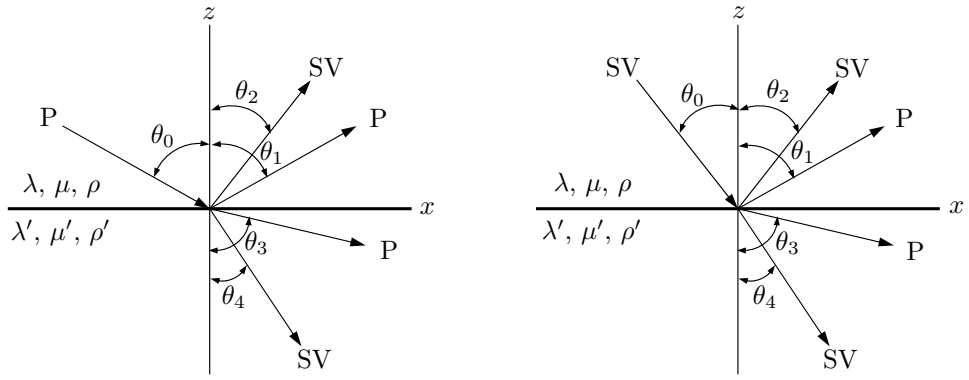

(a) P-wave incidence

(b) SV-wave incidence

Figure 2.1: Reflection and refraction of bulk waves at the interface between two solid half-spaces.

both media as shown in Figure 2.1. Each free wave (shown as a ray in that figure), called a partial wave, can be represented by the expression of the form of (2.13) with the vector $\mathbf{p}$ having only two nonzero components—p_x and p_z. Explicitly, from the expression (2.13), each of these five partial waves can be written as

$$\mathbf{u}^{(n)} = A_n e^{j\eta_n} \mathbf{d}^{(n)}, \tag{2.14}$$

where n runs from 0 to 4 representing incident, reflected P-, reflected SV-, refracted P-, and refracted SV-waves, respectively, and $\eta_n = k_n(c_n t - p_x^{(n)} x - p_z^{(n)} z)$ is the phase of the nth wave. The terms c_n, k_n, $\mathbf{p}^{(n)}$, and $\mathbf{d}^{(n)}$ in the expression (2.14) are to be chosen according to what type of wave the expression represents and which medium that wave is propagating in. For completeness, the choices of c_n, k_n, $\mathbf{p}^{(n)}$, and $\mathbf{d}^{(n)}$ in the cases of P-wave and SV-wave incidences are given in Table 2.1. In the table, the wave velocities in the upper and lower solids are given, respectively, by

$$\begin{aligned} c_L &= \sqrt{\tfrac{\lambda+2\mu}{\rho}}, \qquad c_T = \sqrt{\tfrac{\mu}{\rho}} \qquad \text{for the upper half-space,} \\ c'_L &= \sqrt{\tfrac{\lambda'+2\mu'}{\rho'}}, \qquad c'_T = \sqrt{\tfrac{\mu'}{\rho'}} \qquad \text{for the lower half-space,} \end{aligned}$$

where λ, μ and ρ are material properties, and the primed parameters belong to the lower half-space.

Table 2.1: Choices of c_n, k_n, $\mathbf{p}^{(n)}$, and $\mathbf{d}^{(n)}$ for each partial wave in Figure 2.1.

Partial wave	n	c_n	k_n	$\mathbf{p}^{(n)}$	$\mathbf{d}^{(n)}$
Incident P-wave	0	c_L	$k_L = \frac{\omega}{c_L}$	$\sin\theta_0\,\mathbf{e_x} - \cos\theta_0\,\mathbf{e_z}$	$\sin\theta_0\,\mathbf{e_x} - \cos\theta_0\,\mathbf{e_z}$
Incident SV-wave	0	c_T	$k_T = \frac{\omega}{c_T}$	$\sin\theta_0\,\mathbf{e_x} - \cos\theta_0\,\mathbf{e_z}$	$\cos\theta_0\,\mathbf{e_x} + \sin\theta_0\,\mathbf{e_z}$
Reflected P-wave	1	c_L	$k_L = \frac{\omega}{c_L}$	$\sin\theta_1\,\mathbf{e_x} + \cos\theta_1\,\mathbf{e_z}$	$\sin\theta_1\,\mathbf{e_x} + \cos\theta_1\,\mathbf{e_z}$
Reflected SV-wave	2	c_T	$k_L = \frac{\omega}{c_T}$	$\sin\theta_2\,\mathbf{e_x} + \cos\theta_2\,\mathbf{e_z}$	$\cos\theta_2\,\mathbf{e_x} - \sin\theta_2\,\mathbf{e_z}$
Refracted P-wave	3	c'_L	$k'_L = \frac{\omega}{c'_T}$	$\sin\theta_3\,\mathbf{e_x} - \cos\theta_3\,\mathbf{e_z}$	$\sin\theta_3\,\mathbf{e_x} - \cos\theta_3\,\mathbf{e_z}$
Refracted SV-wave	4	c'_T	$k'_T = \frac{\omega}{c'_L}$	$\sin\theta_4\,\mathbf{e_x} - \cos\theta_4\,\mathbf{e_z}$	$\cos\theta_4\,\mathbf{e_x} + \sin\theta_4\,\mathbf{e_z}$

The sums $\mathbf{u}^{(0)} + \mathbf{u}^{(1)} + \mathbf{u}^{(2)}$ and $\mathbf{u}^{(3)} + \mathbf{u}^{(4)}$ give the expressions for wave fields in the upper and lower half-spaces, respectively. Since each $\mathbf{u}^{(n)}$, with proper c_n and k_n, satisfies the governing equations (2.7), it is clear that the sum of them in the same medium also satisfies such equations. The unknown amplitudes and angles of each reflected or refracted partial wave, A_n's and θ_n's ($n \sim 1$ to 4), can be determined in terms of the given amplitude and angle of an incident wave, A_0 and θ_0, by solving the simultaneous equations derived from the continuity of u_x, u_z, σ_{zx} and σ_{zz} across the interface $z = 0$ (four equations). The detailed analysis is not presented here, but it can be found, with results for some special cases, in the chapter on reflection and refraction of Reference [6] (pages 21–38).

2.1.4 Classical Lamb waves

It can be seen from the previous subsection that the boundary or interface between two different solids will introduce coupling between P- and SV-waves, i.e. a reflected SV-wave can be generated from an incident P-wave, and conversely, a reflected P-wave can be generated from an incident SV-wave. Now if there are two parallel boundaries such as an infinite flat plate, those reflected P- and SV-waves will be reflected back and forth between the two boundaries, and a large number of new P- and SV-waves will be generated. The interferences of all "partial" waves become a new kind of waves propagating in the direction of the two boundaries. These waves are called guided waves because they propagate as if they are guided by the two boundaries.

The characteristics of guided waves are studied through their dispersion relation, which can be derived from the harmonic analysis. This dispersion relations governs how the

velocity of each guided wave mode changes with frequency. This type of waves is first studied by Rayleigh [78] and then further investigated by Lamb [51]. However, the full details and more specific features of dispersion curves are given later by Mindlin [64]. In the classical development, plane-strain guided waves, also called *Lamb waves*, propagating in the infinite flat plate are considered. The medium outside the plate is vacuum; hence, the two boundaries are stress-free. A flat plate with both stress-free boundaries is sometimes referred to as a *free plate*. As usual, the material is assumed to be homogeneous, isotropic and linearly-elastic. The plate of thickness $2h$, with the coordinate system placed such that the x-axis is on the mid-plane of the plate, is setup as shown in Figure 2.2.

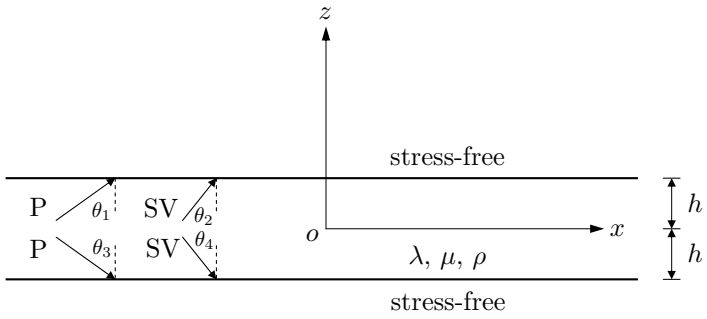

Figure 2.2: Classical Lamb waves in an infinite plate.

What has been developed in Sections. 2.1.2 and 2.1.3 can be extended into this analysis. The development here considers a steady-state wave field, so no partial wave is noted as an incident wave. The total wave field in the plate can be considered as being composed of four partial waves—two P-waves and two SV-waves going toward the top and bottom boundaries—as shown in the figure. The displacement of each partial wave is of the form of (2.13). The vectors $\mathbf{p}$, $\mathbf{d}$ and other parameters can be chosen from Table 2.1 for $n = 1$ to 4, where parameters c'_L, c'_T, k'_L, and k'_T are replaced with c_L, c_T, k_L, and k_T, respectively.

The displacement fields of all partial waves are explicitly

$$\begin{aligned}
\mathbf{u}^{(1)} &= A_1\big(\sin\theta_1\,\mathbf{e_x} + \cos\theta_1\,\mathbf{e_z}\big)e^{j\left[\omega t - k_L(\sin\theta_1\,x + \cos\theta_1\,z)\right]} \\
\mathbf{u}^{(2)} &= A_2\big(\cos\theta_2\,\mathbf{e_x} - \sin\theta_2\,\mathbf{e_z}\big)e^{j\left[\omega t - k_T(\sin\theta_2\,x + \cos\theta_2\,z)\right]} \\
\mathbf{u}^{(3)} &= A_3\big(\sin\theta_3\,\mathbf{e_x} - \cos\theta_3\,\mathbf{e_z}\big)e^{j\left[\omega t - k_L(\sin\theta_3\,x - \cos\theta_3\,z)\right]} \\
\mathbf{u}^{(4)} &= A_4\big(\cos\theta_4\,\mathbf{e_x} + \sin\theta_4\,\mathbf{e_z}\big)e^{j\left[\omega t - k_T(\sin\theta_4\,x - \cos\theta_4\,z)\right]}.
\end{aligned} \tag{2.15}$$

The total displacement field in the plate is thus equal to the sum of all four displacement fields above, $\mathbf{u} = \mathbf{u}^{(1)} + \mathbf{u}^{(2)} + \mathbf{u}^{(3)} + \mathbf{u}^{(4)}$. Since the waves propagating in the x-direction is of interest, the solution is forced to have a factor $e^{j(\omega t - kx)}$. With this factor, k is the wavenumber of Lamb waves which could be generally dependent of frequency. From Equations (2.15), the only possibility that all $\mathbf{u}^{(n)}$'s can be summed to produce an expression with the factor $e^{j(\omega t - kx)}$ is that

$$k_L \sin\theta_1 = k_T \sin\theta_2 = k_L \sin\theta_3 = k_T \sin\theta_4 = k. \tag{2.16}$$

These equations lead to

$$\begin{aligned}
\theta_1 &= \theta_3 = \theta_L \\
\theta_2 &= \theta_4 = \theta_T,
\end{aligned} \tag{2.17}$$

and

$$\sin\theta_T = \frac{c_T}{c_L}\sin\theta_L. \tag{2.18}$$

With another introduction of new parameters $\alpha_L = k_L\cos\theta_L = \sqrt{\frac{\omega^2}{c_L^2} - k^2}$ and $\alpha_T = k_T\cos\theta_T = \sqrt{\frac{\omega^2}{c_T^2} - k^2}$, the total displacement field in Equation (2.15) can be written as

$$\begin{aligned}
u_x &= \left[\big(A_1 e^{-j\alpha_L z} + A_3 e^{j\alpha_L z}\big)\frac{k}{k_L} + \big(A_2 e^{-j\alpha_T z} + A_4 e^{j\alpha_T z}\big)\frac{\alpha_T}{k_T}\right]F \\
&= \left\{\Big[(A_1 + A_3)\cos(\alpha_L z) + j(-A_1 + A_3)\sin(\alpha_L z)\Big]\frac{k}{k_L}\right. \\
&\qquad \left. + \Big[(A_2 + A_4)\cos(\alpha_T z) + j(-A_2 + A_4)\sin(\alpha_T z)\Big]\frac{\alpha_T}{k_T}\right\}F \\
&= \Big\{\big[C_1\cos(\alpha_L z) - jC_2\sin(\alpha_L z)\big]k + \big[(C_3\cos(\alpha_T z) - jC_4\sin(\alpha_T z)\big]\alpha_T\Big\}F,
\end{aligned} \tag{2.19}$$

$$
\begin{aligned}
u_z &= \Big[\big(A_1 e^{-j\alpha_L z} - A_3 e^{j\alpha_L z}\big)\frac{\alpha_L}{k_L} + \big(-A_2 e^{-j\alpha_T z} + A_4 e^{j\alpha_T z}\big)\frac{k}{k_T}\Big]F \\
&= \Big\{\Big[(A_1 - A_3)\cos(\alpha_L z) - j(A_1 + A_3)\sin(\alpha_L z)\Big]\frac{\alpha_L}{k_L} \\
&\qquad + \Big[(-A_2 + A_4)\cos(\alpha_T z) + j(A_2 + A_4)\sin(\alpha_T z)\Big]\frac{k}{k_T}\Big\}F \\
&= \Big\{\big[C_2\cos(\alpha_L z) - jC_1\sin(\alpha_L z)\big]\alpha_L + \big(-C_4\cos(\alpha_T z) + jC_3\sin(\alpha_T z)\big]k\Big\}F,
\end{aligned}
\tag{2.20}
$$

where F stands for the factor $e^{j(\omega t - kx)}$, and the new constants $C_1 = \frac{A_1+A_3}{k_L}$; $C_2 = \frac{A_1-A_3}{k_L}$; $C_3 = \frac{A_2+A_4}{k_T}$; $C_4 = \frac{A_2-A_4}{k_T}$ are used.

Since the geometry of the problem is symmetric with respect to the x-axis or the mid-plane of the plate, the displacement field can be split into the symmetric and anti-symmetric parts. Each part represents the independent Lamb wave mode:

Symmetric modes

$$
\begin{aligned}
u_x^{(s)} &= \big[C_1 k\cos(\alpha_L z) + C_3\alpha_T\cos(\alpha_T z)\big]F \\
u_z^{(s)} &= j\big[-C_1\alpha_L\sin(\alpha_L z) + C_3 k\sin(\alpha_T z)\big]F
\end{aligned}
\tag{2.21}
$$

Anti-symmetric modes

$$
\begin{aligned}
u_x^{(a)} &= -j\big[C_2 k\sin(\alpha_L z) + C_4\alpha_T\sin(\alpha_T z)\big]F \\
u_z^{(a)} &= \big[C_2\alpha_L\cos(\alpha_L z) - C_4 k\cos(\alpha_T z)\big]F.
\end{aligned}
\tag{2.22}
$$

With the use of Equation (2.3), the stress fields of those Lamb modes are (see details in Appendix A.1.3):

Symmetric modes

$$
\begin{aligned}
\sigma_{zz}^{(s)} &= \mu j\big[-(\alpha_T^2 - k^2)C_1\cos(\alpha_L z) + 2k\alpha_T C_3\cos(\alpha_T z)\big]F \\
\sigma_{zx}^{(s)} &= -\mu\big[2k\alpha_L C_1\sin(\alpha_L z) + (\alpha_T^2 - k^2)C_3\sin(\alpha_T z)\big]F
\end{aligned}
\tag{2.23}
$$

Anti-symmetric modes

$$
\begin{aligned}
\sigma_{zz}^{(a)} &= \mu\big[-(\alpha_T^2 - k^2)C_2\sin(\alpha_L z) + 2k\alpha_T C_4\sin(\alpha_T z)\big]F \\
\sigma_{zx}^{(a)} &= -\mu j\big[2k\alpha_L C_2\cos(\alpha_L z) + (\alpha_T^2 - k^2)C_4\cos(\alpha_T z)\big]F.
\end{aligned}
\tag{2.24}
$$

These stress fields must satisfy the stress-free boundary conditions ($\sigma_{zz} = 0$ and $\sigma_{zx} = 0$) at $z = \pm h$. For each Lamb mode, substitution of Equation (2.23) or (2.24) into the boundary conditions gives a homogeneous system of equations which can be written as a matrix equation $\mathbf{Dc} = 0$. In this equation, the matrix $\mathbf{D}$ consists of known elements obtained from known material properties and problem's geometry, and the vector $\mathbf{c}$ contains only unknown constants C_i's ($i = 1$ to 4). The nontrivial solution to each system exists only if the determinant of $\mathbf{D}$ vanishes. This condition results in the dispersion equation of each Lamb wave mode. The systems of equations and dispersion equations of both symmetric and anti-symmetric modes are given as follows:

Symmetric modes

$$\begin{bmatrix} -(\alpha_T^2 - k^2)\cos(\alpha_L h) & 2k\alpha_T \cos(\alpha_T h) \\ 2k\alpha_L \sin(\alpha_L h) & (\alpha_T^2 - k^2)\sin(\alpha_T h) \end{bmatrix} \begin{Bmatrix} C_1 \\ C_3 \end{Bmatrix} = 0. \tag{2.25}$$

The dispersion equation is

$$R_s(\omega, k) \equiv (\alpha_T^2 - k^2)^2 \cos(\alpha_L h)\sin(\alpha_T h) + 4k^2\alpha_L\alpha_T \sin(\alpha_L h)\cos(\alpha_T h) = 0. \tag{2.26}$$

Anti-symmetric modes

$$\begin{bmatrix} -(\alpha_T^2 - k^2)\sin(\alpha_L h) & 2k\alpha_T \sin(\alpha_T h) \\ 2k\alpha_L \cos(\alpha_L h) & (\alpha_T^2 - k^2)\cos(\alpha_T h) \end{bmatrix} \begin{Bmatrix} C_2 \\ C_4 \end{Bmatrix} = 0. \tag{2.27}$$

The dispersion equation is

$$R_a(\omega, k) \equiv (\alpha_T^2 - k^2)^2 \sin(\alpha_L h)\cos(\alpha_T h) + 4k^2\alpha_L\alpha_T \cos(\alpha_L h)\sin(\alpha_T h) = 0. \tag{2.28}$$

Equations (2.26) and (2.28) are written explicitly as functions of ω and k, for given material properties and the plate thickness. These equations are other versions of the well-known Rayleigh-Lamb frequency equations [2]:

$$\begin{aligned} \frac{\tan(\alpha_T h)}{\tan(\alpha_L h)} &= -\frac{4k^2\alpha_L\alpha_T}{(\alpha_T^2 - k^2)^2} \qquad \text{(Symmetric modes)} \\ \frac{\tan(\alpha_T h)}{\tan(\alpha_L h)} &= -\frac{(\alpha_T^2 - k^2)^2}{4k^2\alpha_L\alpha_T} \qquad \text{(Anti-symmetric modes)} \end{aligned} \tag{2.29}$$

At a fixed frequency ω and for a particular Lamb wave mode, these equations give the value of wavenumber k which describes how that frequency component of that particular Lamb

wave mode propagates. This information can be related to a phase velocity c_p or a group velocity c_g of that corresponding frequency component of that Lamb wave mode through simple relations:

$$c_p = \frac{\omega}{k}, \tag{2.30}$$

$$c_g = \frac{\partial \omega}{\partial k}. \tag{2.31}$$

It is clear from the complication of Equations (2.26) and (2.28) that c_p and c_g of each Lamb wave mode vary with frequency. This nature is called *dispersion*. Since it is not possible to generate Lamb waves of exactly one frequency, it is also clear that a Lamb wave packet, containing many frequency components, will change its shape as it propagates. Note that the more conventional way to derive these dispersion equations is to uncouple the displacement equations of motion (2.6) into two wave equations governing two potentials by the use of Helmholtz decomposition[2], and then solve each wave equation to obtain a solution. However, this section chooses the above method, called the partial wave technique, because it demonstrates the closer relations to the physics. This concept will be extended in the next chapter when leaky Lamb waves are developed.

Roots of the dispersion equations, which can be obtained only numerically, are called dispersion curves. These curves can be shown in the ω-k domain or its variations such as ω-c_p, ω-c_g, ω-sl_g, where sl_g, called a group slowness, is the reciprocal of a group velocity c_g. Figure 2.3 shows dispersion curves of Lamb waves propagating in a 1-mm-thick aluminum plate. The plot shows the first six Lamb modes up to 10 MHz. The symmetric and anti-symmetric modes are labelled with Sn and An, respectively. The number of mode n are ordered according to its *cutoff* frequency. The mode's cutoff frequency is the smallest frequency at which that Lamb wave mode exists. The two modes which exist at all frequency are the two fundamental modes, labelled as S0 and A0. These two modes, in general, are always generated regardless of the frequency bandwidth of the excitation.

[2]The detail of the Helmholtz decomposition is given in Section 4.2.1

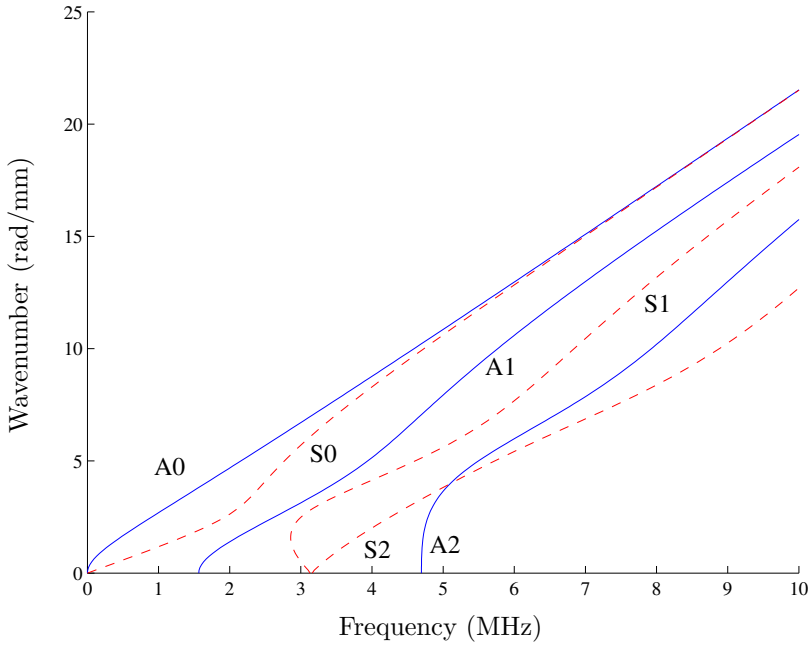

Figure 2.3: Theoretical dispersion curves (roots of Equations (2.26) (dashed lines) and (2.28) (solid lines)), shown in frequency-wavenumber domain, of Lamb waves in a 1-mm-thick aluminum plate.

2.2 Signal processing techniques

This section presents fundamental techniques used in frequency-domain signal analysis. That is, this section presents various forms of the Fourier transform and their relations, starting from the original version. The concept is then extended to the time-frequency representation which is used to developed a spectrum of a signal as a function of time.

2.2.1 Continuous-time Fourier transform

In the classical sense, the Fourier transform was developed in the continuous time domain. Given a function $f(t)$ which is absolutely integrable or $\int_{-\infty}^{\infty} |f(t)|\,dt < \infty$, written as $f \in L^1(\mathbb{R})$, $\mathbb{R}$ is the space of real numbers, the continuous-time Fourier transform (FT) is defined as

$$\mathrm{FT}\{f(t)\} = F(\omega) = \int_{-\infty}^{\infty} f(t)e^{-j\omega t}\,dt. \tag{2.32}$$

The inverse operator, called the inverse Fourier transform, is defined as

$$\mathrm{FT}^{-1}\{F(\omega)\} = f(t) = \frac{1}{2\pi}\int_{-\infty}^{\infty} F(\omega)e^{j\omega t}\,d\omega. \tag{2.33}$$

This inversion is derived from the well-known Fourier integral theorem [89]

$$f(t) = \frac{1}{2\pi} \int_{-\infty}^{\infty} e^{j\omega t}\, d\omega \int_{-\infty}^{\infty} f(s) e^{-j\omega s}\, ds. \tag{2.34}$$

The integrability of $f(t)$ guarantees the existence and the integrability of $F(\omega)$; therefore, Equation (2.33) is well-defined. Note that the integrability condition is only sufficient but not necessary so that there are number of non-absolutely integrable functions which have their Fourier transforms, for example, a Heaviside step function or the function $e^{j\omega_0 t}$. Moreover, strictly speaking, the integrals in both Equations (2.32) and (2.33) must be carried out in the Cauchy principal-value sense: $P.V. \int_{-\infty}^{\infty} f(t)\, dt = \lim_{L\to\infty} \int_{-L}^{L} f(t)\, dt$. It should also be pointed out that since, in the expression (2.32), the integration variable runs over the entire real line (from $-\infty$ to ∞), the same result $F(\omega)$ is obtained if the factor $e^{-j\omega t}$ is replaced by $e^{j\omega t}$. However, this thesis chooses the one as stated in Equation (2.32) because it is consistent with the time-harmonic factor $e^{j\omega t}$ in the wave-propagation model (see Section 2.1) when the frequency is thought to be real and positive.

These definitions can be extended to all functions $f(t)$ which are absolutely square-integrable or $f \in L^2(\mathbb{R})$ due to the fact that the space $L^1(\mathbb{R}) \cap L^2(\mathbb{R})$ is dense[3] in both $L^1(\mathbb{R})$ and $L^2(\mathbb{R})$. For a function $f(t)$ in the space $L^2(\mathbb{R})$ with a proper inner-product introduced, the meaning of $F(\omega)$ can be understood as the complex amplitude of each harmonic basis $e^{j\omega t}$ when $f(t)$ is approximated by the linear combination of those bases. In the context of signal analysis, the magnitude and phase of $F(\omega)$ (called the magnitude and phase spectra) are related to the energy and the arrival time of the frequency component ω.

2.2.2 Discrete-time Fourier transform

In practice, a continuous-time signal is recorded digitally. This signal is hence called a discrete-time signal. With the sampling frequency f_s (in Hz) or the sampling period T_s (in second) $\left(f_s = \frac{1}{T_s}\right)$, a continuous-time signal $f(t)$ is sampled every T_s and becomes a

[3]Let a subset E of a set R is *dense* in R if the smallest closed set which contains E, called $\bar{E}$, is equal to R. This means that a function $f \in R \setminus E$ is a limit point of some sequence of functions in E, and thus, can be approximated by a function in E.

sequence $f[n]$ with the relation

$$f[n] = f(nT_s), \quad n \text{ is an integer.} \tag{2.35}$$

In this expression, the square brackets are used to indicate a signal in the discrete domain or a sequence. For a sequence $f[n]$, the Fourier transform, which is still a continuous function, is called the discrete-time Fourier transform (DTFT) and defined with its inverse as [70]

$$\text{DTFT}\{f[n]\} = F(e^{j\tilde{\omega}n}) = \sum_{n=-\infty}^{\infty} f[n]e^{-j\tilde{\omega}n}, \tag{2.36}$$

and

$$\text{DTFT}^{-1}\{F(e^{j\tilde{\omega}n})\} = f[n] = \frac{1}{2\pi}\int_{-\pi}^{\pi} F(e^{j\tilde{\omega}n})e^{j\tilde{\omega}n}\, d\tilde{\omega}, \tag{2.37}$$

where $\tilde{\omega} = \omega T_s$ is the normalized circular frequency. In comparison to the expression of the continuous-time Fourier transform in Section 2.2.1, the argument of $F(\,)$ is used to distinguish $\text{DTFT}\{f[n]\}$ from $\text{FT}\{f(t)\}$. Similar to that of a continuous-time function $f(t)$, the sufficient condition for a sequence $f[n]$ to ensure existence of its discrete-time Fourier transform is that $f[n]$ must be absolutely summable, i.e. $\sum_{n=-\infty}^{\infty} |f[n]| < \infty$. This condition can be written in mathematical notations as $f \in l^1(\mathbb{R})$.

The nature of sampling causes the the discrete-time Fourier transform to be periodic with a period of 2π; therefore, only the frequency range of 2π of $F(e^{j\tilde{\omega}n})$ is distinct and needs be considered. That is the reason why the limits of integration in the inverse transform are limited to $-\pi$ and π. The concept of magnitude and phase spectra follows those derived from the continuous-time Fourier transform except that the real frequency is normalized by a factor of $f_s = \frac{1}{T_s}$. As a result, the frequency range of the spectrum of a discrete signal (or a sequence) is limited to $-\pi$ to π for the normalized frequency, or $-\frac{\pi}{T_s}$ to $\frac{\pi}{T_s}$ for the real frequency. Hence, for a bandlimited signal with the maximum frequency of $\omega_{\max}$ in radian or $f_{\max}$ in Hz, the sampling period required to maintain all the information of the signal is $\frac{\pi}{\omega_{\max}}$ or $\frac{1}{2f_{\max}}$. If this condition is not met, the signal spectrum at the frequency above $f_s - f_{\max}$ is interfered with the other copy of spectrum in the next period, and thus becomes wrong compared to the spectrum of the original continuous-time signal. This interference is called *aliasing*. In other words, the sampling frequency f_s required to avoid aliasing

must make $f_s - f_{\max} \geq f_{\max}$ or be at least twice of the maximum frequency of a signal, $f_s \geq 2f_{\max}$.

2.2.3 Discrete Fourier transform

Since, in general, the summation in Equation (2.36) cannot be expressed in closed form (as a function of ω) and usually requires calculation by a digital computer, the definitions of Fourier transform and its inverse are modified for practical purposes. This new Fourier transform is called the discrete Fourier transform (DFT) to indicate that a discrete signal $f[n]$ is transformed into a discrete spectrum $F[k]$. The definitions of the discrete Fourier transform and its inverse are:

$$\mathrm{DFT}\{f[n]\} = F[k] = \sum_{n=0}^{N-1} f[n] e^{-j\frac{2\pi}{N}kn}, \tag{2.38}$$

and

$$\mathrm{DFT}^{-1}\{F[k]\} = f[n] = \frac{1}{N} \sum_{k=0}^{N-1} F[k] e^{j\frac{2\pi}{N}kn}. \tag{2.39}$$

Again, the square brackets are used to indicate a sequence. It should be noticed that, to calculate the discrete Fourier transform, only N points of a sequence $f[n]$ are used, and the obtained discrete Fourier transform is no longer a continuous function but a sequence of length N. The relationship between the discrete Fourier transform and the discrete-time Fourier transform can be obtained by the introduction of the discrete Fourier series to represent a periodic sequence made by appending an N-point sequence $f[n]$ together [70]. It turns out that the Fourier series coefficients of such a periodic sequence becomes itself a periodic sequence of length N, and one period of this sequence is the discrete Fourier transform $F[k]$. This $F[k]$ represents a sampled version of one 2π period of the discrete-time Fourier transform of $f[n]$, i.e.

$$\mathrm{DFT}\{f[n]\}[k] = \mathrm{DTFT}\{f[n]\}(e^{j\frac{2\pi}{N}k}), \tag{2.40}$$

where $k = 0, 1, \ldots, N\text{-}1$.

This is a version of the Fourier transform which is implemented in signal analysis applications. The accuracy of it to represent the actual continuous spectrum of the continuous-time signal depends on the sampling frequency f_s and the length of the sequence or DFT-point

N. The use of large N ensures good resolution of the spectrum but does not gain more information after sampling. As a rule, the sampling frequency has to be large enough to maintain all frequency components of the signal after sampling, and the DFT-points must also be large enough to properly represent the spectrum of the signal.

From the expression (2.38), it is seen that one value of $F[k]$ is calculated from all N values of $f[n]$. So, it becomes time-consuming and expensive to calculate the DFT of a very long sequence; the computation cost is proportional to N^2. However, from the structure of the calculation and symmetry of terms in the expression (2.38), the fast algorithm for the discrete Fourier transform was developed. This algorithm is called the fast Fourier transform (FFT) whose computation is proportional to $N \log_2 N$. The same strategy can be employed for the calculation of the inverse transform because of the analogous structures between Equations (2.38) and (2.39).

2.2.4 Short-time Fourier transform

Often times, signals recorded in some systems such as Lamb wave signals, are non-stationary, i.e. signals' frequency contents change with time. For a signal of this type, the normal Fourier transform becomes insufficient to capture the signal's relevant characteristics because it uses the signal at all time and shows the total signal's frequency content over that period of time. A new transform is developed to focus on the signal's spectrum over a short period of time; this technique is called the short-time Fourier transform (STFT) and defined first for a signal $f(t)$ in the continuous domain as

$$\mathrm{STFT}_g f = F_g(t,\omega) = \int_{-\infty}^{\infty} f(\tau) g^*(\tau - t) e^{-j\omega\tau}\, d\tau, \tag{2.41}$$

where * denotes the complex conjugate and $g \neq 0$ is the *window function*. This function g is chosen to be compactly supported with its support centered at the origin so that the $F_g(t,\omega)$ represents the Fourier transform of f in the neighborhood of t. Such window functions are, for example, Gaussian, Hanning, Hamming, etc. To be precise in this expression, $F_g(t,\omega)$ is well-defined if $f, g \in L^2(\mathbb{R})$. In fact, as long as f and g are in dual spaces, i.e. $f \in L^p(\mathbb{R})$ and $f \in L^{p'}(\mathbb{R})$, where $\frac{1}{p} + \frac{1}{p'} = 1$, then $F_g(t,\omega)$ is well-defined because $f(\tau)\, g^*(\tau - t) \in L^1(\mathbb{R})$ and thus, its Fourier transform exists [32]. Note further that an energy density of the STFT

is defined as a *spectrogram*, i.e.

$$\mathrm{SPEC}_g f = |F_g(t,\omega)|^2 = \left| \int_{-\infty}^{\infty} f(\tau) g^*(\tau - t) e^{-j\omega\tau}\, d\tau \right|^2. \tag{2.42}$$

The spectrogram measures the energy of f in the time-frequency neighborhood of (t, ω). It represents how the energy of a particular frequency component is localized at a particular time. This is best presented on the time-frequency plane as a contour surface as shown in Figure 2.4. Since the STFT or spectrogram represents the energy distribution on the time-frequency plane, it belongs to a class of signal processing techniques called a time-frequency representation (TFR). Note that there are a number of other TFR techniques besides the STFT or the spectrogram. To name a few, the wavelet transform (WT) or its energy-density version, called the scalogram, the Wigner distribution, and the Choi-Williams distribution are all the TFR techniques. These techniques have some special advantages over the others depending on the nature of a signal or type of applications [21]. In this study which deals with Lamb wave signals, the STFT is shown to be more appropriate over some other well-known techniques [69].

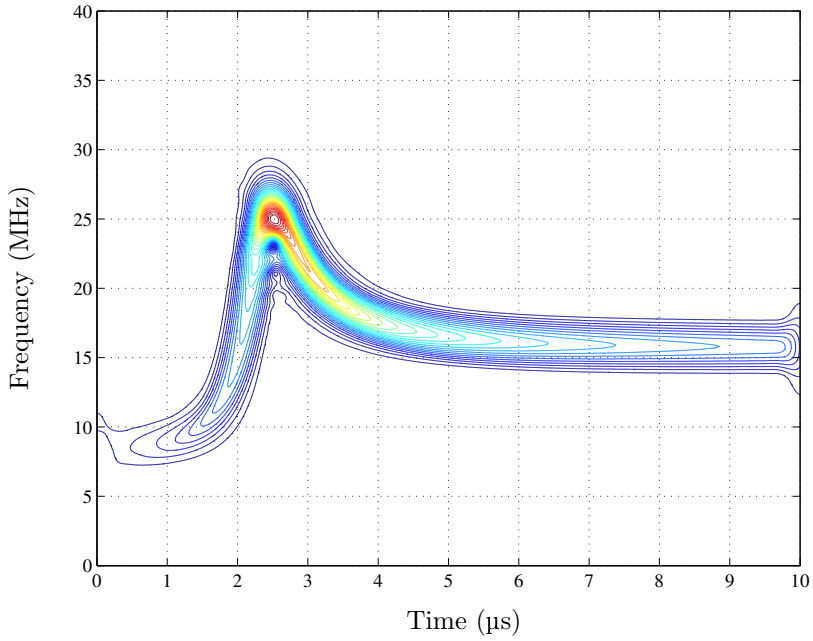

Figure 2.4: Time-frequency representation of a non-stationary signal by the STFT.

Since the TFR is represented as a two-dimensional image (its horizontal and vertical axes

are frequency and time), the quality of the representation can be improved by most image-enhancement techniques. For example, the reassignment method shifts the magnitude of the contour image at each point to the local center of gravity of that surface, thus reduces the spreading of the contour surface [5]. This reassignment method can be further improved by the differential algorithm and the diffusion technique [48]. These improvements gives the operator more controls over the image so that the optimum quality can be achieved.

As other versions of the Fourier transforms, the signal $f(t)$ can be reconstructed from $F_g(\tau, \omega)$ by the inverse transform, however in a much more complicated way. The inversion requires an inner-product; hence, f and g must be in a Hilbert space. Let $f, g \in L^2(\mathbb{R})$ ($L^2(\mathbb{R})$ is a Hilbert space, and thus, $F_g(t, \omega)$ is well-defined) and $\langle ., . \rangle$ represent an inner-product. With another function $\gamma \in L^2(\mathbb{R})$ such that $\langle g, \gamma \rangle \neq 0$. The inversion formula is defined as

$$f(t) = \frac{1}{2\pi \langle g, \gamma \rangle} \int_{-\infty}^{\infty} \int_{-\infty}^{\infty} F_g(\tau, \omega) \gamma(t - \tau) e^{j\omega t} \, d\omega \, d\tau, \tag{2.43}$$

where the inner-product $\langle g, \gamma \rangle$ is defined as

$$\langle g, \, \gamma \rangle = \int_{-\infty}^{\infty} g(t) \gamma^*(t) \, dt. \tag{2.44}$$

If the window function g is used in places of γ, with a proper scaling such that $\langle g, g \rangle = 1$, Equation (2.43) becomes

$$f(t) = \frac{1}{2\pi} \int_{-\infty}^{\infty} \int_{-\infty}^{\infty} F_g(\tau, \omega) g(t - \tau) e^{j\omega t} \, d\omega \, d\tau. \tag{2.45}$$

It is clear that, at a fixed time t, the local spectrum $F_g(t, \omega)$ is calculated from all the value of a signal within the support of the window g centered at time t. This fact indicates that the obtained spectrum still involves some averaging of the information from other times and cannot represent the exact spectrum at that instant. This intuition is stated and proven mathematically as the *uncertainty principle*. The uncertainty principle simply negates the possibility of determining the *instantaneous frequency* at an exact time t in general. However, the concept of the instantaneous frequency is not totally fictional. There are several approaches and notations for the instantaneous frequency which work well for some special classes of signals [21].

There are a number versions of the uncertainty principle depending on the aspects one takes to derive it. The classical uncertainty principle is referred to as the Heisenberg-Pauli-Weyl inequality. It states that, for $f \in L^2(\mathbb{R})$ and arbitrary $u, \xi \in \mathbb{R}$,

$$\left(\frac{1}{\|f\|_2^2}\int_{-\infty}^{\infty}(t-u)^2|f(t)|^2\,dt\right)\left(\frac{1}{2\pi\|f\|_2^2}\int_{-\infty}^{\infty}(\omega-\xi)^2|F(\omega)|^2\,d\omega\right) \geq \frac{1}{4}, \tag{2.46}$$

where $F(\omega)$ is the Fourier transform of f and $\|f\|_2^2$ is the L^2-norm of f defined as

$$\|f\|_2^2 = \langle f, f\rangle = \int_{-\infty}^{\infty}|f(t)|^2\,dt. \tag{2.47}$$

The equality holds if and only if f is Gaussian or of the form $ae^{j\xi t - b(t-u)^2}$, where $a, b \in \mathbb{C}$, $\mathbb{C}$ is a set of complex numbers.

Each term in the parentheses on the left-hand side of Inequality (2.46) can be directly related to the width of the support of the time-frequency atom $e^{j\omega\tau}f^*(\tau - t)$ centered at (t, ω), in each axis—time and frequency. The direct interpretation of Inequality (2.46) is that the support of the mentioned time-frequency atom cannot be made arbitrary small on the time-frequency plane. Consider the window function g and the corresponding time-frequency atom $e^{j\omega\tau}g^*(\tau - t)$. Since the resolution of this atom is represented by the width of its support in each axis, the uncertainty principle implies that the resolution in time can be improved (by reducing the width of a support in the time-axis) at the expense of poorer resolution in frequency (the longer width of a support in the frequency-axis), and vice versa.

The STFT is implemented by its discrete version called the discrete short-time Fourier transform. This version of the STFT is defined by [61]

$$F_g[m,k] = \sum_{n=0}^{N-1} f[n]g^*[n-m]e^{-j\frac{2\pi}{N}kn}, \tag{2.48}$$

where the index k is the frequency index and the index m indicates the location in time. The inverse transform is derived in a similar fashion to that of the discrete Fourier transform. The inversion formula analogous to Equation (2.45) is

$$f[n] = \frac{1}{N}\sum_{m=0}^{N-1}\sum_{k=0}^{N-1} F_g[m,k]g[n-m]e^{j\frac{2\pi}{N}kn}. \tag{2.49}$$

Figure 2.5 shows the procedure to calculate the STFT according to Equation (2.48). In Figure 2.5(a), a sequence $f[n]$ is first multiplied by a window sequence centered at a specific

time (of index m), $g^*[n-m]$, to obtain a windowed sequence $f[n]g^*[n-m]$. Then, this windowed sequence is discretely transformed by the FFT algorithm. The window is moved to another time and the same procedure is repeated. The spectra at different times are stacked along the time axis as shown in Figure 2.5(b). The two-dimensional contour of this three-dimensional plot is an image shown earlier in Figure 2.4.

2.3 Laser ultrasonics

This section presents a background in generation and detection of ultrasonic waves using a laser system. A specific laser-system setup for experiment which is used in this research is also given.

2.3.1 Laser generation

This research uses a Q-switched, Nd:YAG laser to generate ultrasonic waves. This laser sends out an single pulse of energy up to 8 mJ. The energy density level of a pulse is adjustable both internally inside the laser and externally by the use of absorption plates and lenses. The pulse length is around 15 ns which is considered very short for a typical ultrasonic frequency range. The path of a laser pulse can be optically aligned onto the surface of a specimen by the aid of another He-Ne laser, which sends out a continuous beam in the visible frequency range.

Ultrasonic waves are generated by the heating of a material. Once the laser energy is emitted and incident on to the surface of the material, part of that laser energy is absorbed around the top layer of the surface. The absorption mechanism and the amount of absorbed energy depend on the type of the material. The absorbed laser energy usually causes a temperature rise at the surface and thus induces thermal expansion. Since the heated area is localized, i.e. constrained by the surrounding material, a stress is induced from a strain according to thermoelasticity. Depending on the level of laser energy density, various mechanisms such as expansion or vaporization can occur in the material, causing ultrasonic waves with different characteristics. Two major generation mechanisms are thermal expansion and ablation.

When the laser energy density is low, the material is only heated and expands in the

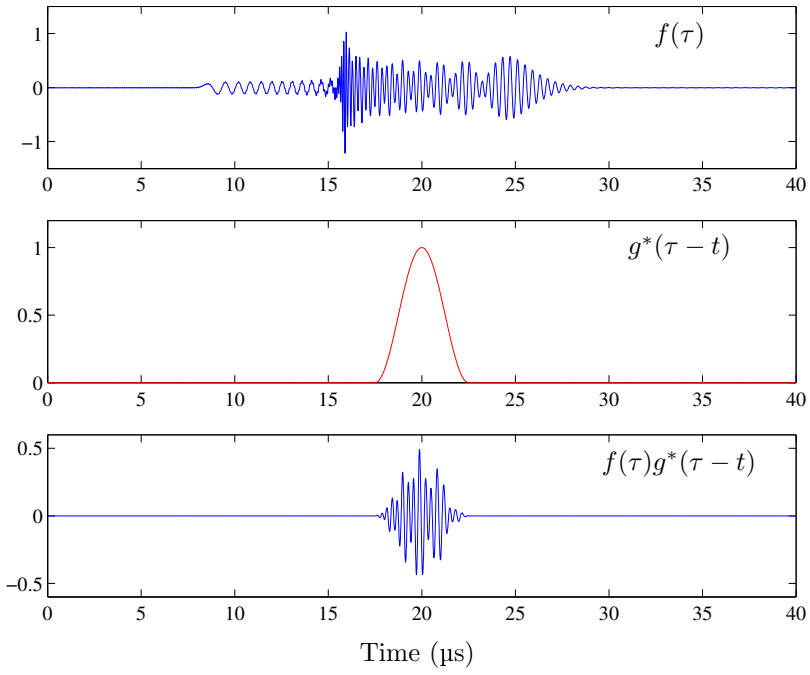

(a) A time-domain signal and its windowed version.

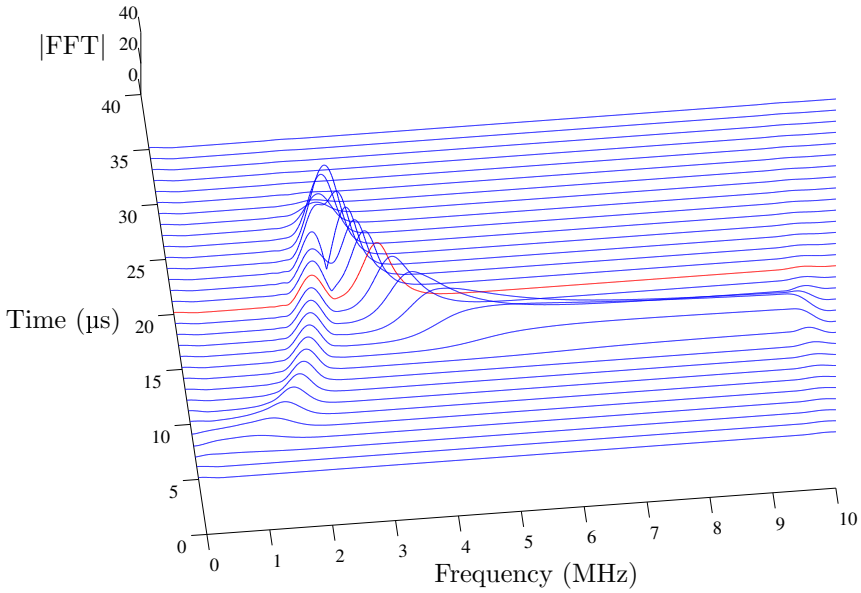

(b) A series of FFT at different times.

Figure 2.5: The STFT algorithm.

lateral direction (normal to the direction of an incident beam); therefore, the induced stress occurs in the direction of expansion (in-plane direction) as shown in Figure 2.6(a). An ultrasonic source created by this mechanism is called a *thermoelastic* source. The induced-stress amplitude can be approximated by [45]

$$\sigma \propto \beta\delta\frac{E_0}{t_0}, \tag{2.50}$$

where β is the coefficient of linear thermal expansion, δ is the skin depth in the material within which the laser energy is absorbed, E_0 is the laser energy, and t_0 is the duration of the laser pulse. The constant related both sides of equation depends on the type of the material.

As the laser energy density increases, a part of the material on the surface starts to melt. When the laser energy density is sufficiently large, some material will eventually be vaporized, and thus ablation occurs. Vaporized particles will produce a net stress to the material in the perpendicular (out-of-plane) direction due to their change of momentum. This kind of ultrasonic source is called an *ablation* source. The schematic diagram of the ablation source is shown in Figure 2.6(b).

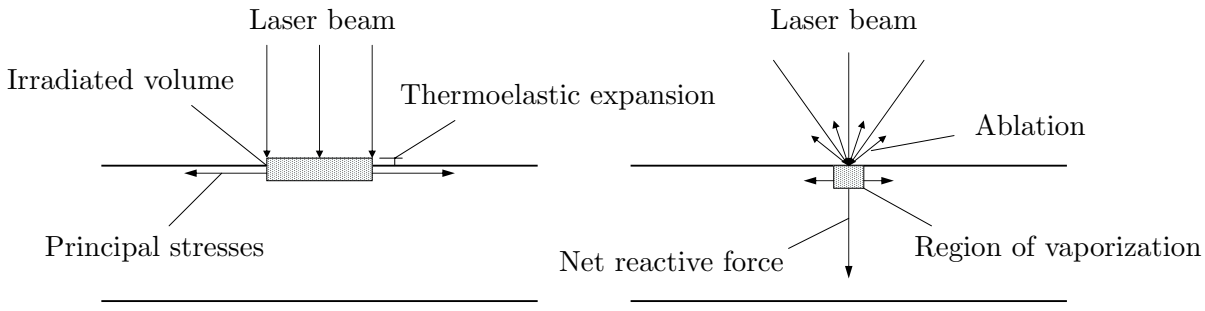

(a) Thermoelastic mechanism. (b) Ablation mechanism.

Figure 2.6: Laser ultrasonic generation using a pulse laser.

In this case, the induced stress can be calculated by the following equation [86]:

$$\sigma = \frac{I^2}{\rho\big[L + C(T_v - T_0)\big]^2}, \tag{2.51}$$

where I is an incident power density, ρ is the material density, L is the latent heat required to vaporize the solid, C is the specific thermal capacity, T_v and T_0 are the initial and vaporization temperatures, respectively.

Note that, in the ablation regime, the surface of the material still undergoes thermal expansion; therefore, a thermoelastic stress also occurs. However, since a normal stress caused by ablation is usually much larger in magnitude than a thermoelastic stress, this thermoelastic stress can be neglected and the laser source can be viewed as a pure ablation source. This is usually the case, in fact, when a laser beam is focused to a point on the surface of the material. In NDE applications, although a part of the material surface will be damaged, an ablation source is, often times, preferred to the thermoelastic one because ultrasonic waves generated by this process are of desired high signal-to-noise ratio (SNR).

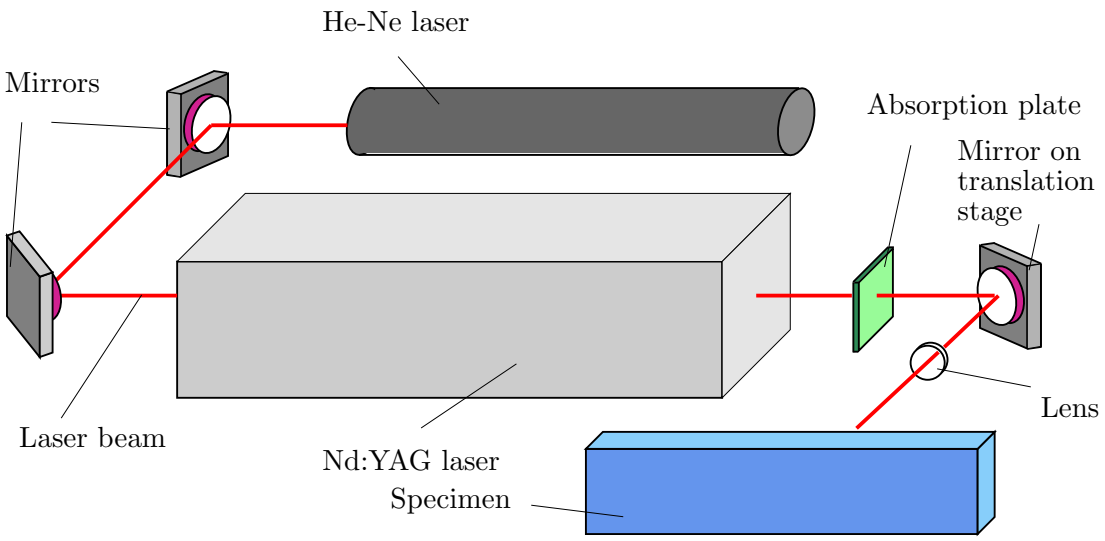

Figure 2.7: Schematic diagram of a laser generation system. (After Benz [8]).

Figure 2.7 shows the setup of the laser generation system used in this research. A He-Ne laser is lined up with the Nd:YAG laser for alignment purposes. The laser energy is reduced by an absorption plate to decrease the damage on the specimen and for safety reasons. The laser beam is focused onto the surface of the specimen by a lens to create a point, ablation source.

2.3.2 Laser detection

On the detection side of a laser system, this research uses the heterodyne interferometer. This laser interferometer employs the Doppler technique to measure the normal (out-of-plane) particle velocity at the surface of a specimen. The setup is shown in Figure 2.8. A vertically-polarized laser beam generated by the Argon-ion laser is split by an acousto-optic modulator (AOM) into frequency-modulated, and non-frequency-modulated beams. The frequency-modulated beam, going directly to photodetector (shown as PD in the figure), is used as a reference beam. The non-frequency-modulated beam, called an object beam, is directed to the surface of a specimen. An object beam goes through a series of changes in polarization to become circularly-polarized before reaching the specimen. This polarization change is for convenience. A reflected object beam, passing through the same series of changes in polarization, is guided to recombine with a reference beam (both beams finally have the same polarization). This combined beam is sent to a photodetector for measurement. The movement on the specimen's surface causes a frequency shift in the reflected object beam due to the Doppler effect. If an object beam is directed perpendicularly to a surface of a specimen, that frequency shift $\delta\nu$ is directly proportional to a magnitude of the out-of-plane, surface particle velocity v by the formula

$$\delta\nu = \frac{2v}{\lambda_b}, \tag{2.52}$$

where λ_b is the wavelength of a laser beam [86].

A photodetector measures the intensity of the combined beam and converts it into an electric signal which still contains the frequency shift $\delta\nu$. This electric signal is sent to the frequency-modulation (FM) discriminator where the frequency shift is converted into output voltage by the following relation

$$V = K\delta\nu, \tag{2.53}$$

where K is the slope of the FM-discriminator response curve which is a constant associated with each individual FM-discriminator [12]. From Equations (2.52) and (2.53), it is clearly seen that the output voltage is directly proportional to the amplitude of the out-of-plane

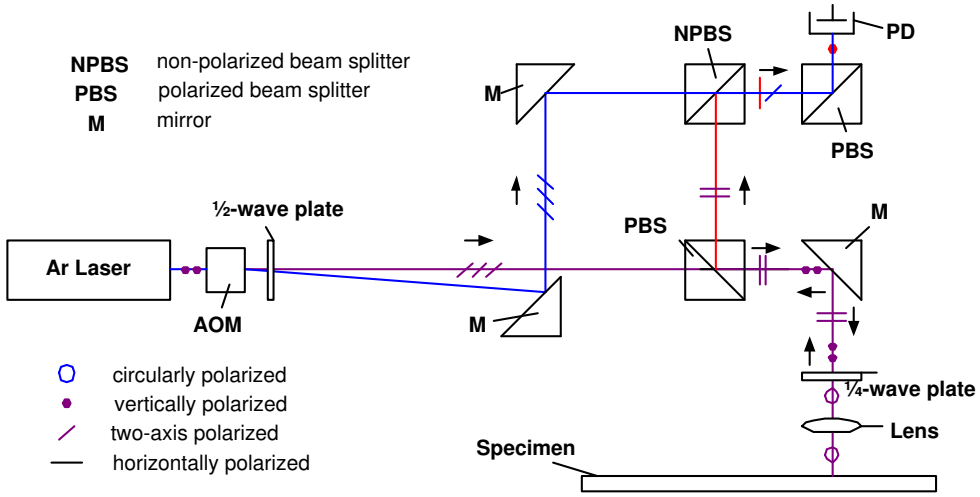

Figure 2.8: Schematic diagram of a laser detection system—the single-probe setup as a part of the dual-probe laser interferometer.

particle velocity; therefore, this converted electric signal directly represents the motion at the surface of the specimen (with a multiplying scalar constant). This signal is recorded by an oscilloscope for post-processing.

The setup described earlier is called a single-probe setup since the laser system is set to measure the movement of a specimen's surface only at one point (one probe). Because lights with different polarization can propagate independently, the other axis of polarization (vertical axis of the object beam after the first polarized beam-splitter) can be used to simultaneously measure the motion at the other point on the surface of the specimen. This setup becomes the dual-probe setup [44]. The dual-probe setup uses the same principle as the single-probe setup but requires more instrumentation. In fact, the setup shown in Figure 2.8 is a part of the dual-probe setup with one probe removed. This can be recognized since the reference beam contains two directions of polarization.

CHAPTER 3

LAMB WAVES WITH ATTENUATION

Classical plane-strain Lamb waves are derived in Chapter 2. It can be seen from the displacement expressions (Equations (2.21) and (2.22)) that the plane-strain Lamb waves undergo no decay as they propagate, thus can propagate forever. This chapter considers the situation when Lamb waves experience decay in amplitude with propagation distance. This behavior is called *attenuation*. In general, Lamb waves will be attenuated by two main mechanisms. The first mechanism is *material absorption*. This mechanism happens when Lamb waves are propagating inside the absorptive material; their energy is absorbed by the material. Usually, absorption is a result of friction between material particles. Wave energy is converted to heat as the waves propagate. This situation occurs when the medium is viscous, or the medium is a *viscoelastic* material. This class of materials includes plastics or polymers, rubbers, cement-pasted materials and concrete, and composite materials. In fact, all materials possess some degrees of viscoelasticity, but in the ultrasonic frequency range, this effect is negligible in some materials, and Hooke's law holds. This latter type of materials includes common metals such as aluminum and steel.

The second mechanism which causes attenuation of Lamb waves is *leakage*. This situation occurs when the layered system in which Lamb waves are propagating is an open system so that Lamb waves' energy is not confined in the system. For example, this situation is encountered when a plate is perfectly attached to a half-space. In this case, when partial P- and SV-waves are incident on the interface between the plate and the half-space, they are not totally reflected. Parts of them are transmitted or "leak" into the other material. Since the other material is a half-space, those transmitted waves will never come back to the plate. That causes reduction in energy of Lamb waves in the plate. Attenuated Lamb waves in this case is specially called *leaky Lamb waves*. This situation could happen even when both materials in the problem are loss-less (or elastic).

This chapter derives mathematically attenuated Lamb waves. The chapter starts with introduction of attenuation into a time-harmonic wave-propagation problem in general. The concept is extended to Lamb waves in later sections. The absorption mechanism is described briefly in Section 3.2 because it is not the main focus in this research. However, the other mechanism or leakage, which is of this research's interest, is explained in full details in Section 3.3. Then, leaky Lamb waves are mathematically derived for the case of an isotropic, elastic plate connected with an isotropic, elastic half-space. This derivation is next shown to already include the case when the half-space is a fluid. The latter inclusion is important because the experiment conducted in this study will be, for simplicity, on a plate loaded with a fluid half-space.

3.1 Time-harmonic wave propagation with attenuation

To demonstrate the general idea, it is sufficient to consider a free, one-dimensional plane wave propagation, say a longitudinal wave propagating in the x-direction. In this case, $u_x(x,t)$ is the only nonzero component of the displacement, and the governing equations of motion (2.6) with no body forces reduce to a single one-dimensional wave equation

$$\frac{\partial^2 u_x}{\partial x^2} = \frac{1}{c_L^2}\frac{\partial^2 u_x}{\partial t^2}. \tag{3.1}$$

Following a time-harmonic plane wave solution given by the expression (2.13), one can write the solution to Equation (3.1) as

$$u_x = Ae^{j(\omega t - kx)}, \tag{3.2}$$

where the wavenumber $k = \frac{\omega}{c_L}$.

If the frequency ω is understood to be real and positive, and the wavenumber k is a complex number represented by

$$k = k_R - jk_I, \tag{3.3}$$

where both k_R and k_I are real and positive, then the solution in Equation (3.2) becomes

$$u_x = Ae^{-k_I x}e^{j(\omega t - k_R x)}. \tag{3.4}$$

In this form, the factor $e^{j(\omega t - k_R x)}$ still represents a time-harmonic wave propagating in the x-direction while the additional exponential term $e^{-k_I x}$ represents the decay over distance as the wave propagates. This exponential decay shows attenuation of the wave. The parameter k_I is called attenuation in *neper* (Np) per length; sometimes, α is used instead of k_I to represent attenuation. The unit neper is dimensionless; it specifies the base of the decay to be e (compared to the unit decibel (dB) which specifies the base of the decay to be 10)[1].

The velocity of this wave can be directly calculated as

$$\begin{aligned} c &= \frac{\omega}{k} \\ &= \frac{\omega}{k_R - jk_I} \\ &= \frac{\frac{\omega}{k_R}}{1 - j\frac{k_I}{k_R}} \\ &= \frac{c_p}{1 - j\frac{\kappa}{2\pi}}. \end{aligned} \tag{3.5}$$

In this formula, $c_p = \frac{\omega}{k_R}$ is the phase velocity of the wave, which is always real and positive; $\kappa = 2\pi\frac{k_I}{k_R}$ represents the attenuation in neper/wavelength (attenuation after the wave travels one wavelength[2].). Note that κ could be a function of ω in general.

This section demonstrates that an attenuated time-harmonic wave can be represented by the factor $e^{j(\omega t - kx)}$ which is also used for a non-attenuated wave (developed in Section 2.1.2). The difference is that, for an attenuated wave, the wavenumber becomes a complex number with its imaginary part representing attenuation. Note that waves with attenuation can alternatively be modelled by keeping the wavenumber real and allowing the frequency to be complex. However, this approach will yield different results from the results of using the complex wavenumber because the two approaches represent different physical problems [53]. The more suitable approach to the wave-propagation problem at hand is the one with the complex wavenumber since the complex wavenumber is directly derived from the well-accepted and fundamental constitutive model for viscoelastic solids.

[1] 1 Np $= 20 \log_{10} e = 8.686$ dB.

[2] It is easy to see that if the wavelength $\frac{2\pi}{k_R}$ is substituted into x in the solution (3.2), the attenuation $k_I x$ becomes κ

3.2 Attenuation by material absorption

Material absorption causes attenuation of a wave. One class of materials which possesses absorption is a viscoelastic material. This section demonstrates briefly how a time-harmonic wave is attenuated while propagating in a material of this class. A one-dimensional problem is again considered for simplicity. The extensive background in viscoelasticity is omitted. A nice treatment in this topic can be found in References [36], [20], [28].

A viscoelastic material has a special feature that its strain response to stress or stress response to strain is a function of time (unlike those of an elastic material). Therefore, the frequency of the loading becomes significant to how the material responds. For time-harmonic field quantities, $\sigma_{ij}(\mathbf{x},t) = \hat{\sigma}_{ij}(\mathbf{x})e^{j\omega t}$, $\varepsilon_{ij}(\mathbf{x},t) = \hat{\varepsilon}_{ij}(\mathbf{x})e^{j\omega t}$ and so on, the stress and strain are related by *complex moduli* which are, in general, functions of frequency ω. For an isotropic, viscoelastic material, the constitutive equations relating the amplitudes of the components of stress and strain tensors, can be described by two complex moduli in the analogous form to Equation (2.3) for an isotropic, elastic material:

$$\hat{\sigma}_{ij}(\mathbf{x}) = \hat{\lambda}(\omega)\delta_{ij}\hat{\varepsilon}_{kk}(\mathbf{x}) + 2\hat{\mu}(\omega)\hat{\varepsilon}_{ij}(\mathbf{x}). \tag{3.6}$$

Each modulus is, in general, complex-valued; if its imaginary part is identically equal to zero and its real part is a constant independent of ω, Equation (3.6) reduces to Equation (2.3), or the material becomes elastic. If the strain and displacement are assumed small, the linearized theory holds even though material behavior is nonlinear (with time). Within the linear framework, kinematical equations and balance of momenta expressed by Equations (2.1), (2.4), and (2.5) still apply. For a time-harmonic problem without body forces, substitution of the new constitutive equations (3.6) into Equations (2.1) and (2.5) gives the equations of motion for an isotropic, viscoelastic material (follow the derivation in Appendix A.1.1 with λ and μ replaced by $\hat{\lambda}(\omega)$ and $\hat{\mu}(\omega)$, respectively):

$$\left[\hat{\lambda}(\omega) + \hat{\mu}(\omega)\right]\hat{u}_{j,ji} + \hat{\mu}(\omega)\hat{u}_{i,jj} + \rho\omega^2\hat{u}_i = 0. \tag{3.7}$$

In these equations, the $\hat{}$ represents the amplitude of time-harmonic quantities (which depend only on the spatial variable $\mathbf{x}$).

For a one-dimensional, longitudinal wave-propagation problem where x is the only independent spatial variable and $\hat{u}_x$ is the only nonzero component of the displacement, Equations (3.7) reduce to the wave equation

$$\frac{\partial^2 \hat{u}_x}{\partial x^2} + \frac{\omega^2}{\hat{c}_L^2}\hat{u}_x = 0, \tag{3.8}$$

where the wave velocity $\hat{c}_L = \sqrt{\frac{\hat{\lambda}(\omega)+2\hat{\mu}(\omega)}{\rho}}$ is a complex function of ω. For a shear wave propagation, the similar equation is obtained with $\hat{u}_x$ replaced by the only nonzero component of the displacement (perpendicular to the propagation direction), $\hat{u}_y$ or $\hat{u}_z$, and $\hat{c}_L$ replaced by the complex shear wave velocity $\hat{c}_T = \sqrt{\frac{\hat{\mu}(\omega)}{\rho}}$.

The comparison of Equation (3.8) to Equation (3.1) suggests that the solution to this equation is of the form described by Equation (3.2) with the wavenumber

$$k = \frac{\omega}{\hat{c}_L(\omega)}. \tag{3.9}$$

This wavenumber is a complex function of frequency; therefore, the wave is attenuated.

For propagation of Lamb waves in a viscoelastic plate, as seen in Section 2.1.4, the solution of a time-harmonic wave propagation in an unbounded medium (such as a solution expressed by Equation (3.2)) can be used to derive the dispersion equation through the partial wave technique. For a plate with both stress-free boundaries, the same dispersion equations, Equations (2.26) and (2.28) are obtained with k, α_L, and α_T all being complex-valued (due to the complex wave velocities). Hence, Lamb waves also experience attenuation as they propagate with the imaginary part of the wavenumber k representing attenuation.

3.3 Attenuation by leakage

The situation which is of more interest in this research is when Lamb waves exhibit attenuation due to leakage. This situation is the main focus because, it models the experiments of this study. The specific problem configuration is Lamb waves propagating in the plate whose one side is attached to a half-space of a different material. Both materials are assumed to be isotropic, linearly-elastic.

In this section, a mathematical model for this wave-propagation problem will be developed. The dispersion equation which is a complex equation will be derived. The section

starts with the derivation of Lamb waves' dispersion equation when a half-space is a solid. The result developed in this case will be shown to cover the case when the half-space is a fluid. The dispersion relation for the case when the half-space is an ideal fluid will be given explicitly in Section 3.3.3.

3.3.1 A solid plate on a solid half-space

In this subsection, a system consisting of an elastic plate attached to an elastic half-space by a perfect bond is considered. The perfect bond enforces continuity of all displacement and stress components. To start with, the problem is setup similarly to the configuration shown in Figure 2.2 except that one stress-free boundary becomes a perfect bond between two materials. The problem is assumed to be plane-strain in the y-direction; all problem's parameters shown in Figure 3.1. Since there is a half-space, two additional partial waves representing bulk P- and SV-waves going away from the plate must be included. Note that there are not partial waves coming to the plate from the half-space because those partial waves going into the half-space will not be reflected. The top surface remains stress-free.

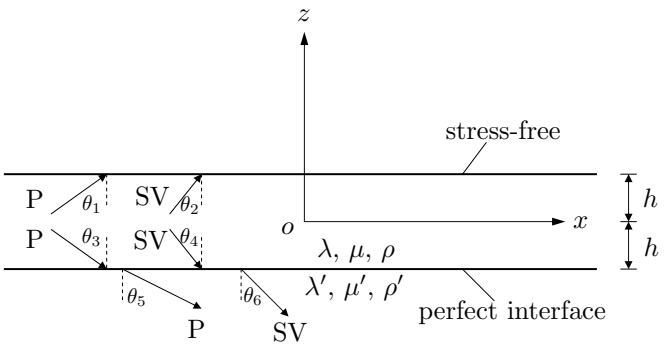

Figure 3.1: Leaky Lamb waves in an infinite plate attached on a half-space.

The derivation in Section 2.1.4 can be extended to this problem. Displacement fields due to four partial waves are given by Equations (2.15) while two more displacement fields

in the half-space are

$$\begin{aligned}\mathbf{u}^{(5)} &= A_5(\sin\theta_5\,\mathbf{e_x} - \cos\theta_5\,\mathbf{e_z})e^{j\left[\omega t - k'_L(\sin\theta_5\,x - \cos\theta_5\,z)\right]} \\ \mathbf{u}^{(6)} &= A_6(\cos\theta_6\,\mathbf{e_x} + \sin\theta_6\,\mathbf{e_z})e^{j\left[\omega t - k'_T(\sin\theta_6\,x - \cos\theta_6\,z)\right]},\end{aligned} \tag{3.10}$$

where $k'_L = \frac{\omega}{c'_L}$ and $k'_T = \frac{\omega}{c'_T}$ are the longitudinal and shear wavenumbers in the half-space, respectively.

If the time-harmonic wave field in the plate is assumed to have a factor $F = e^{j(\omega t - kx)}$, the wavenumbers of all partial waves in the x-direction must match, i.e.

$$k_L \sin\theta_1 = k_T \sin\theta_2 = k_L \sin\theta_3 = k_T \sin\theta_4 = k'_L \sin\theta_5 = k'_T \sin\theta_2 = k. \tag{3.11}$$

These equations give the relationships:

$$\begin{aligned}\theta_1 = \theta_3 = \theta_L, \qquad & \theta_5 = \theta'_L, \\ \theta_2 = \theta_4 = \theta_T, \qquad & \theta_6 = \theta'_T.\end{aligned} \tag{3.12}$$

Now, the total displacement field in the plate, $\mathbf{u}^{(p)} = \mathbf{u}^{(1)} + \mathbf{u}^{(2)} + \mathbf{u}^{(3)} + \mathbf{u}^{(4)}$, is equal to the sum of Equations (2.21) and (2.22) while the total displacement field in the half-space can be obtained from $\mathbf{u}^{(hs)} = \mathbf{u}^{(5)} + \mathbf{u}^{(6)}$. In terms of new parameters $\alpha'_L = k'_L \cos\theta'_L = \sqrt{\frac{\omega^2}{{c'_L}^2} - k^2}$ and $\alpha'_T = k'_T \cos\theta'_T = \sqrt{\frac{\omega^2}{{c'_T}^2} - k^2}$, the displacement components in the half-space are given by

$$\begin{aligned}u_x^{(hs)} &= \Big(A_5 \frac{k}{k'_L} e^{j\alpha'_L z} + A_6 \frac{\alpha'_T}{k'_T} e^{j\alpha'_T z}\Big) F \\ &= \Big(C_5 k e^{j\alpha'_L z} + C_6 \alpha'_T e^{j\alpha'_T z}\Big) F,\end{aligned} \tag{3.13}$$

and

$$\begin{aligned}u_z^{(hs)} &= \Big(-A_5 \frac{\alpha'_L}{k'_L} e^{j\alpha'_L z} + A_6 \frac{k}{k'_T} e^{j\alpha'_T z}\Big) F \\ &= \Big(-C_5 \alpha'_L e^{j\,\alpha'_L z} + C_6 k e^{j\alpha'_T z}\Big) F,\end{aligned} \tag{3.14}$$

where $C_5 = \frac{A_5}{k'_L}$ and $C_6 = \frac{A_6}{k'_T}$ are new constants.

Note that since the problem does not possess symmetry with respect to the x-axis, the notion of symmetric and anti-symmetric modes becomes meaningless, and the motion

cannot be split into pure symmetric and anti-symmetric parts. The stress components σ_{zz} and σ_{zx} are calculated in each domain. In the plate, the stress components are the sum of those in Equations (2.23) and (2.24). They are explicitly

$$\begin{aligned}\sigma_{zz}^{(p)} &= \mu\big[-j(\alpha_T^2-k^2)C_1\cos(\alpha_L z)-(\alpha_T^2-k^2)C_2\,\sin(\alpha_L z)\\ &\qquad +2jk\alpha_T C_3\cos(\alpha_T z)+2k\alpha_T C_4\sin(\alpha_T z)\big]F, \qquad (3.15)\\ \sigma_{zx}^{(p)} &= -\mu\big[2k\alpha_L C_1\sin(\alpha_L z)+2jk\alpha_L C_2\cos(\alpha_L z)\\ &\qquad +(\alpha_T^2-k^2)C_3\sin(\alpha_T z)+j(\alpha_T^2-k^2)C_4\cos(\alpha_T z)\big]F. \qquad (3.16)\end{aligned}$$

In the half-space, the expressions follow the same formulas; the results are (see details in Appendix A.2.3)

$$\begin{aligned}\sigma_{zz}^{(hs)} &= \mu' j\Big[-({\alpha'_T}^2-k^2)C_5 e^{j\alpha'_L z}+2k\alpha'_T C_6 e^{j\alpha'_T z}\Big]F, \qquad (3.17)\\ \sigma_{zx}^{(hs)} &= \mu' j\Big[2k\alpha'_L C_5 e^{j\alpha'_L z}+({\alpha'_T}^2-k^2)C_6 e^{j\alpha'_T z}\Big]F. \qquad (3.18)\end{aligned}$$

The boundary conditions for this problem consist of six conditions; they are two stress-free conditions at the top of the plate ($z=h$) and four stress- and displacement-continuity conditions at the interface between a plate and a half-space ($z=-h$). Satisfying these boundary conditions results in a system of six homogeneous equations with six unknowns, C_1, C_2, …, C_6,

- $\sigma_{zz}^{(p)}=0$ @ $z=h$:

$$-j(\alpha_T^2-k^2)C_1\cos(\alpha_L h)-(\alpha_T^2-k^2)C_2\sin(\alpha_L h)+2jk\alpha_T C_3\cos(\alpha_T h)$$
$$+2k\alpha_T C_4\sin(\alpha_T h)=0. \qquad (3.19)$$

- $\sigma_{zx}^{(p)}=0$ @ $z=h$:

$$2k\alpha_L C_1\sin(\alpha_L h)+2jk\alpha_L C_2\cos(\alpha_L h)+(\alpha_T^2-k^2)C_3\sin(\alpha_T h)$$
$$+j(\alpha_T^2-k^2)C_4\cos(\alpha_T h)=0. \qquad (3.20)$$

- $\sigma_{zz}^{(p)}=\sigma_{zz}^{(hs)}$ @ $z=-h$:

$$-j(\alpha_T^2-k^2)C_1\cos(\alpha_L h)+(\alpha_T^2-k^2)C_2\sin(\alpha_L h)+2jk\alpha_T C_3\cos(\alpha_T h)$$
$$-2k\alpha_T C_4\sin(\alpha_T h)=\frac{\mu'}{\mu}j\Big[-({\alpha'_T}^2-k^2)C_5 e^{-j\alpha'_L h}+2k\alpha'_T C_6 e^{-j\alpha'_T h}\Big]. \qquad (3.21)$$

- $\sigma_{zx}^{(p)} = \sigma_{zx}^{(hs)}$ @ $z = -h$:

$$2k\alpha_L C_1 \sin(\alpha_L h) - 2jk\alpha_L C_2 \cos(\alpha_L h) + (\alpha_T^2 - k^2) C_3 \sin(\alpha_T h)$$
$$- j(\alpha_T^2 - k^2) C_4 \cos(\alpha_T h) = \frac{\mu'}{\mu} j \Big[2k\alpha'_L C_5 e^{-j\alpha'_L h} + ({\alpha'_T}^2 - k^2) C_6 e^{-j\alpha'_T h} \Big]. \quad (3.22)$$

- $u_z^{(p)} = u_z^{(hs)}$ @ $z = -h$:

$$j\alpha_L C_1 \sin(\alpha_L h) + \alpha_L C_2 \cos(\alpha_L h) - jkC_3 \sin(\alpha_T h) - kC_4 \cos(\alpha_T h)$$
$$= -\alpha'_L C_5 e^{-j\alpha'_L h} + kC_6 e^{-j\alpha'_T h}. \quad (3.23)$$

- $u_x^{(p)} = u_x^{(hs)}$ @ $z = -h$:

$$kC_1 \cos(\alpha_L h) + jkC_2 \sin(\alpha_L h) + \alpha_T C_3 \cos(\alpha_T h) + j\alpha_T C_4 \sin(\alpha_T h)$$
$$= kC_5 e^{-j\alpha'_L h} + \alpha'_T C_6 e^{-j\alpha'_T h}. \quad (3.24)$$

The constants C_5 and C_6 can be written in terms of C_1–C_4 by the use of Equations (3.23) and (3.24) as

$$(k^2 + \alpha'_L \alpha'_T) C_5 e^{-j\alpha'_L h}$$
$$= \big[k^2 \cos(\alpha_L h) - j\alpha_L \alpha'_T \sin(\alpha_L h)\big] C_1 + \big[jk^2 \sin(\alpha_L h) - \alpha_L \alpha'_T \cos(\alpha_L h)\big] C_2$$
$$+ \big[\alpha_T k \cos(\alpha_T h) + jk\alpha'_T \sin(\alpha_T h)\big] C_3 + \big[j\alpha_T k \sin(\alpha_T h) + k\alpha'_T \cos(\alpha_T h)\big] C_4, \quad (3.25)$$

$$(k^2 + \alpha'_L \alpha'_T) C_6 e^{-j\alpha'_T h}$$
$$= \big[k\alpha'_L \cos(\alpha_L h) + j\alpha_L k \sin(\alpha_L h)\big] C_1 + \big[jk\alpha'_L \sin(\alpha_L h) + \alpha_L k \cos(\alpha_L h)\big] C_2$$
$$+ \big[\alpha_T \alpha'_L \cos(\alpha_T h) - jk^2 \sin(\alpha_T h)\big] C_3 + \big[j\alpha_T \alpha'_L \sin(\alpha_T h) - k^2 \cos(\alpha_T h)\big] C_4. \quad (3.26)$$

Substitution of Equations (3.25) and (3.26) into Equations (3.19)–(3.22) eliminates terms of C_5 and C_6; the result is a system of four homogeneous equations with C_1–C_4 as unknowns. This system of equations can be written in matrix form $\tilde{\mathbf{D}}\mathbf{c} = 0$ as

$$\begin{bmatrix} D_{11} & D_{12} & D_{13} & D_{14} \\ D_{21} & D_{22} & D_{23} & D_{24} \\ D_{11} + d_{31} & -D_{12} + d_{32} & D_{13} + d_{33} & -D_{14} + d_{34} \\ D_{21} + d_{41} & -D_{22} + d_{42} & D_{23} + d_{43} & -D_{24} + d_{44} \end{bmatrix} \begin{Bmatrix} C_1 \\ C_2 \\ C_3 \\ C_4 \end{Bmatrix} = 0, \quad (3.27)$$

where

$$
\begin{aligned}
D_{11} &= -j(\alpha_T^2 - k^2)\cos(\alpha_L h), & D_{21} &= 2k\alpha_L \sin(\alpha_L h),\\
D_{12} &= -(\alpha_T^2 - k^2)\sin(\alpha_L h), & D_{22} &= 2jk\alpha_L \cos(\alpha_L h),\\
D_{13} &= 2jk\alpha_T \cos(\alpha_T h), & D_{23} &= (\alpha_T^2 - k^2)\sin(\alpha_T h),\\
D_{14} &= 2k\alpha_T \sin(\alpha_T h), & D_{24} &= j(\alpha_T^2 - k^2)\cos(\alpha_T h),
\end{aligned}
\tag{3.28}
$$

$$
\begin{aligned}
d_{31} &= \frac{\mu'}{\mu} j \Bigg\{ \frac{{\alpha'_T}^2 - k^2}{k^2 + \alpha'_L \alpha'_T} \left[k^2 \cos(\alpha_L h) - j\alpha_L \alpha'_T \sin(\alpha_L h) \right] \\
&\qquad - \frac{2k\alpha'_T}{k^2 + \alpha'_L \alpha'_T} \left[k\alpha'_L \cos(\alpha_L h) + j\alpha_L k \sin(\alpha_L h) \right] \Bigg\}, \\
d_{32} &= \frac{\mu'}{\mu} j \Bigg\{ \frac{{\alpha'_T}^2 - k^2}{k^2 + \alpha'_L \alpha'_T} \left[jk^2 \sin(\alpha_L h) - \alpha_L \alpha'_T \cos(\alpha_L h) \right] \\
&\qquad - \frac{2k\alpha'_T}{k^2 + \alpha'_L \alpha'_T} \left[jk\alpha'_L \sin(\alpha_L h) + \alpha_L k \cos(\alpha_L h) \right] \Bigg\}, \\
d_{33} &= \frac{\mu'}{\mu} j \Bigg\{ \frac{{\alpha'_T}^2 - k^2}{k^2 + \alpha'_L \alpha'_T} \left[\alpha_T k \cos(\alpha_T h) + jk\alpha'_T \sin(\alpha_T h) \right] \\
&\qquad - \frac{2k\alpha'_T}{k^2 + \alpha'_L \alpha'_T} \left[\alpha_T \alpha'_L \cos(\alpha_T h) - jk^2 \sin(\alpha_T h) \right] \Bigg\}, \\
d_{34} &= \frac{\mu'}{\mu} j \Bigg\{ \frac{{\alpha'_T}^2 - k^2}{k^2 + \alpha'_L \alpha'_T} \left[j\alpha_T k \sin(\alpha_T h) + k\alpha'_T \cos(\alpha_T h) \right] \\
&\qquad - \frac{2k\alpha'_T}{k^2 + \alpha'_L \alpha'_T} \left[j\alpha_T \alpha'_L \sin(\alpha_T h) - k^2 \cos(\alpha_T h) \right] \Bigg\},
\end{aligned}
$$

$$
\begin{aligned}
d_{41} &= \frac{\mu'}{\mu} j \Bigg\{ - \frac{2k\alpha'_L}{k^2 + \alpha'_L \alpha'_T} \left[k^2 \cos(\alpha_L h) - j\alpha_L \alpha'_T \sin(\alpha_L h) \right] \\
&\qquad - \frac{{\alpha'_T}^2 - k^2}{k^2 + \alpha'_L \alpha'_T} \left[k\alpha'_L \cos(\alpha_L h) + j\alpha_L k \sin(\alpha_L h) \right] \Bigg\}, \\
d_{42} &= \frac{\mu'}{\mu} j \Bigg\{ - \frac{2k\alpha'_L}{k^2 + \alpha'_L \alpha'_T} \left[jk^2 \sin(\alpha_L h) - \alpha_L \alpha'_T \cos(\alpha_L h) \right] \\
&\qquad - \frac{{\alpha'_T}^2 - k^2}{k^2 + \alpha'_L \alpha'_T} \left[jk\alpha'_L \sin(\alpha_L h) + \alpha_L k \cos(\alpha_L h) \right] \Bigg\}, \\
d_{43} &= \frac{\mu'}{\mu} j \Bigg\{ - \frac{2k\alpha'_L}{k^2 + \alpha'_L \alpha'_T} \left[\alpha_T k \cos(\alpha_T h) + jk\alpha'_T \sin(\alpha_T h) \right] \\
&\qquad - \frac{{\alpha'_T}^2 - k^2}{k^2 + \alpha'_L \alpha'_T} \left[\alpha_T \alpha'_L \cos(\alpha_T h) - jk^2 \sin(\alpha_T h) \right] \Bigg\}, \\
d_{44} &= \frac{\mu'}{\mu} j \Bigg\{ - \frac{2k\alpha'_L}{k^2 + \alpha'_L \alpha'_T} \left[j\alpha_T k \sin(\alpha_T h) + k\alpha'_T \cos(\alpha_T h) \right] \\
&\qquad - \frac{{\alpha'_T}^2 - k^2}{k^2 + \alpha'_L \alpha'_T} \left[j\alpha_T \alpha'_L \sin(\alpha_T h) - k^2 \cos(\alpha_T h) \right] \Bigg\}.
\end{aligned}
\tag{3.29}
$$

The determinant of matrix $\tilde{\mathbf{D}}$ must vanish for a nontrivial solution. This gives

$$\begin{vmatrix} D_{11} & D_{12} & D_{13} & D_{14} \\ D_{21} & D_{22} & D_{23} & D_{24} \\ D_{11}+d_{31} & -D_{12}+d_{32} & D_{13}+d_{33} & -D_{14}+d_{34} \\ D_{21}+d_{41} & -D_{22}+d_{42} & D_{23}+d_{43} & -D_{24}+d_{44} \end{vmatrix} = 0. \tag{3.30}$$

This equation $|\tilde{\mathbf{D}}| = 0$ gives the dispersion equation as a function of ω and k. Note that the equation $|\mathbf{D}| = 0$ when the matrix $\mathbf{D}$ is the matrix $\tilde{\mathbf{D}}$ with all d_{ij}'s removed, represents the dispersion equation of classical Lamb waves, i.e. $R_s R_a = 0$, where R_s and R_a are given in Equations (2.26) and (2.28) (in fact, $|\mathbf{D}| = 4R_s R_a$ as shown in Appendix A.2.1).

It can be clearly seen that since d_{ij}'s are generally complex functions, the dispersion equation for this problem will be a complex equation. If the frequency ω is fixed to be real and positive, the wavenumber k must be complex in general. According to the discussion in Section 3.1, it can be concluded that Lamb waves in this case exhibit attenuation behavior. Attenuation of each Lamb mode is a complicated function of ω due to the complexity of Equation (3.30). In fact, as in the classical, non-attenuated case, the complex roots (ω, k) of Equation (3.30) can be solved only numerically.

3.3.2 Treatment of fluids

It is desirable to have one formulation that works for both solids and fluids, especially for numerical programming purposes. This subsection develops an "equivalent" solid to be used when the material is a fluid. This development is based on the analogy between solid and fluid mechanics. Only a time-harmonic case is considered since it is the case used in the analytical model. It will be seen that the time-harmonic case offers a simple replacement of a fluid by an equivalent isotropic solid.

A fluid in this development is assumed to be Newtonian (called a Newtonian fluid). This class of fluids is based on fundamental assumptions proposed by Stokes. In brief, these assumptions state the following:

- The fluid is homogeneous and isotropic.

- The stress σ_{ij} is a continuous function of only the rate of deformation (the time derivative of the strain) and the local thermodynamic state.
- The stress is hydrostatic when there is no deformation.

A fluid whose behavior follows these assumptions are called a Stokesian fluid. In general, the stress tensor in a Stokesian fluid can be expressed as

$$\sigma_{ij} = -p\delta_{ij} + P_{ij}, \tag{3.31}$$

where p is the hydrostatic stress or the pressure when the fluid is at rest; P_{ij} is the stress due to movement, called the viscous stress. This viscous stress is a continuous function of the strain rate $\dot{\varepsilon}_{ij}$ according to the stated assumptions.

A Newtonian fluid is a Stokesian fluid whose the stress components depend linearly on the rate of information, i.e. P_{ij} is a linear function function of $\dot{\varepsilon}_{ij}$. Then, the constitutive equations (3.31) can be written as [62]

$$\sigma_{ij} = (-p + \bar{\lambda}\dot{\varepsilon}_{kk})\delta_{ij} + 2\bar{\mu}\dot{\varepsilon}_{ij}, \tag{3.32}$$

where $\bar{\lambda}$ and $\bar{\mu}$ are two material constants analogous to the Lamé constants of an isotropic, elastic solid. By the consideration of a simple shear flow, $\bar{\mu}$ is found to be a constant relating the shear stress and the velocity gradient. This constant is defined as the *dynamic viscosity*. The dynamic viscosity has a dimension of stress multiplied by time (or mass per time per length) such as $\mathrm{Ns/m^2}$ and will be denoted by η hereafter ($\bar{\mu} = \eta$). The hydrostatic stress p can be obtained by the static consideration. In this case,

$$\sigma_{xx} = \sigma_{yy} = \sigma_{zz} = -p = \lambda_f(\varepsilon_{xx} + \varepsilon_{yy} + \varepsilon_{zz}) = \lambda_f\varepsilon_{kk}, \tag{3.33}$$

where λ_f is the bulk stiffness of the fluid (not to be confused with $\bar{\lambda}$). Hence, for the time-harmonic case with a factor $e^{j\omega t}$, Equation (3.32) can be written, in terms of λ_f, $\bar{\lambda}$ and η as material parameters, as

$$\hat{\sigma}_{ij} = \big(\lambda_f + j\omega\bar{\lambda}\big)\hat{\varepsilon}_{kk}\delta_{ij} + 2j\omega\eta\hat{\varepsilon}_{ij}, \tag{3.34}$$

where the $\hat{}$ denotes the amplitude of a time-harmonic quantity as used in Section 3.2.

If a fluid is assumed to satisfy Stokes' hypothesis, i.e. its bulk viscosity $\bar{k}$, defined as $\bar{k} = \bar{\lambda} + \frac{2}{3}\bar{\mu}$, vanishes, the viscosity can be defined by only one parameter η. Hence, the constitutive model (3.34) can be described by two material parameters, λ_f and η, as

$$\hat{\sigma}_{ij} = \Big(\lambda_f - \frac{2}{3}j\omega\eta\Big)\hat{\varepsilon}_{kk}\delta_{ij} + 2j\omega\eta\hat{\varepsilon}_{ij}. \tag{3.35}$$

Comparing these time-harmonic constitutive equations to their counterparts for an isotropic material,

$$\hat{\sigma}_{ij} = \lambda\hat{\varepsilon}_{kk}\delta_{ij} + 2\mu\hat{\varepsilon}_{ij}, \tag{3.36}$$

one can see that the time-harmonic formulation for an elastic solid can be extended to cover a Newtonian fluid by the use of an equivalent (isotropic) solid. The modification for the fluid domain can be done by replacing the proper λ and μ in the formulation presented in Section 3.3.1 by the equivalent properties λ_e and μ_e:

$$\begin{aligned} \lambda_e &= \lambda_f - \frac{2}{3}j\omega\eta \\ \mu_e &= j\omega\eta. \end{aligned} \tag{3.37}$$

The Stokes' hypothesis $\bar{k} = 0$ implies that both bulk longitudinal and shear waves are attenuated as they propagate in the fluid. If this hypothesis is relaxed, one can choose to have an equivalent solid with any degrees of absorption of a bulk longitudinal wave. For example, if a viscous fluid is modelled by an equivalent solid which does not absorb a bulk longitudinal wave, $\lambda_e + 2\mu_e$ is chosen to be λ_f. This implies that $\lambda_e = \lambda_f - 2j\omega\eta$ and $\bar{\lambda} = -2\eta$ or $\bar{k} = -\frac{4}{3}\eta$. Other choices the λ_e can be chosen, but different models will give in different numerical results [68]. The model described by Equations (3.35) is preferred since it leads to sound (bulk) wave absorption in accordance with the classical approximation [47] (see details in Appendix A.2.2)

$$k_I = -\Im\left\{\omega\sqrt{\frac{\rho_f}{\lambda_f + \frac{4}{3}j\omega\eta}}\right\} \approx \frac{2\omega^2\eta}{3c_f^3\rho_f}, \tag{3.38}$$

where k_I is the imaginary part of the complex wavenumber introduced in Section 3.1; c_f and ρ_f are the fluid's sound wave velocity and density, respectively.

In general, both longitudinal and shear wave velocities of an equivalent solid are complex-valued due to the complex stiffnesses. As seen in Section 3.2, an equivalent solid can be viewed as a viscoelastic solid, and therefore, waves propagating inside it will be attenuated.

3.3.3 A solid plate on a fluid half-space

To study Lamb waves with attenuation experimentally, this research uses a solid plate loaded with a fluid half-space as a specimen. A fluid is further assumed inviscid (ideal fluid) for simplicity. This assumption also limits attenuation to be caused by leakage only. This present case is analyzed in details and the corresponding dispersion relation of leaky Lamb waves is obtained explicitly. The strategy here is to use an equivalent solid (to a fluid) developed in Section 3.3.2 into the general formulation developed in Section 3.3.1.

Consider the geometry set up in Section 3.3.1. Since an ideal fluid does not support the shear stress, an equivalent solid will have a zero shear stiffness, i.e. $\mu' = 0$ and thus, $\lambda' = \lambda_f$, where λ_f is the bulk stiffness. This gives the bulk wave velocity in fluid $c'_T = 0$ and $c'_L = \sqrt{\frac{\lambda_f}{\rho'}}$. This velocity c'_L is the sound velocity in that fluid. For the derivation, since a shear wave does not exist in the half-space, the only partial wave in the half-space is a P-wave (partial wave (5) in Figure 3.1). The displacement field in the half-space thus becomes $\mathbf{u}^{(hs)} = \mathbf{u}^{(5)}$, where $\mathbf{u}^{(5)}$ is given in Equation (3.10). By Equations (3.13) and (3.14), one can explicitly write the components of displacement as

$$\begin{aligned} u_x^{(hs)} &= C_5 k e^{j\alpha'_L z} F, \\ u_z^{(hs)} &= -C_5 \alpha'_L e^{j\alpha'_L z} F. \end{aligned} \tag{3.39}$$

The stress components can be obtained from Equations (3.17) and (3.18) with the limits of $C_6 \to 0$ and $\mu' \to 0$ (this makes $\mu'({\alpha'_T}^2 - k^2) = \rho'\omega^2 - \mu' k^2 = \rho'\omega^2$),

$$\begin{aligned} \sigma_{zz}^{(hs)} &= -j\rho'\omega^2 C_5 e^{j\alpha'_L z} F, \\ \sigma_{zx}^{(hs)} &= 0. \end{aligned} \tag{3.40}$$

Since $\sigma_{zx}^{(hs)} = 0$, a slip condition is permitted at the interface between the plate and the half-space, i.e. the displacement in the x-direction is allowed to be discontinuous. Then, six boundary conditions reduce to five conditions which are stated in Equations (3.19)–(3.23).

Again, in the limit $C_6 \to 0$ and $\mu' \to 0$, Equations (3.19) and (3.20) are still the same, and Equations (3.21)–(3.23), respectively, become

$$-j(\alpha_T^2 - k^2)C_1\cos(\alpha_L h) + (\alpha_T^2 - k^2)C_2\sin(\alpha_L h) + 2jk\alpha_T C_3\cos(\alpha_T h) - 2k\alpha_T C_4\sin(\alpha_T h) = -j\frac{\rho'\omega^2}{\mu}C_5 e^{-j\alpha'_L h}, \quad (3.41)$$

$$2k\alpha_L C_1\sin(\alpha_L h) - 2jk\alpha_L C_2\cos(\alpha_L h) + (\alpha_T^2 - k^2)C_3\sin(\alpha_T h) - j(\alpha_T^2 - k^2)C_4\cos(\alpha_T h) = 0, \quad (3.42)$$

$$j\alpha_L C_1\sin(\alpha_L h) + \alpha_L C_2\cos(\alpha_L h) - jkC_3\sin(\alpha_T h) - kC_4\cos(\alpha_T h) = -\alpha'_L C_5 e^{-j\alpha'_L h}. \quad (3.43)$$

Substitution of Equation (3.43) into Equation (3.41) to eliminate $C_5 e^{-j\alpha'_L h}$ results in the equation

$$-j(\alpha_T^2 - k^2)C_1\cos(\alpha_L h) + (\alpha_T^2 - k^2)C_2\sin(\alpha_L h) + 2jk\alpha_T C_3\cos(\alpha_T h) - 2k\alpha_T C_4\sin(\alpha_T h) = j\frac{\rho'\omega^2}{\mu\alpha'_L}\Big[j\alpha_L C_1\sin(\alpha_L h) + \alpha_L C_2\cos(\alpha_L h) - jkC_3\sin(\alpha_T h) - kC_4\cos(\alpha_T h)\Big]. \quad (3.44)$$

Equation (3.44) together with Equations (3.19), (3.20), and (3.42) constitute a homogeneous system of four equations with four unknowns C_1–C_4. This system can be written in the same matrix form, $\tilde{\mathbf{D}}\mathbf{c} = 0$, as in Equation (3.27), where all D_{ij}'s are given in Equations (3.28); d_{4j}'s are all zero; and d_{3j}'s are

$$\begin{aligned} d_{31} &= \frac{\rho'}{\rho}\frac{\omega^2}{c_T^2}\frac{\alpha_L}{\alpha'_L}\sin(\alpha_L h), \\ d_{32} &= -j\frac{\rho'}{\rho}\frac{\omega^2}{c_T^2}\frac{\alpha_L}{\alpha'_L}\cos(\alpha_L h), \\ d_{33} &= -\frac{\rho'}{\rho}\frac{\omega^2}{c_T^2}\frac{k}{\alpha'_L}\sin(\alpha_T h), \\ d_{34} &= j\frac{\rho'}{\rho}\frac{\omega^2}{c_T^2}\frac{k}{\alpha'_L}\cos(\alpha_T h). \end{aligned} \quad (3.45)$$

Note that since the derivation in Section 3.3.1 is general, all D_{ij}'s and d_{ij}'s in this special case can be obtained from Equations (3.28) and (3.29) with a proper limiting process. Since D_{ij}'s are not affected by the half-space, only d_{ij}'s will be modified. The details of how to obtain d_{ij}'s in Equations (3.45) are given in Appendix A.2.4.

The characteristic equation $|\tilde{\mathbf{D}}| = 0$ is the dispersion relation of leaky Lamb waves in this case. Explicitly, this dispersion relation is given by (see details in Appendix A.2.5)

$$D(\omega, k) \equiv R_s R_a - jQ\big[R_s \cos(\alpha_L h)\cos(\alpha_T h) - R_a \sin(\alpha_L h)\sin(\alpha_T h)\big] = 0, \tag{3.46}$$

where $R_s(\omega, k)$ and $R_a(\omega, k)$ are given in Equations (2.26) and (2.28), respectively, and the term Q is given by

$$Q(\omega, k) = \frac{1}{2}\frac{\rho'}{\rho}\frac{\omega^4}{c_T^4}\frac{\alpha_L}{\alpha_L'}. \tag{3.47}$$

Equation (3.46) is then clearly complex, at least in some range of frequency and wavenumber where all parameters are real. Therefore, if the frequency ω is fixed to be real and positive, in general, the roots k of this equation must be complex. This complex wavenumber demonstrates attenuation.

When the roots of the dispersion equation are complex (this includes the case presented in Section 3.2), it is advisable to present them in two separated sets of dispersion curves (as compared to one set for classical Lamb waves). The first set of curves, plotted between frequency ω and the real part of the wavenumber $\Re\{k\}$, are called *propagation dispersion curves*. These dispersion curves represent the (real) wavenumber with which a Lamb wave propagate, at a specific frequency. The dispersion curves of Lamb waves without attenuation (such as in the classical case) are in fact propagation dispersion curves. The second set of dispersion curves are plotted between frequency ω and the imaginary part of the wavenumber $\Im\{k\}$. These dispersion curves are called *attenuation dispersion curves* because they represent attenuation of a Lamb wave mode at a specific frequency (and a specific propagation wavenumber). The two sets of dispersion curves together completely describe the behavior of Lamb waves in a system. An example of these dispersion curves is shown in Figure 3.2 for a system consisting of a 1-mm-thick aluminum plate loaded with a water half-space. Figure 3.2(a) shows the propagation dispersion curves while Figure 3.2(b) shows the attenuation parts. The figures show only six Lamb modes for clarity; one branch of curves is associated with one Lamb mode.

Since, usually, the stiffness of a fluid is much lower than that of a solid plate, the propagation dispersion curves of Lamb waves in a plate on a half-space will not be noticeably

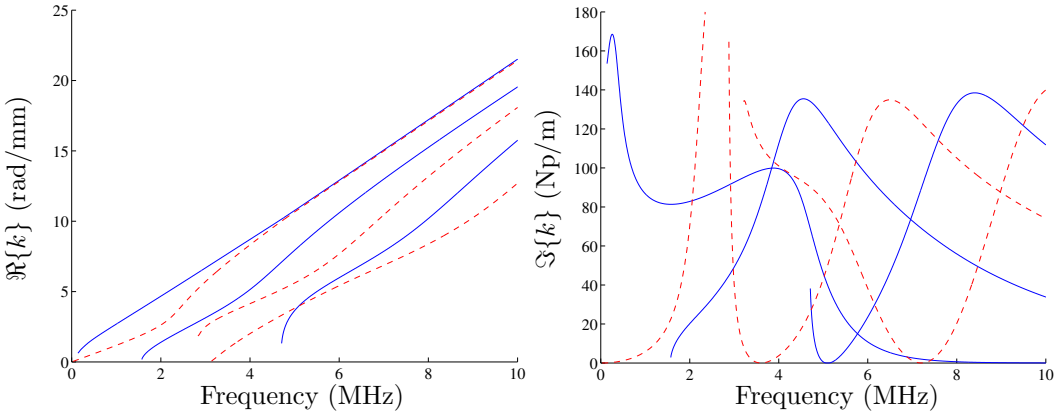

(a) Propagation part.

(b) Attenuation part.

Figure 3.2: Dispersion curves of Lamb waves propagating in a 1-mm-thick aluminum plate loaded with a water half-space.

different from those of Lamb waves in a free plate. Lamb waves in this case can be thought as Lamb waves in a free plate with an additional and uncoupled attenuation. This behavior allows for the simulation of an attenuated Lamb wave signal from a non-attenuated one, which will be discussed in Chapter 4. Moreover, a Lamb wave mode in this case can be called according to the corresponding mode in the case without attenuation. For example, the pseudo-S0 mode is understood as the mode whose real wavenumber follows that of the S0 mode of classical Lamb waves. In Figure 3.2, the dispersion curves are plotted according to this naming scheme. The solid curves correspond with the family of anti-symmetric modes of Lamb waves in a 1-mm-thick aluminum free plate, whereas the dash curves follow the curves of the symmetric modes (see Figure 2.3 for comparison). Note that, however, mode shapes of Lamb waves with leakage in this case are not pure symmetric or anti-symmetric, so it is not strictly correct to call each mode symmetric or anti-symmetric, and the name with "pseudo- " is then adopted.

It is important to note that in this system, Lamb waves are not always attenuated. To see this, one can consider Lamb waves of the real wavenumber k travelling with a phase velocity smaller than both shear wave velocity in a plate and sound wave velocity in a fluid, $c_p = \frac{\omega}{k} < c_T$ and $c_p < c'_L$. As a consequence, all α_L, α_T and α'_L become pure imaginary.

Introduce real quantities: $\bar{\alpha}_L = \sqrt{k^2 - \frac{\omega^2}{c_L^2}}$, $\bar{\alpha}_T = \sqrt{k^2 - \frac{\omega^2}{c_T^2}}$ and $\bar{\alpha}'_L = \sqrt{k^2 - \frac{\omega^2}{c_L'^2}}$. Then, $\alpha_L = -j\bar{\alpha}_L$, $\alpha_T = -j\bar{\alpha}_T$, and $\alpha'_L = -j\bar{\alpha}'_L$. Note that the negative sign of each quantity is chosen to be consistent with the current time-harmonic factor $e^{j(\omega t - kx)}$. With this choice of signs, the resulting partial waves will be bounded at far away from the plate, which is physically expected. Substituting these new real parameters into Equation (2.26) and (2.28), with the use of identities: $\cos(-ja) = \cosh(a)$ and $\sin(-ja) = -j\sinh(a)$, where a is a real quantity, leads to

$$\begin{aligned} R_s &= (-\bar{\alpha}_T^2 - k^2)^2 \cosh(\bar{\alpha}_L h)\big[-j\sinh(\bar{\alpha}_T h)\big] - 4k^2\bar{\alpha}_L\bar{\alpha}_T\big[-j\sinh(\bar{\alpha}_L h)\big]\cosh(\bar{\alpha}_T h) \\ &= -j\bar{R}_s, \end{aligned} \tag{3.48}$$

$$\begin{aligned} R_a &= (-\bar{\alpha}_T^2 - k^2)^2\big[-j\sinh(\bar{\alpha}_L h)\big]\cosh(\bar{\alpha}_T h) - 4k^2\bar{\alpha}_L\bar{\alpha}_T\cosh(\bar{\alpha}_L h)\big[-j\sinh(\bar{\alpha}_T h)\big] \\ &= -j\bar{R}_a, \end{aligned} \tag{3.49}$$

where $\bar{R}_s$ and $\bar{R}_a$ are real functions of ω and k:

$$\bar{R}_s(\omega, k) = (\bar{\alpha}_T^2 + k^2)^2 \cosh(\bar{\alpha}_L h)\sinh(\bar{\alpha}_T h) - 4k^2\bar{\alpha}_L\bar{\alpha}_T \sinh(\bar{\alpha}_L h)\cosh(\bar{\alpha}_T h), \tag{3.50}$$

$$\bar{R}_a(\omega, k) = (\bar{\alpha}_T^2 + k^2)^2 \sinh(\bar{\alpha}_L h)\cosh(\bar{\alpha}_T h) - 4k^2\bar{\alpha}_L\bar{\alpha}_T \cosh(\bar{\alpha}_L h)\sinh(\bar{\alpha}_T h). \tag{3.51}$$

The dispersion equation (3.46) becomes (see details in Appendix A.2.6)

$$\bar{D}(\omega, k) \equiv \bar{R}_s\bar{R}_a + \bar{Q}\big[R_s\cosh(\bar{\alpha}_L h)\cosh(\bar{\alpha}_T h) + \bar{R}_a\sinh(\bar{\alpha}_L h)\sinh(\bar{\alpha}_T h)\big] = 0, \tag{3.52}$$

where

$$\bar{Q}(\omega, k) = \frac{1}{2}\frac{\rho'}{\rho}\frac{\omega^4}{c_T^4}\frac{\bar{\alpha}_L}{\bar{\alpha}'_L}. \tag{3.53}$$

Equation (3.52) is real and thus can have real roots k for a given real frequency ω. Therefore, in this frequency-wavenumber range, Lamb waves can propagate without attenuation. In the fluid half-space, only vibration at the interface occurs. This vibration is non-propagating and its amplitude decays exponentially with the distance from the interface. A wave in the plate for this case is referred a subsonic plate wave (the word "subsonic" is adopted because a phase velocity of a wave in plate is smaller than a sound velocity in a fluid). Since a vibration in a fluid is confined to only at the interface and non-propagating, it does not carry any energy. So, there is no energy radiation from the plate to the fluid. However, this

no-radiation case is limited to low frequency range in most situations because the phase velocity of Lamb waves, of most frequency and Lamb modes, is higher than the shear wave velocity of a plate, which is usually higher than the sound velocity in a fluid.

CHAPTER 4

SIMULATION OF LAMB WAVES SIGNALS

Since this research aims to develop signal processing techniques to extract attenuation information from measured experimental signals, it is critical to develop synthetic signals to test such proposed techniques. To ensure validity of the tests, the synthetic signals should have similar characteristics to real signals. Instead of using any modified versions of standard non-stationary signals such as chirp signals, this research develops a computer program that numerically calculates the out-of-plane surface response of the plate due to a normal point excitation. This program simulates time-domain signals recorded in the experiments by laser ultrasonic techniques since, as explained in Section 2.3, the laser generation by ablation mechanism generates a stress point-excitation normal to the plate, and the laser detection measures the out-of-plane component of the velocity of the surface particle.

The simulation is basically the numerical solution of a boundary-valued problem (BVP)—a partial differential equation with prescribed boundary conditions—describing a particular wave phenomenon (waves in a plate, in this research). To numerically solve the setup BVP, a number of approaches can be used, for example, finite element, finite difference, boundary element, integral transform. This research employs the *normal-mode expansion* or *eigen-expansion* technique which has been widely used for problems of vibration type. The keys to this selection are the following:

- Lamb wave propagation problem is of the vibration type. The characteristics of vibrational modes are known and fully described, so this approach is suitable. Moreover, the simulation results are physically meaningful (not just pure numerical) since the simulation process is almost purely analytical.

- Lamb wave characteristics developed in Section 2.1.4 and Chapter 3 are described and

understood in "modal" sense. These Lamb wave modes directly correspond to those normal (vibrational) modes.

- This normal-mode approach automatically gives the time response of each individual Lamb mode. This is desirable and greatly benefits the verification of attenuation measurement techniques because Lamb waves' attenuation (i.e. attenuation dispersion curves) are represented as functions of Lamb modes.

- This approach is semi-analytical, thus, requires much less computational time and resources in comparison to those purely-numerical approaches such as finite element or finite difference.

This chapter presents the development of a simulation. The general formulation is presented first followed by its application to the problem at hand. The approximate unit-impulse response of the plate is analytically obtained. The simulation code is developed and the calculation results are shown. Then, the simulated results are studied in several aspects and finally compared with the real experimental time-domain signals. The incorporation of the real source characteristics is included for better comparison. The final section presents the extension of the simulation code to include attenuation.

4.1 General BVP formulation

This section presents the general concept of how the normal-mode expansion can be used to solve a boundary-valued problem. Then, the concept is applied to the wave propagation problem in general. The section presents two formulations used for different source terms—explicitly, body forces and surface forces.

4.1.1 General concept of the normal-mode expansion approach

The idea of the normal-mode approach to solve the differential equation is demonstrated for a simple case when the governing equation is a nonhomogeneous ordinary different equation and the boundary conditions are homogeneous. Given a domain interval (a, b), consider a

general setup of a BVP with homogeneous boundary conditions:

$$\begin{cases} Lu(x) = f(x) \quad \text{in the interval } (a, b) \\ u(a) = 0,\ u(b) = 0, \end{cases} \tag{4.1}$$

where u is an unknown function of x to be solved; L is a linear operator describing the governing equation. Let u belong to some real Hilbert space of infinite dimension $\mathcal{H}$, equipped with a proper inner-product $\langle ., . \rangle$. Also, let $u_m(x)$, $m = 1, 2, \ldots$, be a set of eigenfunctions of an operator L, i.e. $Lu_m(x) = \lambda_m u_m(x)$, where λ_m is the eigenvalue associated with u_m, and $\langle u_m, u_n \rangle = M_{mn}\delta_{mn}$, where δ_{mn} is the Kronecker delta. With this setup, if the operator L is self-adjoint, i.e.

$$\langle Lu, v \rangle = \langle u, Lv \rangle, \tag{4.2}$$

for all u and v in $\mathcal{H}$, all eigenvalues λ_m will be real and the eigenfunctions $u_m(x)$ form an orthogonal basis spanning the space $\mathcal{H}$. Then, the solution of Equation (4.1), $u(x)$, can be written in the form

$$u(x) = \sum_{m=1}^{\infty} A_m u_m(x), \tag{4.3}$$

for some coefficients, $A_1, A_2, \ldots$. The eigenfunction u_m can be called as a normal mode, so Equation (4.3) is referred to as the normal-mode expansion. Since the normal modes, u_m's, are obtained by solving an eigenvalue problem of the operator L which is totally independent of the source term in the governing equation, $f(x)$, they are known once L is given and the only task to obtain the solution in Equation (4.3) is to determine the coefficient A_m of each mode. These coefficients will depend on the source term and can be obtained by substitution of the expansion (4.3) into the governing equation (4.1):

$$Lu = \sum_{m=1}^{\infty} A_m (Lu_m) = f.$$

Application of the inner-product with the different normal mode, u_n, on both sides of the equation, together with the uses of quantities defined earlier and the orthogonal property

between modes, leads to

$$\begin{aligned}
\sum_{m=1}^{\infty} A_m \langle L u_m, u_n \rangle &= \langle f, u_n \rangle \\
\sum_{m=1}^{\infty} A_m \lambda_m \langle u_m, u_n \rangle &= \langle f, u_n \rangle \\
A_n \lambda_n M_{nn} &= \langle f, u_n \rangle \\
A_n &= \frac{\langle f, u_n \rangle}{\lambda_n M_{nn}}.
\end{aligned} \tag{4.4}$$

This gives the solution

$$u(x) = \sum_{m=1}^{\infty} \frac{\langle f, u_m \rangle}{\lambda_m M_{mm}} u_m(x). \tag{4.5}$$

The generalized idea of this normal-mode approach consists of two main steps. First, the eigenvalue problem of the operator L is solved to obtain the normal modes, u_m's, and their corresponding eigenvalues, λ_m's. This eigenvalue problem is sometimes referred to as a free-vibration problem. This part concerns the characteristics of the vibration of the body, so it is time-independent. The second step is to substitute those normal modes and their eigenvalues into the final formula (4.5). This concept can be extended to the problem involving a partial differential equation with nonhomogeneous boundary conditions. This extension is formulated explicitly in the next subsections for the specific wave-propagation BVP. The formulation is divided into two cases depending on the type of source terms. When the source term is the body force, the formulation can follow the development in this subsection directly. However, when the source term is the surface force, the boundary condition of the problem becomes nonhomogeneous and the development in this subsection needs be modified. The modification is made for the case when the source term in the governing equation vanishes or the governing equation becomes homogeneous. The general problem when both body forces and surface forces are present can be divided into two subproblems, each of which falls into one of the two derived categories.

4.1.2 Body-force formulation

For a wave-propagation problem, given a volume domain V with surface S, the displacement field must satisfy the governing equations of motion (2.6) in V where its value on the

surface (boundary) is prescribed. Since a transient response is now studied, either the governing equation or the boundary condition must be nonhomogeneous and time-dependent. Consider the setup where the governing equation is nonhomogeneous and time-dependent by the presence of the body force $\mathbf{f}^{(V)}$, and the boundary condition is kept homogeneous. From Equations (2.8), the problem is setup as

$$\begin{cases} L\mathbf{u}(\mathbf{x},t) = -\mathbf{f}^{(V)}(\mathbf{x},t) + \rho\ddot{\mathbf{u}}(\mathbf{x},t) \quad \text{in } V \\ B\mathbf{u}(\mathbf{x}^0,t) = 0 \quad \text{on } S, \end{cases} \tag{4.6}$$

where the vector $\mathbf{x}^0$ explicitly indicates the vector position on the surface S.

In this setup, the linear operators L and B are defined as (see details in Appendix A.3.1)

$$\begin{aligned} L\mathbf{u} &\equiv (\lambda+2\mu)\nabla(\nabla\cdot\mathbf{u}) - \mu\nabla\times\nabla\times\mathbf{u}, \\ B\mathbf{u} &\equiv \lambda(\nabla\cdot\mathbf{u})\mathbf{n} + \mu\big[\nabla\mathbf{u} + (\nabla\mathbf{u})^T\big]\mathbf{n}, \end{aligned} \tag{4.7}$$

where $\mathbf{n}$ is the outward unit normal vector to the surface and $\nabla\mathbf{u}$ is a matrix defined $\big[\nabla\mathbf{u}\big]_{ij} = u_{j,i}$. Explicitly, $\big[\nabla\mathbf{u} + (\nabla\mathbf{u})^T\big]_{ij} = u_{j,i} + u_{i,j}$ gives a symmetric matrix

$$\nabla\mathbf{u} + (\nabla\mathbf{u})^T = \begin{bmatrix} u_{1,1}+u_{1,1} & u_{2,1}+u_{1,2} & u_{3,1}+u_{1,3} \\ u_{1,2}+u_{2,1} & u_{2,2}+u_{2,2} & u_{3,2}+u_{2,3} \\ u_{1,3}+u_{3,1} & u_{2,3}+u_{3,2} & u_{3,3}+u_{3,3} \end{bmatrix}. \tag{4.8}$$

It should be emphasized that the operators L and B operating on a vector $\mathbf{u}$ result in a vector. The multiplication $\big[\nabla\mathbf{u} + (\nabla\mathbf{u})^T\big]\mathbf{n}$ is supposed to follow the matrix multiplication rule; the result becomes a vector (or a 3×1 matrix). In the indicial notations, the operators L and B are given by

$$Lu_i = (\lambda+\mu)u_{j,ji} + \mu u_{i,jj}, \tag{4.9}$$

$$Bu_i = \lambda u_{k,k}n_i + \mu(u_{i,j}+u_{j,i})n_j. \tag{4.10}$$

In connection with the elasticity thoery, the operator L operating on the displacement gives the spatial derivative of the stress tensor $\sigma_{ij,j}$ while the operator B operating on the displacement represents the surface traction t_i. This surface traction is defined as a force

applied on a unit surface area. In terms of the stress components, the surface traction is given in indicial notation by [30]

$$t_i = \sigma_{ji} n_j, \tag{4.11}$$

where n_j is a component of the outward unit normal vector to the surface. Hence, Equations (4.9) and (4.10) can be written in terms of stress, where the displacement dependency is implicitly implied, as

$$Lu_i = \sigma_{ij,j}, \tag{4.12}$$

$$Bu_i = \sigma_{ij} n_j. \tag{4.13}$$

Let the displacement field $\mathbf{u}$ at a particular time belong to some Hilbert space $\mathcal{H}$, say $L^2(V) \cap C^2(V)$—a set of functions which are continuous, twice differentiable and absolutely square-integrable in the domain V—equipped with an inner-product,

$$\langle \mathbf{v}_1(\mathbf{x}), \mathbf{v}_2(\mathbf{x}) \rangle = \int_V \mathbf{v}_1(\mathbf{x}) \cdot \mathbf{v}_2(\mathbf{x}) \, dV. \tag{4.14}$$

For now, it can be assumed that the solution of Equation (4.6) can then be expanded as[1]

$$\mathbf{u}(\mathbf{x}, t) = \sum_{m=1}^{\infty} q_m(t) \mathbf{u}_m(\mathbf{x}). \tag{4.15}$$

In this equation, the normal mode $\mathbf{u}_m(\mathbf{x})$ is explicitly a solution of Equation (4.6) when the body force term is dropped:

$$\begin{cases} L\mathbf{u}_m(\mathbf{x}) = -\rho \omega_m^2 \mathbf{u}_m(\mathbf{x}) & \text{in } V \\ B\mathbf{u}_m(\mathbf{x}^0) = 0 & \text{on } S \end{cases} \tag{4.16}$$

Substitution of Equation (4.15) into Equation (4.6) with the use of Equation (4.16) results in

$$\sum_{m=1}^{\infty} q_m(t) L\mathbf{u}_m(\mathbf{x}) = \rho \sum_{m=1}^{\infty} \ddot{q}_m(t) L\mathbf{u}_m(\mathbf{x}) - \mathbf{f}^{(V)}(\mathbf{x}, t). \tag{4.17}$$

If $\mathbf{f}^{(V)}(\mathbf{x}, t)$ is assumed to be in the same Hilbert space as $\mathbf{u}(\mathbf{x}, t)$, it can also be expanded by the normal modes, $\mathbf{u}_m(\mathbf{x})$'s, as

$$\mathbf{f}^{(V)}(\mathbf{x}, t) = \sum_{m=1}^{\infty} f_m^{(V)}(t) \mathbf{u}_m(\mathbf{x}). \tag{4.18}$$

[1] See the discussion in Section 4.1.4.

The amplitude of each mode in the expansion $f_m^{(V)}(t)$ (which is a scalar function) can be obtained by applying the inner-product with another normal mode $\mathbf{u}_n(\mathbf{x})$ to both sides of Equation (4.18) and employing the orthogonality of the normal modes

$$\begin{aligned} \langle \mathbf{f}^{(V)}, \mathbf{u}_n \rangle &= \sum_{m=1}^{\infty} f_m^{(V)} \langle \mathbf{u}_m, \mathbf{u}_n \rangle \\ \langle \mathbf{f}^{(V)}, \mathbf{u}_n \rangle &= f_n^{(V)} M_{nn} \\ f_n^{(V)} &= \frac{\langle \mathbf{f}^{(V)}, \mathbf{u}_n \rangle}{M_{nn}}, \end{aligned} \tag{4.19}$$

where $M_{nn} = \langle \mathbf{u}_n, \mathbf{u}_n \rangle = \|\mathbf{u}_n\|^2$ is the norm-square (induced by the chosen inner-product) of $\mathbf{u}_n$. Combining Equations (4.18) and (4.16) into Equation (4.17) results in

$$\begin{aligned} \sum_{m=1}^{\infty} q_m(t) L\mathbf{u}_m(\mathbf{x}) &= \rho \sum_{m=1}^{\infty} \ddot{q}_m(t) L\mathbf{u}_m(\mathbf{x}) - \sum_{m=1}^{\infty} f_m^{(V)}(t) \mathbf{u}_m(\mathbf{x}) \\ \sum_{m=1}^{\infty} \left[\ddot{q}_m(t) + \omega_m^2 q_m(t) - \frac{f_m^{(V)}(t)}{\rho} \right] \mathbf{u}_m(\mathbf{x}) &= 0. \end{aligned}$$

Because all normal modes are independent from each other, the above equation can be satisfied when each coefficient of $\mathbf{u}_m(\mathbf{x})$ vanishes, i.e.

$$\ddot{q}_m(t) + \omega_m^2 q_m(t) = \frac{f_m^{(V)}(t)}{\rho} \qquad \text{for all } m. \tag{4.20}$$

If the initial conditions of each normal mode are given as: $q_m(0) = q_{m,0}$ and $\dot{q}_m(0) = \dot{q}_{m,0}$, using the Duhamel integral[2], one can express the solution of Equation (4.20), for $t > 0$, as

$$q_m(t) = q_{m,0} \cos(\omega_m t) + \frac{\dot{q}_{m,0}}{\omega_m} \sin(\omega_m t) + \frac{1}{\rho \omega_m} \int_0^t f_m^{(V)}(\tau) \sin\left[\omega_m (t-\tau)\right] d\tau. \tag{4.21}$$

For a special case of zero initial conditions, the solution of Equation (4.20) reduces to

$$q_m(t) = \frac{1}{\rho \omega_m} \int_0^t f_m^{(V)}(\tau) \sin\left[\omega_m (t-\tau)\right] d\tau. \tag{4.22}$$

[2]In solving a one-dimensional equation of motion, $\ddot{q} + \omega^2 q = p$, the Duhamel integral approximates the effect of an impulse loading by the abrupt change in velocity. As a result, with initial conditions $q(0) = q_0$ and $\dot{q}(0) = \dot{q}_0$, the solution of that equation can be expressed as [19]

$$q(t) = q_0 \cos(\omega t) + \frac{\dot{q}_0}{\omega} \sin(\omega t) + \frac{1}{\omega} \int_0^t p(\tau) \sin\left[\omega (t-\tau)\right] d\tau.$$

Thus, from Equation (4.15), the solution of Equation (4.6) is given by

$$\mathbf{u}(\mathbf{x},t) = \sum_{m=1}^{\infty} \left(\frac{1}{\rho\omega_m} \int_0^t f_m^{(V)}(\tau) \sin\left[\omega_m(t-\tau)\right] d\tau \right) \mathbf{u}_m(\mathbf{x}), \tag{4.23}$$

where $f_m^{(V)}$ is calculated from Equation (4.19).

4.1.3 Surface-force formulation

Of more practical interest, the wave excitation appears as a surface force. This surface force must be included in the problem only as a surface traction. This makes the prescribed boundary condition nonhomogeneous. Since the body force can be handled according to the previous subsection, this subsection explains the generalization of the normal-mode approach to deal with nonhomogeneous boundary conditions. The problem is setup as

$$\begin{cases} L\mathbf{u}(\mathbf{x},t) = \rho\ddot{\mathbf{u}}(\mathbf{x},t) \quad \text{in } V \\ B\mathbf{u}(\mathbf{x}^0,t) = \mathbf{f}^{(S)}(\mathbf{x}^0,t) \quad \text{on } S, \end{cases} \tag{4.24}$$

where the operators L and B are defined in Equation (4.7). Note that the superscripts $^{(S)}$ and $^{(V)}$ of an excitation $\mathbf{f}$ are used to indicate types of the source terms (or forces). These two excitation forces are of different types, so, strictly speaking, they do not have any connections to one another mathematically.

The normal-mode shapes, $\mathbf{u}_m(\mathbf{x})$'s, are still defined in the same way as in the body-force formulation because they represent the same free-vibrational modes of the problem described by Equation (4.16). It can be easily seen that the series solution of the form of Equation (4.15) would not be the solution of Equation (4.24) since this series solution always gives homogeneous boundary conditions. The solution for this case can be split into two parts as

$$\mathbf{u}(\mathbf{x},t) = \mathbf{w}(\mathbf{x},t) + \sum_{m=1}^{\infty} q'_m(t)\mathbf{u}_m(\mathbf{x}), \tag{4.25}$$

where each $\mathbf{u}_m(\mathbf{x})$ is the normal mode described by Equation (4.16), and $\mathbf{w}(\mathbf{x},t)$ is a solution of the problem

$$\begin{cases} L\mathbf{w}(\mathbf{x},t) = 0 \quad \text{in } V \\ B\mathbf{w}(\mathbf{x}^0,t) = \mathbf{f}^{(S)}(\mathbf{x}^0,t) \quad \text{on } S. \end{cases} \tag{4.26}$$

Clearly, the solution $\mathbf{u}(\mathbf{x},t)$ expressed in Equation (4.25) is the solution of Equation (4.24). The unknown functions now are $\mathbf{w}(\mathbf{x},t)$ and all coefficients $q'_m(t)$'s. Note that the prime $'$ symbol here does not represent the derivative with respect to the argument; it is used to distinguish the amplitudes of the terms in the series of normal modes in between this formulation and the formulation in Section 4.1.2.

Substitution of $\mathbf{u}(\mathbf{x},t)$ in Equation (4.25) into Equation (4.24) leads to the requirement

$$\begin{aligned} L\mathbf{w}(\mathbf{x},t) + \sum_{m=1}^{\infty} q'_m(t) L\mathbf{u}_m(\mathbf{x}) &= \rho\ddot{\mathbf{w}}(\mathbf{x},t) + \rho\sum_{m=1}^{\infty} \ddot{q}'_m(t)\mathbf{u}_m(\mathbf{x}) \\ -\rho\sum_{m=1}^{\infty} q'_m(t)\omega_m^2\mathbf{u}_m(\mathbf{x}) &= \rho\ddot{\mathbf{w}}(\mathbf{x},t) + \rho\sum_{m=1}^{\infty} \ddot{q}'_m(t)\mathbf{u}_m(\mathbf{x}) \\ \sum_{m=1}^{\infty}\left[\ddot{q}'_m(t) + \omega_m^2 q'_m(t)\right]\mathbf{u}_m(\mathbf{x}) &= -\ddot{\mathbf{w}}(\mathbf{x},t). \end{aligned} \tag{4.27}$$

Now, introduce a new function $\mathbf{f}'(\mathbf{x},t) = -\rho\ddot{\mathbf{w}}(\mathbf{x},t)$; again, the prime $'$ does not represent differentiation. This new function is defined in the volume V, and can be viewed as a body force. Following the similar trick presented in the previous subsection, one can expand $\mathbf{f}'(\mathbf{x},t)$ as a series of normal modes

$$\mathbf{f}'(\mathbf{x},t) = \sum_{m=1}^{\infty} f'_m(t)\mathbf{u}_m(\mathbf{x}), \tag{4.28}$$

where the coefficients $f'_m(t)$ can be obtained by

$$f'_m(t) = \frac{\langle \mathbf{f}', \mathbf{u}_m\rangle}{M_{mm}}. \tag{4.29}$$

Use of Equation (4.28) in Equation (4.27) results in

$$\sum_{m=1}^{\infty}\left[\ddot{q}'_m(t) + \omega_m^2 q'_m(t) - \frac{f'_m(t)}{\rho}\right]\mathbf{u}_m(\mathbf{x}) = 0.$$

Since all $\mathbf{u}_m(\mathbf{x})$ are independent, this equation can be satisfied when all coefficients of $\mathbf{u}_m(\mathbf{x})$'s are identically zero, i.e.

$$\ddot{q}'_m(t) + \omega_m^2 q'_m(t) = \frac{f'_m(t)}{\rho}, \qquad \text{for all } m. \tag{4.30}$$

By the Duhamel integral principle, for given initial conditions, the general expression for $g'_m(t)$ follows the form given in Equation (4.20). When all initial conditions are zero,

the solution of Equation (4.30) at $t > 0$ is (see Equation (4.22))

$$q'_m(t) = \frac{1}{\rho\omega_m}\int_0^t f'_m(\tau)\sin\big[\omega_m(t-\tau)\big]\,d\tau. \tag{4.31}$$

However, this is not the final solution because the term f'_m contains the function $\mathbf{w}$ which is still unknown. Consider Equation (4.31) with the substitution of f'_m from Equation (4.29)

$$\begin{aligned} q'_m(t) &= \frac{1}{\rho\omega_m}\int_0^t \frac{\langle \mathbf{f}'(\mathbf{x},\tau), \mathbf{u}_m(\mathbf{x})\rangle}{M_{mm}}\sin\big[\omega_m(t-\tau)\big]\,d\tau \\ &= \frac{1}{\omega_m}\int_0^t \frac{\langle -\ddot{\mathbf{w}}(\mathbf{x},\tau), \mathbf{u}_m(\mathbf{x})\rangle}{M_{mm}}\sin\big[\omega_m(t-\tau)\big]\,d\tau. \end{aligned}$$

By the Leibniz's integral rule, the facts that the change in the boundary of the domain V is negligible[3] and u_m is independent of time, allow the above equation to be written as (see details in Appendix A.3.2)

$$q'_m(t) = -\frac{1}{\omega_m M_{mm}}\int_0^t \frac{\partial^2}{\partial\tau^2}\Big(\langle \mathbf{w}(\mathbf{x},\tau), \mathbf{u}_m(\mathbf{x})\rangle\Big)\sin\big[\omega_m(t-\tau)\big]\,d\tau.$$

Integration by parts twice with zero initial conditions that $\mathbf{w}(\mathbf{x},\tau) = 0$ and $\dot{\mathbf{w}}(\mathbf{x},\tau) = 0$ leads to the result (see details in Appendix A.3.3)

$$q'_m(t) = -\frac{\langle \mathbf{w}(\mathbf{x},t), \mathbf{u}_m(\mathbf{x})\rangle}{M_{mm}} + \frac{\omega_m}{M_{mm}}\int_0^t \langle \mathbf{w}(\mathbf{x},\tau), \mathbf{u}_m(\mathbf{x})\rangle\sin\big[\omega_m(t-\tau)\big]\,d\tau. \tag{4.32}$$

With this expression, Equation (4.25) becomes

$$\begin{aligned} \mathbf{u}(\mathbf{x},t) &= \mathbf{w}(\mathbf{x},t) - \sum_{m=1}^{\infty}\frac{\langle \mathbf{w}(\mathbf{x},t), \mathbf{u}_m(\mathbf{x})\rangle}{M_{mm}}\mathbf{u}_m(\mathbf{x}) \\ &\quad + \sum_{m=1}^{\infty}\frac{\omega_m}{M_{mm}}\Big(\int_0^t \langle \mathbf{w}(\mathbf{x},\tau), \mathbf{u}_m(\mathbf{x})\rangle\sin\big[\omega_m(t-\tau)\big]\,d\tau\Big)\mathbf{u}_m(\mathbf{x}). \end{aligned} \tag{4.33}$$

Consider the first and second terms of Equation (4.33):

$$\begin{aligned} \langle \mathbf{w} - \sum_m \frac{\langle \mathbf{w}, \mathbf{u}_m\rangle}{M_{mm}}\mathbf{u}_m, \mathbf{u}_n\rangle &= \langle \mathbf{w}, \mathbf{u}_n\rangle - \sum_m \frac{\langle \mathbf{w}, \mathbf{u}_m\rangle}{M_{mm}}\langle \mathbf{u}_m, \mathbf{u}_n\rangle \\ &= \langle \mathbf{w}, \mathbf{u}_n\rangle - \frac{\langle \mathbf{w}, \mathbf{u}_n\rangle}{M_{nn}}\langle \mathbf{u}_n, \mathbf{u}_n\rangle \\ &= 0. \end{aligned}$$

[3]Under the linear theory, the change in the volume V is small compared to its size; therefore, the volume V' at the current state and the volume V at the reference state are approximately the same.

Since $\mathbf{w} - \sum_m \frac{\langle \mathbf{w}, \mathbf{u}_m \rangle}{M_{mm}} \mathbf{u}_m$ is not entirely orthogonal to $\mathbf{u}_n$ and $\mathbf{u}_n$ is not zero, the above equation shows that the term $\mathbf{w} - \sum_m \frac{\langle \mathbf{w}, \mathbf{u}_m \rangle}{M_{mm}} \mathbf{u}_m$ must be zero. Hence, the first and the second terms in Equation (4.33) cancel each other, and the solution $\mathbf{u}(\mathbf{x}, t)$, with zero initial conditions, reduces to

$$\mathbf{u}(\mathbf{x}, t) = \sum_{m=1}^{\infty} \frac{\omega_m}{M_{mm}} \Big(\int_0^t \langle \mathbf{w}(\mathbf{x}, \tau), \mathbf{u}_m(\mathbf{x}) \rangle \sin \big[\omega_m (t - \tau) \big] \, d\tau \Big) \mathbf{u}_m(\mathbf{x}). \tag{4.34}$$

Since $\mathbf{w}$ is still unknown, the next step in the formulation is to determine the unknown term in Equation (4.34) which is $\langle \mathbf{w}, \mathbf{u}_m \rangle$.

For convenience in writing (which shall be seen), $\mathbf{v}$ will be used instead of $\mathbf{u}_m$ when m is not specified. Then, letting the stress associated with the displacements $\mathbf{v}$ and $\mathbf{w}$ be $\sigma_{ij}^{(v)}$ and $\sigma_{ij}^{(w)}$, from the definitions given in Equations (4.12)–(4.13) and the fact from Equation (4.26) that $Lw_i = 0$, one can equate

$$\begin{aligned} -\int_V w_i (L v_i) \, dV &= \int_V \big[v_i (L w_i) - w_i (L v_i) \big] \, dV \\ &= \int_V (\sigma_{ij,j}^{(w)} v_i - \sigma_{ij,j}^{(v)} w_i) \, dV \\ &= \int_V \big[(\sigma_{ij}^{(w)} v_i)_{,j} - (\sigma_{ij}^{(v)} w_i)_{,j} \big] \, dV \\ &\qquad - \int_V (\sigma_{ij}^{(w)} v_{i,j} - \sigma_{ij}^{(v)} w_{i,j}) \, dV. \end{aligned} \tag{4.35}$$

Note that, in this equation, both indices i and j are summed because of the dot-product (the left-hand side is just a scalar function of t). Consider the second term on the right-hand side of Equation (4.35)

$$\begin{aligned} \sigma_{ij}^{(w)} v_{i,j} &= \big[\lambda \delta_{ij} w_{k,k} + \mu (w_{i,j} + w_{j,i}) \big] v_{i,j} \\ &= \lambda w_{k,k} v_{j,j} + \mu (w_{i,j} + w_{j,i}) v_{i,j} \\ &= \lambda w_{k,k} v_{k,k} + \mu w_{i,j} v_{i,j} + \mu w_{j,i} v_{i,j}. \end{aligned} \tag{4.36}$$

Similarly,

$$\sigma_{ij}^{(v)} w_{i,j} = \lambda v_{k,k} w_{k,k} + \mu v_{i,j} w_{i,j} + \mu v_{j,i} w_{i,j}. \tag{4.37}$$

Since the indices i and j in the last terms of Equations (4.36) and (4.37) can be interchanged, $w_{i,j} v_{i,j} = v_{j,i} w_{i,j}$, then $\sigma_{ij}^{(w)} v_{i,j} = \sigma_{ij}^{(v)} w_{i,j}$. Hence, it can be concluded that, from

Equation (4.35),

$$-\int_V w_i(Lv_i)\,dV = \int_V \left[(\sigma_{ij}^{(w)}v_i)_{,j} - (\sigma_{ij}^{(v)}w_i)_{,j}\right] dV. \tag{4.38}$$

Applying the divergence theorem:

$$\int_V F_{i,i}\,dV = \int_S F_i n_i\,dS, \tag{4.39}$$

to the right-hand side of Equation (4.38), one obtain

$$\begin{aligned} -\int_V w_i(Lv_i)\,dV &= \int_S (\sigma_{ij}^{(w)}v_i n_j - \sigma_{ij}^{(v)}w_i n_j)\,dS \\ &= \int_S (t_i^{(w)}v_i - t_i^{(v)}w_i)\,dS \\ &= \int_S \left[(Bw_i)v_i - (Bv_i)w_i\right] dS \\ &= \int_S (Bw_i)v_i\,dS, \end{aligned}$$

where the property $Bv_i = 0$ from Equation (4.16) is used. In the vector form, this equation simply proves the identity:

$$-\int_V \mathbf{w}\cdot L\mathbf{u}_m\,dV = \int_S B\mathbf{w}\cdot\mathbf{u}_m\,dS. \tag{4.40}$$

This identity is useful since it relates the unknown quantity $\mathbf{w}$ to the known one, $B\mathbf{w}$, which is given in Equation (4.26). This result can be used in Equation (4.34) by noticing that $\mathbf{u}_m = -\frac{L\mathbf{u}_m}{\rho\omega_m^2}$; this gives

$$\begin{aligned} \langle \mathbf{w}, \mathbf{u}_m\rangle &= \int_V \mathbf{w}\cdot\mathbf{u}_m\,dV \\ &= -\frac{1}{\rho\omega_m^2}\int_V \mathbf{w}\cdot L\mathbf{u}_m\,dV \\ &= \frac{1}{\rho\omega_m^2}\int_S B\mathbf{w}\cdot\mathbf{u}_m\,dS \\ &= \frac{1}{\rho\omega_m^2}\int_S \mathbf{f}^{(S)}\cdot\mathbf{u}_m\,dS. \end{aligned} \tag{4.41}$$

Hence, $\mathbf{u}(\mathbf{x},t)$ in Equation (4.34) can be expressed in an analogous form as in Equation (4.23) as

$$\mathbf{u}(\mathbf{x},t) = \sum_{m=1}^{\infty}\left(\frac{1}{\rho\omega_m}\int_0^t f_m^{(S)}(\tau)\sin\left[\omega_m(t-\tau)\right]d\tau\right)\mathbf{u}_m(\mathbf{x}), \tag{4.42}$$

where the term $f_m^{(S)}(t)$ is given by

$$f_m^{(S)}(t) = \frac{1}{M_{mm}} \int_S \mathbf{f}^{(S)} \cdot \mathbf{u}_m \, dS. \tag{4.43}$$

Note that the term $\mathbf{u}_m$ in Equation (4.40), and thus Equation (4.43), is understood to be the normal-mode shape at the surface S. Then, Equation (4.43) can be explicitly written as

$$f_m^{(S)}(t) = \frac{1}{M_{mm}} \int_S \mathbf{f}^{(S)}(\mathbf{x}^0, t) \cdot \mathbf{u}_m(\mathbf{x}^0) \, dS. \tag{4.44}$$

4.1.4 Remarks for the general BVP formulation

Formulations for body forces and surface forces together constitute the formulation for the general case where both kinds of forces exert on the body V. The general problem can be setup as

$$\begin{cases} L\mathbf{u}(\mathbf{x}, t) = -\mathbf{f}^{(V)}(\mathbf{x}, t) + \rho\ddot{\mathbf{u}}(\mathbf{x}, t) \quad \text{in } V \\ B\mathbf{u}(\mathbf{x}^0, t) = \mathbf{f}^{(S)}(\mathbf{x}^0, t) \quad \text{on } S. \end{cases} \tag{4.45}$$

Because of the linearity of the operators L and B, this general problem can be handled by splitting the solution $\mathbf{u}(\mathbf{x}, t)$ into two parts:

$$\mathbf{u}(\mathbf{x}, t) = \mathbf{u}^{(V)}(\mathbf{x}, t) + \mathbf{u}^{(S)}(\mathbf{x}, t), \tag{4.46}$$

such that each part satisfies the problem with only one kind of forces,

$$\begin{cases} L\mathbf{u}^{(V)}(\mathbf{x}, t) = -\mathbf{f}^{(V)}(\mathbf{x}, t) + \rho\ddot{\mathbf{u}}^{(V)}(\mathbf{x}, t) \quad \text{in } V \\ B\mathbf{u}^{(V)}(\mathbf{x}^0, t) = 0 \quad \text{on } S, \end{cases} \tag{4.47}$$

and

$$\begin{cases} L\mathbf{u}^{(S)}(\mathbf{x}, t) = \rho\ddot{\mathbf{u}}^{(S)}(\mathbf{x}, t) \quad \text{in } V \\ B\mathbf{u}^{(S)}(\mathbf{x}^0, t) = \mathbf{f}^{(S)}(\mathbf{x}^0, t) \quad \text{on } S. \end{cases} \tag{4.48}$$

It can be easily verified that the solution of the form (4.46) satisfies the governing equation (4.45). Once the problem is properly split into two subproblems, each of the subproblems can be handled separately as developed in previous subsections.

To the more generalization, the operator L defined as Equation (4.7) is shown to be self-adjoint with respect to the inner-product defined in Equation (4.14), i.e.

$$\int_V L\mathbf{v}_1(\mathbf{x}) \cdot \mathbf{v}_2(\mathbf{x}) \, dV = \int_V \mathbf{v}_1(\mathbf{x}) \cdot L\mathbf{v}_2(\mathbf{x}) \, dV, \tag{4.49}$$

for all functions $\mathbf{v}_1$ and $\mathbf{v}_2$ in the defined Hilbert space, when the combination of displacement and stress vanishes at the boundary,

$$\mathbf{e}_i \cdot \Big[a_i \mathbf{u}(\mathbf{x}^0, t) + b_i \mathbf{t}(\mathbf{x}^0, t) \Big] = 0, \qquad i = 1,\, 2,\, 3 \quad \text{(not summed)}. \tag{4.50}$$

The parameters a_i's and b_i's can be chosen arbitrarily as long as they are not both zero at the same point on the boundary [97]. Different choices of a_i's and b_i's represent different homogeneous boundary conditions. For example, the choice of $a_i = 0$ and $b_i = 1$ for all i's represents the traction-free boundary conditions; the choice of $a_1 = 0$, $b_1 = 1$ and $a_2 = 1$, $b_2 = 0$ of a two-dimensional problem represents the sliding boundary condition which restrains the displacement in one direction and allows the movement in the other direction. This fact allows the formulation in the previous two subsections to include the cases when some components of stress are nonzero.

By the self-adjointness of L, the normal modes $\mathbf{u}_m$'s which are the eigenfunctions of L, are proven to form a complete orthogonal set of eigenfunctions under the defined inner-product (described in Equation (4.14)) [26]; this fact guarantees that the expansion (4.15) is legal and the series is convergent.

4.2 Transient response of a circular plate

This section applies the concepts developed earlier to the problem of wave propagation in a solid plate. The aim is to develop a simulation of a transient response resembling what will be measured in the experiment. The experiment will be conducted by laser ultrasonic techniques where the wave excitation is an ablation source and the detection measures the out-of-plane component of the particle velocity on the surface of the specimen (see Section 2.3). Because the excitation is modelled as a normal-stress point-source which possesses symmetry about its axis, it is suggestive to simulate the problem with axial symmetry. The problem with this kind of symmetry is called an *axisymmetric* problem. This simulation considers a circular plate of radius R and thickness $2h$. The cylindrical coordinates (r, θ, z) are used with the $r\theta$-plane lying on the midplane of the plate and the z-axis passing through the center of the plate. The source is assumed to be axisymmetric but yet specified. The schematic sketch of the plate is shown in Figure 4.1. In this problem,

the volume V is the inside of the plate, and the surface S is a combined area of all surfaces of the plate.

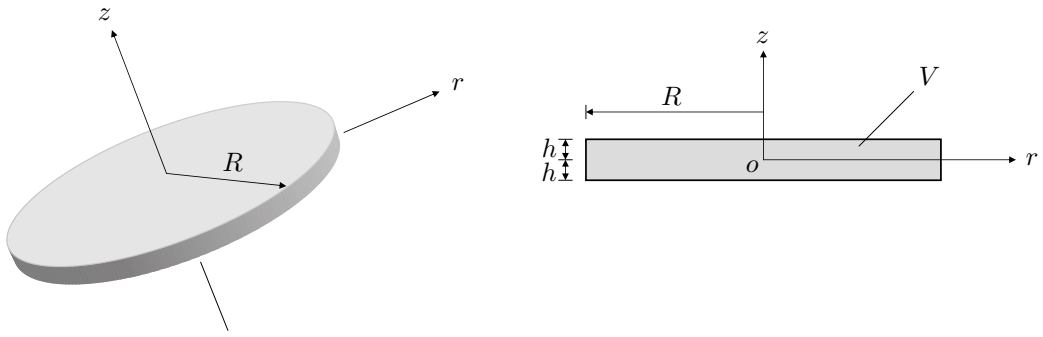

(a) A three-dimensional sketch.

(b) A cross-section along the diameter.

Figure 4.1: A circular plate of radius R and thickness $2h$ with the cylindrical coordinate system.

Since the laser excitation is modelled as a normal point source on the surface of the plate, the surface formulation developed in Section 4.1.3 will be employed. As seen in that section, to obtain the transient response, the first step is to obtain the normal modes from free-vibration analysis. The transient solution is then written as a linear combination of all normal modes. The magnitude of each mode or the coefficient corresponding to each mode in the series expansion is determined for a given specific loading force.

4.2.1 Free vibration

Because the problem possesses the axial symmetry, only r and z of the cylindrical coordinates are the spatial variables, and the problem is effectively two-dimensional. The two-dimensional nature of the problem also suggests that the normal modes should be characterized in two directions, r and z. Therefore, the normal modes should be numbered with two subscripts, m and n, rather than one subscript m as used in Section 4.1. The m and n indices indicate the normal mode in the z- and r-directions, respectively, and a particular normal mode is explicitly expressed as $\mathbf{u}_{mn}$.

With the operators L and B defined in Equation (4.7), the free-vibration problem is

setup as

$$\begin{cases} L\mathbf{u}_{mn} = -\rho\omega_{mn}^2\mathbf{u}_{mn} & \text{in } V \\ B\mathbf{u}_{mn} = 0 & \text{on } S, \end{cases} \tag{4.51}$$

where the independent variables, r, z, and t are dropped. To solve Equation (4.51), first, $\mathbf{u}_{mn}$ is resolved into one scalar potential ϕ_{mn} and one vector potential $\boldsymbol{\psi}_{mn}$ by the Helmholtz decomposition,

$$\mathbf{u}_{mn} = \nabla\phi_{mn} + \nabla \times \boldsymbol{\psi}_{mn}. \tag{4.52}$$

This can be done because $\mathbf{u}_{mn}$ is assumed to be differentiable in V. Since the three unknown functions of three components of $\mathbf{u}_{mn}$ are now represented by four unknown functions of the potentials ϕ_{mn} and $\boldsymbol{\psi}_{mn}$ (one ϕ_{mn} and three components of $\boldsymbol{\psi}_{mn}$), another condition, called *gauge condition*, must be provided to guarantee the uniqueness of the determination of $\mathbf{u}_{mn}$. Usually, the condition

$$\nabla \cdot \boldsymbol{\psi}_{mn} = 0 \tag{4.53}$$

is used following the original derivation of the theory[4]. However, this choice for additional condition is not mandatory because the proof of completeness of the representation (4.52) can be shown independently of the gauge condition (4.53) [52].

Substitution of $\mathbf{u}_{mn}$ in Equation (4.52) into Equation (4.51) decouples this governing equation into two Helmholtz equations:

$$\begin{aligned} \nabla^2\phi_{mn} + \frac{\omega_{mn}^2}{c_L^2}\phi_{mn} &= 0 \\ \nabla^2\boldsymbol{\psi}_{mn} + \frac{\omega_{mn}^2}{c_T^2}\boldsymbol{\psi}_{mn} &= 0. \end{aligned} \tag{4.54}$$

Let $\mathbf{u}_{mn}$ be written in the component form as

$$\mathbf{u}_{mn} = u_{mn}\,\mathbf{e}_r + v_{mn}\,\mathbf{e}_\theta + w_{mn}\,\mathbf{e}_z. \tag{4.55}$$

[4]In the original development, a piecewise continuously differentiable $\mathbf{F}$ in a domain V is represented by a twice-differentiable function $\mathbf{v}$ through the vector Poisson's equation: $\nabla^2\mathbf{v} = \mathbf{F}$ inside the volume V. The expansion of the left-hand side of this equation by the vector identity $\nabla^2\mathbf{v} = \nabla(\nabla \cdot \mathbf{v}) - \nabla \times \nabla \times \mathbf{v}$ gives

$$\mathbf{F} = \nabla\phi + \nabla \times \boldsymbol{\psi},$$

where the potentials ϕ and $\boldsymbol{\psi}$ are chosen to be $\phi = \nabla \cdot \mathbf{v}$ and $\boldsymbol{\psi} = -\nabla \times \mathbf{v}$. With this choice, the condition $\nabla \cdot \boldsymbol{\psi} = 0$ is implicitly implied.

For an axisymmetric problem, $v_{mn} \equiv 0$; as a consequence, by explicit expansion, it can be seen that the r- and z-components of $\boldsymbol{\psi}_{mn}$ must vanish. So, if the θ-component of $\boldsymbol{\psi}_{mn}$ is a scalar function ψ_{mn}, the nonzero components of the normal mode $\mathbf{u}_{mn}$ can be written according to Equation (4.52) as (see Appendix B)

$$u_{mn} = \frac{\partial \phi_{mn}}{\partial r} - \frac{\partial \psi_{mn}}{\partial z} \tag{4.56}$$

$$w_{mn} = \frac{\partial \phi_{mn}}{\partial z} + \frac{\partial \psi_{mn}}{\partial r} + \frac{\psi_{mn}}{r}. \tag{4.57}$$

A vector equation governing the vector potential $\boldsymbol{\psi}_{mn}$ becomes a scalar equation governing the scalar potential ψ_{mn}. In particular, the governing equations (4.54) of this axisymmetric problem in cylindrical coordinates become (see Appendix B)

$$\begin{aligned} \nabla^2 \phi_{mn} + \frac{\omega_{mn}^2}{c_L^2} \phi_{mn} &= 0 \\ \nabla^2 \psi_{mn} - \frac{\psi_{mn}}{r^2} + \frac{\omega_{mn}^2}{c_T^2} \psi_{mn} &= 0, \end{aligned} \tag{4.58}$$

where the operator $\nabla^2 = \frac{\partial^2}{\partial r^2} + \frac{1}{r}\frac{\partial}{\partial r} + \frac{\partial^2}{\partial z^2}$. Employing the separation of variables method, one can find that the solutions of Equations (4.58) are of the form (the following solutions can be verified by direct substitution into Equations (4.58)):

$$\begin{aligned} \phi_{mn}(r,z) &= \Big[A_{1;mn}\cos(\alpha_{L;mn} z) + A_{2;mn}\sin(\alpha_{L;mn} z)\Big] J_0(k_{mn} r) \\ \psi_{mn}(r,z) &= \Big[B_{1;mn}\cos(\alpha_{T;mn} z) + B_{2;mn}\sin(\alpha_{T;mn} z)\Big] J_1(k_{mn} r), \end{aligned} \tag{4.59}$$

where k_{mn} is a positive real parameter; $A_{1;mn}$, $A_{2;mn}$, $B_{1;mn}$, $B_{2;mn}$ are unknown constants; the parameters $\alpha_{L;mn}$ and $\alpha_{T;mn}$ are defined as

$$\alpha_{L;mn} = \sqrt{\frac{\omega_{mn}^2}{c_L^2} - k_{mn}^2}, \quad \text{and} \quad \alpha_{T;mn} = \sqrt{\frac{\omega_{mn}^2}{c_T^2} - k_{mn}^2}. \tag{4.60}$$

It is important to note that, although the development in Section 4.1 is within the real domain, the constants $A_{i;mn}$'s, $B_{i;mn}$'s, $i \sim 1, 2$, and parameters $\alpha_{L;mn}$, $\alpha_{T;mn}$ in Equations (4.59) are not yet specified and allowed to be real or complex. However, these parameters will be forced to be real in the implementation stage which will be discussed in Section 4.2.3. Also, in the derivation of the forms of solutions in Equation (4.59), the condition that these potentials ϕ_{mn} and ψ_{mn} must be bounded at the center of the plate

$(r = 0)$ is invoked. This physical fact nulls off the terms containing the Bessel functions of the second kinds, $Y_0(k_{mn}r)$ and $Y_1(k_{mn}r)$, which initially exist in the complete solutions of Equations. (4.58).

The relevant stress components are given, in the cylindrical coordinates, in terms of the displacement components by

$$\begin{aligned}
\sigma_{zz;mn} &= \lambda\Big(\frac{\partial u_{mn}}{\partial r} + \frac{u_{mn}}{r} + \frac{\partial w_{mn}}{\partial z}\Big) + 2\mu\frac{\partial w_{mn}}{\partial z} \\
&= \mu\Big[\frac{c_L^2}{c_T^2}\Big(\frac{\partial u_{mn}}{\partial r} + \frac{u_{mn}}{r} + \frac{\partial w_{mn}}{\partial z}\Big) - 2\Big(\frac{\partial u_{mn}}{\partial r} + \frac{u_{mn}}{r}\Big)\Big] \qquad (4.61) \\
\sigma_{zr;mn} &= \mu\Big(\frac{\partial u_{mn}}{\partial z} + \frac{\partial w_{mn}}{\partial r}\Big). \qquad (4.62)
\end{aligned}$$

For convenience, introduce

$$\begin{aligned}
f_{mn}(z) &= A_{1;mn}\cos(\alpha_{L;mn}z) + A_{2;mn}\sin(\alpha_{L;mn}z) \\
g_{mn}(z) &= B_{1;mn}\cos(\alpha_{T;mn}z) + B_{2;mn}\sin(\alpha_{T;mn}z). \qquad (4.63)
\end{aligned}$$

This introduction gives

$$\begin{aligned}
\phi_{mn}(r,z) &= f_{mn}(z)J_0(k_{mn}r) \\
\psi_{mn}(r,z) &= g_{mn}(z)J_1(k_{mn}r). \qquad (4.64)
\end{aligned}$$

Substituting ϕ_{mn} and ψ_{mn} in Equations (4.64) into Equations (4.56), (4.57), (4.61), and (4.62), with the use of the identities in Section 9.1.27 of Reference [1]:

$$\begin{aligned}
\frac{d}{dx}J_0(x) &= -J_1(x) \\
\frac{d}{dx}J_1(x) &= J_0(x) - \frac{J_1(x)}{x}, \quad \text{for } x \neq 0, \qquad (4.65)
\end{aligned}$$

one obtains (see details in Appendix A.3.4)

$$\begin{aligned}
u_{mn}(r,z) &= -\Big[k_{mn}f_{mn}(z) + g'_{mn}(z)\Big]J_1(k_{mn}r) \\
w_{mn}(r,z) &= \Big[f'_{mn}(z) + k_{mn}g_{mn}(z)\Big]J_0(k_{mn}r) \\
\sigma_{zz;mn}(r,z) &= \mu\Big[-\big(\alpha_{T;mn}^2 - k_{mn}^2\big)f_{mn}(z) + 2k_{mn}g'_{mn}(z)\Big]J_0(k_{mn}r) \\
\sigma_{zr;mn}(r,z) &= \mu\Big[-2k_{mn}f'_{mn}(z) + \big(\alpha_{T;mn}^2 - k_{mn}^2\big)g_{mn}(z)\Big]J_1(k_{mn}r), \qquad (4.66)
\end{aligned}$$

where the prime $'$ represents the derivative with the argument.

The boundary conditions will give the conditions required for existing ω_{mn} and k_{mn}, or dispersion relations, and also the relative magnitudes of the constants $A_{i;mn}$'s, $B_{i;mn}$'s. Keep in mind that only the relative magnitudes of $A_{i;mn}$'s, $B_{i;mn}$'s can be determined since this is an eigenvalue problem. For a specific m and n, these relative magnitudes constitute a mode shape of the normal mode (or the free-vibrational mode) mn. For this problem, the obvious boundary conditions are traction-free conditions on both top and bottom surfaces of the plate, i.e. $\sigma_{zz;mn}(r, \pm h) = 0$ and $\sigma_{zr;mn}(r, \pm h) = 0$ for all r. As for the boundary conditions at the edge of the plate $r = R$, the most convenient conditions are chosen. This is justified because those conditions have negligible effects on the field quantities around the middle of the plate when the radius R approaches infinity or is very large compared to the distance from the excitation to the point of interest.

From the form of expressions (4.66), the boundary conditions $u_{mn}(R, z) = 0$ and $\sigma_{rz;mn}(R, z)$ for all z, are chosen. These conditions are easily satisfied when the equation

$$J_1(k_{mn}R) = 0 \tag{4.67}$$

holds[5]. These chosen conditions represent realistic "sliding" boundary conditions. By these boundary conditions, the edge of the plate is restrained in the radial direction but allowed to move freely in the vertical direction. Equation (4.67) is the radial dispersion equation governing the parameter k_{mn} for a given radius of the plate R. By the nature of the Bessel function $J_1(x)$, Equation (4.67) has infinitely many roots k_{mn}'s. This means that there exist infinitely many modes in the radial direction for this type of vibration. The parameter k_{mn}, as expected, can be understood as the rate of vibration in the radial direction or the spatial frequency or wavenumber. Note that the roots of Equation (4.67) or existing wavenumbers are independent of the medium in the plate. In fact, they depend only on the radius of the plate R. Therefore, those roots can be written with only one index n as k_n, $n = 1, 2, \ldots$. However, the expression with k_{mn} is kept for generality in later presentation and should

[5]It can be easily shown that $\sigma_{rr;mn}$ contains terms with both $J_0(k_{mn}r)$ and $J_1(k_{mn}r)$. So, the stress-free or other conditions at $r = R$ involving $\sigma_{rr;mn}$ are not easily satisfied (see Appendix B for the expression of $\sigma_{rr;mn}$).

not be confused even though the index m is redundant. Another observation is that as the radius of the plate R increases, the spacing between the roots k_{mn} decreases and becomes infinitesimal when $R \to \infty$. This confers with the study of classical Lamb waves in an infinite free plate where the wavenumber k ranges over the non-negative real line.

From Equations (4.66), the stress-free boundary conditions at the top and bottom surfaces of the plate lead to

$$\begin{aligned} -\big(\alpha_{T;mn}^2 - k_{mn}^2\big) f_{mn}(\pm h) + 2k_{mn} g'_{mn}(\pm h) &= 0 \\ 2k_{mn} f'_{mn}(\pm h) - \big(\alpha_{T;mn}^2 - k_{mn}^2\big) g_{mn}(\pm h) &= 0. \end{aligned} \tag{4.68}$$

These equations form a homogeneous system of four equations governing the four unknowns $A_{i;mn}$'s and $B_{i;mn}$'s. The characteristic equation of this system is the dispersion equation in the z-direction (thickness direction). The dispersion equation which is a function of ω_{mn} and k_{mn} governs existing temporal frequency ω_{mn} for a given spatial frequency k_{mn}. This equation also provides the nontrivial solutions for $A_{i;mn}$'s and $B_{i;mn}$'s, and thus the mode shape of the normal mode mn corresponding to a specific (ω_{mn}, k_{mn}).

As in the study of classical Lamb waves presented in Section 2.1.4, due to the symmetry of the problem, the normal modes in the z-direction can be divided into two independent groups: symmetric and anti-symmetric modes. From the expressions of f_{mn} and g_{mn} in Equations (4.63), these two functions can be divided into symmetric and anti-symmetric parts with respect to the mid-plane of the plate:

$$\begin{aligned} &f_{mn}(z) = A_{1;mn} \cos(\alpha_{L;mn} z), \quad g_{mn}(z) = B_{2;mn} \sin(\alpha_{T;mn} z) && \text{for symmetric modes} \\ &f_{mn}(z) = A_{2;mn} \sin(\alpha_{L;mn} z), \quad g_{mn}(z) = B_{1;mn} \cos(\alpha_{T;mn} z) && \text{for anti-symmetric modes.} \end{aligned} \tag{4.69}$$

With this division, the homogeneous system of four equations in Equations (4.68) breaks into two homogeneous systems of two equations, each of which is governing each type of modes. The dispersion equation and mode shape for each type are given as the following:

- *Symmetric modes*

$$\begin{bmatrix} -(\alpha_{T;mn}^2 - k_{mn}^2)\cos(\alpha_{L;mn}h) & 2k_{mn}\alpha_{T;mn}\cos(\alpha_{T;mn}h) \\ 2k_{mn}\alpha_{L;mn}\sin(\alpha_{L;mn}h) & (\alpha_{T;mn}^2 - k_{mn}^2)\sin(\alpha_{T;mn}h) \end{bmatrix} \begin{Bmatrix} A_{1;mn} \\ B_{2;mn} \end{Bmatrix} = 0. \tag{4.70}$$

The dispersion equation:

$$\begin{aligned} R_{s;mn} \equiv\ & (\alpha_{T;mn}^2 - k_{mn}^2)^2 \cos(\alpha_{L;mn}h)\sin(\alpha_{T;mn}h) \\ & +4k_{mn}^2\alpha_{L;mn}\alpha_{T;mn}\sin(\alpha_{L;mn}h)\cos(\alpha_{T;mn}h) = 0. \end{aligned} \tag{4.71}$$

Mode shape:

$$\frac{A_{1;mn}}{B_{2;mn}} = \frac{2k_{mn}\alpha_{T;mn}\cos(\alpha_{T;mn}h)}{(\alpha_{T;mn}^2 - k^2)\cos(\alpha_{L;mn}h)} = -\frac{(\alpha_{T;mn}^2 - k_{mn}^2)\sin(\alpha_{T;mn}h)}{2k_{mn}\alpha_{L;mn}\sin(\alpha_{L;mn}h)}. \tag{4.72}$$

- *Anti-symmetric modes*

$$\begin{bmatrix} -(\alpha_{T;mn}^2 - k_{mn}^2)\sin(\alpha_{L;mn}h) & 2k_{mn}\alpha_{T;mn}\sin(\alpha_{T;mn}h) \\ 2k_{mn}\alpha_{L;mn}\cos(\alpha_{L;mn}h) & (\alpha_{T;mn}^2 - k_{mn}^2)\cos(\alpha_{T;mn}h) \end{bmatrix} \begin{Bmatrix} A_{2;mn} \\ B_{1;mn} \end{Bmatrix} = 0. \tag{4.73}$$

The dispersion equation:

$$\begin{aligned} R_{a;mn} \equiv\ & (\alpha_{T;mn}^2 - k_{mn}^2)^2 \sin(\alpha_{L;mn}h)\cos(\alpha_{T;mn}h) \\ & +4\,k_{mn}^2\alpha_{L;mn}\alpha_{T;mn}\cos(\alpha_{L;mn}h)\sin(\alpha_{T;mn}h) = 0. \end{aligned} \tag{4.74}$$

Mode shape:

$$\frac{A_{2;mn}}{B_{1;mn}} = -\frac{2k_{mn}\alpha_{T;mn}\sin(\alpha_{T;mn}h)}{(\alpha_{T;mn}^2 - k^2)\sin(\alpha_{L;mn}h)} = \frac{(\alpha_{T;mn}^2 - k_{mn}^2)\cos(\alpha_{T;mn}h)}{2k_{mn}\alpha_{L;mn}\cos(\alpha_{L;mn}h)}. \tag{4.75}$$

Equations (4.71) and (4.74) are the same as Equations (2.26) and (2.28) in Section 2.1.4, but they are repeated here with the indices mn to emphasize the discrete roots (ω_{mn}, k_{mn}) in this finite-domain problem.

4.2.2 Transient response to the surface-force excitation

The results from the free-vibration analysis will be used in this subsection for a transient problem. Suppose that there are no body forces and the excitation is a surface force represented by

$$\mathbf{f}^{(S)}(r,z,t) = \delta(z-h)\mathbf{F}(r,t), \tag{4.76}$$

where $\delta(z)$ is the Dirac delta function[6]. This expression clearly represents an axisymmetric surface force applied on the top surface of the plate. From the development in Section 4.1.3, especially Equation (4.42), the transient displacement response can be expressed as

$$\mathbf{u}(r,z,t) = \sum_{m=1}^{\infty}\sum_{n=1}^{\infty}\Big(\frac{1}{\rho\omega_{mn}}\int_0^t f_{mn}^{(S)}(\tau)\sin\left[\omega_{mn}(t-\tau)\right]d\tau\Big)\mathbf{u}_{mn}(r,z). \tag{4.77}$$

In this equation, with the inner-product[7] defined by

$$\langle \mathbf{v}_1, \mathbf{v}_2\rangle = \int_V \mathbf{v}_1\cdot\mathbf{v}_2\,dS = 2\pi\int_0^R\int_{-h}^h \mathbf{v}_1\cdot\mathbf{v}_2\,dz\,r\,dr, \tag{4.78}$$

the function $f_{mn}^{(S)}$, which is a function of t only, is defined by (see Equation (4.43))

$$f_{mn}^{(S)}(t) = \frac{2\pi}{M_{mn}}\int_0^R \mathbf{F}(r,t)\cdot\mathbf{u}_{mn}(r,h)r\,dr, \tag{4.79}$$

where M_{mn} is the square of the norm of the normal mode mn. This quantity can be expressed as

$$\begin{aligned} M_{mn} &= \langle \mathbf{u}_{mn}, \mathbf{u}_{mn}\rangle \\ &= 2\pi\int_0^R\int_{-h}^h \mathbf{u}_{mn}\cdot\mathbf{u}_{mn}\,dz\,r\,dr \\ &= 2\pi\int_0^R\int_{-h}^h (u_{mn}^2 + w_{mn}^2)\,dz\,r\,dr, \end{aligned} \tag{4.80}$$

where the r- and z-components of $\mathbf{u}_{mn}$ in Equation (4.55) are shown explicitly.

From Equations (4.66), u_{mn} and w_{mn} can be written in the form

$$\begin{aligned} u_{mn} &= G_{u;mn}(z)J_1(k_{mn}r) \\ w_{mn} &= G_{w;mn}(z)J_0(k_{mn}r). \end{aligned} \tag{4.81}$$

[6]The Dirac delta function $\delta(x)$ is defined by two properties:

$$\delta(x) = 0 \quad \text{for } x \neq 0, \text{ and } \quad \int_D \delta(x)\,dx = 1,$$

where D is the domain of x. From these two properties, the Dirac delta function can be viewed as a functional which has the property

$$\int_D \delta(x-x_0)f(x)\,dx = f(x_0),$$

when it is operated on a function $f(x)$.

[7]Since the normal-mode shape represents the physical characteristics, the dot-product of two modes is assumed integrable over each domain r and z. Therefore, by Fubini's theorem, the order of the integration in the definition (4.78) is interchangeable.

Then, in terms of $G_{u;mn}(z)$ and $G_{w;mn}(z)$, M_{mn} can be written as

$$M_{mn} = 2\pi \int_{-h}^{h} \Big[G_{u;mn}^2(z) \int_0^R J_1(k_{mn}r) r \, dr + G_{w;mn}^2(z) \int_0^R J_0(k_{mn}r) r \, dr \Big] \, dz. \qquad (4.82)$$

The property of k_{mn} which satisfies Equation (4.67), leads to the identities (see details in Appendix A.3.5):

$$\begin{aligned} \int_0^R J_1(k_{mn}r) r \, dr &= \frac{R^2}{2} \big[J_1'(k_{mn}R) \big]^2 \\ \int_0^R J_0(k_{mn}r) r \, dr &= \frac{R^2}{2} \big[J_0(k_{mn}R) \big]^2, \end{aligned} \qquad (4.83)$$

where the $'$ represents the derivative with the argument. Substitution of these identities into Equation (4.82) gives the expression for M_{mn} as

$$M_{mn} = \pi R^2 \Big\{ \big[J_1'(k_{mn}R) \big]^2 \int_{-h}^{h} G_{u;mn}^2(z) \, dz + \big[J_0(k_{mn}R) \big]^2 \int_{-h}^{h} G_{w;mn}^2(z) \, dz \Big\}. \qquad (4.84)$$

Note that M_{mn} does not depend on the excitation so that it can be readily calculated once the normal modes are found. The only term in the solution (4.77) that is dependent of the excitation is $f_{mn}^{(S)}(t)$.

When a pulse laser is used for ultrasonic-wave generation, the ablation source can be modelled as a stress point source normally-applied to the top surface of the plate. Therefore, of interest is the excitation of the form of Equation (4.76) with

$$\mathbf{F}(r,t) = Q \frac{\delta(r)}{2\pi r} H(t - t_0) \, \mathbf{e}_z, \qquad (4.85)$$

where $\frac{\delta(r)}{2\pi r}$ is the Dirac delta function in the polar coordinates (r,θ)[8]; $H(t)$ is the Heaviside step function. This choice of a step-function time-dependence is chosen because it simplifies mathematical manipulations and also can be extended to give a transient response to a

[8]The form of the Dirac delta function in the polar coordinates $\delta_p(r,\theta)$ is governed by the property that

$$\int_0^{2\pi} \int_0^{\infty} \delta_p(r,\theta) r \, dr \, d\theta = 1.$$

For an axisymmetric delta function, this property holds when

$$\delta_p(r) = \frac{\delta(r)}{2\pi r},$$

where $\delta(r)$ is understood as a regular Dirac delta function.

general excitation by approximation. This scheme will be discussed at the end of this subsection.

With this choice of $\mathbf{F}(r,t)$, $f_{mn}^{(S)}(t)$ in Equation (4.79) becomes

$$\begin{aligned} f_{mn}^{(S)}(t) &= \frac{Q}{M_{mn}} \int_0^R \delta(r)\, \mathbf{e}_z \cdot \mathbf{u}_{mn}(r,h)\, dr H(t-t_0) \\ &= \frac{Q}{M_{mn}} \int_0^R \delta(r) w_{mn}(r,h)\, dr H(t-t_0) \\ &= \frac{Q}{M_{mn}} G_{w;mn}(h) \int_0^R \delta(r) J_0(k_{mn} r)\, dr H(t-t_0) \\ &= \frac{Q G_{w;mn}(h)}{M_{mn}} H(t-t_0), \end{aligned} \tag{4.86}$$

where the property $J_0(0) = 1$ is used.

Further, for any $t > t_0$, the integral

$$\begin{aligned} \int_0^t f_{mn}^{(S)}(\tau) \sin\big[\omega_{mn}(t-\tau)\big]\, d\tau &= \frac{Q G_{w;mn}(h)}{M_{mn}} \int_0^t H(\tau - t_0) \sin\big[\omega_{mn}(t-\tau)\big]\, d\tau \\ &= \frac{Q G_{w;mn}(h)}{M_{mn}} \int_{t_0}^t \sin\big[\omega_{mn}(t-\tau)\big]\, d\tau \\ &= \frac{Q G_{w;mn}(h)}{M_{mn}\omega_{mn}} \Big(1 - \cos\big[\omega_{mn}(t-t_0)\big]\Big). \end{aligned}$$

Hence, from Equation (4.77), the transient response due to a point source with a step-function time-dependence $H(t)$, is

$$\mathbf{u}^{H_{t_0}}(r,z,t) = \frac{Q}{\rho} \sum_{m=1}^{\infty} \sum_{n=1}^{\infty} \frac{G_{w;mn}(h)}{M_{mn}\omega_{mn}^2} \Big(1 - \cos\big[\omega_{mn}(t-t_0)\big]\Big) \mathbf{u}_{mn}(r,z). \tag{4.87}$$

In particular, when $t_0 = 0$, the *step response* of the plate is

$$\mathbf{u}^{H}(r,z,t) = \frac{Q}{\rho} \sum_{m=1}^{\infty} \sum_{n=1}^{\infty} \frac{G_{w;mn}(h)}{M_{mn}\omega_{mn}^2} \big[1 - \cos(\omega_{mn} t)\big] \mathbf{u}_{mn}(r,z). \tag{4.88}$$

Notice that it is obvious from the expression (4.87) that the plate response to the excitation can be viewed as an output of the linear time-invariant (LTI) system whose step response is given by Equation (4.88). Since the component of displacement which will be measured is the out-of-plane component of a particle at the top surface of the plate, if $\mathbf{u}^H(r,z,t) = u_r^H\, \mathbf{e}_r + u_z^H\, \mathbf{e}_z$, then

$$\begin{aligned} u_z^H(r,h,t) &= \frac{Q}{\rho} \sum_{m=1}^{\infty} \sum_{n=1}^{\infty} \frac{G_{w;mn}(h)}{M_{mn}\omega_{mn}^2} \big[1 - \cos(\omega_{mn} t)\big] G_{w;mn}(h) J_0(k_{mn} r) \\ &= \frac{Q}{\rho} \sum_{m=1}^{\infty} \sum_{n=1}^{\infty} \frac{G_{w;mn}^2(h)}{M_{mn}\omega_{mn}^2} \big[1 - \cos(\omega_{mn} t)\big] J_0(k_{mn} r). \end{aligned} \tag{4.89}$$

The out-of-plane surface displacement due to the impulse, called a *impulse response*, u_z^δ, can be determined as a limiting case of the obvious superposition between two step responses starting at different times

$$\begin{aligned} u_z^\delta(r,h,t) &= \lim_{\Delta t\to 0}\frac{1}{\Delta t}\left[u_z^H(r,h,t)-u_z^H(r,h,t-\Delta t)\right] \\ &= \frac{\partial}{\partial t}u_z^H(r,h,t) \\ &= \frac{Q}{\rho}\sum_{m=1}^{\infty}\sum_{n=1}^{\infty}\frac{G_{w;mn}^2(h)}{M_{mn}\omega_{mn}}\sin(\omega_{mn}t)J_0(k_{mn}r). \end{aligned} \tag{4.90}$$

The *unit-impulse response* is the impulse response due to the unit impulse. It can be obtained from Equation (4.90) by replacing Q with 1.

Now consider a general time-dependent point source, i.e. in Equation (4.76),

$$\mathbf{F}(r,t) = Q\frac{\delta(r)}{2\pi r}F(t)\,\mathbf{e}_z. \tag{4.91}$$

Let the time function $F(t)$ be smooth enough and $F(t)=0$ for $t<0$. Then, the out-of-plane surface displacement due to this general excitation can be obtained from the convolution integral

$$\begin{aligned} u_z(r,h,t) &= \int_0^t F(\tau)u_z^\delta(r,h,t-\tau)\,d\tau \\ &= \frac{Q}{\rho}\sum_{m=1}^{\infty}\sum_{n=1}^{\infty}\frac{G_{w;mn}^2(h)}{M_{mn}\omega_{mn}}\left(\int_0^t F(\tau)\sin\left[\omega_{mn}(t-\tau)\right]d\tau\right)J_0(k_{mn}r). \end{aligned} \tag{4.92}$$

Note that, in this expression, the fact that $u_z^\delta(r,h,t)=0$ for $t<0$ is implicitly assumed.

Another way to approximate the response to certain point excitation with arbitrary time-dependence—the point source defined in Equation (4.91)—is to write the time-dependent function, $F(t)$, in an increment form. Let the time axis be discretized by t_0, t_1, ... The function $F(t)$ can be approximated as

$$\tilde{F}(t) \approx \sum_{i=0}^{\infty}\Delta F_i H(t-t_i), \tag{4.93}$$

where ΔF_i is the a properly-chosen increment in amplitude of $F(t)$ such as $\Delta F_i = F(t_i) - F(t_{i-1})$. This value can be negative when the function decreases. The transient response can then be approximately calculated by the superposition

$$u_z(r,h,t) = \sum_i \Delta F_i u_z^{H_{t_i}}(r,z,t), \tag{4.94}$$

where $u_z^{H_{t_i}}(r,z,t)$ is calculated from Equation (4.87). The two schemes are depicted in Figure 4.2.

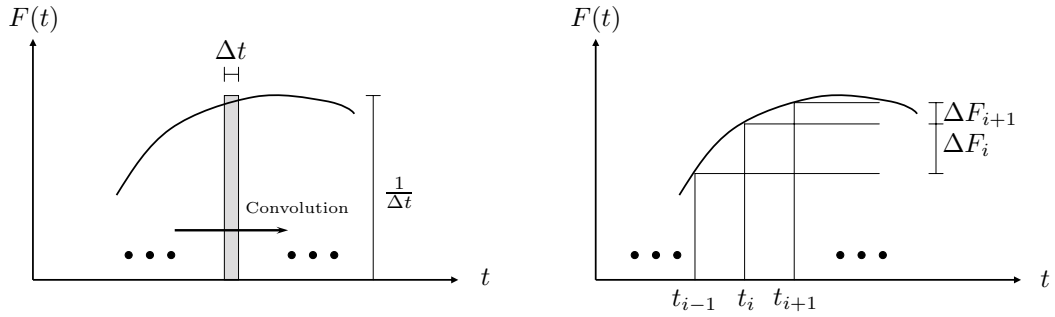

(a) Approximation by $u_z^{\delta}(r,h,t)$.

(b) Approximation by $u_z^{H}(r,h,t)$.

Figure 4.2: Approximation schemes for an excitation with arbitrary time-dependent function $F(t)$.

4.2.3 Implementation

The derivation in the previous subsection is implemented on a computer to simulate the out-of-plane displacement at the surface $u_z^H(r,h,t)$ or $u_z^{\delta}(r,h,t)$. The inputs are material properties and problem's geometry and the output is the out-of-plane surface response at a particular position away from the excitation $r = r_0$. The procedure is summarized as follows.

Input: c_L, c_T, ρ, R, h, and Q.

Output: $u_z^H(r_0,h,t)$ or $u_z^{\delta}(r_0,h,t)$.

Procedure:

1. Solve Equation (4.67) for the existing wavenumber k_1, k_2, ... Since there are infinitely many roots of this equation, this step is stopped after a sufficiently large number N of roots; k_1, k_2, ..., k_N, are found.

2. For each k_n, $n \sim 1$ to N, solve Equations (4.71) and (4.74) for corresponding frequency ω_{1n}, ω_{2n}, ... Since there are also infinitely many Lamb modes at each wavenumber, this step includes the number of Lamb modes up to M modes, ω_{Mn}.

3. For each Lamb wave mode m, for all $k_n's$,

   - calculate $\alpha_{L;mn}$ and $\alpha_{T;mn}$ from their definitions given by Equations (4.60);
   - calculate M_{mn} and $G_{w;mn}(h)$ from Equations (4.82) and (4.81);
   - calculate the modal response

$$u^H_{z;m}(r_0,h,t) = \frac{Q}{\rho}\sum_{n=1}^{N}\frac{G^2_{w;mn}(h)}{M_{mn}\omega^2_{mn}}\big[1-\cos(\omega_{mn}t)\big]J_0(k_{mn}r_0), \tag{4.95}$$

   and

$$u^\delta_{z;m}(r_0,h,t) = \frac{Q}{\rho}\sum_{n=1}^{N}\frac{G^2_{w;mn}(h)}{M_{mn}\omega_{mn}}\sin(\omega_{mn}t)J_0(k_{mn}r_0). \tag{4.96}$$

4. Repeat the previous step for every Lamb mode m, $m \sim 1$ to M.

5. Calculate the total response from the equation

$$u_z(r_0,h,t) = \sum_{m=1}^{M} u_{z;m}(r_0,h,t). \tag{4.97}$$

Note that, usually, the limiting numbers for existing wavenumber and Lamb mode can be determined from a given frequency limit. For a given maximum frequency limit, say 10 MHz, only finitely many Lamb modes exist. Also, with a fixed frequency limit and R, only finitely many wavenumber roots of Equation (4.67) can be found since, for each mode, the higher wavenumber is corresponding to the higher frequency which will reach the limit at some point.

An attention should be paid to the implementation when all the developments in Sections 4.2.1 and 4.2.2 are carried out under the real-space framework, but some parameters are expressed in the formulas which can yield complex numbers. In particular, the normal modes $\mathbf{u}_{mn}$'s are assumed to be real functions while the parameters are $\alpha_{L;mn}$ and $\alpha_{T;mn}$ expressed in Equations (4.60) and their consequences can be either real or pure imaginary depending on the values of ω_{mn} and k_{mn} (the frequency and wavenumber are always real and positive in this development). This difficulty can be overcome by dividing the ranges of ω_{mn} and k_{mn} into domains where all functions calculated are always real. The forms of the displacement potentials in Equations (4.59) can be unambiguously stated with real parameters and functions once the relations between $\frac{\omega_{mn}}{c_L}$ or $\frac{\omega_{mn}}{c_T}$ and k_{mn} are specified. This

scheme can be implemented in the functions f_{mn} and g_{mn} in Equations (4.63). Specifically, let those two functions be written as

$$\begin{aligned} f_{mn}(z) &= A_{s;mn} f_{s;mn}(z) + A_{a;mn} f_{a;mn}(z) \\ g_{mn}(z) &= B_{a;mn} g_{a;mn}(z) + B_{s;mn} g_{s;mn}(z), \end{aligned} \tag{4.98}$$

where all constants—$A_{s;mn}$, $A_{a;mn}$, $B_{a;mn}$ and $B_{s;mn}$—are real. The functions $f_{I;mn}(z)$ and $g_{I;mn}(z)$, $I \sim s$ or a in the above equations are not specified, but they are all real involving the cosine and sine or hyperbolic-cosine and hyperbolic-sine functions. Those functions will have following properties: $f_{s;mn}(z)$ and $g_{a;mn}(z)$ are even functions of z (cosine or hyperbolic-cosine); $f_{a;mn}(z)$ and $g_{s;mn}(z)$ are odd functions of z (sine or hyperbolic-sine). Note that the symmetric part of function g_{mn} (or $B_{s;mn} g_{s;mn}(z)$) is itself anti-symmetric (odd) because the displacement components involve the derivative of g_{mn} with respect to z, which will turn anti-symmetric g to symmetric g and vice versa.

With this form of the potentials, the Lamb modes can be divided into two groups—symmetric and anti-symmetric modes—as in Equations (4.69) as

$$\begin{aligned} &f_{mn}(z) = A_{s;mn} f_{s;mn}(z), \quad g_{mn}(z) = B_{s;mn} g_{s;mn}(z) \qquad \text{for symmetric modes} \\ &f_{mn}(z) = A_{a;mn} f_{a;mn}(z), \quad g_{mn}(z) = B_{a;mn} g_{a;mn}(z) \qquad \text{for anti-symmetric modes.} \end{aligned} \tag{4.99}$$

These f_{mn} and g_{mn} can be substituted into Equation (4.68) to obtain two homogeneous systems of two equations, each of which represents each type of normal modes. Both systems of equations can be written in the same matrix form as

$$\begin{bmatrix} -(\alpha_{T;mn}^2 - k_{mn}^2) f_{I;mn}(h) & 2k_{mn} g'_{I;mn}(h) \\ 2k_{mn} f'_{I;mn}(h) & -(\alpha_{T;mn}^2 - k_{mn}^2) g_{I;mn}(h) \end{bmatrix} \begin{Bmatrix} A_{I;mn} \\ B_{I;mn} \end{Bmatrix} = 0, \tag{4.100}$$

where I is either s or a according to the type of modes, and the symbol $'$ denotes the derivative with respect to the argument. Note that the term $\alpha_{T;mn}$ is the one defined in Equations (4.60). This term is fine because it appears as a square which is always real and $\alpha_{T;mn}^2 - k_{mn}^2 = \frac{\omega_{mn}^2}{c_T^2} - 2k_{mn}^2$.

The corresponding dispersion equation and mode shape are

$$R_{I;mn} \equiv (\alpha_{T;mn}^2 - k_{mn}^2)^2 f_{I;mn}(h) g_{I;mn}(h) - 4k_{mn}^2 f'_{I;mn}(h) g'_{I;mn}(h) = 0 \tag{4.101}$$

$$\frac{A_{I;mn}}{B_{I;mn}} = \frac{2k_{mn}g'_{I;mn}(h)}{(\alpha^2_{T;mn} - k^2_{mn})f_{I;mn}(h)} = \frac{(\alpha^2_{T;mn} - k^2_{mn})g_{I;mn}(h)}{2k_{mn}f'_{I;mn}(h)}. \tag{4.102}$$

Now the key is to specify the forms of f_{mn} and g_{mn} according to the range of ω_{mn} and k_{mn}. Besides the expressions of dispersion relations and mode shapes, these functions also affect functions $G_{u;mn}$, $G_{w;mn}$, and thus M_{mn} introduced the previous subsection. Explicitly, the forms of f_{mn} and g_{mn} in Equations (4.63) can be used when both $\alpha_{L;mn}$ and $\alpha_{T;mn}$ are real, or, equivalently, $\frac{\omega_{mn}}{c_L} > k_{mn}$ (note that $\frac{\omega_{mn}}{c_L}$ is always smaller than $\frac{\omega_{mn}}{c_T}$ because c_L is always greater than c_T). The corresponding $G_{u;mn}$, $G_{w;mn}$, and all expressions for dispersion equations and mode shapes in Equations (4.70)–(4.75) apply. For other cases, the modifications are the following. If $k_{mn} > \frac{\omega_{mn}}{c_T}$, the parameters $\alpha_{L;mn}$ and $\alpha_{T;mn}$ are both pure imaginary; thus, they need to be changed. Since both $\frac{\omega^2_{mn}}{c^2_L} - k^2_{mn}$ and $\frac{\omega^2_{mn}}{c^2_T} - k^2_{mn}$ are negative real, the general solutions Equations (4.58), expressed in terms of real functions, must be

$$\begin{aligned} \phi_{mn}(r,z) &= \Big[\bar{A}_{1;mn}\cosh(\bar{\alpha}_{L;mn}z) + \bar{A}_{2;mn}\sinh(\bar{\alpha}_{L;mn}z)\Big]J_0(k_{mn}r), \\ \psi_{mn}(r,z) &= \Big[\bar{B}_{1;mn}\cosh(\bar{\alpha}_{T;mn}z) + \bar{B}_{2;mn}\sinh(\bar{\alpha}_{T;mn}z)\Big]J_1(k_{mn}r), \end{aligned} \tag{4.103}$$

where the new real parameters $\bar{\alpha}_{L;mn}$ and $\bar{\alpha}_{T;mn}$ are defined as

$$\bar{\alpha}_{L;mn} = \sqrt{k^2_{mn} - \frac{\omega^2_{mn}}{c^2_L}}, \quad \text{and} \quad \bar{\alpha}_{T;mn} = \sqrt{k^2_{mn} - \frac{\omega^2_{mn}}{c^2_T}}. \tag{4.104}$$

The bars on the constants are used to distinguish this form of solution from the one in Equations (4.59), but the constants in both forms are just real constants. The resulting $f_{I;mn}$ and $g_{I;mn}$ in this case become

$$\begin{aligned} f_{s;mn}(z) &= \cosh(\bar{\alpha}_{L;mn}z), \quad f_{a;mn}(z) = \sinh(\bar{\alpha}_{L;mn}z) \\ g_{s;mn}(z) &= \sinh(\alpha_{T;mn}z), \quad g_{a;mn}(z) = \cosh(\alpha_{T;mn}z). \end{aligned}$$

In the case when $\frac{\omega_{mn}}{c_T} > k_{mn} > \frac{\omega_{mn}}{c_L}$, the term $\alpha_{T;mn}$ as defined in Equations (4.60) is real so that the functions ψ_{mn}, and thus g_{mn}, remain unchanged from the ones in Section 4.2.1. On the other hand, since $\frac{\omega^2_{mn}}{c^2_L} - k^2_{mn} < 0$, the function ϕ_{mn} must take the form in Equations (4.103). Once the forms of f_{mn} and g_{mn} are selected, the rest of the calculation is the same. The dispersion equations and mode shapes then follow from Equations (4.101)

and (4.102). Functions $G_{u;mn}$ and $G_{w;mn}$ are obtained from functions f_{mn} and g_{mn} by comparing Equations (4.66) and Equations (4.81), with the constants (mode shape) chosen from Equations (4.102). That is, if the first equation of Equations (4.102) is used,

$$\begin{aligned}
G^{(I)}_{u;mn}(z) &= -\Big[k_{mn}f_{mn}(z) + g'_{mn}(z)\Big] \\
&= -\Big[k_{mn}A_{I;mn}f_{I;mn}(z) + B_{I;mn}g'_{I;mn}(z)\Big] \\
&= -\Big[2k^2_{mn}g'_{I;mn}(h)f_{I;mn}(z) + (\alpha^2_{T;mn} - k^2_{mn})f_{I;mn}(h)g'_{I;mn}(z)\Big] \\
G^{(I)}_{w;mn}(z) &= f'_{mn}(z) + k_{mn}g_{mn}(z), \\
&= A_{I;mn}f'_{I;mn}(z) + B_{I;mn}k_{mn}g_{I;mn}(z) \\
&= 2k_{mn}g'_{I;mn}(h)f'_{I;mn}(z) + (\alpha^2_{T;mn} - k^2_{mn})k_{mn}f_{I;mn}(h)g_{I;mn}(z). \quad (4.105)
\end{aligned}$$

Since this modification is straightforward, only the results are presented here. Functions $f_{I;mn}$ and $g_{I;mn}$ are summarized in Table 4.1.

Table 4.1: Functions $f_{I;mn}$ and $g_{I;mn}$ used in Equations (4.69)–(4.102).

Range	$f_{s;mn}$	$f_{a;mn}$	$g_{s;mn}$	$g_{a;mn}$
$\frac{\omega_{mn}}{c_L} > k_{mn}$	$\cos(\alpha_{L;mn}z)$	$\sin(\alpha_{L;mn}z)$	$\sin(\alpha_{T;mn}z)$	$\cos(\alpha_{T;mn}z)$
$\frac{\omega_{mn}}{c_T} > k_{mn} > \frac{\omega_{mn}}{c_L}$	$\cosh(\bar{\alpha}_{L;mn}z)$	$\sinh(\bar{\alpha}_{L;mn}z)$	$\cos(\alpha_{T;mn}z)$	$\sin(\alpha_{T;mn}z)$
$k_{mn} > \frac{\omega_{mn}}{c_T}$	$\cosh(\bar{\alpha}_{L;mn}z)$	$\sinh(\bar{\alpha}_{L;mn}z)$	$\sinh(\bar{\alpha}_{T;mn}z)$	$\cosh(\bar{\alpha}_{T;mn}z)$

The dispersion equations, mode shapes, $G_{u;mn}$ and $G_{w;mn}$ for each case, are given explicitly in the following expressions. Also, the expressions for the integration of $G^2_{u;mn}$, $G^2_{w;mn}$ over the thickness, which are used to calculate M_{mn} in Equations (4.84), are given in closed form. In these expressions, the indices mn are dropped everywhere for brevity and clarity.

I. $\frac{\omega}{c_L} > k$

Symmetric modes $\Big(f(z) = A\cos(\alpha_L z), g(z) = B\sin(\alpha_T z)\Big)$

The dispersion equation:

$$(\alpha^2_T - k^2)^2\cos(\alpha_L h)\sin(\alpha_T h) + 4k^2\alpha_L\alpha_T\sin(\alpha_L h)\cos(\alpha_T h) = 0 \quad (4.106)$$

Selected mode shape:

$$A = 2k\alpha_T \cos(\alpha_T h), \qquad \text{and} \qquad B = (\alpha_T^2 - k^2)\cos(\alpha_L h) \tag{4.107}$$

Functions $G_u(z)$ and $G_w(z)$:

$$\begin{aligned} G_u(z) &= -Ak\cos(\alpha_L z) - B\alpha_T \cos(\alpha_T z) \\ G_w(z) &= -A\alpha_L \sin(\alpha_L z) + Bk\sin(\alpha_T z) \end{aligned} \tag{4.108}$$

$$\begin{aligned} \int_{-h}^{h} G_u^2(z)\,dz &= k^2\Big[h + \frac{\sin(2\alpha_L h)}{2\alpha_L}\Big]A^2 + \alpha_T^2\Big[h + \frac{\sin(2\alpha_T h)}{2\alpha_T}\Big]B^2 \\ &\quad + \frac{4c_L^2 c_T^2 k\alpha_T}{\omega^2(c_L^2 - c_T^2)}\Big[\alpha_T\cos(\alpha_L h)\sin(\alpha_T h) - \alpha_L \sin(\alpha_L h)\cos(\alpha_T h)\Big]AB \\ \int_{-h}^{h} G_w^2(z)\,dz &= \alpha_L^2\Big[h - \frac{\sin(2\alpha_L h)}{2\alpha_L}\Big]A^2 + k^2\Big[h - \frac{\sin(2\alpha_T h)}{2\alpha_T}\Big]B^2 \\ &\quad - \frac{4c_L^2 c_T^2 k\alpha_L}{\omega^2(c_L^2 - c_T^2)}\Big[\alpha_L\cos(\alpha_L h)\sin(\alpha_T h) - \alpha_T \sin(\alpha_L h)\cos(\alpha_T h)\Big]AB \end{aligned} \tag{4.109}$$

<u>*Anti-symmetric modes*</u> $\Big(f(z) = A\sin(\alpha_L z), g(z) = B\cos(\alpha_T z)\Big)$

The dispersion equation:

$$(\alpha_T^2 - k^2)^2 \sin(\alpha_L h)\cos(\alpha_T h) + 4k^2\alpha_L\alpha_T \cos(\alpha_L h)\sin(\alpha_T h) = 0 \tag{4.110}$$

Selected mode shape:

$$A = 2k\alpha_T \sin(\alpha_T h), \qquad \text{and} \qquad B = -(\alpha_T^2 - k^2)\sin(\alpha_L h) \tag{4.111}$$

Functions $G_u(z)$ and $G_w(z)$:

$$\begin{aligned} G_u(z) &= -Ak\sin(\alpha_L z) + B\alpha_T \sin(\alpha_T z) \\ G_w(z) &= A\alpha_L \cos(\alpha_L z) + Bk\cos(\alpha_T z) \end{aligned} \tag{4.112}$$

$$\begin{aligned} \int_{-h}^{h} G_u^2(z)\,dz &= k^2\Big[h - \frac{\sin(2\alpha_L h)}{2\alpha_L}\Big]A^2 + \alpha_T^2\Big[h - \frac{\sin(2\alpha_T h)}{2\alpha_T}\Big]B^2 \\ &\quad - \frac{4c_L^2 c_T^2 k\alpha_T}{\omega^2(c_L^2 - c_T^2)}\Big[\alpha_L\cos(\alpha_L h)\sin(\alpha_T h) - \alpha_T \sin(\alpha_L h)\cos(\alpha_T h)\Big]AB \\ \int_{-h}^{h} G_w^2(z)\,dz &= \alpha_L^2\Big[h + \frac{\sin(2\alpha_L h)}{2\alpha_L}\Big]A^2 + k^2\Big[h + \frac{\sin(2\alpha_T h)}{2\alpha_T}\Big]B^2 \\ &\quad + \frac{4c_L^2 c_T^2 k\alpha_L}{\omega^2(c_L^2 - c_T^2)}\Big[\alpha_T\cos(\alpha_L h)\sin(\alpha_T h) - \alpha_L \sin(\alpha_L h)\cos(\alpha_T h)\Big]AB \end{aligned} \tag{4.113}$$

II. $\frac{\omega}{c_T} > k > \frac{\omega}{c_L}$

Symmetric modes $\Big(f(z) = A\cosh(\bar{\alpha}_L z), g(z) = B\sin(\alpha_T z)\Big)$

The dispersion equation:

$$(\alpha_T^2 - k^2)^2 \cosh(\bar{\alpha}_L h)\sin(\alpha_T h) - 4k^2\bar{\alpha}_L\alpha_T \sinh(\bar{\alpha}_L h)\cos(\alpha_T h) = 0 \qquad (4.114)$$

Selected mode shape:

$$A = 2k\alpha_T \cos(\alpha_T h), \qquad \text{and} \qquad B = (\alpha_T^2 - k^2)\cosh(\bar{\alpha}_L h) \qquad (4.115)$$

Functions $G_u(z)$ and $G_w(z)$:

$$\begin{aligned} G_u(z) &= -Ak\cosh(\bar{\alpha}_L z) - B\alpha_T \cos(\alpha_T z) \\ G_w(z) &= A\bar{\alpha}_L \sinh(\bar{\alpha}_L z) + Bk\sin(\alpha_T z) \end{aligned} \qquad (4.116)$$

$$\begin{aligned} \int_{-h}^{h} G_u^2(z)\,dz &= k^2\Big[h + \frac{\sinh(2\bar{\alpha}_L h)}{2\bar{\alpha}_L}\Big]A^2 + \alpha_T^2\Big[h + \frac{\sin(2\alpha_T h)}{2\alpha_T}\Big]B^2 \\ &\quad + \frac{4c_L^2 c_T^2 k\alpha_T}{\omega^2(c_L^2 - c_T^2)}\Big[\alpha_T\cosh(\bar{\alpha}_L h)\sin(\alpha_T h) + \bar{\alpha}_L\sinh(\bar{\alpha}_L h)\cos(\alpha_T h)\Big]AB \\ \int_{-h}^{h} G_w^2(z)\,dz &= \bar{\alpha}_L^2\Big[-h + \frac{\sinh(2\bar{\alpha}_L h)}{2\bar{\alpha}_L}\Big]A^2 + k^2\Big[h - \frac{\sin(2\alpha_T h)}{2\alpha_T}\Big]B^2 \\ &\quad + \frac{4c_L^2 c_T^2 k\bar{\alpha}_L}{\omega^2(c_L^2 - c_T^2)}\Big[\bar{\alpha}_L\cosh(\bar{\alpha}_L h)\sin(\alpha_T h) - \alpha_T\sinh(\bar{\alpha}_L h)\cos(\alpha_T h)\Big]AB \end{aligned} \qquad (4.117)$$

Anti-symmetric modes $\Big(f(z) = A\sinh(\bar{\alpha}_L z), g(z) = B\cos(\alpha_T z)\Big)$

The dispersion equation:

$$(\alpha_T^2 - k^2)^2 \sinh(\bar{\alpha}_L h)\cos(\alpha_T h) + 4k^2\bar{\alpha}_L\alpha_T \cosh(\bar{\alpha}_L h)\sin(\alpha_T h) = 0 \qquad (4.118)$$

Selected mode shape:

$$A = 2k\alpha_T \sin(\alpha_T h), \qquad \text{and} \qquad B = -(\alpha_T^2 - k^2)\sinh(\bar{\alpha}_L h) \qquad (4.119)$$

Functions $G_u(z)$ and $G_w(z)$:

$$\begin{aligned} G_u(z) &= -Ak\sinh(\bar{\alpha}_L z) + B\alpha_T \sin(\alpha_T z) \\ G_w(z) &= A\bar{\alpha}_L \cosh(\bar{\alpha}_L z) + Bk\cos(\alpha_T z) \end{aligned} \qquad (4.120)$$

$$
\begin{aligned}
\int_{-h}^{h} G_u^2(z)\,dz &= k^2\Big[-h+\frac{\sinh(2\bar{\alpha}_L h)}{2\bar{\alpha}_L}\Big]A^2+\alpha_T^2\Big[h-\frac{\sin(2\alpha_T h)}{2\alpha_T}\Big]B^2 \\
&\quad -\frac{4c_L^2c_T^2k\alpha_T}{\omega^2(c_L^2-c_T^2)}\Big[\bar{\alpha}_L\cosh(\bar{\alpha}_L h)\sin(\alpha_T h)-\alpha_T\sinh(\bar{\alpha}_L h)\cos(\alpha_T h)\Big]AB \\
\int_{-h}^{h} G_w^2(z)\,dz &= \bar{\alpha}_L^2\Big[h+\frac{\sinh(2\bar{\alpha}_L h)}{2\bar{\alpha}_L}\Big]A^2+k^2\Big[h+\frac{\sin(2\alpha_T h)}{2\alpha_T}\Big]B^2 \\
&\quad +\frac{4c_L^2c_T^2k\bar{\alpha}_L}{\omega^2(c_L^2-c_T^2)}\Big[\alpha_T\cosh(\bar{\alpha}_L h)\sin(\alpha_T h)+\bar{\alpha}_L\sinh(\bar{\alpha}_L h)\cos(\alpha_T h)\Big]AB
\end{aligned}
\tag{4.121}
$$

III. $k > \frac{\omega}{c_T}$

<u>*Symmetric modes*</u> $\Big(f(z)=A\cosh(\bar{\alpha}_L z), g(z)=B\sinh(\bar{\alpha}_T z)\Big)$

The dispersion equation:

$$
(\bar{\alpha}_T^2+k^2)^2\cosh(\bar{\alpha}_L h)\sinh(\bar{\alpha}_T h)-4k^2\bar{\alpha}_L\bar{\alpha}_T\sinh(\bar{\alpha}_L h)\cosh(\bar{\alpha}_T h)=0 \tag{4.122}
$$

Selected mode shape:

$$
A=2k\bar{\alpha}_T\cosh(\bar{\alpha}_T h), \qquad \text{and} \qquad B=-(\bar{\alpha}_T^2+k^2)\cosh(\bar{\alpha}_L h) \tag{4.123}
$$

Functions $G_u(z)$ and $G_w(z)$:

$$
\begin{aligned}
G_u(z) &= -Ak\cosh(\bar{\alpha}_L z)-B\bar{\alpha}_T\cosh(\bar{\alpha}_T z) \\
G_w(z) &= A\bar{\alpha}_L\sinh(\bar{\alpha}_L z)+Bk\sinh(\bar{\alpha}_T z)
\end{aligned}
\tag{4.124}
$$

$$
\begin{aligned}
\int_{-h}^{h} G_u^2(z)\,dz &= k^2\Big[h+\frac{\sinh(2\bar{\alpha}_L h)}{2\bar{\alpha}_L}\Big]A^2+\bar{\alpha}_T^2\Big[h+\frac{\sinh(2\bar{\alpha}_T h)}{2\bar{\alpha}_T}\Big]B^2 \\
&\quad -\frac{4c_L^2c_T^2k\bar{\alpha}_T}{\omega^2(c_L^2-c_T^2)}\Big[\bar{\alpha}_T\cosh(\bar{\alpha}_L h)\sinh(\bar{\alpha}_T h)-\bar{\alpha}_L\sinh(\bar{\alpha}_L h)\cosh(\bar{\alpha}_T h)\Big]AB \\
\int_{-h}^{h} G_w^2(z)\,dz &= \bar{\alpha}_L^2\Big[-h+\frac{\sinh(2\bar{\alpha}_L h)}{2\bar{\alpha}_L}\Big]A^2+k^2\Big[-h+\frac{\sinh(2\bar{\alpha}_T h)}{2\bar{\alpha}_T}\Big]B^2 \\
&\quad +\frac{4c_L^2c_T^2k\bar{\alpha}_L}{\omega^2(c_L^2-c_T^2)}\Big[\bar{\alpha}_L\cosh(\bar{\alpha}_L h)\sinh(\bar{\alpha}_T h)-\bar{\alpha}_T\sinh(\bar{\alpha}_L h)\cosh(\bar{\alpha}_T h)\Big]AB
\end{aligned}
\tag{4.125}
$$

<u>*Anti-symmetric modes*</u> $\Big(f(z)=A\sinh(\bar{\alpha}_L z), g(z)=B\cosh(\bar{\alpha}_T z)\Big)$

The dispersion equation:

$$
(\bar{\alpha}_T^2+k^2)^2\sinh(\bar{\alpha}_L h)\cosh(\bar{\alpha}_T h)-4k^2\bar{\alpha}_L\bar{\alpha}_T\cosh(\bar{\alpha}_L h)\sinh(\bar{\alpha}_T h)=0 \tag{4.126}
$$

Selected mode shape:

$$A = 2k\bar{\alpha}_T \sinh(\bar{\alpha}_T h), \qquad \text{and} \qquad B = -(\bar{\alpha}_T^2 + k^2)\sinh(\bar{\alpha}_L h) \tag{4.127}$$

Functions $G_u(z)$ and $G_w(z)$:

$$\begin{aligned} G_u(z) &= -Ak\sinh(\bar{\alpha}_L z) - B\bar{\alpha}_T \sinh(\bar{\alpha}_T z) \\ G_w(z) &= A\bar{\alpha}_L \cosh(\bar{\alpha}_L z) + Bk\cosh(\bar{\alpha}_T z) \end{aligned} \tag{4.128}$$

$$\begin{aligned} \int_{-h}^{h} G_u^2(z)\,dz &= k^2\Big[-h + \frac{\sinh(2\bar{\alpha}_L h)}{2\bar{\alpha}_L}\Big]A^2 + \bar{\alpha}_T^2\Big[-h + \frac{\sinh(2\bar{\alpha}_T h)}{2\bar{\alpha}_T}\Big]B^2 \\ &\quad + \frac{4c_L^2 c_T^2 k\bar{\alpha}_T}{\omega^2(c_L^2 - c_T^2)}\Big[\bar{\alpha}_L\cosh(\bar{\alpha}_L h)\sinh(\bar{\alpha}_T h) - \bar{\alpha}_T\sinh(\bar{\alpha}_L h)\cosh(\bar{\alpha}_T h)\Big]AB \\ \int_{-h}^{h} G_w^2(z)\,dz &= \bar{\alpha}_L^2\Big[h + \frac{\sinh(2\bar{\alpha}_L h)}{2\bar{\alpha}_L}\Big]A^2 + k^2\Big[h + \frac{\sinh(2\bar{\alpha}_T h)}{2\bar{\alpha}_T}\Big]B^2 \\ &\quad - \frac{4c_L^2 c_T^2 k\bar{\alpha}_L}{\omega^2(c_L^2 - c_T^2)}\Big[\bar{\alpha}_T\cosh(\bar{\alpha}_L h)\sinh(\bar{\alpha}_T h) - \bar{\alpha}_L\sinh(\bar{\alpha}_L h)\cosh(\bar{\alpha}_T h)\Big]AB \end{aligned} \tag{4.129}$$

To obtain the above results, closed-form integrals of a function involving a product of trigonometric or hyperbolic functions are derived. Those derivations are given in Appendix C.

Note that the modification to force all the variables real can also be done through the use of identities: $\cos(ja) = \cosh(a)$ and $\sin(ja) = j\sinh(a)$, where a is a real quantity, into Equations (4.71), (4.72), (4.74), and (4.75). The imaginary unit from the use of these identities can be absorbed into the constant associated with that particular term. The dispersion equation will always be a real equation after some normalization. Similarly, the ratio between two constants representing the mode shape is also real for all cases with some normalization. This scheme is easily verified to lead to the same real results presented earlier in Equations (4.106)–(4.129).

4.3 Verification of the simulation

This section examines several aspects of the simulation through simulated time-domain signals. Dispersion curves of the system are extracted from a simulated signal by the short-time Fourier transform; these "synthetic" dispersion curves are compared with the analytical

curves. The characteristics—the excitability in particular—of the signals are studied and compared to the references. Lastly, the simulated signal is compared to the real signal from the experiment.

4.3.1 Simulated signals and their general characteristics

This simulation is carried on in the computer program, MATLAB. A typical simulated signal for $u_z^\delta(r, h, t)$ (calculated from Equation (4.90)) is shown in Figure 4.3. For this signal, the medium is a 1-mm-thick aluminum plate of a radius of 2 m, with the following properties: $c_L = 6320$ m/s, $c_T = 3130$ m/s, $\rho = 2700$ m/s. The excitation amplitude Q used is unity. The time step is 0.01 µs. The maximum frequency limit is set to 10 MHz. Within this limit, ten Lamb modes—five symmetric modes and five anti-symmetric modes—are included in the simulation. The propagation in this simulation is 46 mm which is much smaller than the radius R, so the simulation approximates the response of an infinite plate. The simulation takes about 190 s to finish with a personal computer, P4 2.0 GHz, 1 GB RAM. Note that this computation time does not include the time used in the calculation of the roots of the dispersion equations in the thickness direction (4.71) and (4.74) (the simulation does include the calculation of the roots of the dispersion equation in the radial direction (4.67)). However, these roots are obtained by a commercial software DISPERSE [71]. The software can finish calculating the roots of dispersion equations for a free plate in less than 15 s.

It is clearly seen that the simulated time-domain signal in Figure 4.3 possesses high signal-to-noise ratio (SNR). The noise, which is from numerical errors in the simulation, can be approximated by the non-causal part of the signal. Here, the non-causal part of the signal is the beginning part that arrives the receiver before the extensional wave. Analytically, this extensional wave can be obtained by consideration of longitudinal waves in a thin plate [31]. The word "thin plate" means the plate to which the classical (thin) plate theory applies. This situation occurs when the wavelengths of waves are much larger than the plate thickness. In the analysis presented in Section 2.1.4, this extensional wave is the first symmetric Lamb wave (S0 mode) in the limit of small frequency, $\omega \to 0$. This wave is the fastest propagating Lamb wave. Its energy travels with the extensional wave velocity, c_e,

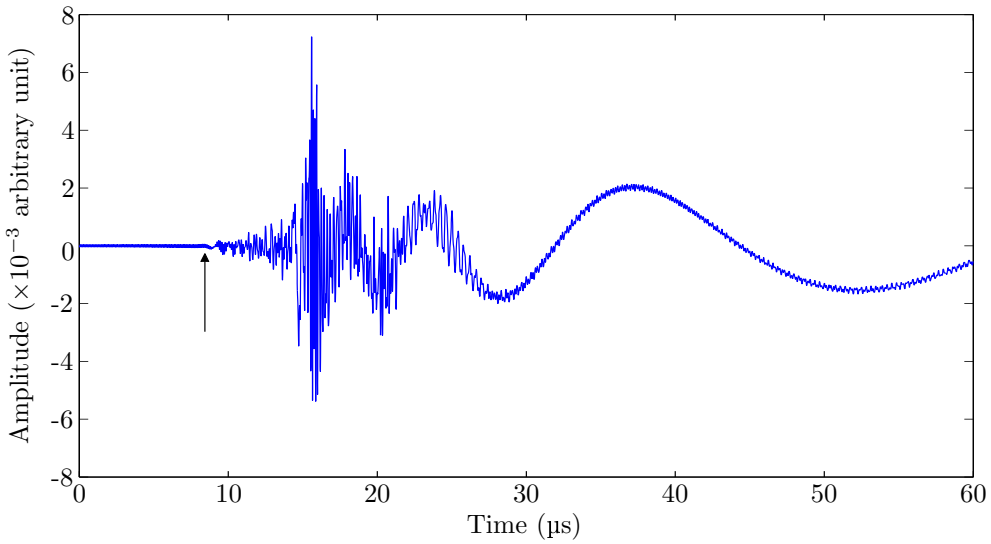

Figure 4.3: The simulated out-of-plane surface impulse response, $u_z^{\delta}(r, h, t)$, of a 1-mm-thick aluminum plate. The propagation distance is 46 mm.

given by [2]

$$c_e = 2c_T\sqrt{1 - \frac{c_T^2}{c_L^2}}. \tag{4.130}$$

From the material properties used in this simulation, the extensional wave velocity is calculated to be 5428 m/s. Hence, for a propagation distance of 46 mm, the first wave packet should arrive around 8.5 μs. This first arrival is pointed by an arrow in Figure 4.3.

The non-causal part of in this synthetic signal is mainly due to the frequency limit at 10 MHz. A close-up look, which can be seen in Figure 4.4, reveals that this part of a signal has its energy confined at 10 MHz. This instance, also encountered by Weaver and Pao [97], is common when time-harmonic normal modes, which have no time information or causality, are used to approximate a transient response. Ideally, if there is no limit on the frequency and the number of modes included in the calculation, this non-causal part will tend to zero at least in the least-square sense. With this non-causal part as a noise, the signal-to-noise ratio is generally estimated to be around 40 dB. This signal-to-noise ratio can be even improved by filtering the signal by a 10-MHz low-pass filter. The improvement is demonstrated in Figure 4.4. In that figure, the solid line is the non-causal part of the signal shown in Figure 4.3 after filtering; the original noise before filtering is also shown by a dotted line. Note that the dynamic range (vertical scale) of this plot is 1% of the one in

Figure 4.3.

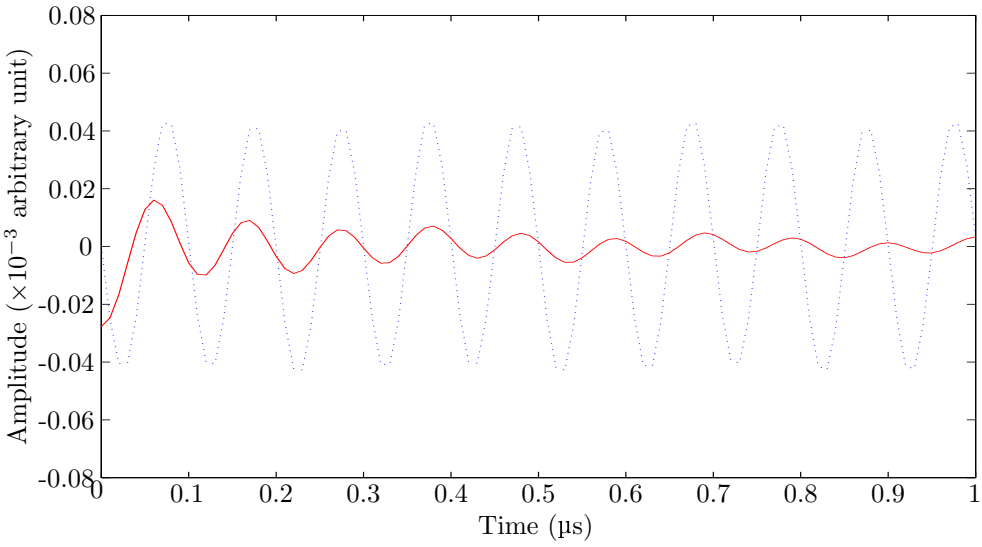

Figure 4.4: Removal of a non-causal part in the signal by low-pass filtering. This non-causal part of the signal in Figure 4.3 is shown before (dotted line) and after (solid line) 10-MHz low-pass filtering.

The modal responses of all existing Lamb modes are readily available once the simulation is done. For an impulse point excitation, the theoretical expression for each modal impulse response can be easily obtained from Equation (4.90), i.e. for mode m,

$$u^{\delta}_{z;m}(r,h,t) = \frac{Q}{\rho}\sum_{n=1}^{\infty}\frac{G^2_{w;mn}(h)}{M_{mn}\omega_{mn}}\sin(\omega_{mn}t)J_0(k_{mn}r). \tag{4.131}$$

The practical version of this equation is given in Equation (4.96) where the number of existing wavenumbers is truncated to a finite number N. The individual modal responses to the normal excitation according to Equation (4.131) are shown in Figure 4.5. This figure presents all ten Lamb modes which are used to calculate the total impulse response shown in Figure 4.3. In this figure, the higher-order modes' responses (those of S1–S4 and A1–A4 modes') are plotted in the amplitude scale of eight times smaller than the scale for the two fundamental modes (S0 and A0). This emphasizes the domination of the fundamental modes. The plot suggests that, as expected, the contribution of the higher-order mode is smaller as the number of mode increases. This observation confirms the implementation that the number of modes can be truncated to include only a few first modes. This is equivalent to setting up the maximum frequency limit since the higher number of mode

starts to exist at higher frequency.

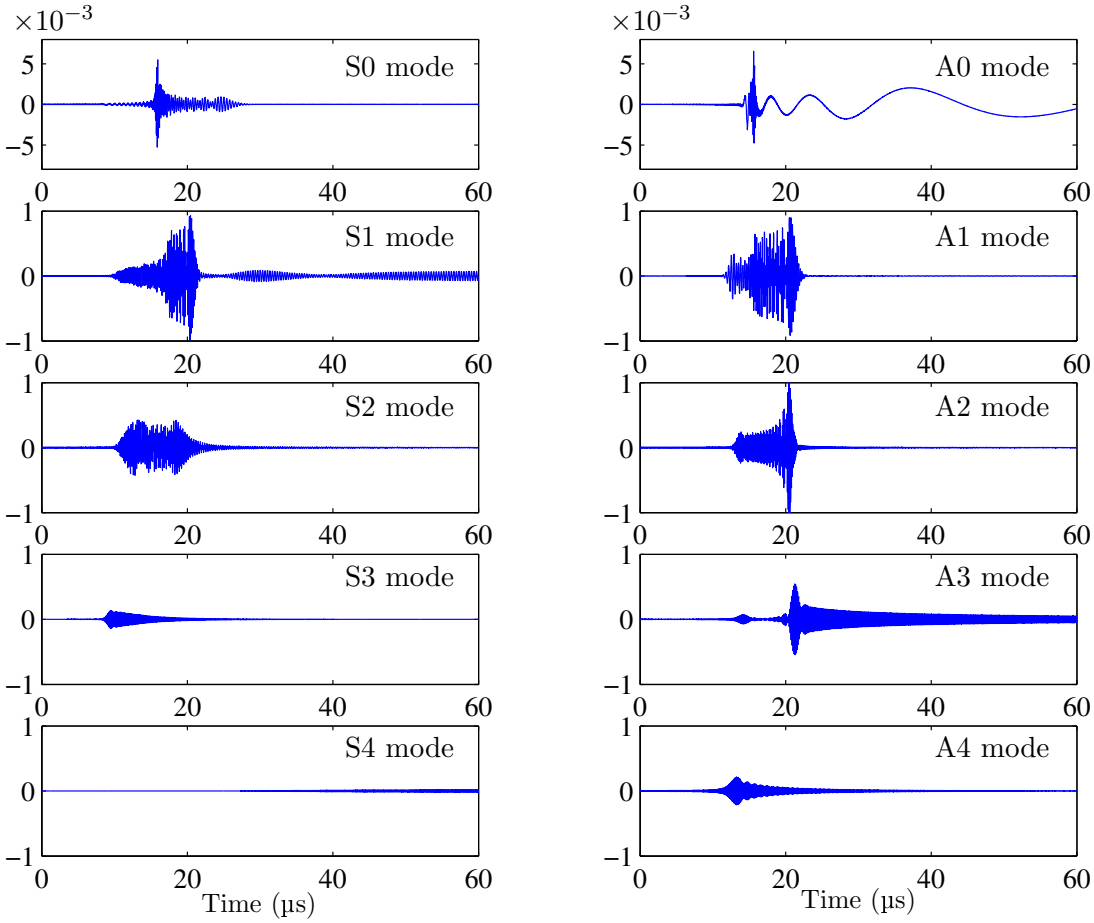

Figure 4.5: Individual modal responses constituting the total signal in Figure 4.3. The plot shows the first ten Lamb modes.

The dispersion curves of the system can be extracted from this time-domain signal by the short-time Fourier transform (STFT). As seen in Section 2.2.4, the STFT gives the contour plot in the time-frequency domain. This contour plot represents the dispersion curves of the system if the time axis is converted to the energy velocity or energy slowness by the simple relations

$$c_e = \frac{d}{t} \tag{4.132}$$

$$sl_e = \frac{t}{d}. \tag{4.133}$$

For a free plate, this energy velocity or energy slowness matches the group velocity ($c_g = \frac{\partial \omega}{\partial k}$)

or group slowness ($sl_g = \frac{1}{c_g}$) so that the derived contour with this normalized axis can be directly compared to the dispersion curves in the f-c_g or f-sl_g domain. This statement holds for the most frequency even in the case of leaky Lamb waves, provided that leakage is small enough [9]. Since small leakage is the case in this research, the terms "group velocity (or slowness)" and "energy velocity (or slowness)" are used interchangeably throughout this thesis. Figure 4.6 shows the STFT of the simulated signal in Figure 4.3. The time axis (vertical axis) is divided by a propagation distance of 46 mm to obtain the group (or energy) slowness axis. The window in the STFT is chosen to be a 5-µs Hanning window applied every 0.1 µs. Analytical dispersion curves are shown in the same plot as dashed lines for comparison. Note that the contour plot must match the analytical curves since those dispersion information (through those analytical dispersion curves) is the input in the simulation. Figure 4.6 simply confirms this validation.

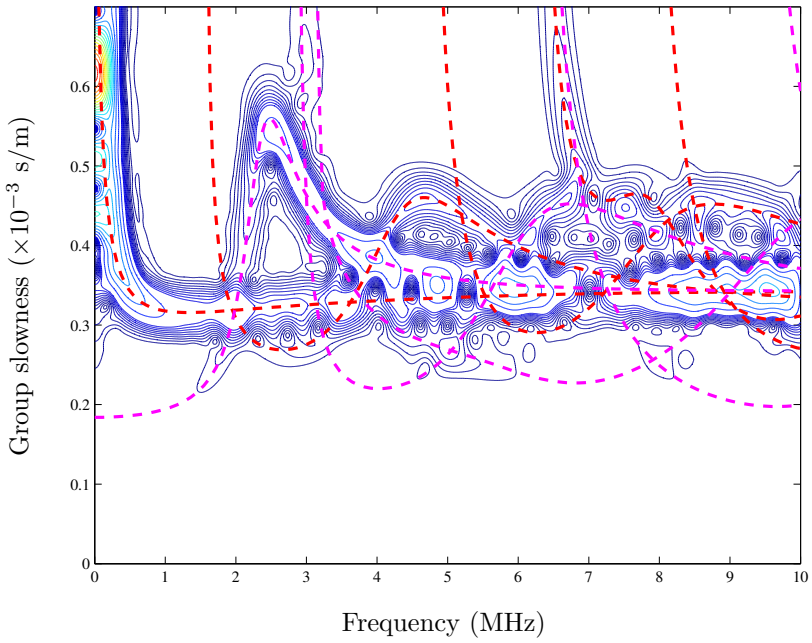

Figure 4.6: Dispersion curves of the simulated time-domain signal in Figure 4.3, obtained by the STFT. Analytical dispersion curves in frequency-slowness domain are shown by dashed lines.

4.3.2 Excitability of Lamb modes

Next, the simulation is verified with the concept of excitability. Basically, the excitability of a Lamb mode is the magnitude of that Lamb mode which can be excited in comparison to the strength of the excitation; clearly, it is a function of frequency and Lamb mode. The term "excitability" alone is generally ambiguous since it depends on the quantity under consideration and also the character of the excitation. For example, the excitability of the out-of-plane component of the displacement due to a normal excitation will be different from both the excitability of the in-plane component by the same source and the excitability of the same component by the in-plane excitation. In this study, this excitability term is specifically defined for the "out-of-plane" component of the displacement due to the "normal" point excitation to be coincide with the experiment and the analytical model developed earlier.

Excitability can be obtained from the time-harmonic analysis of the current problem, i.e. the current problem with a time-harmonic the excitation. This time-harmonic assumption causes all resulting field quantities to be also time-harmonic. Several methods such as integral transform, ray theory and reciprocity can be used to calculate the excitability [99]. This analysis differs from the analysis of classical Lamb waves and free-vibration because now, a certain excitation must be specified and included in the analysis. This inclusion of an excitation results in a set of non-homogeneous boundary conditions, and thus, non-trivial solutions can be obtained directly from solving simultaneous equations.

Explicitly in a mathematical formula, if the normal point excitation on the surface of the plate is assumed to have the time-dependent factor of $Qe^{j\omega t}$, where Q is the strength of the excitation, the out-of-plane displacement response of a particular Lamb mode n at the surface of the plate will assume the form

$$u_z^{(n)}(r,h) = E^{(n)}(\omega) Q\, H_0^{(2)}\big[k^{(n)}(\omega) r\big] e^{j\omega t}, \tag{4.134}$$

where $E^{(n)}(\omega)$ is the excitability of that Lamb mode n as a function of frequency; $k^{(n)}(\omega)$ is the wavenumber which is also a function of frequency and depends on a Lamb mode. The superscript $^{(n)}$ is included to emphasize the dependency on a Lamb mode; this superscript

will be usually dropped later on to avoid unnecessary complication in the expressions. Again, in Equation (4.134), the real part of the complex expression is implicitly assumed.

The derivation of a specific excitability defined in this research is carried out by the method of integral transform. The extensive details are presented in Appendix D. From the analysis, the excitability of symmetric and anti-symmetric Lamb modes, E_s and E_a, respectively, are

$$\begin{aligned} E_s(\omega) &= -\frac{j}{4\mu}\frac{\omega^2}{c_T^2}\frac{k\alpha_L \sin(\alpha_T h)\sin(\alpha_L h)}{R_s'(k)} \\ E_a(\omega) &= \frac{j}{4\mu}\frac{\omega^2}{c_T^2}\frac{k\alpha_L \cos(\alpha_T h)\cos(\alpha_L h)}{R_a'(k)}, \end{aligned} \tag{4.135}$$

where the wavenumber k is the corresponding k to the frequency ω of a particular Lamb mode according the dispersion relation; the symbol $'$ denotes the derivative with respect to the argument k. It can be noticed that the excitability in Equations (4.135) can be either real or pure imaginary for the present problem (with no dissipation), so its magnitude can be simply calculated by neglecting the imaginary unit. The imaginary unit j can be absorbed in the exponential term in the expression (4.134) and thought as a phase shift of π in the response.

In the far-field, the circularly-spreading Lamb waves in this axisymmetric problem, behave as plane waves. This can be viewed by the asymptotic expression of the Hankel function at a large argument. By the formula in Section 9.2.4 of Reference [1]: for $|z| \to \infty$,

$$H_0^{(2)}(z) \sim \sqrt{\frac{2}{\pi z}} e^{-j(z-\frac{\pi}{4})}, \qquad (-2\pi < \arg z < \pi), \tag{4.136}$$

the representation of the modal response in Equation (4.134) becomes of the form

$$u_z^{(n)}(r,h) \sim \frac{1}{\sqrt{r}}\tilde{E}^{(n)}(\omega) Q e^{j(\omega t - k^{(n)}(\omega) r + \frac{\pi}{4})}, \tag{4.137}$$

where $\tilde{E}^{(n)}(\omega)$ is the net excitability in the far-field, defined as

$$\tilde{E}^{(n)}(\omega) = \sqrt{\frac{2}{\pi k^{(n)}(\omega)}} E^{(n)}(\omega). \tag{4.138}$$

To verify the synthetic signals from simulation with the concept of excitability, one can do it by the direct and indirect ways. For the direct way, the transient excitation is decomposed into a linear combination of the time-harmonic excitation of various frequency by the

Fourier integral. Then, the modal and total displacement responses are calculated based on the excitability concept following Equation (4.134) or (4.137). This frequency-domain response can be inverted back into the time-domain response and compared with the transient response directly obtained from the transient formulation (e.g. from Equation (4.131)). However, the direct comparison in time domain can be hard to judge since the transient time-domain signal is usually complicated and contains many frequency components. Numerical errors in different simulation processes can cause different errors in the final time responses. This similar comparison—between the results from time-harmonic analysis and the direct transient formulation—was made for a similar problem in Reference [94] with the referenced results from Reference [97]. The result of comparison is "qualitatively" good after a careful treatment in the time-harmonic analysis.

This study makes a simpler but more quantitative comparison using the indirect way. Basically, the excitability of each mode is compared in the frequency domain. The excitability in the frequency domain by the time-harmonic analysis is readily obtained as presented in Equations (4.135) or (4.138) for a far-field response, while the excitability by the transient formulation can be directly calculated from the spectrum of the simulated time response. This magnitude spectrum is easily obtained from the magnitude of the Fourier transform, and it can be interpreted as the strength of the modal response when the far-field is considered. Since there is still the transient effect due to the difference in excitation in two analyses (one is time-harmonic while the other is transient), the excitability must be normalized before being compared. The normalization is realized from the fact that, at a fixed frequency, the excitability of a Lamb mode in relation to that of a fixed reference mode must be the same regardless of the excitation. The normalization eliminates the strength of the excitation and the effect of the propagation distance presented in terms of the geometric spreading of $\frac{1}{\sqrt{r}}$ as shown in Equation (4.138). This study chooses the excitability of the S0 mode as a reference because it is well-behaved (smooth) and covers the entire frequency range. Since the response in the far-field is considered, from Equation (4.138), the relative

excitability of a Lamb mode n is defined as

$$\begin{aligned} E_{\text{rel}}^{(n)} &= \frac{\tilde{E}^{(n)}}{\tilde{E}^{(\text{S0})}} \\ &= \sqrt{\frac{k^{(\text{S0})}(\omega)}{k^{(n)}(\omega)}} \frac{E^{(n)}}{E^{(\text{S0})}}, \end{aligned} \tag{4.139}$$

where $E^{(n)}$ and $E^{(\text{S0})}$ are calculated according to Equations (4.135). Also, from the time-domain responses, the magnitude of the same relative excitability ratio can be calculated as

$$E_{\text{rel}}^{(n)} = \frac{|\text{DFT}\{u_z^{(n)}\}|}{|\text{DFT}\{u_z^{(\text{S0})}\}|}, \tag{4.140}$$

where $u_z^{(n)}$ is the modal transient response in the time domain. Note that the formula in Equation (4.140) already accounts for the discrete nature of simulated responses. The comparison of two relative excitability obtained from Equations (4.139) and (4.140) is shown in Figure 4.7. To obtain this figure, the modal responses at 46 mm shown in Figure 4.5 are used. The figure shows good agreement between two sets of relative excitabilities, and thus, verifies the simulation including its underlying assumptions and approximations. Note that, in fact, a 5-point moving average algorithm is applied to each of the magnitude spectra of the DFT of $u_z^{(n)}$ before the relative excitability is calculated. This moving average reduces the effect of numerical error and makes the spectra smoother. However, the difference between the result with and without this averaging process is hardly seen since the error is small.

4.3.3 Comparison to the experimental signal

This subsection presents the comparison between the simulated and experimental time-domain signals. In the experiment, the laser techniques, described in Section 2.3, are used to generate and detect ultrasonic waves in the specimen, which is a 1-mm-thick aluminum plate. On the generation side, the laser beam is focused to a point on the plate so that an ablation mechanism takes place and thus the normal point source can be approximately generated. However, the time-dependence of the excitation or the "laser source function" is unknown. It can be recalled that if this source function is known, the final displacement

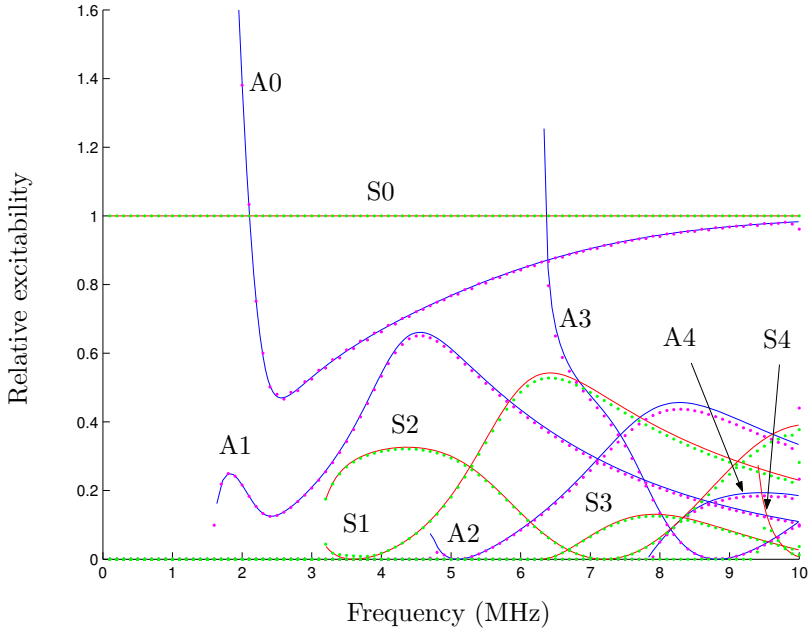

Figure 4.7: Comparison of the magnitudes of relative excitability obtained from (i) Equation (4.139) (solid lines) and (ii) Equation (4.140) (dots). The modal responses at $r = 46$ mm shown in Figure 4.5 are used in Equation (4.140).

can be calculated from the simulated unit-impulse response by the convolution integral in Equation (4.92). So, the first step is to find the laser (ablation) source function.

The laser source function can be measured from a more well-studied, less complicated system, referred as a reference system. The impulse response of this system is derived analytically and the experiment (with that system) is carried out. Similarly to the plate system, since the reference system is also linear, the total response, which is to be measured, can be expressed as a convolution integral as in Equation (4.92). The unknown source function can then be calculated from an inversion of a convolution, called the *deconvolution* procedure.

The reference system used in this study is an isotropic solid half-space. The unit-impulse response of this system is more definite since it can be obtained almost purely analytically (by, for example, the method of integral transform). In fact, for a half-space, the impulse response of the out-of-plane displacement due to a normal point excitation is completely obtained analytically for a medium with the Poisson's ratio of 0.25 [72]. For a general solid, only the numerical integration in the final step is required. The impulse response of this

system is much less complicated than that of the plate system since the main contribution is caused by the three wave components—longitudinal, shear, and surface waves, and they are clearly identified (unlike the multi-mode nature of Lamb waves for the plate).

For a free half-space of a general solid, with the cylindrical coordinate system (r, θ, z) similar to that in Figure 4.1, except that the plane $z = 0$ corresponds to the free surface of a half-space, the out-of-plane surface displacement at a distance r from a point, *step* excitation of magnitude Q, where the positive sign is assumed for a positive normal stress, is given by [2]

$$u_z^H(r,0,t) = \begin{cases} 0, & \text{for } t \le s_L r \\ \frac{Q}{\pi^2}\frac{s_T^2}{\mu} F_1\big(\frac{t}{r}\big), & \text{for } s_L r \le t \le s_T r \\ \frac{Q}{\pi^2}\frac{s_T^2}{\mu}\Big[F_1(s_T) + F_2\big(\frac{t}{r}\big)\Big], & \text{for } s_T r \le t, \end{cases} \tag{4.141}$$

where s_L and s_T are longitudinal and shear slownesses ($s_L = \frac{1}{c_L}$ and $s_T = \frac{1}{c_T}$), and the functions F_1 and F_2 are defined by

$$F_1\Big(\frac{t}{r}\Big) = \int_{s_L}^{\frac{t}{r}} \frac{s(s^2 - s_L^2)^{\frac{1}{2}}(s_T^2 - 2s^2)^2(t^2 - s^2r^2)^{-\frac{1}{2}}}{(s_T^2 - 2s^2)^4 + 16s^4(s^2 - s_L^2)(s_T^2 - s^2)}\, ds \tag{4.142}$$

$$F_2\Big(\frac{t}{r}\Big) = P.V. \int_{s_T}^{\frac{t}{r}} \frac{s(s^2 - s_L^2)^{\frac{1}{2}}(t^2 - s^2r^2)^{-\frac{1}{2}}}{(s_T^2 - 2s^2)^2 - 4s^2(s^2 - s_L^2)^{\frac{1}{2}}(s^2 - s_T^2)^{\frac{1}{2}}}\, ds. \tag{4.143}$$

The superscript ^{H} of u_z is used to emphasize the step time-dependency of the excitation. To evaluate these integrals correctly, one needs to be careful in choosing a proper numerical method because the integrands might contain singularity. Note that what is of interest is u_z^H according to Equation (4.141) at a fixed r as a function of time t.

Consider F_1. From Equation (4.142), with an introduction of a new variable

$$s_t = \frac{t}{r}, \tag{4.144}$$

this integral can be expressed as

$$F_1(s_t) = \int_{s_L}^{s_t} f_1(s)\, ds, \tag{4.145}$$

where

$$f_1(s) = \frac{s(s^2 - s_L^2)^{\frac{1}{2}}(s_T^2 - 2s^2)^2}{r(s_t^2 - s^2)^{\frac{1}{2}}\Big[(s_T^2 - 2s^2)^4 + 16s^4(s^2 - s_L^2)(s_T^2 - s^2)\Big]}. \tag{4.146}$$

In the first range of Equation (4.141) when $s_L < s_t < s_T$, since the integration variable s, starting from s_L to s_t, always makes the function $(s_T^2 - 2s^2)^4 + 16s^4(s^2 - s_L^2)(s_T^2 - s^2)$ positive for all s_t, this function does not possess any zero. Hence, the integrand has only one pole at $s = s_t$ for each evaluation (or each t). This function can be further rearranged into the form

$$F_1(s_t) = \frac{1}{r}\int_{s_L}^{s_t} \frac{\tilde{f}_1(s)}{\sqrt{s_t^2 - s^2}}\, ds,$$

where the function $\tilde{f}_1(s)$ is continuous and has no singularity. This form suggests that the integral $F_1(s_t)$ can be evaluated efficiently by the Gauss-Chebyshev quadratures [67] with a proper normalization of the integration variable to arrange the integrand and the limits of integration into the standard form[9]. For s_t in the next range or $s_t \geq s_T$, F_1 is evaluated at s_T. The procedure described above still applies.

The difficulty is encountered when one needs to evaluate F_2. From Equation (4.143), consider F_2 in the form

$$F_2(s_t) = P.V. \int_{s_T}^{s_t} f_2(s)\, ds, \tag{4.147}$$

where

$$f_2(s_t) = \frac{s(s^2 - s_L^2)^{\frac{1}{2}}}{r(s_t^2 - s^2)^{\frac{1}{2}}\left[(s_T^2 - 2s^2)^2 - 4s^2(s^2 - s_L^2)^{\frac{1}{2}}(s^2 - s_T^2)^{\frac{1}{2}}\right]}.$$

From the above equation, it is not difficult for one to notice that the equation $D(s) \equiv (s_T^2 - 2s^2)^2 - 4s^2(s^2 - s_L^2)^{\frac{1}{2}}(s^2 - s_T^2)^{\frac{1}{2}} = 0$, when $s \neq 0$, reduces to the Rayleigh equation in terms of slowness [2]:

$$\left(2 - \frac{s_T^2}{s^2}\right)^2 - 4\left(1 - \frac{s_L^2}{s^2}\right)^{\frac{1}{2}}\left(1 - \frac{s_T^2}{s^2}\right)^{\frac{1}{2}} = 0. \tag{4.148}$$

This Rayleigh equation is the frequency equation of a free surface wave governing its velocity. The only positive real root which has a physical meaning of Equation (4.148) is at $s = s_R$, where s_R is the slowness of a surface wave. Since the surface wave velocity c_R is always smaller than the shear wave velocity c_T, this zero of $D(s)$ or the only real singularity of the integrand in Equation (4.147), except the one at the end point $s = s_t$, is located on the right

[9]The Gauss-Chebyshev quadratures are suitable for an integral of a standard form of $\int_{-1}^{1} \frac{f(x)}{\sqrt{1-x^2}}\, dx$. This scheme applies to any arbitrary integration domain $[a, b]$ of z by the transformation $z = \frac{(b-a)x+a+b}{2}$.

of s_T on the real line of s. Then, the integral F_2 is evaluated in the form of Equation (4.147) with the principal value (*P.V.*) dropped, if $s_t < s_R$, and in the form of

$$F_2(s_t) = \lim_{\varepsilon \to 0} \left(\int_{s_T}^{s_R - \varepsilon} f_2(s)\, ds + \int_{s_R + \varepsilon}^{s_t} f_2(s)\, ds \right), \tag{4.149}$$

where $\varepsilon > 0$, if $s_t \geq s_R$. By the same reason as in the numerical integration of F_1, the Gauss-Chebyshev quadratures (with proper normalization) are used to evaluate the integral F_2 in Equation (4.147) when s_t is far away from s_R. That is, the integral in Equation (4.147) is rearranged into the form

$$F_2(s_t) = \frac{1}{r} \int_{s_T}^{s_t} \frac{\tilde{f}_2(s)}{\sqrt{s_t^2 - s^2}}\, ds,$$

where $\tilde{f}_2(s)$ is a continuous function that has no singularity.

As when s_t approaches s_R, the integrand approaches infinity more strongly, and the integration scheme is modified. The idea of the new scheme is to move the singularity at the end point to infinity by the change of the integral variable that results in the integration interval of $[-\infty, \infty]$[10]. The integral is then evaluated by the extended trapezoidal rule, which is shown to be most efficient for such an interval [67]. For this particular integral F_2, as $s_t \to s_R$, the result of the extended trapezoidal rule is compared to that by the Gauss-Chebyshev quadratures of 100 points. The numerical values show no difference, so the Gauss-Chebyshev quadratures are used throughout the range $s_t < s_R$ for evaluation of F_2. As for the range when $s_t \geq s_R$, it can be argued physically that, at a point after the arrival of a surface wave, the dynamic response due to a step point source should approach the static response due to the constant point load because a surface wave is the last disturbance to arrive. Therefore, the response in this range is replaced by a simple static response obtained the corresponding static analysis—using equilibrium equations, rather than equations of motions, as governing equations. From the analysis presented in Section 138 of Reference [91], the static surface step-response in terms of variables and direction used in this thesis is

$$u_z^H(r, 0) = -\frac{Q}{\pi r} \frac{1}{2\mu} (1 - \nu), \tag{4.150}$$

[10] One way to transform a variable z in a finite interval $[a, b]$ into a variable x in an infinite domain $[-\infty, \infty]$ is to use a mapping $x = \operatorname{arctanh}\left(\frac{2z - a - b}{b - a}\right)$.

where ν is the Poisson's ratio of the medium. Hence, the final surface step-response is expressed in terms of slowness $s_t = \frac{t}{r}$ by

$$u_z^H(r,0,t) = \begin{cases} 0, & \text{for } s_t \leq s_L \\ \frac{Q}{\pi^2}\frac{s_T^2}{\mu}F_1(s_t), & \text{for } s_L \leq s_t \leq s_T \\ \frac{Q}{\pi^2}\frac{s_T^2}{\mu}[F_1(s_T) + F_2(s_t)], & \text{for } s_T \leq s_t \leq s_R \\ -\frac{Q}{\pi r}\frac{1}{2\mu}(1-\nu), & \text{for } s_R \leq s_t. \end{cases} \tag{4.151}$$

Figure 4.8 shows the step response calculated by Equation (4.151) for an excitation of $Q = 1$ N. The material properties ρ, c_L, and c_T are the same as those used for the calculation of the plate response; the propagation distance is 46 mm. The corresponding unit-impulse response of this reference system is obtained from the differentiation of the calculated step-response in Equation (4.151), i.e.

$$u_z^\delta(r,0,t) = \frac{\partial}{\partial t}u_z^H(r,0,t). \tag{4.152}$$

This step is done numerically by the central finite difference scheme. The calculated unit-impulse response of the reference system is then shown in Figure 4.9. The arrows with the letters P, SV, and R correspond to the arrivals of P-, SV- and surface (R) waves, respectively. Note that the response is unbounded at the arrival of a surface wave. This is the mathematical nature of a surface wave within the linear-elastodynamics framework and cannot be avoided.

The unit-impulse response is preferred to the step response because, in contrast to an infinitely-long step response, the unit-impulse response is of a finite length. This trait will be of great advantage in the deconvolution procedure to find the source function. Another advantage in using the unit-impulse response is seen in the simulation of Lamb wave response. The response of the plate to the step point-excitation is greatly dominated by slowly-arriving low-frequency components, especially of the A0 mode, which blurs the details of other higher-frequency components[11].

Now, the experiment with a half-space specimen is conducted. The laser techniques used for both generation and detection are exactly the same as described earlier in this

[11]The plate step-response is not shown in this thesis, but it can be seen in References [97] and [94].

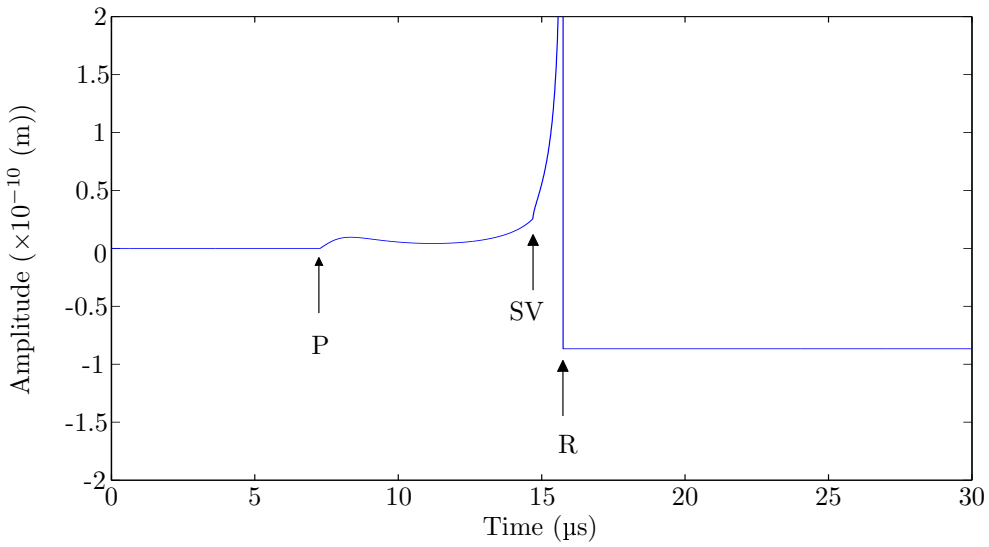

Figure 4.8: The out-of-plane surface step response, $u_z^H(r, 0, t)$, of an aluminum half-space. The propagation distance is 46 mm.

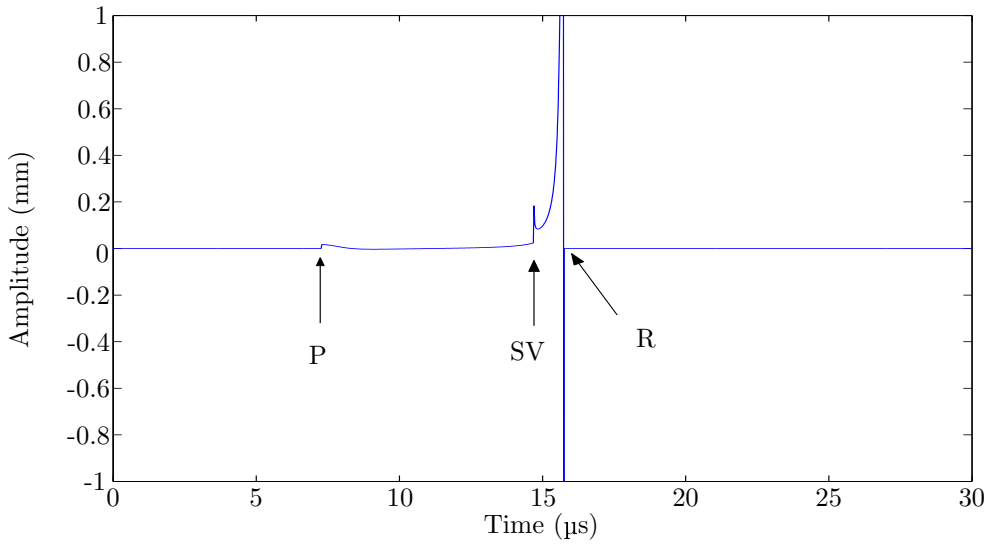

Figure 4.9: The out-of-plane surface unit-impulse response, $u_z^\delta(r, 0, t)$, of an aluminum half-space. The propagation distance is 46 mm.

subsection for the plate. An aluminum block is used for a half-space; its thickness of 103 mm guarantees no reflection from the other side of the block in the time window of interest. The signal measured at the distance of 46 mm is shown in Figure 4.10.

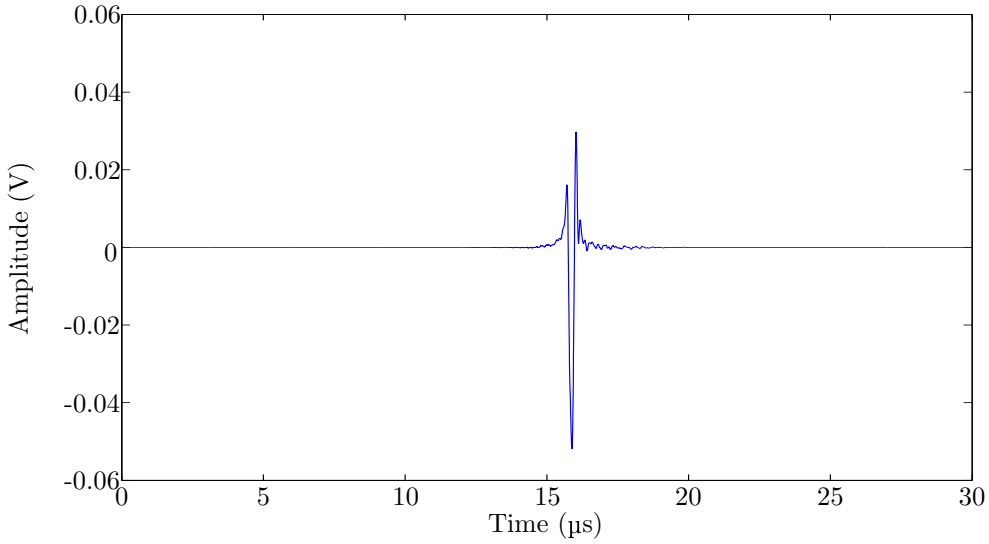

Figure 4.10: The experimental signal, $u_z(r, 0, t)$, of an aluminum half-space. The propagation distance is 46 mm.

The experimental signal shown in Figure 4.10 can be modelled as the output of a linear time-invariant (LTI) system shown by the diagram in Figure 4.11(a). One entire system can be thought to be composed of two subsystems. The first subsystem combines all the effects of instrumentation in the setup on both generation and detection sides; this subsystem is called the *instrumentation subsystem* and assumed to have the unit-impulse response $g[n]$. Combining the responses of the instrumentation before and after a specimen (on generation and detection sides) is possible because all of the systems the input has to go through are assumed to be linear and thus, can be reshuffled. The other subsystem, called the *specimen subsystem*, is the system concerning only a specimen, which is a half-space for Figure 4.11(a). The unit-impulse response of the specimen subsystem is understood to be the out-of-plane displacement on the surface of a specimen due to a unit, normal point source. This impulse response is derived earlier as given by $u_z^{\delta}(r, 0, t)$ in Equation (4.152) at a fixed r. The input to the entire system, denoted by $s[n]$ in Figure 4.11(a), is a stress wave generated by a laser; in particular, it is a normal stress excitation as a function of

time. Note that all of the signals and systems are shown in a discrete form since the actual implementation is done in a discrete domain.

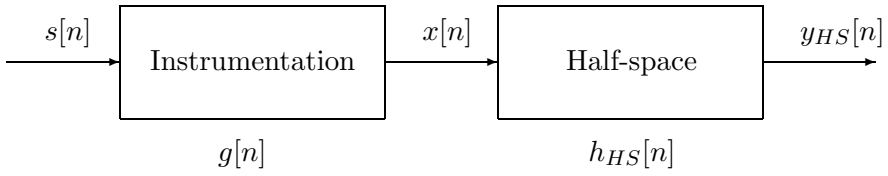

(a)

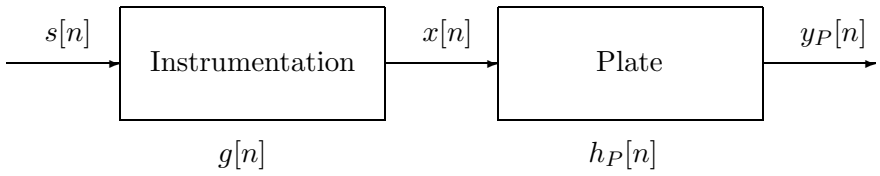

(b)

Figure 4.11: Modelled LTI system diagrams for (a) a half-space system, and (b) a plate system.

Recall that the output of an LTI system $y[n]$ is related to the input $x[n]$ and the unit-impulse response of that system $h[n]$ by the discrete linear convolution [70] (in short, *convolution*) defined by

$$y[n] = x[n] * h[n] = \sum_{m=-\infty}^{\infty} x[m]h[n-m]. \tag{4.153}$$

In this equation, the symmetry of the convolution operator can be easily observed so that the roles of $x[n]$ and $h[n]$ can be interchanged.

The experiment of the half-space system is used to obtained the unknown "net" source function which is a combination of the real source function and other effects except from the specimen. This net source function can be viewed as the input of the specimen subsystem or the output of the actual laser source passing through the instrumentation subsystem, i.e. $x[n]$ in Figure 4.11(a). The output of the specimen subsystem is simply a measured signal. Since the output of the reference system and the unit-impulse response, denoted by

$y_{HS}[n]$ and $h_{HS}[n]$, respectively, are known, the net source function can be calculated by the inversion of the convolution, or the deconvolution, of Equation (4.153).

Several available deconvolution methods can be categorized into two major types—deconvolution in frequency and time domains. Comparison of both types of methods, including their advantages and disadvantages, are presented for a similar setup in Reference [49]. This thesis chooses the direct deconvolution in the time domain; the specific method chosen is called the "least-squares deconvolution." This method has advantages of stable numerical calculation and efficient computation if some assumptions (stated later) are invoked.

Consider Equation (4.153) with the roles of $x[n]$ and $h[n]$ reversed:

$$y[n] = x[n] * h[n] = \sum_{m=-\infty}^{\infty} h[m]x[n-m]. \tag{4.154}$$

Note that the sequence $h[n]$ is known from the analysis, and the sequence $y[n]$ is the measured signal (the subscript $_{HS}$ is dropped since the derivation in this part is applicable to any LTI systems modelled by Figure 4.11). If both $x[n]$ and $h[n]$ are assumed causal, i.e. $x[n] = 0$ and $h[n] = 0$ for all $n < 0$, Equation (4.154) can be rewritten as

$$y[n] = \sum_{m=0}^{n} h[m]x[n-m]. \tag{4.155}$$

If it is further assumed that both sequences, $x[n]$ and $h[n]$, are of finite lengths M and N, respectively, i.e. $x[n] = 0$ for $n \geq M$ and $h[n] = 0$ for $n \geq N$, the output $y[n]$ will clearly has a finite length of $N + M - 1$ or $y[n] = 0$ for $n \geq N + M - 1$ (the last term of the sequence $y[n]$ is, from Equation (4.155), calculated by $y[N + M - 2] = h[N - 1]x[M - 1]$).

It can be seen that, for sequences of finite lengths, Equation (4.155) poses a system of simultaneous linear equations which has the number of equations $(N + M - 1)$ greater than the number of unknowns (M); therefore, the solution of this system of equations, in general, does not exist. However, in this case, the unique "optimal" solution can be found. This optimal solution is the solution which minimizes the (least-square) error function

$$\mathcal{E} = \sum_{n=0}^{N+M-2} \big(y[n] - \hat{y}[n]\big)^2, \tag{4.156}$$

where the predicted output $\hat{y}[n]$ is the result of the convolution Equation (4.155). In a matrix form, if $N < M$, Equation (4.155) can be explicitly written as

$$\begin{bmatrix} h[0] & 0 & \cdots & 0 & 0 & \cdots & 0 \\ h[1] & h[0] & \cdots & 0 & 0 & \cdots & 0 \\ \vdots & \vdots & \ddots & \vdots & \vdots & \ddots & \vdots \\ h[N-1] & h[N-2] & \cdots & h[0] & 0 & \cdots & 0 \\ 0 & h[N-1] & \cdots & h[1] & h[0] & \cdots & 0 \\ \vdots & \vdots & \ddots & \vdots & \vdots & \ddots & \vdots \\ 0 & 0 & \cdots & h[M-N] & h[M-N-1] & \cdots & h[0] \\ 0 & 0 & \cdots & h[M-N+1] & h[M-N] & \cdots & h[1] \\ \vdots & \vdots & \ddots & \vdots & \vdots & \ddots & \vdots \\ 0 & 0 & \cdots & 0 & 0 & \cdots & h[N-1] \end{bmatrix}_{(N+M-1)\times M} \times \begin{Bmatrix} x[0] \\ x[1] \\ \vdots \\ x[M-1] \end{Bmatrix}_{M\times 1} = \begin{Bmatrix} \hat{y}[0] \\ \hat{y}[1] \\ \vdots \\ \hat{y}[N+M-1] \end{Bmatrix}_{(N+M-1)\times 1}, \quad (4.157)$$

or, in short,

$$\mathbf{A}\mathbf{x} = \hat{\mathbf{y}}, \quad (4.158)$$

where $\mathbf{A}$ represents the $(N+M-1)\times M$ matrix containing $h[n]$'s; $\mathbf{x}$ and $\hat{\mathbf{y}}$ represent vectors of the unknown source function and predicted output, respectively. The representation for the case when $N > M$ can be obtained in a similar fashion.

Let $a[n, m]$ represent the element in the nth row and mth column of matrix $\mathbf{A}$. These elements can be calculated from the sequence $h[n]$ and are known. Then, Equation (4.158) can be represented by $N + M - 1$ index equations of the form

$$\sum_{m=0}^{M-1} a[n, m]x[m] = \hat{y}[n], \quad (4.159)$$

for $n = 0, 1, \ldots, N+M-2$. Hence, the error function in Equation (4.156) can be expressed

as

$$\mathcal{E} = \sum_{n=0}^{N+M-2} \Big(y[n] - \sum_{m=0}^{M-1} a[n,m]x[m] \Big)^2. \tag{4.160}$$

The minimizer $\mathbf{x}$ of $\mathcal{E}$ can be determined by solving the equations

$$\frac{\partial \mathcal{E}}{\partial x[l]} = 0, \qquad \text{for } l = 0,\, 1, \ldots,\, M-1. \tag{4.161}$$

This equation leads to (see details in Appendix A.3.6)

$$\sum_{n=0}^{N+M-2} y[n]a[n,l] - \sum_{m=0}^{M-1} x[m] \Big(\sum_{n=0}^{N+M-2} a[n,m]a[n,l] \Big) = 0, \tag{4.162}$$

which can be written as a matrix equation as

$$\mathbf{A}^T\mathbf{y} - \mathbf{A}^T\mathbf{A}\mathbf{x} = 0, \tag{4.163}$$

where the superscript ^{T} denotes the matrix transpose. A system of equations (4.163) can be easily solved; the solution is

$$\mathbf{x} = (\mathbf{A}^T\mathbf{A})^{-1}\mathbf{A}^T\mathbf{y}. \tag{4.164}$$

So, finding the optimal solution in this problem can be viewed as solving a linear system of equations: $\mathbf{R}\mathbf{x} = \mathbf{b}$, where the square matrix $\mathbf{R} = \mathbf{A}^T\mathbf{A}$ is the *autocorrelation matrix*, and the right-hand side $\mathbf{b} = \mathbf{A}^T\mathbf{y}$. In general, inverting $\mathbf{R}$ is very computationally intensive since the dimension of $\mathbf{R}$ is usually large ($M \times M$). However, by the nature of matrix $\mathbf{A}$, the product $\mathbf{A}^T\mathbf{A}$ (or $\mathbf{R}$) is a symmetric Toeplitz matrix (all of the elements of $\mathbf{R}$ along each of the diagonals have the same value), and consequently, Equation (4.163) can be efficiently solved by two algorithms. First, a Toeplitz matrix $\mathbf{R}$ can be inverted by the Toeplitz matrix inversion recursion, which employed the Cholesky decomposition[12] and the Levinson-Durbin recursion[13]. The other efficient way is to solve Equation (4.163) directly without calculating $\mathbf{R}^{-1}$ by using the general Levinson recursion [39].

[12]The Cholesky (or LDU) decomposition factorizes a Hermitian (or conjugate symmetric) matrix $\mathbf{C}$ into a product of the form

$$\mathbf{C} = \mathbf{L}\mathbf{D}\mathbf{L}^H,$$

where $\mathbf{L}$ is a lower triangular matrix with ones along the diagonal and $\mathbf{D}$ is a diagonal matrix. The symbol ^{H} denotes the Hermitian transpose which becomes transpose if all elements of matrix $\mathbf{C}$ are real.

[13]The Levinson-Durbin recursion is a recursive algorithm for solving the equation

$$\mathbf{A}\mathbf{x} = \epsilon\mathbf{u}_1,$$

where matrix $\mathbf{A}$ is a symmetric Toeplitz matrix; $\mathbf{u}_1$ is a vector with one at the first element and zeros at other elements; and ϵ is a scalar constant.

From a physical perspective, the source function should start at rest or $x[0] = 0$. This condition can easily seen by the fact that the first values of the unit-impulse response and the output, $h[0]$ and $y[0]$, respectively, are both zero (which satisfy the convolution in Equation (4.154) for $n = 0$: $y[0] = h[0]x[0]$). Since the deconvolution method presented earlier calculates $x[n]$ based on all available $y[n]$, the optimal solution $x[n]$ might not necessarily have the first value equal to zero. However, the derived deconvolution process can be easily modified to accommodate the constraint $x[0] = 0$. Suppose the algorithm is developed for the case $M = N$ (the presented algorithm applies to all cases of finite-length signals by zero-padding). The idea is to choose the length of $x[n]$ to be $N + 1$ (instead of N) and then neglect the first row and column of the matrix in Equation (4.157). The resulting matrix $\mathbf{A}$ will be of the dimension $(2N-1) \times N$, similar to what obtained in the derivation. The unknown variables now are N values of $x[n]$, for $n = 1, 2, \ldots, N$. Then, the same optimization procedure from Equation (4.159) to Equation (4.164) follows.

The deconvolution algorithm described above is applied to the half-space specimen subsystem in Figure 4.11(a). The output $y_{HS}[n]$ and the unit-impulse response $h_{HS}[n]$ are shown in Figures 4.10 and 4.9, respectively. Both signals are sampled every 0.01 μs (the sampling frequency is 100 MHz). The Levinson recursion is used to solve for the net source function $x[n]$ with $N = 3000$ (so that $x[n]$ has a length of 3001 with the first value forced to be zero). This length N equals to the time duration of 30 μs which well covers the entire duration of both the net source function and the unit-impulse response at $r = 46$ mm. The resulting net source function is shown, with the reconstructed signal $\hat{y}[n]$ in comparison with the measured signal $y[n]$, in Figure 4.12(b).

Note that, in the application of the derived deconvolution algorithm, often times the autocorrelation matrix $\mathbf{R}$ is ill-conditioned or nearly singular. This condition can result in a very long net source function with too much oscillation which is against the physical nature. This difficulty can be handled by small perturbation on the diagonal elements of that matrix. The net source function shown in Figure 4.12(a) is obtained with the perturbation of 0.1% along the diagonal of $\mathbf{R}$. In this specific case, with that amount of perturbation, the

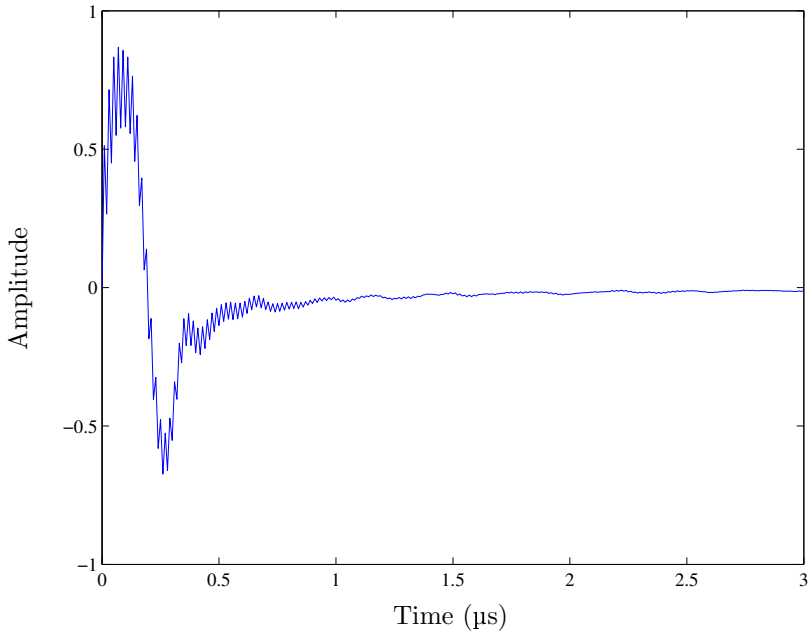

(a) Calculated net source function

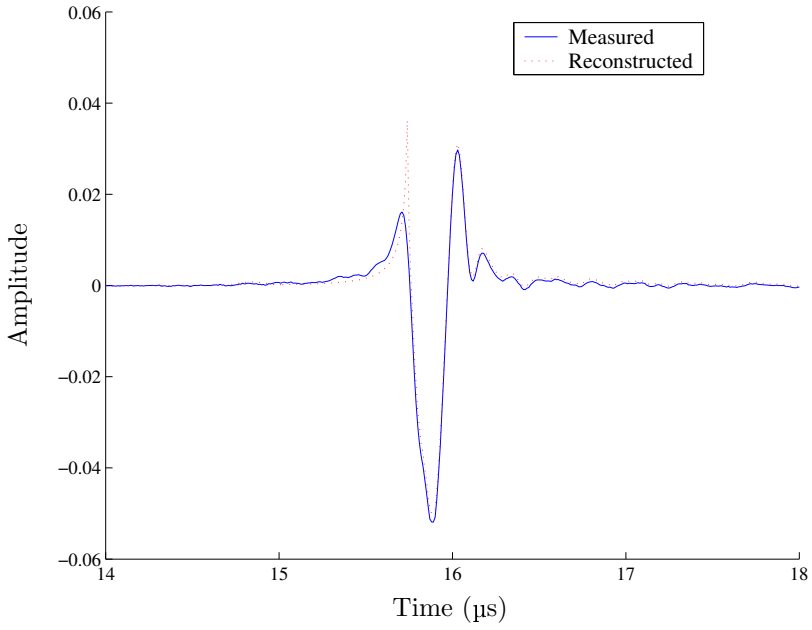

(b) Reconstructed surface response

Figure 4.12: Deconvolution results from the half-space measurement (propagation distance = 46 mm).

condition number[14] of the matrix $\mathbf{R}$ reduces from 1.9×10^6 to 1.8×10^3 so that the inverted result can be reliable. The net source function derived from the unperturbed matrix $\mathbf{R}$ is shown in Figure 4.13. This figure can be compared directly to the result of using the perturbed matrix shown in Figure 4.12(a).

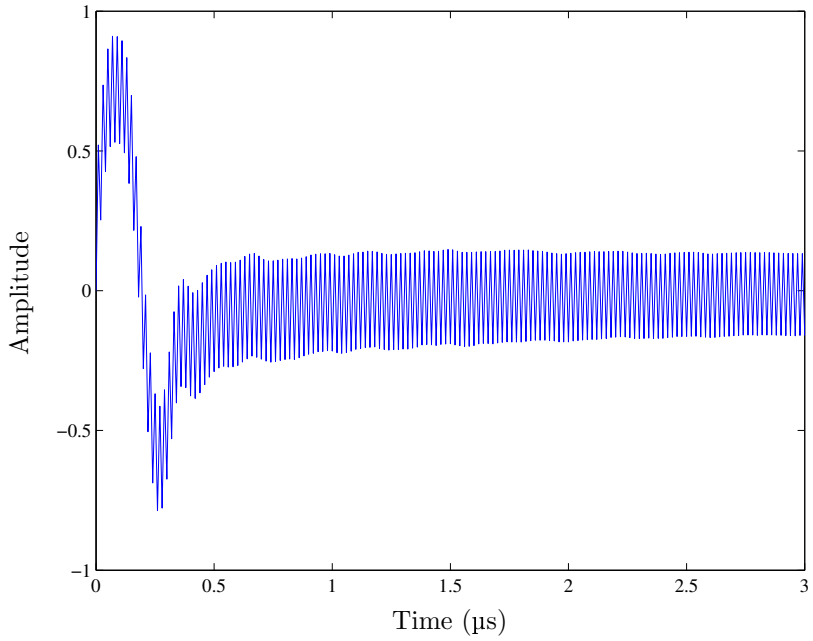

Figure 4.13: The net source function by the unperturbed autocorrelation matrix. The algorithm applies to the same set of signals used to derive Figure 4.12(a).

The deconvolution results shown in Figure 4.12 demonstrate the decaying net source function which agrees well with reality. The reconstructed output $\hat{y}[n]$ resembles the measured signal in overall. The discrepancy appears at the first arrival of surface wave. The sharp peak in the reconstructed signal is largely due to the strong discontinuity of the unit-impulse response (see Figure 4.9). This discontinuity is strong since it is derived from the differentiation of another discontinuity.

The net source function $x[n]$ calculated from the half-space measurement can be used

[14]The condition number of a matrix indicates the degree to which that matrix is ill-conditioned. The higher condition number implies the closer to singularity. For a symmetric matrix $\mathbf{C}$ (or Hermitian for a complex matrix), the condition number corresponding to the l_2-norm, denoted $k_2(\mathbf{C})$, is calculated from [65]

$$k_2(\mathbf{C}) = \frac{\lambda_{\max}}{\lambda_{\min}},$$

where $\lambda_{\max}$ and $\lambda_{\min}$ are the eigenvalues of $\mathbf{C}$ with largest and smallest moduli, respectively.

to calculate the predicted experimental plate response. Similar to the half-space, the plate response is modelled as an output of an LTI system as shown in Figure 4.11(b). The entire system consists of two subsystems concerning the measurement setup and the specimen in the analogous way to that for the half-space. Both subsystems are also called instrumentation and specimen subsystems, respectively, as in the half-space model. Since the experimental setup and the material of the specimen remain unchanged, the net source function in this case, shown by $x[n]$ in Figure 4.11(b), should remain the same as the one calculated from the half-space system. The unit-impulse response of the specimen subsystem which is now a plate, denoted by $h_P[n]$, is readily available from the simulation; it is the sampled version of $u_z^{\delta}(r, h, t)$ in Equation (4.90). The output $y_P[n]$ which is the out-of-plate surface displacement of the plate, can be calculated from the direct convolution between $x[n]$ and $h_P[n]$, represented by Equation (4.155). This calculated response is shown together with the actual measured signal in Figure 4.14. Also, to aid better comparison, the spectrograms of both calculated and measured plate responses are shown in Figure 4.15. These spectrograms are operated with the same parameters which are used to obtain Figure 4.6—Hanning window of a length of 5 µs applied every 0.1 µs.

Figure 4.14 shows good agreement in overall between the simulated and measured plate responses. In that figure, the most obvious distinction is at the slowly-propagating, low-frequency component which belongs to the A0 mode and is the major part of each signal after 25 µs. It can be seen from the scale that the frequency of that "slow" component in the experimental signal (Figure 4.14(b)) is a little lower than that of the same component in the simulated signal. This discrepancy can be associated to small differences in material properties among the plate specimen, the half-space specimen and the values used in the simulation. The deviation of the actual thickness of the plate specimen also contribute to this difference. From Figure 4.15, it can be clearly observed that all high-frequency components in the calculated response are lower in amplitude than the corresponding components in the measured response. This observation is believed to be a result of the strong discontinuity of the unit-impulse response of the half-space subsystem $h_{HS}[n]$ at the arrival of a surface wave (see Figure 4.9). The discontinuity results in a large magnitude at

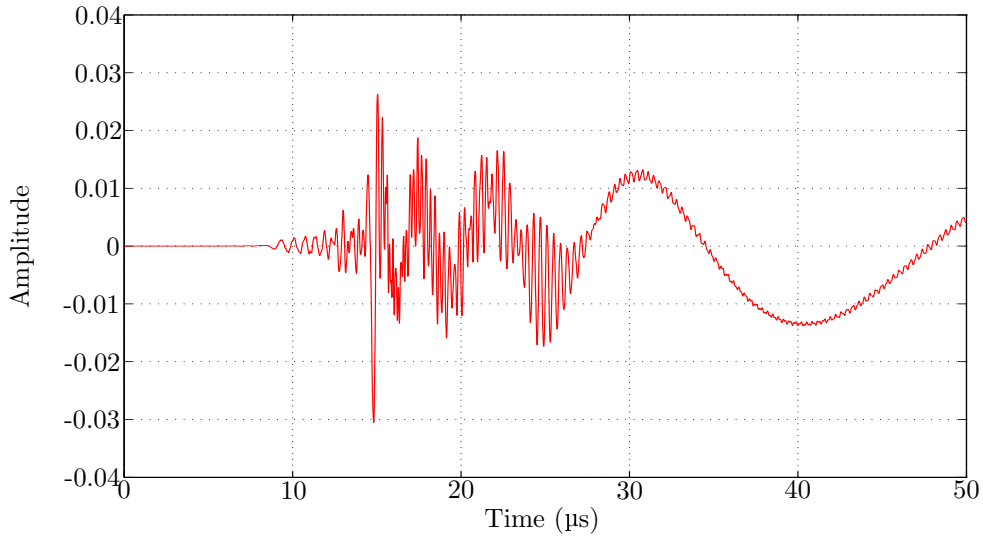

(a) Calculated response.

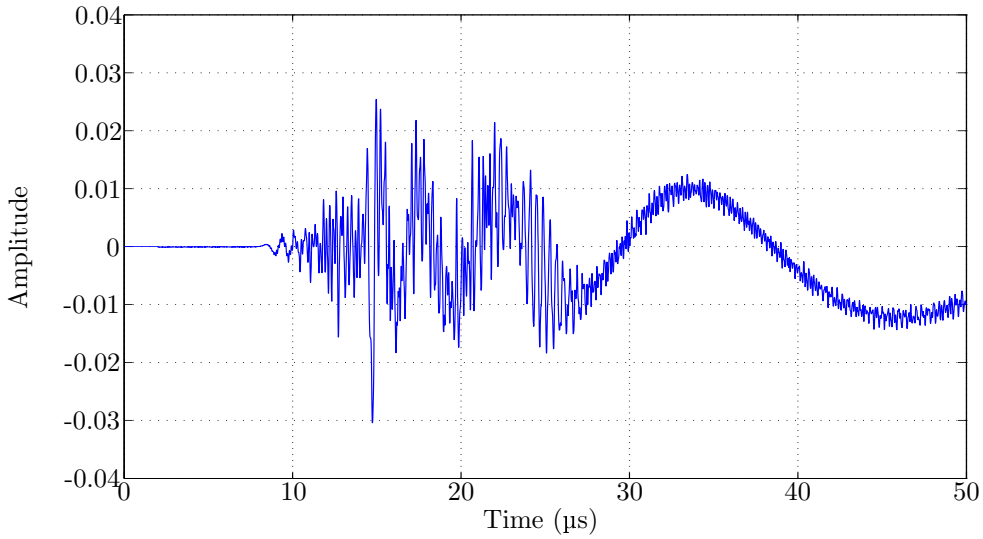

(b) Measured response.

Figure 4.14: Comparison between calculated and measured time-domain responses for the plate specimen (propagation distance = 46 mm).

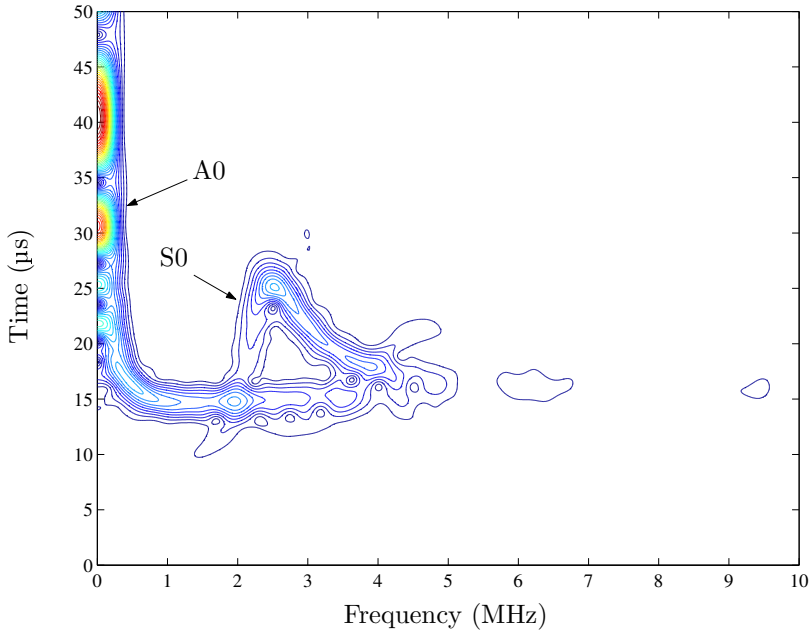

(a) Calculated response.

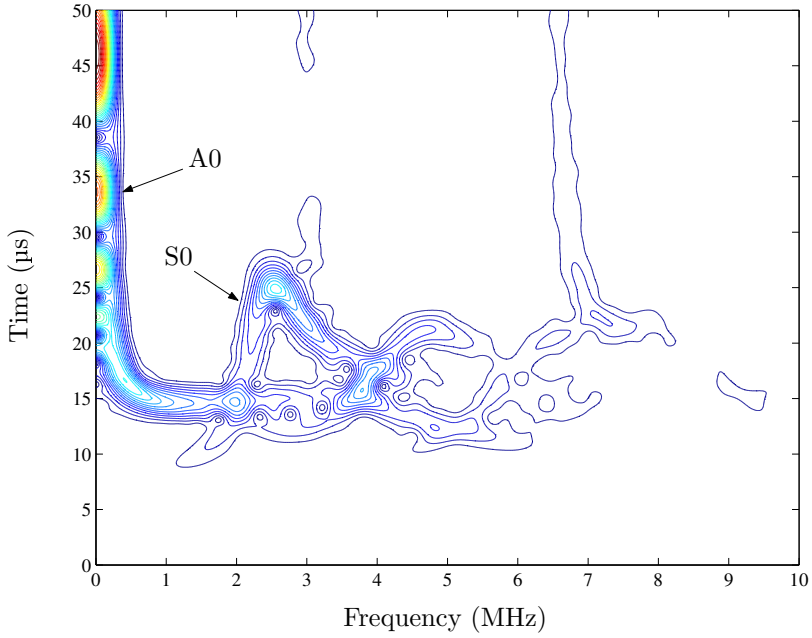

(b) Measured response.

Figure 4.15: Comparison between the spectrograms of calculated and measured time-domain responses for the plate specimen (propagation distance = 46 mm).

high-frequency components of $h_{HS}[n]$. Hence, after the deconvolution, the high-frequency components in the measured half-space signal $y_{HS}[n]$ are absorbed into the unit-impulse response more than the net source function $x[n]$ (see Figure 4.12(a)). This leads to the smaller high-frequency components in the calculated plate response. Apart from sure numerical and experimental errors, another source of overall difference between the measured and calculated responses is from the neglect of the in-plane component in the laser wave generation (see Figure 2.6(b)). The in-plane component, though small, also contributes to the out-of-plane displacement of the specimen. Its effect, in general, is different when the specimen is different, e.g. a plate or a half-space. This effect is expected to be more pronounced in the plate than in the half-space due to the bottom boundary which reflects back some of the disturbances to the top surface. However, the developed simulation captures the important features of the real Lamb wave response as a whole, and is satisfactory for the purpose of generating good synthetic signals.

4.4 Synthetic signals with attenuation

The development in Section 4.2 can be modified for the simulation of leaky Lamb wave signals. The idea is just to add the proper exponential decay into each part of a Lamb wave signal. Remember that the attenuation of a Lamb mode m as a function of frequency, denoted by $\alpha_m(\omega)$, is readily obtained from solving the dispersion equation of the system, e.g. Equation (3.46) for a solid plate loaded with a fluid half-space. For a finite plate, this function is sampled at the frequency ω_{mn} and added into the corresponding modal response. Explicitly, consider the derivation in Section 4.2.2. Let the attenuation value corresponding to the existing frequency ω_{mn} be denoted by α_{mn}, which is always real and positive. The attenuated transient response due to an impulse of a magnitude Q can be obtained by multiplying the term inside the summation in the expression (4.90) by the factor $e^{-\alpha_{mn}r}$, i.e.

$$u_z^{\delta}(r,h,t) = \frac{Q}{\rho}\sum_{m=1}^{\infty}\sum_{n=1}^{\infty}\frac{G_{w;mn}^2(h)}{M_{mn}\omega_{mn}}\sin(\omega_{mn}t)e^{-\alpha_{mn}r}J_0(k_{mn}r), \tag{4.165}$$

where all parameters are calculated in the same way as described in Section 4.2.3. This modification is possible for the case when the leakage does not noticeably alter the propagation wavenumbers of the referenced non-leaky Lamb waves, i.e. $\frac{\alpha_{mn}}{k_{mn}} \ll 1$, which is the case considered in this study.

Figure 4.16 shows a typical attenuated Lamb wave response calculated for a 1-mm aluminum plate (same properties as given in Section 4.3.1) connected with a water half-space ($c'_L = 1500$ m/s and $\rho' = 1000$ kg/m^3) and $Q = 1$ N; the propagation is again 46 mm. The spectrogram of this signal, also calculated with the same parameters and plotted in the same way as Figure 4.6 in Section 4.3.1, is shown in Figure 4.17.

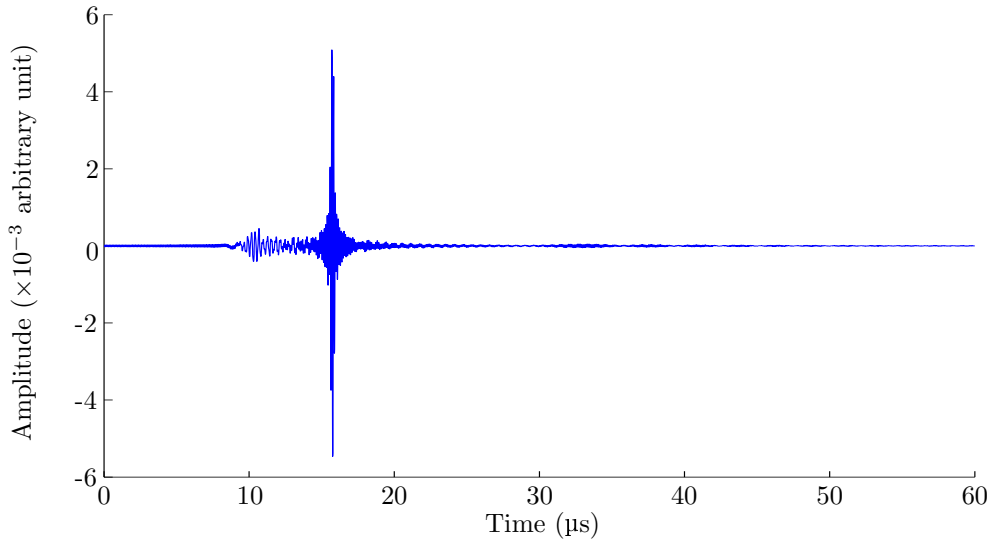

Figure 4.16: The attenuated, out-of-plane surface impulse response, $u_z^{\delta}(r, h, t)$, of a 1-mm-thick aluminum plate loaded with a water half-space. The propagation distance is 46 mm.

Figures 4.16 and 4.17 should be directly compared with Figures 4.3 and 4.6, respectively, for the effect of a water half-space. From the analysis in Section 3.3.3, especially the dispersion curves shown in Figure 3.2, the slowly-propagating, low-frequency components of the pseudo-A0 mode (below 0.5 MHz) exhibit large attenuation; therefore, they decay very quickly and do not appear in the simulated signal. This can be obviously seen in both Figures 4.16 and 4.17. However, below around 0.1 MHz, the components of the pseudo-A0 mode are expected to re-appear since from Figure 3.2(b), the attenuation of those

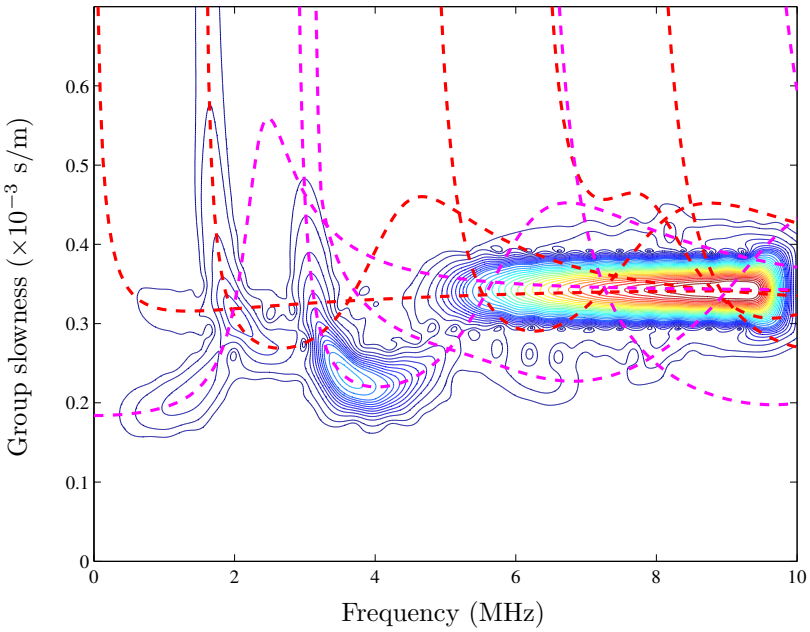

Figure 4.17: The dispersion curves of the simulated signal in Figure 4.16, obtained by the STFT. Analytical dispersion curves in frequency-slowness domain for a free plate are shown by dashed lines.

very low-frequency components seems to drop, and their excitabilities become unbounded. This is not seen in the simulation because the dispersion equation of the system in that very low-frequency range becomes ill-conditioned and its roots cannot be found accurately. These roots, and thus their modal responses, are then excluded from the calculation in Equation (4.165).

Another difference due to the presence of a half-space which can be easily seen from Figure 4.17, is the relatively large amplitude of the high-frequency components of the pseudo-A0 mode, or the *pseudo-surface waves*. In this high-frequency range, the vibration of the pseudo-A0 mode becomes confined on the surface of the plate, thus is less influenced by the half-space. Hence, these components leak very little, which can be seen by very small attenuation over the same frequency range in Figure 3.2(b).

The last major effect of the water half-space can be observed for the pseudo-S0 mode in the frequency range of 2–3 MHz. Attenuation of the pseudo-S0 mode starts to rise after around 2 MHz (see Figure 3.2(b)) since the vibration of that mode becomes larger at both

boundaries of the plate—one of those boundaries is the interface between the plate and the half-space. This leads to a large leakage and thus large attenuation. This effect can be observed in the spectrogram in Figure 4.17. The part of the spectrogram between 2–3 MHz, which is clearly present in Figure 4.6 for a free plate specimen, effectively disappears in Figure 4.17.

In conclusion, the synthetic signal representing leaky Lamb waves is simulated effectively. The previously-created simulation code for a free plate (non-leaky Lamb wave) is easily modified to include attenuation. A simulated response has some limitation at the very low frequency where the roots of the dispersion equation of the problem are numerically difficult to find. This shortcoming should not affect the practicality of the simulation since those mentioned low frequency components propagate very slowly and are usually filtered out in the real applications. The synthetic signals with attenuation will be used as reference time-domain signals to develop and verify the proposed attenuation extraction techniques, which will be presented in Chapter 5.

CHAPTER 5

ATTENUATION MEASUREMENT

This chapter presents techniques to extract attenuation information of Lamb waves from time-domain signals, or simply, the techniques to measure attenuation of Lamb waves. This stage makes use of synthetic signals obtained from the numerical simulation developed in Chapter 4 as base signals to develop systematic procedures of measuring attenuation. These systematic procedures are called the *attenuation extraction* techniques. This chapter starts with the meaning of attenuation and the ideas of how to measure it. Then, in the next section, this research develops the attenuation extraction techniques following the ideas presented in the first section by the uses of the physical meanings of some signal processing procedures. The attenuation extraction techniques are developed with synthetic single-mode signals since the principles can be easily verified. The developed techniques are then tested with synthetic multi-mode signals—double-mode signals, in particular. Testing with synthetic double-mode signals will not only result in the ideas of how the developed techniques perform with real experimental signals, but will also reveal limitations and shortcomings of the proposed techniques. Next, the developed techniques are applied to the real measured time-domain signals. This section shows two sets of measurements—one concerns narrowband signals and the other concerns broadband signals. Narrowband signals are also of interest since, often times, narrowband sources and receivers are used in the measurements, and several times, only attenuation at one frequency is sufficient for certain applications. These kinds of application are presented in the next chapter. Lastly, this chapter presents attenuation measurement over a frequency range. Time-domain signals used in this section are broadband and of the most general case.

5.1 The idea of practical attenuation measurement

Recall the introduction of attenuation in Section 3.1; the time-harmonic signal representing a measurable quantity, such as displacement at the surface of a plate, measured at the distance x away from the source, is expressed in the form of Equation (3.4), i.e.

$$u(x,t) = Ae^{-\alpha x}e^{j(\omega t - kx)}, \tag{5.1}$$

where k_R and k_I in Equation (3.4) are conventionally replaced by k and α for the real (propagating) wavenumber and attenuation, respectively. With this form, the spectrum of that signal or the Fourier transform of that signal as a function of frequency can be easily derived as

$$\mathrm{FT}\{u(x,t)\} = U(x,\omega) = Ae^{-\alpha x}e^{-jkx}. \tag{5.2}$$

In both Equations (5.1) and (5.2), the net signal amplitude A, the real wavenumber k and attenuation α are generally functions of frequency ω. In the most general case, the net signal amplitude A can also depend on the propagation distance x when diffraction and geometric spreading are taken into account. However, the dependency of x can be separated so that the net signal amplitude can be written as [80]

$$A(x,\omega) = F(x,\omega)Q(\omega), \tag{5.3}$$

where $Q(\omega)$ is the absolute source strength and the factor $F(x,\omega)$ accounts for diffraction and geometric spreading. Note that, although this factor $F(x,\omega)$ can be directly calculated from the geometry of the problem, the source strength $Q(\omega)$ is usually difficult to measure; as a result, the total factor A is also difficult to measure. Since A is not easy to measure, the practical way to obtain attenuation α is to compare the magnitude spectra of two signals measured at different distances from the excitation. To see this, let two such spectra of the form of Equation (5.2) measured at x_1 and x_2 be U_1 and U_2, respectively. Incorporating the form of the amplitude in Equation (5.3) into Equation (5.2), one can write the magnitudes of U_1 and U_2 as

$$|U_i(x_i,\omega)| = |F_i(x_i,\omega)||Q(\omega)|e^{-\alpha(\omega)x_i}, \tag{5.4}$$

for $i = 1$ or 2. It should be emphasized that in this equation, x_i's are known, $|F_i$'s can be calculated, and $|U_i|$'s are measurable; therefore, the only unknowns in the two equations are $|Q|$ and α. Then, the attenuation α can be obtained from the formula (see details in Appendix A.4.1)

$$\alpha(\omega) = \frac{1}{x_2 - x_1} \ln\left(\frac{|U_1(x_1,\omega)|}{|U_2(x_2,\omega)|}\frac{|F_2(x_2,\omega)|}{|F_1(x_1,\omega)|}\right). \tag{5.5}$$

As a special case, which is applicable to this research, the modification factor $F(x,\omega)$, concerning geometric spreading and diffraction of the amplitudes of Lamb waves excited by a point source, is real, inversely proportional to the square root of the propagation distance and independent of frequency, i.e.

$$F(x_i,\omega) = \frac{1}{\sqrt{x_i}}. \tag{5.6}$$

For this case, one can simply normalize the measured time-domain signals with their corresponding propagation distances and formulate the attenuation calculation by the normalized magnitude spectrum $|\tilde{U}_i|$, which is defined as

$$|\tilde{U}_i(x_i,\omega)| = \frac{|U_i(x_i,\omega)|}{|F_i(x_i,\omega)|} = |U_i(x_i,\omega)|\sqrt{x_i}. \tag{5.7}$$

Then, from Equation (5.4), these normalized magnitude spectra will be related to the attenuation as

$$|\tilde{U}_i(x_i,\omega)| = |Q(\omega)|e^{-\alpha(\omega)x_i}, \tag{5.8}$$

for $i = 1$ or 2, and Equation (5.5) becomes

$$\alpha(\omega) = \frac{1}{x_2 - x_1} \ln\left(\frac{|\tilde{U}_1(x_1,\omega)|}{|\tilde{U}_2(x_2,\omega)|}\right). \tag{5.9}$$

From this formula, it can be seen that the key to success in attenuation measurement is the accuracy of $|\tilde{U}_i|$'s (or $|U_i|$'s). Therefore, it is critical to choose the proper way to obtain or measure $|\tilde{U}|$'s. Note that, if more than two time-domain signals, say N signals, are available, the attenuation can be obtained from fitting the normalized magnitude spectra $|\tilde{U}_i|$'s at each frequency of all time-domain signals into an exponential function of x_i. In other words, if the least-square scheme is used, the magnitude of the source strength $|Q|$

and attenuation α together are the minimizer of the error function

$$\mathcal{E} = \sum_{i=1}^{N} \left(|\tilde{U}_i| - |Q| e^{-\alpha x_i} \right)^2, \tag{5.10}$$

where the frequency ω is a fixed parameter. This approach is clearly more robust, though at the expense of more work, than using the formula (5.9) since a large error in a specific measurement will have less effect in the extracted $|Q|$ and α.

Note that, when N time-domain signals are available, instead of using the exponentially-decaying model of the form (5.8), one can choose to consider the linear relationship

$$\begin{aligned} \ln |\tilde{U}_i(x_i, \omega)| &= \ln \left(|Q(\omega)| e^{-\alpha(\omega) x_i} \right) \\ &= -\alpha(\omega) x_i + \ln |Q(\omega)|, \end{aligned} \tag{5.11}$$

which is directly derived from Equation (5.8), and try to minimize the new error function

$$\hat{\mathcal{E}} = \sum_{i=1}^{N} \Big[\ln |\tilde{U}_i| - \big(-\alpha x_i + \ln |Q| \big) \Big]^2. \tag{5.12}$$

With this modification, the minimizer ($-\alpha$ and $\ln |Q|$) can be determined analytically by the formula (see details in Appendix A.4.2)

$$\begin{Bmatrix} -\alpha \\ \ln |Q| \end{Bmatrix} = \begin{bmatrix} \sum_{i=1}^{N} x_i^2 & \sum_{i=1}^{N} x_i \\ \sum_{i=1}^{N} x_i & N \end{bmatrix}^{-1} \begin{Bmatrix} \sum_{i=1}^{N} x_i \ln |\tilde{U}_i| \\ \sum_{i=1}^{N} \ln |\tilde{U}_i| \end{Bmatrix}. \tag{5.13}$$

This last alternative is more efficient than using the nonlinear (exponential) model since it does not involve iterative procedure.

5.2 Development of attenuation extraction algorithm

This section develops systematic techniques to extract attenuation from time-domain signals. The idea is based on Equation (5.9) and its variation when more than two signals are available. The most critical key to this equation is the appropriate way to obtain the magnitude of a specific frequency component which propagates with a specific slowness (or velocity). It is important to note that, for a dispersive or non-stationary signal, the way to obtain such magnitude to the utmost accuracy is not possible since the time and frequency information cannot be exact at the same time. This fact was already explained by

the uncertainty principle presented in Section 2.2.4. However, it is believed that the way to obtain acceptable attenuation information can be developed, even systematically. This research proposes two approaches in the following.

5.2.1 Attenuation extraction by the spectrogram

Since Lamb wave signals are dispersive, it is natural to employ the time-frequency representation to analyze the signals. This research specifically uses the short-time Fourier transform (STFT), in the form of the spectrogram (the square of the magnitude of the STFT), as it is shown to give a better representation in the time-frequency domain in comparison to other common techniques [69]. Moreover, since the spectrogram also represents the localization of the energy of the signal on the time-frequency domain, the magnitude of the displacement obtained from the contour of the spectrogram seems to be an obvious choice for $|\tilde{U}_i|$ in Equation (5.9). By the obvious reason, the attenuation extraction technique developed in this section will be referred to as the "spectrogram" method.

The idea of the spectrogram method can be implemented as follows. First, the spectrograms of two Lamb wave signals recorded at different locations are obtained and normalized into the slowness-frequency domain for correct comparison. Ideally, the projections of those two spectrograms in the slowness-frequency domain should look identical since they both represent the same dispersion curves (which are independent of propagation distance). However, in reality, the two spectrograms are different in contour spreading because the window function used in both processing are fixed to be of the same type and length in time. With a fixed-length window in time, the spreading of the contours in both spectrograms will be the same in time-frequency domain, and thus, different in slowness-frequency domain due to different scaling of propagation distance (see Equation (4.133)). Note that this spreading of energy localization over a point in the time-frequency domain is a result of the uncertainty principle. Lastly, the magnitudes of the two contours at a specific frequency and slowness are obtained for the magnitude spectra, $|\tilde{U}_1|$ and $|\tilde{U}_2|$, and the attenuation corresponding to that particular frequency and slowness (or Lamb mode) follows from the formula (5.9). Note that the magnitude spectrum $|\tilde{U}|$ can be obtained from the spectrogram by a number

of logical ways—for instance, the square root of a single peak at a specific frequency, the square root of the cross-sectional area of a fixed slowness interval at a specific frequency, or the square root of the contour's volume of a box centered at a specific frequency and slowness. The choice of calculating the volume is preferred since it will give a better-averaged $|\tilde{U}|$, but what really dictates the choice is the condition of the measured time-domain signals. For example, if there exist two Lamb modes propagating with close slownesses and they are not well-separated in time, parts of those two modes in the time direction may interfere with each other; this situation can result in a larger error if a cross-sectional area over a slowness range or a volume over a slowness-frequency region is calculated, so a value from a single peak might be preferred. It will be shown later that, for accurately-measured single-mode signals such as synthetic time-domain signals, all three choices for $|\tilde{U}|$ will give similar results, especially between using a cross-secional area and a volume. It should be pointed out that the calculation of the area in the fixed slowness at a specific frequency must be done in the time domain to eliminate the dependency of the propagation distance. This can be seen by looking at the dimension of such area. If the area is calculated in the slowness domain, it will have the dimension of time×energy/length, which still depends on the propagation distance (length) even after multiplying the frequency dimension (1/time).

To demonstrate the implementation, the described technique is tested with six synthetic time-domain signals. Synthetic signals are the simulated, circularly-spread Lamb wave responses with known attenuation for the case of a 1-mm-thick aluminum plate loaded with a water half-space. For a verification purpose, single-mode signals—specifically, the modal responses of the pseudo-S0 mode—are chosen. The propagation distances are from 36 mm to 46 mm, every 2 mm. These six synthetic (single-mode) signals are shown in Figure 5.1 with their dispersion characteristics shown in Figure 5.2.

Typical spectrograms are shown in the slowness-frequency domain in Figure 5.3. This figure shows two different spectrograms from the signals recorded at different propagation distances. Different spreading is clear in the figure. The solid lines in the figure represent the analytical curve shown earlier in Figure 5.2(a). From the figure, it can be observed that the magnitudes of both spectrograms (or the magnitude spectra of the signals) after around

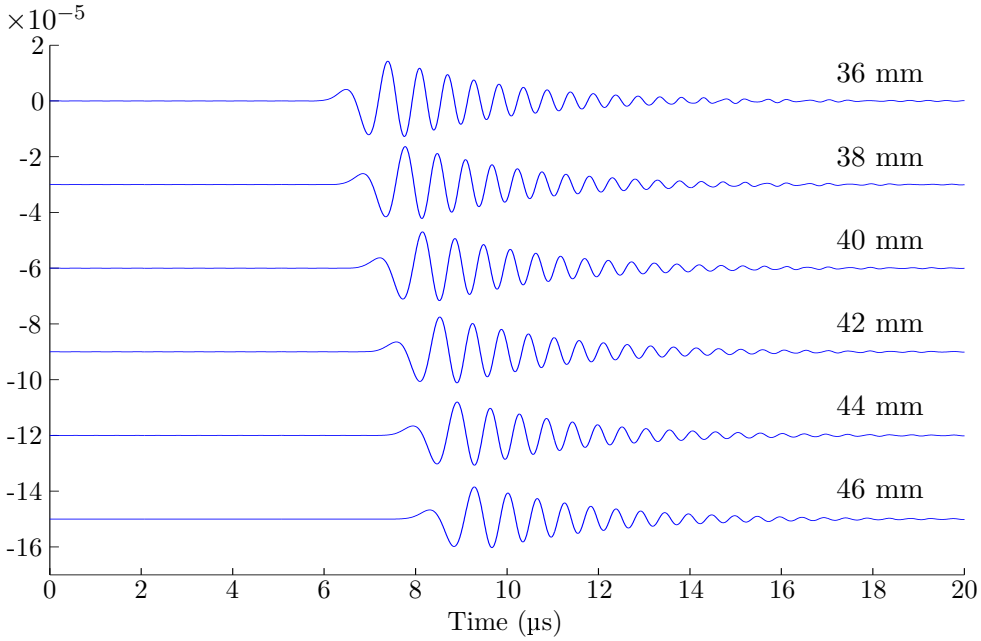

Figure 5.1: Six synthetic pseudo-S0-mode signals with known attenuation. The propagation distances are 36–46 mm, every 2 mm.

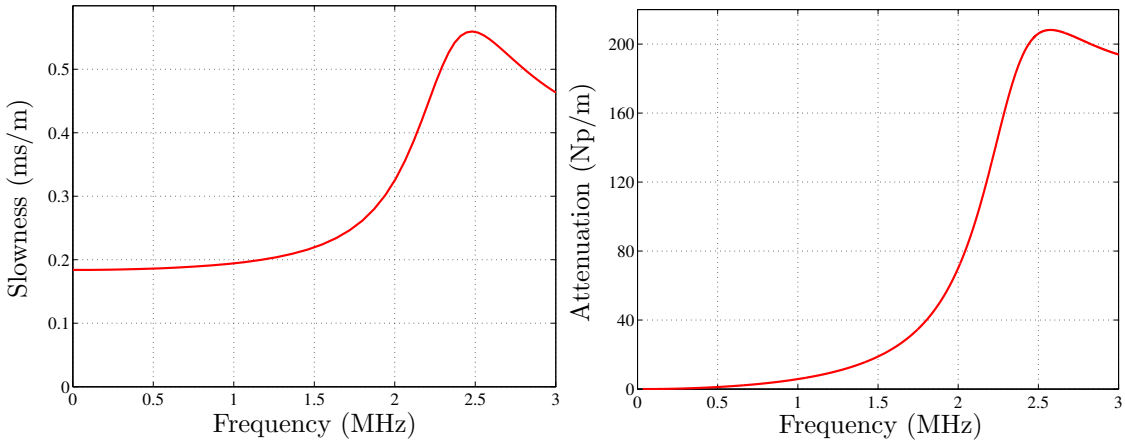

(a) Propagation part.

(b) Attenuation part.

Figure 5.2: The analytical dispersion curve of the pseudo-S0 mode for a 1-mm-thick aluminum plate loaded with a water half-space.

2.2 MHz are very small as compared to the other parts. This is due to large attenuation of the pseudo-S0 mode after 2.2 MHz (> 120 Np/m).

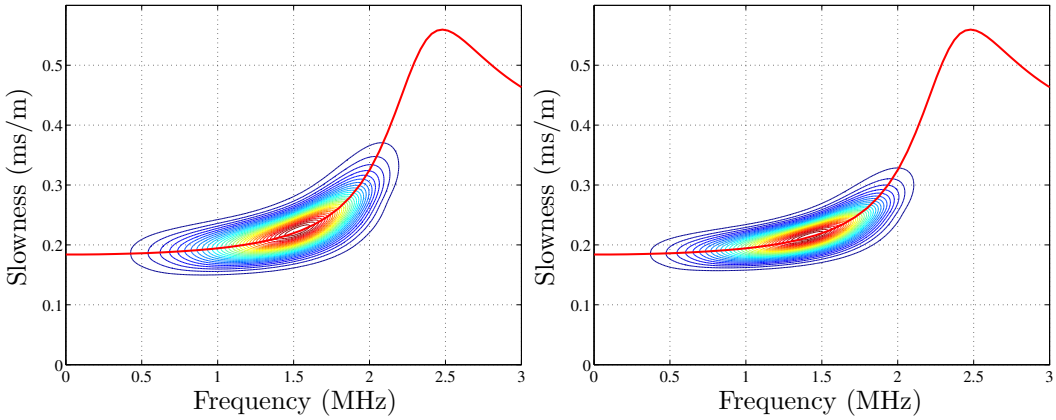

(a) Propagation distance = 36 mm. (b) Propagation distance = 46 mm.

Figure 5.3: Typical spectrograms obtained from synthetic pseudo-S0-mode signals with attenuation.

The attenuation of the six synthetic signals is calculated according to the scheme described in Section 5.1 at 0.5 MHz to 2 MHz, every 0.1 MHz. At each frequency, the magnitude spectra $|\tilde{U}|$'s from six signals are fitted in the decreasing exponential model and the attenuation value is calculated. The representative values for $|\tilde{U}_i|$'s at a specific frequency are obtained by (i) the square roots of the peaks of the spectrograms at that frequency; (ii) the square roots of the areas under the section of the spectrograms at that frequency; and (iii) the square roots of the volumes under the spectrograms' surfaces in the fixed frequency range (0.1 MHz in this example). These three choices are shown in Figure 5.4 for the spectrogram in Figure 5.3(b) at the frequency 1 MHz. Different series of attenuation as functions of frequency calculated by different choices of $|\tilde{U}_i|$'s are plotted in Figure 5.5 with the exact curve shown as a solid line.

Figure 5.5 shows that the developed technique works well when the measured signals are accurate. At the higher frequency (above around 1.7 MHz), the error is larger because the signals' amplitudes are smaller and the signals are more dispersive. The dispersion contributes more to the error for these synthetic signals; however, the effect of the small signal amplitudes on the error of calculated attenuation is expected to be more pronounced

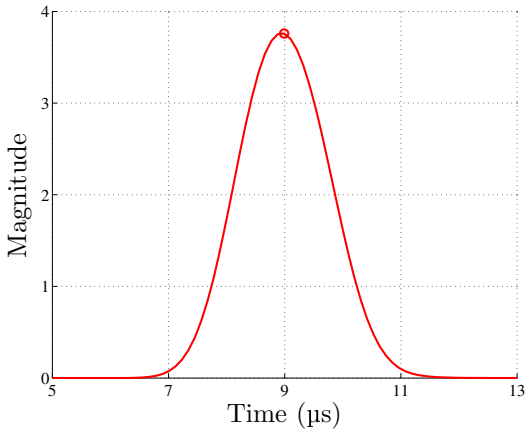

(a) Choice 1.

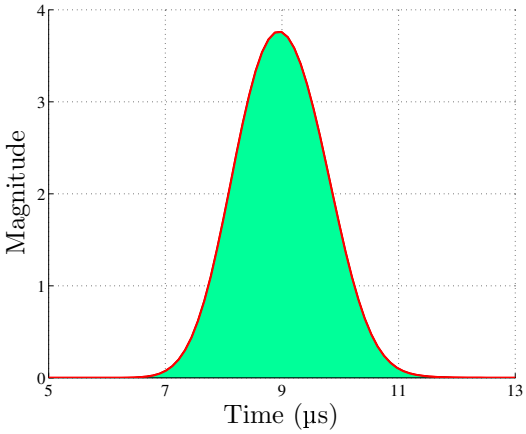

(b) Choice 2.

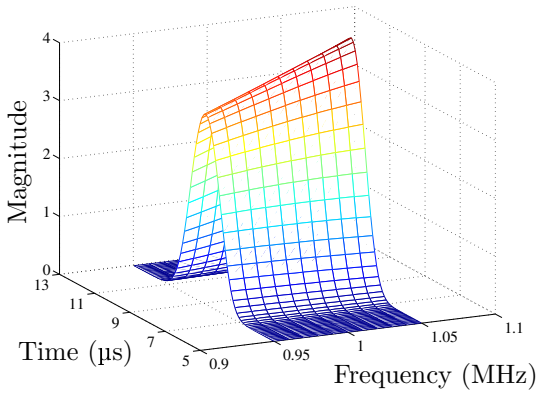

(c) Choice 3.

Figure 5.4: Three representative choices for $|\tilde{U}_i|$'s. The figure shows for $|\tilde{U}|$ at 1 MHz of the signal recorded at 46 mm.

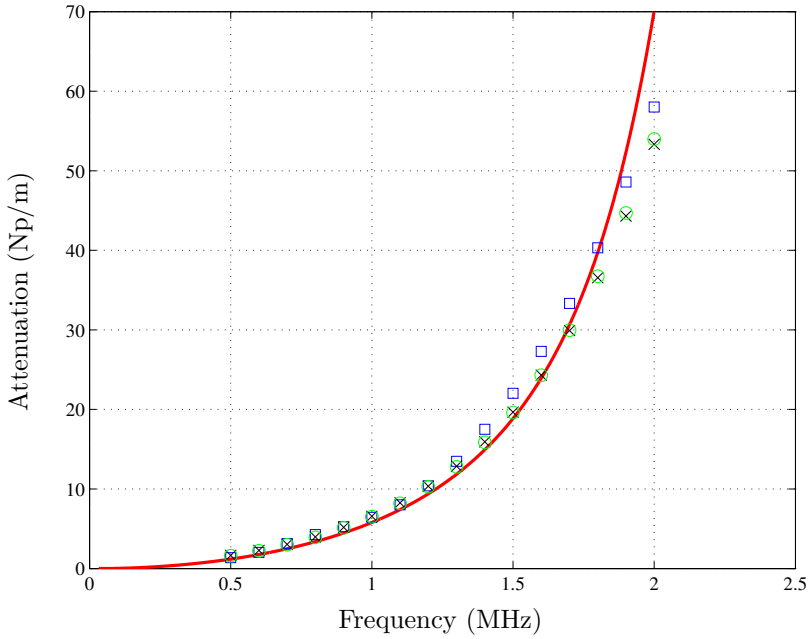

Figure 5.5: Calculated attenuation of synthetic pseudo-S0-mode signals by the spectrogram method using three different choices of $|\tilde{U}_i|$'s according to Figure 5.4. Choices (i), (ii) and (iii) are plotted as squares, circles and crosses, respectively. The exact curve is shown by a solid line.

in the real measurement when the noise level is higher than in the present example. Choices (ii) and (iii) of $|\tilde{U}_i|$'s give a little better results than Choice (i), so either one of them is preferred. However, all three choices of $|\tilde{U}_i|$'s give good results for these well-controlled measurements.

5.2.2 Attenuation extraction by the multi-bandpass-filtering technique

This section develops another technique to extract attenuation information from time-domain signals. The motivation is from the technique using the spectrogram presented in the previous section. By using the spectrogram, a signal is basically bandpass filtered in the time domain (typically called windowing) by a window function at a series of time points, and then, the magnitude $|\tilde{U}|$ at a specific frequency is chosen from the spectrum of the proper windowed signal depending on the choice of $|\tilde{U}|$. The drawback of this method is that, in order to calculate attenuation at a specific frequency, it requires a complete set of spectra of windowed signals at different time points or the entire spectrogram. Therefore,

it is suggestive to reverse the order of operations in the previous technique, i.e a signal is bandpass filtered in the frequency domain and its magnitude is compared (with other signals') in the time (or slowness) domain. To obtain attenuation over a certain frequency range, the bandpass filter is moved to another frequency point and the entire process is repeated. Since this technique is processed by a series of bandpass filtering, it is therefore referred to throughout this thesis as the "multi-bandpass-filtering (MBF)" method.

In implementation, first, time-domain signals recorded from different propagation distances are bandpass filtered in the frequency domain at a specific frequency of interest. This can be done either in the time or frequency domain. This research chooses filtering in the frequency domain done by multiplying the signals' spectra with a simple window function in the frequency domain. The reason for this choice of filtering is that, when the phase information of the signals is not important, this approach allows for the use of very narrowband bandpass filters without difficulties in filter design and implementation. With this choice, the filter-design process is simple since the filter is just a window function in the frequency domain; an example of such filter is a Gaussian filter, which is a Gaussian function of frequency. In the second step, all signals filtered at the same frequency are transformed back to the time domain, and the magnitudes of the components which travel with the same slowness are substituted into Equation (5.9) as $|\tilde{U}_i|$'s at the center frequency of the filter. Then, attenuation at that frequency follows. The curve-fitting scheme works with this technique in a similar fashion to what was described in the previous section. It should be noted that, although the bandwidth of a filter can be designed to be as small as desired, this bandwidth should not be taken to be too small since the narrower (in bandwidth) filter will worsen the resolution of the filtered signals in the time domain, and will have the adverse effect in the magnitude comparison process. The filter bandwidth will affect the final attenuation result, and a proper choice is problem-dependent. This same statement also holds for the window function (in time) when the spectrogram is used because the effect is rooted from the same cause—the uncertainty principle; therefore, neither technique will have an advantage as far as this consideration is concerned.

To present this technique mathematically, let the recorded signal be $s_i(t)$, where $i = 1$,

$2, \ldots$ indicates the distinct propagation distance d_i. For each $s_i(t)$, its spectrum, $S_i(\omega)$, is obtained from the Fourier transform given in Equation (2.32). This spectrum is filtered or multiplied by a bandpass filter $H(\omega; \omega_c, B_\omega)$, where ω_c and B_ω are two given parameters indicating the center frequency and the half-bandwidth of a filter. The filtered signal can be expressed in the frequency domain as

$$\tilde{S}_i(\omega; \omega_c, B_\omega) = S_i(\omega) H(\omega; \omega_c, B_\omega). \tag{5.14}$$

Note that this spectrum of the filtered signal is confined within an interval of the full-bandwidth ($2B_\omega$) around the center frequency ω_c. To obtain the filtered signal in the time domain, the inverse Fourier transform (Equation (2.33)) is applied to $\tilde{S}_i(\omega; \omega_c, B_\omega)$; the result is the signal $\tilde{s}_i(t; \omega_c, B_\omega)$. Lastly, the magnitude of $\tilde{s}_i(t; \omega_c, B_\omega)$ at a particular slowness sl_c is obtained as

$$|\tilde{U}_i| = \left|\tilde{s}_i(t_i; \omega_c, B_\omega)\right|, \tag{5.15}$$

where $t_i = sl_c d_i$. This $|\tilde{U}_i|$ represents the magnitude of the signal $s_i(t)$ corresponding to a point (ω_c, sl_c) on the dispersion curve. All $|\tilde{U}_i|$'s will be used to calculate attenuation of that point on the dispersion curve by Equation (5.9). Note that, in the real implementation, each $|\tilde{U}_i|$ will have a multiplicative constant on its exact values due to the processing (such as the filter and the inverse Fourier transform). Although this constant can be tracked, it is not necessary as long as that constant is the same for all $|\tilde{U}_i|$'s since only the ratio of these magnitudes is important for attenuation calculation (see e.g. Equation (5.9)).

This developed technique is demonstrated with the same set of time-domain signals used for the verification of the technique by the spectrogram in the previous section. All of signals are shown in Figure 5.1. Again, attenuation in the frequency range of 0.5–2 MHz, at every 0.1 MHz, will be calculated. At every frequency point, a Gaussian filter of a full-bandwidth of 1 MHz, centered at that frequency, is generated and applied to the spectra of the test signals. Note that a bandwidth can be defined as a frequency interval in which the magnitude of the filter is within D_ω dB from the maximum magnitude which is taken to be unity for simplicity. If a filter is Gaussian, it assumes the form

$$H(\omega; \omega_c, B_\omega) = e^{-a_\omega(\omega-\omega_c)^2}, \tag{5.16}$$

where a_ω is a constant related to the half-bandwidth of a filter, B_ω. For given D_ω (in dB) and B_ω, the constant a_ω can be obtained by comparing the magnitude of a filter at $\omega = \omega_c - B_\omega$ and $\omega = \omega_c$:

$$\begin{aligned} 20\log_{10}\left(\frac{1}{e^{-a_\omega B_\omega^2}}\right) &= D_\omega \\ 20a_\omega B_\omega^2 \log_{10} e &= D_\omega \\ a_\omega &= \left(\frac{\ln 10}{20}\right)\frac{D_\omega}{B_\omega^2}. \end{aligned} \tag{5.17}$$

In this study, D_ω is taken to be 60 dB. Figure 5.6 shows a typical spectrum of a pseudo-S0-mode signal $S(\omega)$, a filter described above $H(\omega;\omega_c,B_\omega)$ and a spectrum of a filtered signal $\tilde{S}(\omega;\omega_c,B_\omega)$. Note that, in this figure, only magnitudes are shown for complex spectra. Typical filtered signals $\tilde{x}_i(t)$'s in the time domain are shown in Figure 5.7(a) for signals recorded at 36 and 46 mm. Figure 5.7(b) shows the magnitudes of two filtered signals in Figure 5.7(a) in the slowness domain to emphasize that the magnitudes, $|\tilde{U}_i|$'s, must be compared at the same slowness. As in the technique using the spectrogram, $|\tilde{U}_i|$'s can be obtained by several logical ways. This section shows the results by two choices of choosing $|\tilde{U}_i|$'s—peaks or areas under the curves shown in Figure 5.7(b) in the time domain. These attenuation results are obtained by the curve-fitting scheme in the same way as in the previous section and plotted in reference to the exact value in Figure 5.8.

The comparison result shown in Figure 5.8 indicates the indifference in using peaks or areas, at least in this case when the measured signals are accurate and single-mode. Using the peaks seems to give a better result in the more dispersive part of the signals (above around 1.7 MHz). Effects of dispersion and amplitudes of signals reduce the accuracy as in the spectrogram method. It should be pointed out that in both spectrogram and MBF methods, using a peak of a point (either in frequency or slowness domain) to represent $|\tilde{U}|$ already includes some averaging since that one peak is derived from all data points inside the time interval of the window function for the spectrogram method or the frequency bandwidth of the bandpass filter for the MBF method. As pointed out in the previous section, for the multi-mode signals, using the peaks for $|\tilde{U}_i|$'s is expected to give a better attenuation result in overall because the peaks will be less affected by the interferences

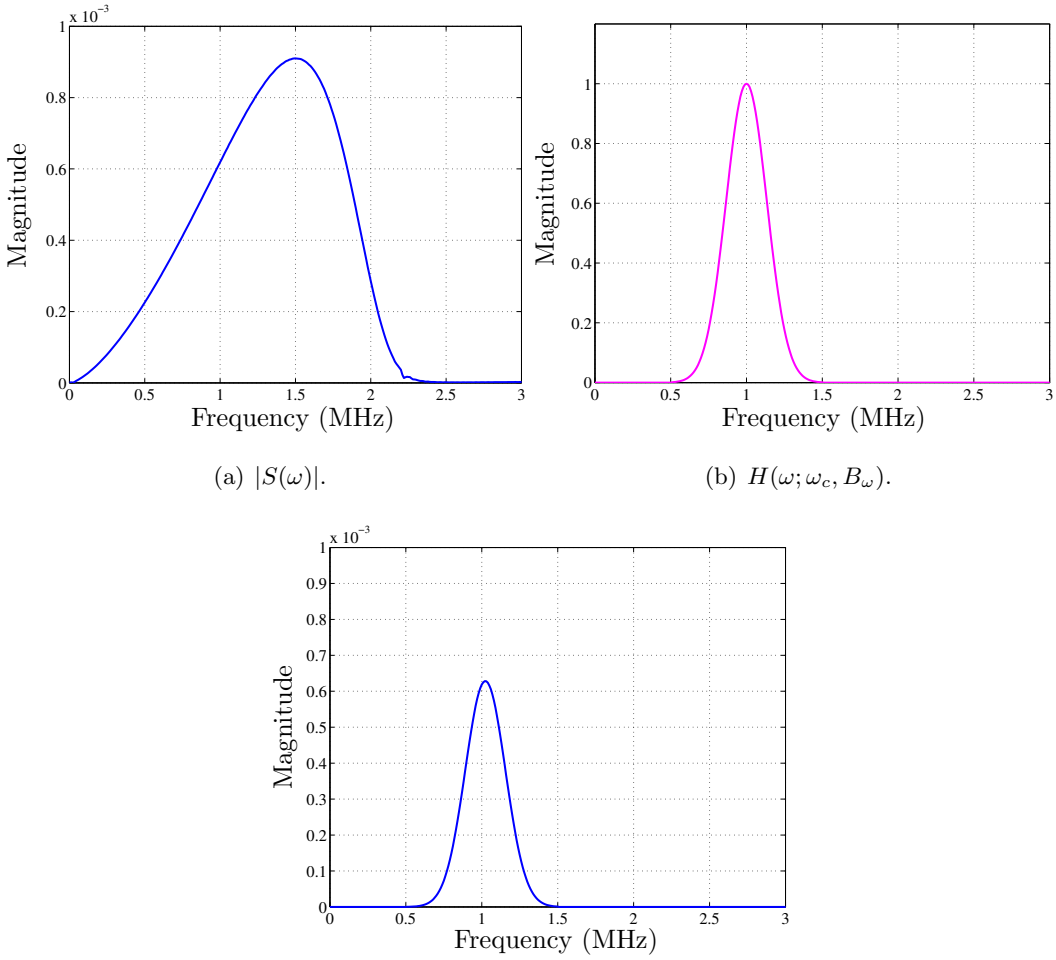

(a) $|S(\omega)|$.

(b) $H(\omega;\omega_c, B_\omega)$.

(c) $|\tilde{S}(\omega;\omega_c, B_\omega)|$.

Figure 5.6: A typical synthetic pseudo-S0-mode spectrum and the bandpass filtering process. The spectrum in Part (a) is derived from a time-domain signal recorded at 46 mm. A designed Gaussian filter with the center frequency of 1 MHz and the (full) bandwidth of 1 MHz is shown in Part (b). Part (c) shows the spectrum of the filtered signal.

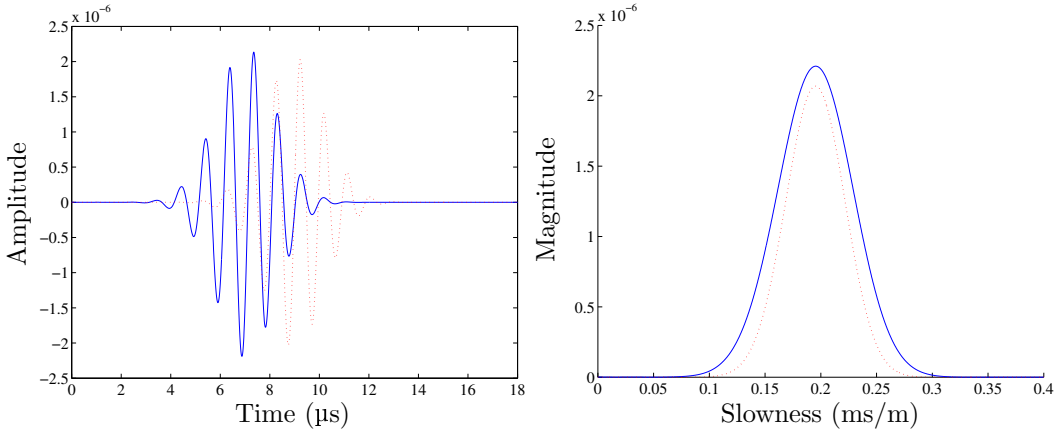

(a) Filtered signals in the time domain.

(b) Magnitudes in the slowness domain.

Figure 5.7: Filtered signals in the time domain, $\tilde{s}_i(t)$'s, of the pseudo-S0-mode signals recorded at 36 mm (solid lines) and 46 mm (dotted lines). Part (a) shows the real parts of the signals in the time domain, and Part (b) shows their magnitudes in the slowness domain. The filter used is shown in Figure 5.6(b).

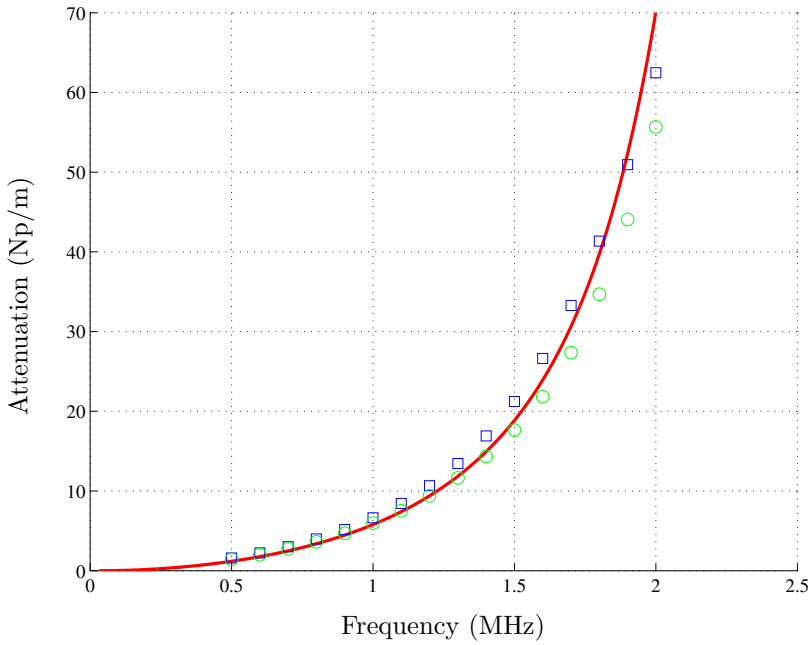

Figure 5.8: Calculated attenuation of synthetic pseudo-S0-mode signals by the MBF method using different choices of $|\tilde{U}_i|$'s. The choices of peaks and cross-sectional areas are plotted as squares and circles, respectively. The exact curve is shown by a solid line.

between existing Lamb modes.

5.3 Tests with synthetic multi-mode signals

It can be seen from Sections 5.2.1 and 5.2.2 that both attenuation extraction techniques using the spectrogram and bandpass filters work well for single-mode signals under controlled environment. However, real measured signals are hardly single-mode, especially signals generated and measured by the broadband laser systems used in this research. Therefore, it is advisable to test the developed techniques with synthetic multi-mode signals to obtain better insights of their performance and their limitations.

Test time-domain signals are "double-mode" signals consisting of the two fundamental modes—pseudo-S0 and pseudo-A0 modes—measured, again, at 36–46 mm, every 2 mm. Those six pre-conditioned, double-mode synthetic signals are shown in Figure 5.9. This choice of signals is natural since those two fundamental modes exist at all frequencies and are also easiest to be generated and detected from the standpoint of the present laser ultrasonic setup (see the excitability curves in Figure D.3). Those test signals are also lowpass filtered so that their frequency bandwidth is confined below 3 MHz. This step represents a typical signal pre-conditioning process which is common while dealing with real measured signals. Corresponding known dispersion characteristics—both propagation and attenuation—of the two Lamb modes are shown in Figure 5.10 for better interpretation of the results. Figure 5.9 shows clearly the multi-mode nature. From a comparison with Figure 5.1, in general, the pseudo-A0 mode can be seen to arrive after the pseudo-S0 mode. In other words, the pseudo-A0 mode propagates with higher slowness (lower velocity) than the pseudo-S0 mode. This observation is confirmed by the propagation dispersion curves of those two modes shown in Figure 5.10(a). Another general observation is that the pseudo-A0 mode decays faster over the propagation distance than the pseudo-S0 mode. This is explained by the larger attenuation of the pseudo-A0 mode shown in Figure 5.10(b).

As seen in the results presented in two previous sections that there is no significant difference of choosing a peak, an area under the curve, or a volume under the surface, to represent $|\tilde{U}|$, the attenuation extraction techniques for multi-mode signals here will use a

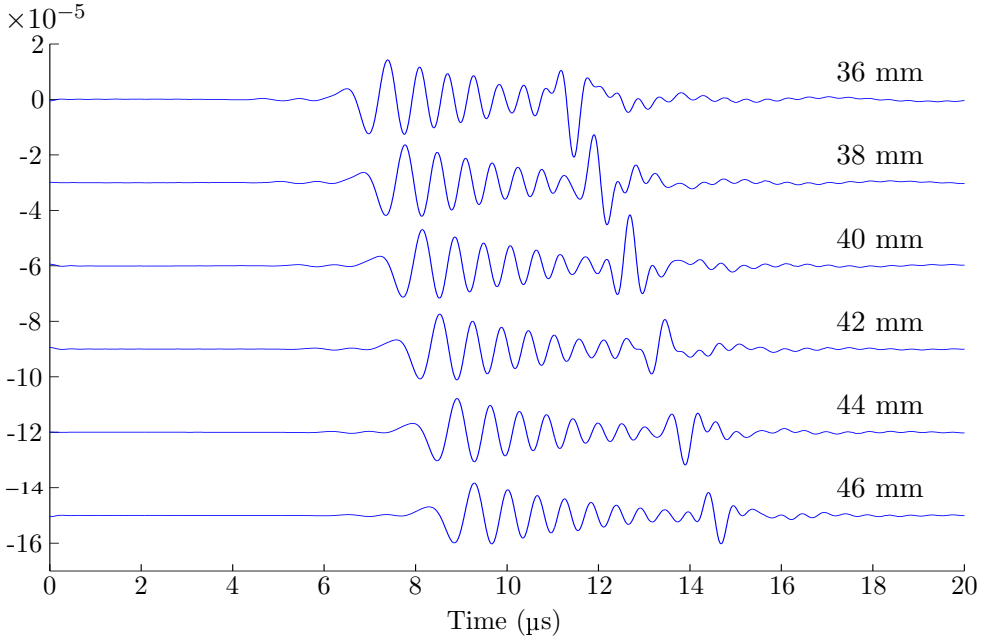

Figure 5.9: Six synthetic double-mode signals with known attenuation. The propagation distances are 36–46 mm, every 2 mm.

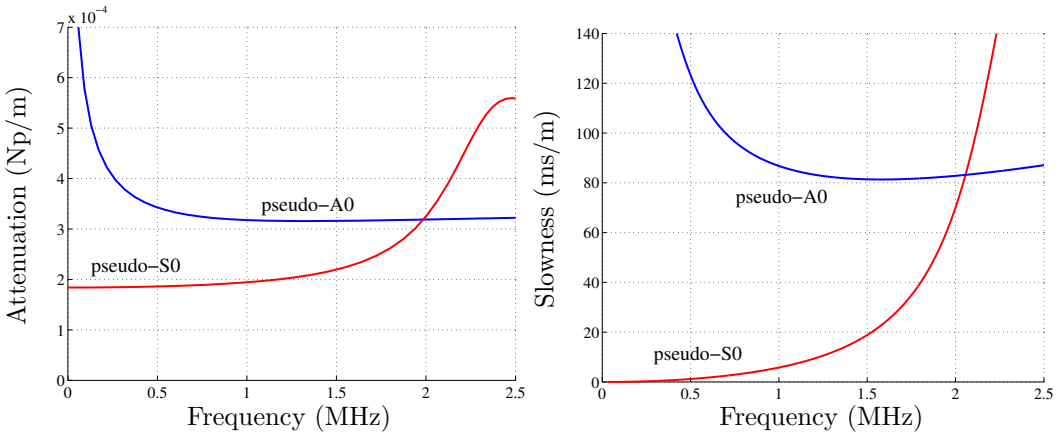

(a) Propagation part.

(b) Attenuation part.

Figure 5.10: Analytical dispersion curves of the pseudo-S0 and pseudo-A0 Lamb modes for a 1-mm-thick aluminum plate loaded with a water half-space.

peak due to its simplicity. The more critical issue when more than one mode is present is the right constraints to ensure reliable attenuation results. Clearly, this concerned issue arises in the frequency range at which two modes propagate with close velocities. Since two modes propagate independently and have different dispersion characteristics, they will interfere differently at different locations or propagation distances. This instance leads to inaccuracy of peak extraction when those two modes are not completely separated, i.e. a part of one mode interferes with a part of the other mode, especially near the peak. This inaccuracy is presented as a shift in the arrival slowness of the interfered mode; its magnitude is also affected. Therefore, peaks of a particular Lamb mode extracted from test signals which will be used as $|\tilde{U}_i|$'s in attenuation calculation must arrive within a set slowness tolerance to limit the effect of interference. This tolerance will depend on the accuracy of the measurements and the acceptability level of the calculated attenuation results. If all peaks do not lie within the given slowness range, the attenuation extraction algorithm will reject the results and identify the range as incalculable. For well-controlled measurements as in the test process, this slowness tolerance can be made very strict.

The entire procedure of attenuation extraction technique used for multi-mode signals can be described as follows. First, the contour surfaces representing a time-frequency localization of the energy of all signals are obtained. This step can be done by either using the spectrogram or the MBF method. Next, at each frequency of interest, the magnitude of that frequency component as a function of slowness is considered for each signal. Peaks of all measurements which fall in the given slowness range are used as $|\tilde{U}_i|$'s for attenuation calculation. Certain criteria must be imposed on a point in the slowness domain to qualify as a valid peak. In this research, those criteria are the following:

I. The magnitude of that point has to be greater than the threshold level set by the noise level in the measurement. This criterion rejects the unreliable parts of the signal or the part which is of the same order as noises. For a test with synthetic signals, the threshold is set at 5% of the maximum peak (of that particular component) obtained from a signal measured at the farthest distance.

II. The magnitude of that point must be the highest over a certain time interval. This research regards peaks which arrive within 1.1 µs to be non-resolvable, and does not qualify either of both peaks as a local maximum. This criterion depends wholly on the condition of the measurements, i.e. the noises, because the presence of noises will cause a number of local peaks.

After valid peaks are picked, some of them are discarded if they do not arrive within the slowness tolerance for all measurements. This criterion is set to reject the situation when two more peaks are largely interfered with each other. This situation occurs at short propagation distance in which different Lamb modes do not have enough distance to separate. Attenuation will be calculated for the points (on the slowness-frequency domain) at which peaks from all measurements are valid and accurate within given tolerances. Figure. 5.11 shows three possible situations in which the developed algorithm will decide whether it will calculate attenuation. For clarity purposes, only results from two signals measured at the closest and farthest distances (instead of all six curves) are shown in each of the subfigures; solid lines are results from a signal measured at 36 mm while dashed lines represent results from a signal measured at 46 mm. Figure. 5.11(a) is for the 1-MHz component. This plot shows good separation between both pseudo-S0 and pseudo-A0 modes; therefore, attenuation is calculated for both modes. In Figure 5.11(b) which shows the results for the 1.7-MHz component, the second peak from a signal measured at 36 mm fails to qualify as a local maximum because it comes within 1.1 µs of a part of the other peak which is higher than itself. Hence, the developed algorithm denies to calculate attenuation at that slowness even though the results from other distances are valid. Lastly, in Figure 5.11(c) showing the results for the 2-MHz component, both pseudo-S0 and pseudo-A0 modes propagate with almost the same slowness (see Figure 5.10(a)) so that they completely interfere each other. As a result, two peaks become one, but occur at different slownesses (since they do not propagate at exactly the same slowness) which differ from each other by more than the setup tolerance. Hence, attenuation is not calculated at this frequency. Note that, in the real application, the frequencies at which two or more Lamb modes are propagating at the close slownesses are excluded from the attenuation extraction procedure beforehand.

Then, the situation when two modes arrive at exactly the same time and the combined peaks pass all the criteria for all signals is not possible. These "intersect" frequencies can be pre-determined by a preliminary signal analysis using a time-frequency representation. This point will be mentioned in Section 5.4.2 when the developed algorithm is applied to real, broadband, multi-mode signals.

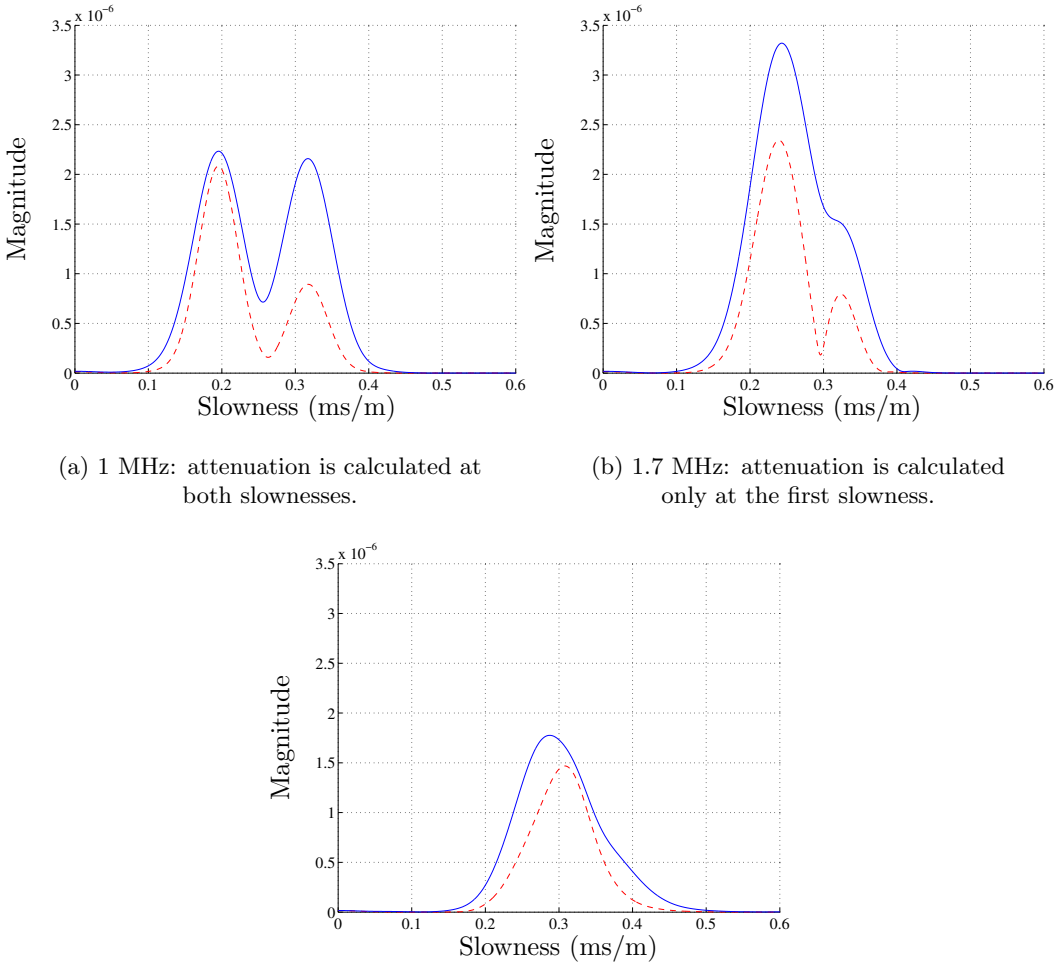

(a) 1 MHz: attenuation is calculated at both slownesses.

(b) 1.7 MHz: attenuation is calculated only at the first slowness.

(c) 2 MHz: attenuation is not calculated.

Figure 5.11: Three possible situations in attenuation calculation for double-mode signals. Only two results from signals measured at 36 mm (solid lines) and 46 mm (dashed lines) are shown.

With all the mentioned criteria, the developed algorithm is able to calculate attenuation over around 1-MHz range from 0.5 MHz to 1.5 MHz. The calculated attenuation is plotted versus exact curves in Figure 5.12. The figure shows both the results from the spectrogram

and MBF methods. Keep in mind that both methods differ only in the intermediate step at which the energy localization is obtained. Both methods use the same criteria to qualify local maxima and calculate attenuation. From the figure, the attenuation extraction of the pseudo-A0 mode stops after 1.5 MHz. The reason for this rejection is that, at 36 mm, a part of the pseudo-A0 mode is always interfered by a part of the pseudo-S0 mode. This interference is worsened when both modes' velocities are closer (at higher frequency) and when the pseudo-S0 mode dominates. At 1.7 MHz, for a time-domain signal measured at 36 mm, the arrival of the pseudo-A0 mode is hardly seen due to large attenuation. As a result, the peak of the pseudo-A0 mode is unresolvable as shown in Figure 5.11(b) and its attenuation is not calculated. From 1.8 MHz on, the two existing modes propagate with slownesses closer than 0.6×10^{-4} s/m. This slowness difference is equivalent to 2 µs in time for a signal measured at 36 mm. Although valid peaks may be detected and the situation is not as bad as what is shown in Figure 5.11(c), the interference between the two modes is large enough to affect the locations of the peaks at some propagation distances. Hence, reliable attenuation cannot be obtained at these frequencies. From the performance in overall, it can be concluded that the developed attenuation-calculation procedure using either the spectrogram or MBF method is capable of obtaining accurate attenuation, provided that all measurements are well-controlled and accurate.

5.4 Attenuation extraction from real measurements

The attenuation calculation of synthetic double-mode signals presented in the previous section is encouraging. Both developed methods show potentials to be applicable to real time-domain signals from real measurements. This section presents the uses of the developed algorithm to real measured signals. This section is divided into two subsections concerning two different sets of measurements. The first set consists of narrowband time-domain signals when attenuation at one specific frequency is to be determined. The next subsection considers time-domain signals measured by the laser system so that all of them are broadband and multi-mode. This subsection shows the most general application of the developed methodology since no mode is generated or detected specifically.

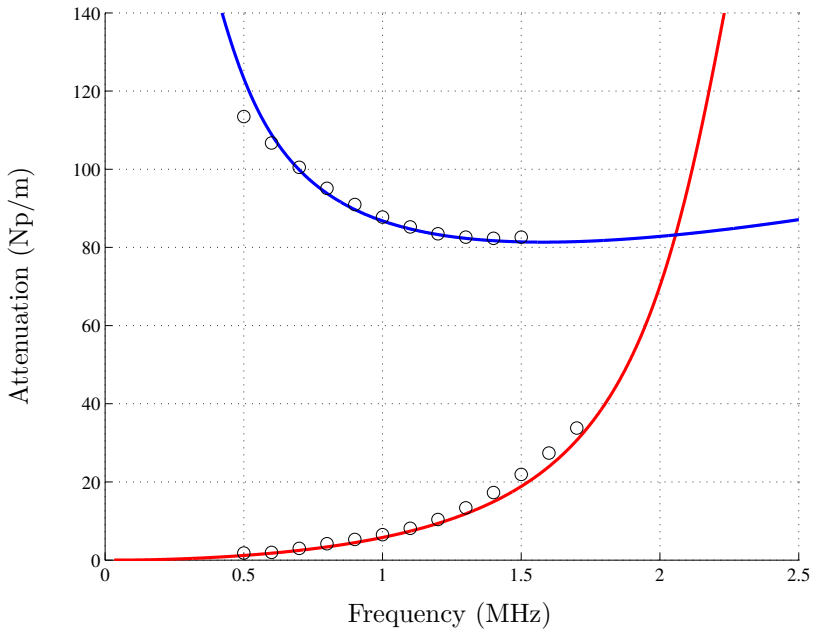

(a) Spectrogram method.

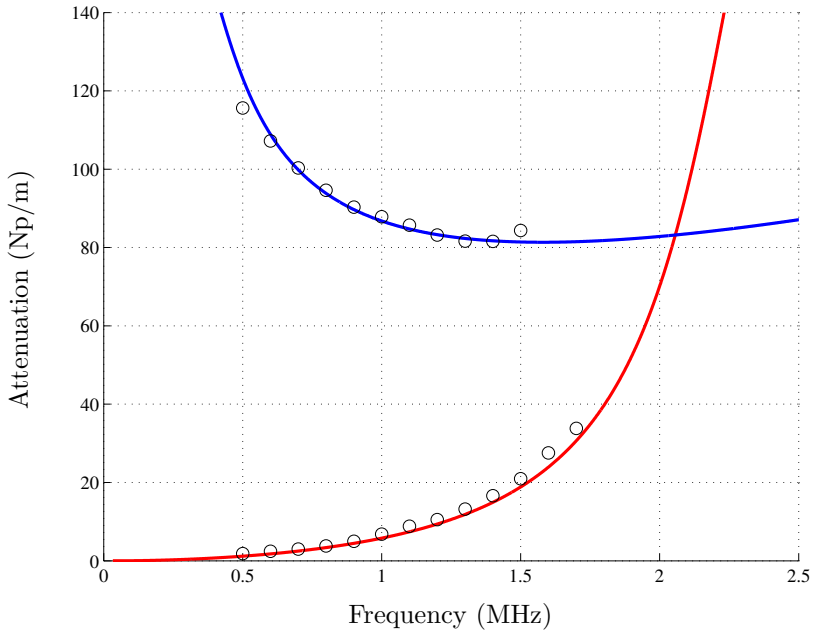

(b) Multi-bandpass-filtering method.

Figure 5.12: Calculated attenuation of synthetic double-mode signals shown in Figure 5.9.

5.4.1 Attenuation extraction of narrowband signals

The first subsection goes another step further than the previous section. The time-domain signals considered here are real, but their frequency bandwidth are limited to a narrow range. This kind of time-domain signals are usually obtained when conventional piezoelectric transducers (PZT) are used in the measurements. The PZT transducers can generate and detect ultrasonic waves mechanically by direct contact to the specimen. Unlike the laser system which responds to oscillations at all frequencies without any bias, a PZT transducer respond well to only oscillations with frequencies around its resonance frequency.

Two piezoelectric transducers are used—one as a transmitter (T) and the other one as a receiver (R)—in the experiment for this subsection. The specimen is a stainless-steel tank of a thickness of 0.76 mm. The experimental setup is shown Figure 5.13 where the two transducers are attached to the tank at the fixed distance $d = 100$ mm apart, and water is filled into the tank so that its level is in between the two transducers. In the tests, narrowband ultrasonic Lamb waves propagating along the thickness of the tank are sent from the higher transducer to the lower transducer. These Lamb waves are attenuated as they propagate along the part of the tank which is in contact with water. Attenuation is induced by leakage as discussed in Section 3.3.3 since water in the tank behaves as a water half-space. Therefore, as the water level rises closer to the transmitting transducer, the total attenuation (e.g. in neper) is larger since the propagation path with leakage is longer. For this case, the magnitude of a specific Lamb wave mode at a fixed frequency extracted from a time-domain signal, $|\tilde{U}|$, can be expressed in terms of attenuation α (in neper per length) and the water level measured from the receiving transducer y as

$$|\tilde{U}| = |Q|e^{-\alpha y}. \tag{5.18}$$

In this expression, all modifications due to diffraction and geometric spreading are absorbed in the term $|Q|$. This term $|Q|$ also includes the excitation strength, the effect of instrumentation and the effect of coupling between each transducer and the plate, which are all constant from measurement to measurement if the test configuration is fixed. Since the form of Equation (5.18) is exactly the same as that of Equation (5.8), attenuation of Lamb

waves (at this fixed frequency and mode) in this experiment can be obtained by two or more time-domain signals using the concepts presented in Section 5.1.

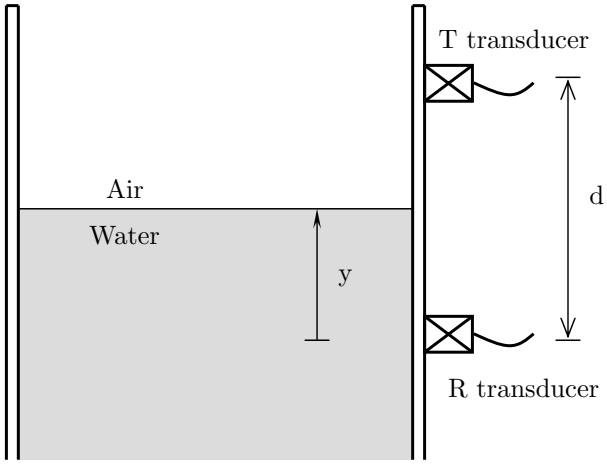

Figure 5.13: Experimental configuration for attenuation measurement of attenuated, narrowband guided waves.

The dispersion curves for a 0.76-mm-thick steel plate loaded with a water half-space are simulated and shown in Figure 5.14. The material properties used to calculate these curves are: $c_{L,\text{steel}} = 5490$ m/s, $c_{T,\text{steel}} = 3080$ m/s, $\rho_{\text{steel}} = 8000$ kg/m^3, $c_{\text{water}} = 1500$ m/s, and $\rho_{\text{water}} = 1000$ kg/m^3. Those numbers for stainless-steel are obtained from its specifications, while the numbers for water are standard. In the experiment, the excitation signal is a 10-cycle Gaussian toneburst with a center frequency at 1.5 MHz; this excitation is shown in Figure 5.15(a). From Figure 5.14, at this excitation frequency, only two fundamental Lamb wave modes are expected to exist. Predicted characteristics of those two modes are shown in Figure 5.15(b), which are the zoomed versions of the sets of dispersion curves around the center frequency of the excitation. In the figure, the solid and dashed lines represent the pseudo-A0 and pseudo-S0 modes, respectively.

The time-domain signals are recorded when the water level y is raised from 0 to 24 mm, every 2 mm (the total of 13 time-domain signals). Some of them are shown in Figure 5.16.

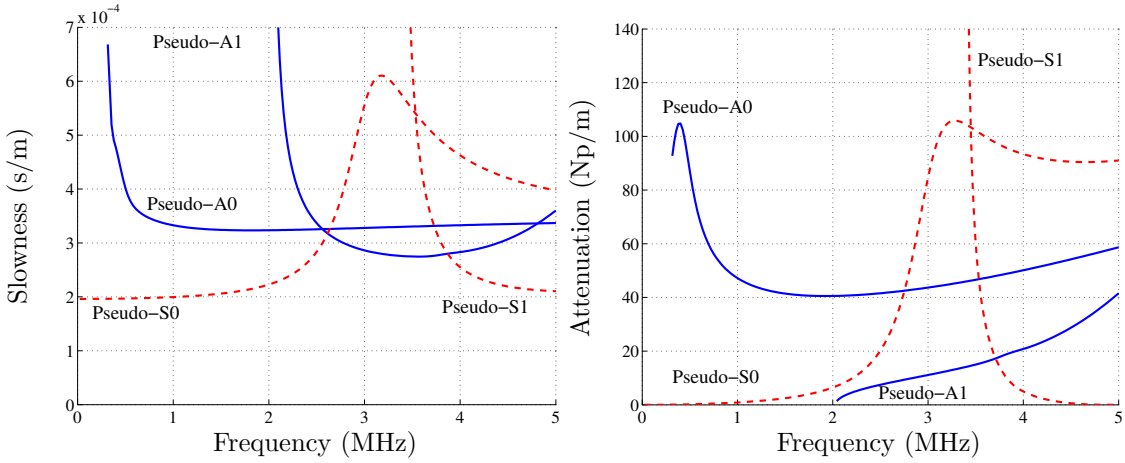

(a) Propagation part.

(b) Attenuation part.

Figure 5.14: Analytical dispersion curves for a 0.76-mm-thick stainless-steel plate loaded with a water half-space.

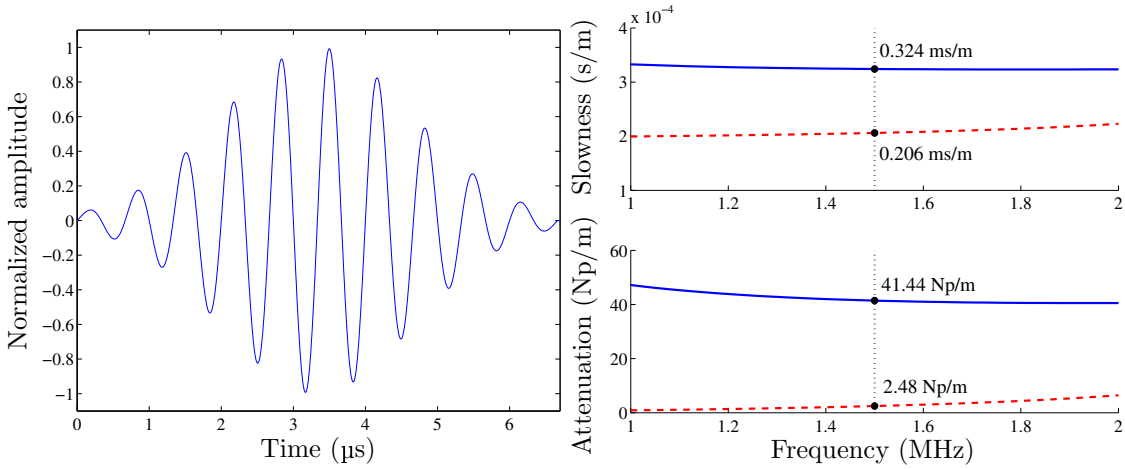

(a) Excitation signal.

(b) Zoomed dispersion curves.

Figure 5.15: The excitation signal for the experiment—10-cycle Gaussian tone-burst at 1.5 MHz, and predicted slownesses and attenuation of existing Lamb wave modes. The solid and dashed lines represent the pseudo-A0 and pseudo-S0 modes, respectively.

From the predicted slownesses shown in Figure 5.15(b), the pseudo-S0 and pseudo-A0 modes should arrive at the receiving transducer at around 21.6 and 34.0 µs, respectively. Hence, it is evident that, of the time-domain signals shown in Figure 5.16, the first wave packet represents the pseudo-S0 mode while the second wave packet is the pseudo-A0 mode. Small differences in arrival times from the predictions can be caused by differences in material properties and geometry, errors in the measurements and some time-delays in the instrumentation. But these differences are not critical since they are constant in all recorded signals.

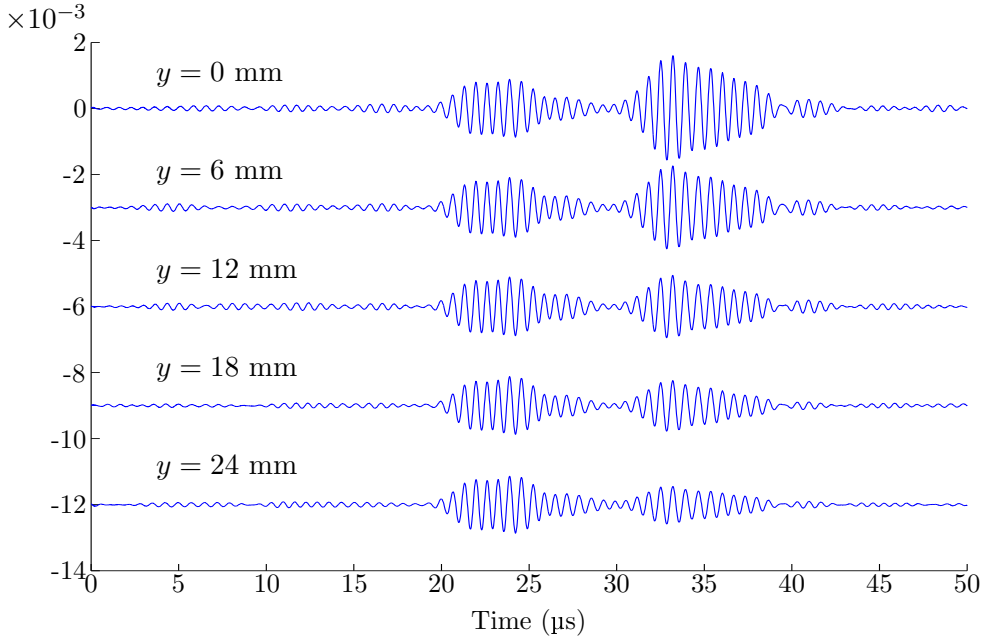

Figure 5.16: Five time-domain narrowband signals with varying attenuation. Signals are shown for the water elevations of 0–24 mm, every 6 mm.

Attenuation for this case will be obtained by the spectrogram method and the curve-fitting scheme. First, the spectrograms of all time-domain signals are calculated. Figure 5.17 shows typical spectrograms for the measured signals. The same contour lines are used in both subfigures. This same set of contour lines demonstrates the obvious magnitude decay of the pseudo-A0 mode as the water level rises, and, at the same time, also indicates no visible decay of the pseudo-S0 mode because of its small attenuation. Both spectrograms show clear separation between the two existing modes, so the square root of the volume under the surface of the spectrogram will be used as $|\tilde{U}|$ for each signal. The frequency

range included in the calculation is 1–2 MHz, while the slowness ranges are 0.19–0.29 ms/m for the pseudo-S0 mode and 0.3–0.4 ms/m for the pseudo-A0 mode.

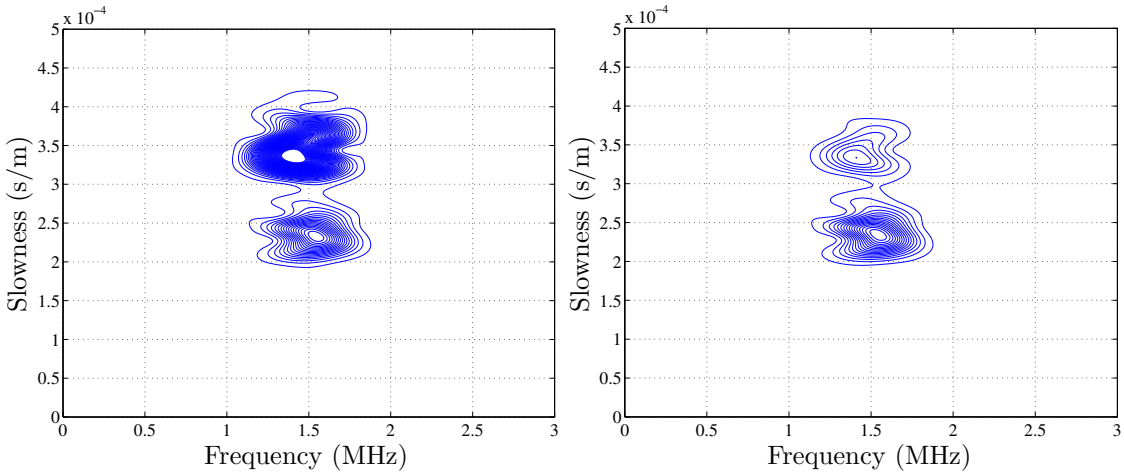

(a) $y = 0$ mm. (b) $y = 24$ mm.

Figure 5.17: Typical spectrograms of the signals in Figure 5.16.

Figures 5.18 show the results of the attenuation extraction algorithm for both Lamb modes. Each subfigure—for each Lamb mode—shows the extracted wave magnitudes, $|\tilde{U}_i|$'s, versus the water elevations, y_i's. The best-fitted curve following the model in Equation (5.18) is shown as a solid line. For each Lamb mode, the best-fitted attenuation value, is a result of a successful curve-fitting procedure, which is done in the semi-log domain. That is, a linear model is fitted to the data between y_i's and $\ln|\tilde{U}_i|$'s, and the parameters α and $\ln|Q|$ are calculated according to Equation (5.13). Since the propagation distance does not change from measurement to measurement, the extracted magnitudes, $|\tilde{U}|$'s occur at the same slowness in all signals and are accepted.

Although the minimizer calculated from the formula (5.13) ensures the optimality of the sum-square error between the model and the measured data, it does not guarantee that the measured $|\tilde{U}|$'s follow the exponential model (in a linear scale) closely or the experimental errors are small. The other consideration which can be considered to eliminate results from the error-sensitive measured data is the goodness of fit. There are a number of parameters which indicate the goodness of the fitting (or some related aspects). Examples of common

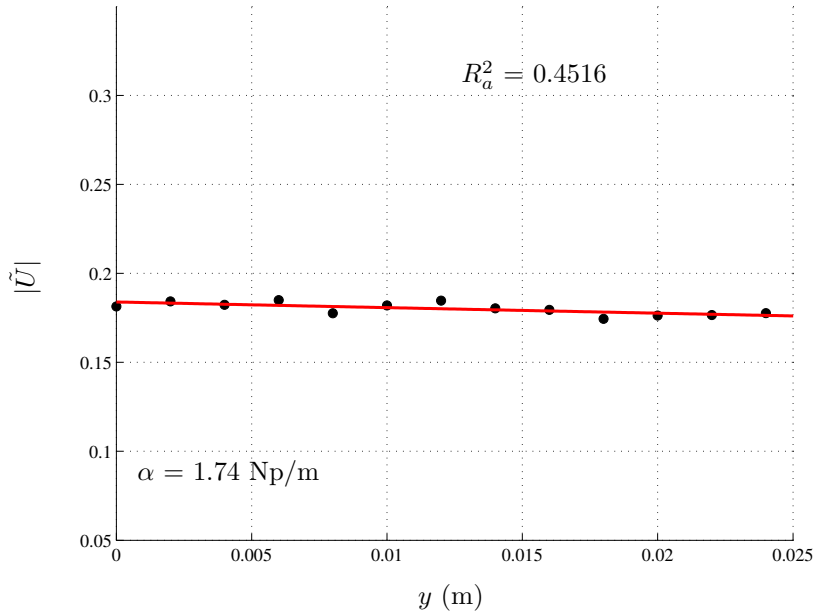

(a) Pseudo-S0 mode.

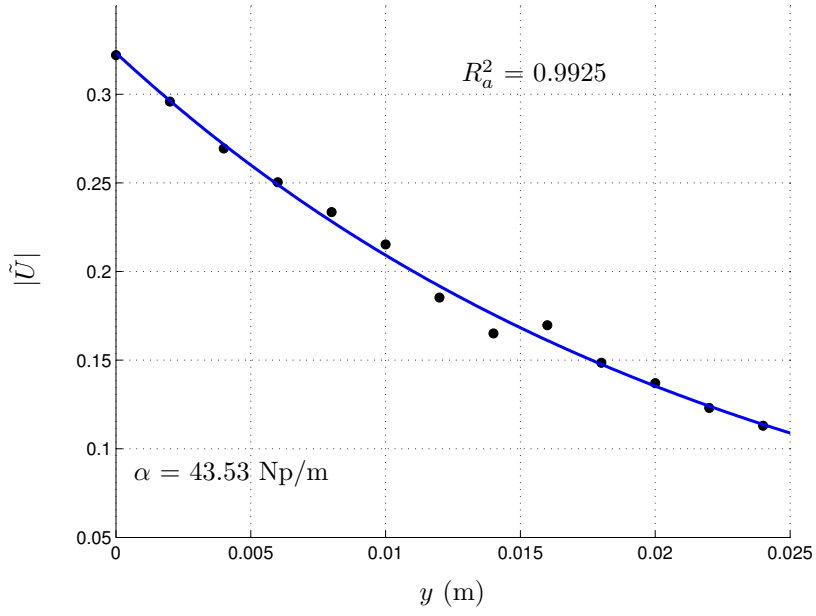

(b) Pseudo-A0 mode.

Figure 5.18: Attenuation calculation for narrowband Lamb wave signals at 1.5 MHz.

parameters are the sum-square error, the root-mean-square error, R-square, etc. Since the absolute parameters such as the sum-square error and the root-mean-square error are usually small for successful iteration, the parameter which explains the variation of the data (in comparison to the model) is the R-square value. The R-square value, or the coefficient of determination, is defined without a weight function as

$$R^2 = \frac{\sum_{i=1}^{N} \left(\ln|Q| - \alpha y_i - \overline{\ln|\tilde{U}|} \right)^2}{\sum_{i=1}^{N} \left(\ln|\tilde{U}_i| - \overline{\ln|\tilde{U}|} \right)^2}, \tag{5.19}$$

where $\overline{\ln|\tilde{U}|}$ is the average of the measured data, i.e.

$$\overline{\ln|\tilde{U}|} = \frac{\sum_{i=1}^{N} \ln|\tilde{U}_i|}{N}.$$

This parameter, which ranges from 0 to 1, basically indicates the variance of the fitting model relative to the variance of the measured data. This parameter provides the information of how much the measured data can be "explained" by the fitting model. The value of R^2 close to 1 indicates that the model explains almost all of the measured data, or the measured data follow the model closely. However, since the value of R^2 increases with the number of measured data, it is more informative to consider the adjusted version of R^2 defined as [50]

$$R_a^2 = R^2 \left(\frac{N-1}{\nu} \right), \tag{5.20}$$

where ν is the number of degrees of freedom, equal to the number of measured data (N) subtracted by the number of coefficients in the fitting model ($\nu = 2$ for this case—α and $\ln|Q|$). This adjusted version of R^2 eliminates the positive effect of including more measured data to the calculation of R^2, and is more suitable for goodness consideration. It should be emphasized that the parameter R^2 or R_a^2 indicates how well the fitting model can explain the measured data, but its value close to 1 does not necessarily imply a good fit without considering other parameters (such as the sum-square error). However, since this research is interested in the attenuation value following a linear model (between $\ln|\tilde{U}|$ and α), it is appropriate to use R_a^2 to justify the extracted results.

In Figure 5.18, the values of R_a^2 are given for both successful fitting. It can be seen clearly that the measured magnitudes $|\tilde{U}|$'s of the pseudo-A0 mode can be explained very

well by the exponential model ($R_a^2 = 0.9925$), whereas this is not the case for the pseudo-S0 mode ($R_a^2 = 0.4516$). So, the calculated attenuation of the pseudo-A0 mode can be considered reliable from the mathematical model standpoint, but the one for the pseudo-S0 mode needs justification.

For the pseudo-S0 mode, the exponential model can explain only around 45% of the measured data. This is not surprising since the absolute attenuation value of the pseudo-S0 mode, which is around 2.48 Np/m from the prediction, is very small in comparison to other variations and errors in the experiment when the 24-mm range of a distance with attenuation is considered. The magnitude of this pseudo-S0 mode is expected to decay only 5.8% over 24 mm distance with attenuation; this decay is so small that experimental errors can have more influence in the change in amplitudes of the measured signals. This means that the measured magnitudes of the pseudo-S0 mode are too sensitive to the errors in the experiment and signal processing to be reliable. Therefore, the calculated attenuation value of the pseudo-S0 mode at this frequency should not be further used. However, Figure 5.18(a) shows that, although there are some variations in the measured magnitudes of the pseudo-S0, the overall trend of the data is decreasing and the final attenuation result is obtained acceptably well in the absolute magnitude when several measurements are used. The value of attenuation of this mode is off by just 0.74 Np/m from the predicted value. This difference might seem relatively large in comparison to the absolute value, but its effect will not be significantly seen over a small distance with attenuation.

In overall, the developed attenuation extraction technique can give acceptable values for both Lamb modes, especially the pseudo-A0 mode. The attenuation value of the pseudo-S0 mode is too sensitive to be further used for this set of measurements, but the attenuation value of the pseudo-A0 mode is reliable and can be used in the application as presented in Section 6.2.

5.4.2 Attenuation extraction of broadband signals

This subsection considers the most general case when measured Lamb wave time-domain signals are broadband and multi-mode. The experiment is conducted on an aluminum

box with water filled inside. The size of the box is 375 mm×375 mm×55 mm; the box's thickness is 1 mm. This testing configuration is shown in Figure 5.19(a) for the three-dimensional schematics. The laser generation starts at the distance of 60 mm and moves towards the detection every 2 mm. The last measurement is made at 40 mm (the total of 11 measurements). For this set of propagation distances, the dimensions of the box are large enough to ensure that no reflection from any of the box's sides, including the opposite face of the box, will be captured in the time window of interest. Therefore, this test system can be viewed as a 1-mm-thick aluminum plate loaded with a water half-space as shown in Figure 5.19(b). This test specimen is called a *fluid-plate* specimen. The other test specimen is a regular 1-mm-thick aluminum free plate, which is the same aluminum box without water. This specimen, called a *free-plate* specimen, is used as a reference to observe qualitative behaviors of leaky Lamb waves.

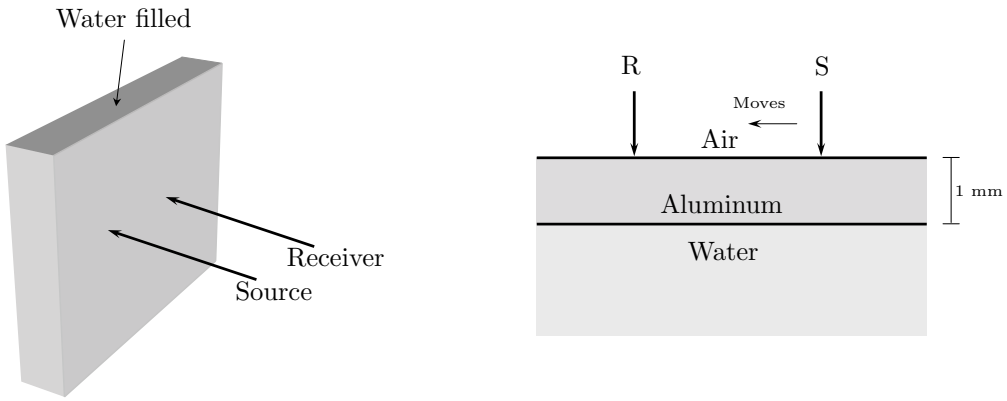

(a) 3D view.

(b) Model (top view).

Figure 5.19: Experimental configuration for attenuated broadband Lamb waves.

Figure 5.20(a) shows a typical time-domain signal recorded for a fluid-plate specimen in the described test setup. The signal shown in this figure is measured at 46 mm. This signal presents the similar complicated multi-mode behavior as seen for a free-plate specimen, which is shown in Figure 5.20(b) for the same propagation distance. From the comparison between two signals, the significant decrease in overall amplitude is observed due to the loss

of energy from the plate to a water half-space, or attenuation. It is also observed that when the system is leaky (a fluid-plate specimen), the recorded signal is more dominated by the surface wave component arriving around 16 µs. This behavior is explained by the fact that, as the frequency increases, the part of the pseudo-A0 mode which converges to a surface wave has its motion confined only at the surface of the plate. So, the motion on the other side of the plate—the side which is in contact with a water half-space—becomes smaller. This makes the amount of energy transferred from the plate to the half-space smaller as well, which leads to smaller attenuation. Hence, that part of the signal can still be clearly seen while other parts experience larger decays of amplitudes due to larger attenuation. In both time-domain signals, the slowly-propagating, low-frequency components arriving after 20 µs are still relatively large. This is partly because of their high excitability. Although these parts of waves have high attenuation, in short propagation distances used in this experiment, they are still dominant.

Signal interpretation can be enhanced when both signals are studied in the time-frequency domain. Figures 5.21(a) and (b) show the STFT's of signals from a fluid-plate specimen and a free-plate specimen, respectively. The solid lines in both figures represent analytical dispersion curves calculated numerically; those curves are also shown alone in Figure 5.22(a). The parameters used in the STFT algorithm are the same as the ones used elsewhere in this research. For better interpretation, Figure 3.2 is reproduced here as Figure 5.22 with the use of the slowness-frequency domain for the propagation part instead of the frequency-real wavenumber domain. Labels for the corresponding Lamb modes of a free plate of the same properties are given. Note that this labelling also indicates the names for modes of a fluid-plate specimen since those names can be easily obtained with the prefix "pseudo-" on the existing labels.

The main features of the STFT of a signal from a fluid-plate specimen shown in Figure 5.21(a) matches what is expected from the analytical dispersion curves. The pseudo-S0 mode components of higher than 2 MHz exhibit large attenuation. This causes the disappearance of the pseudo-S0 mode in the frequency range of 2–4 MHz, which is one of the main components of a signal from a free-plate specimen (area I, compared to the same area

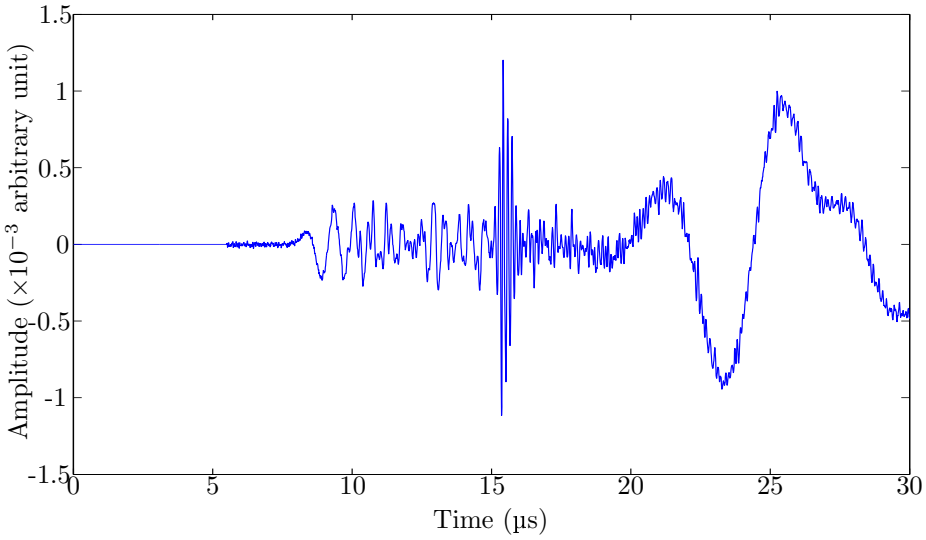

(a) A fluid-plate specimen.

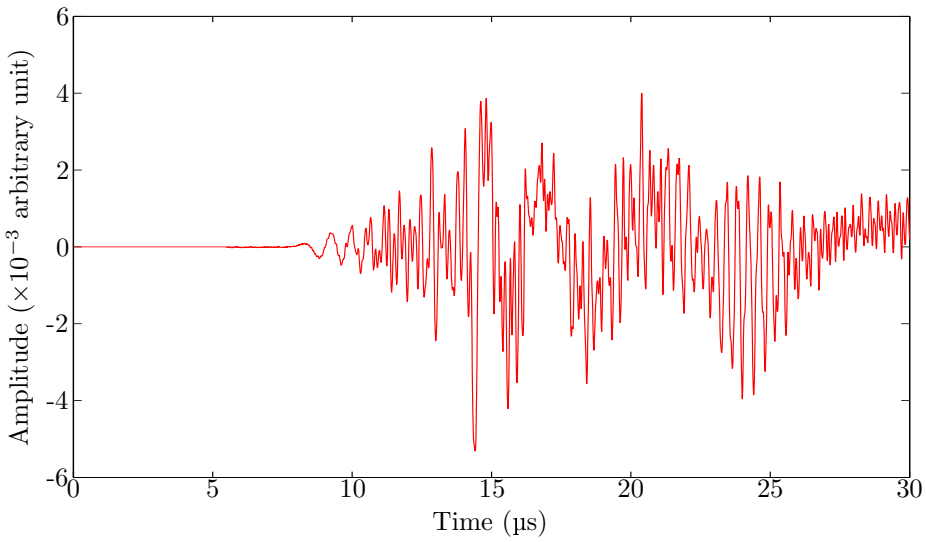

(b) A free-plate specimen.

Figure 5.20: Typical experimental time-domain signals from fluid-plate and free-plate specimens. The signals shown are measured at 46 mm.

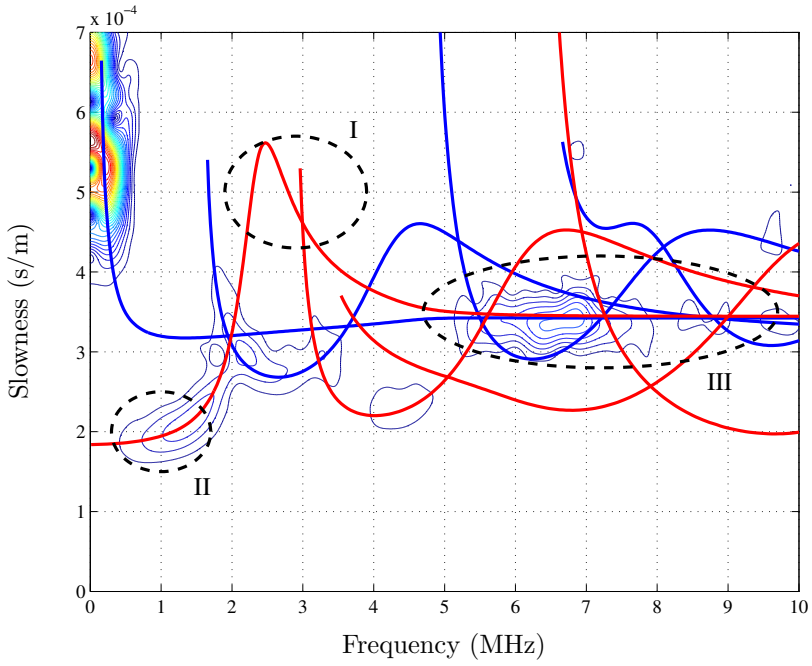

(a) A fluid-plate specimen.

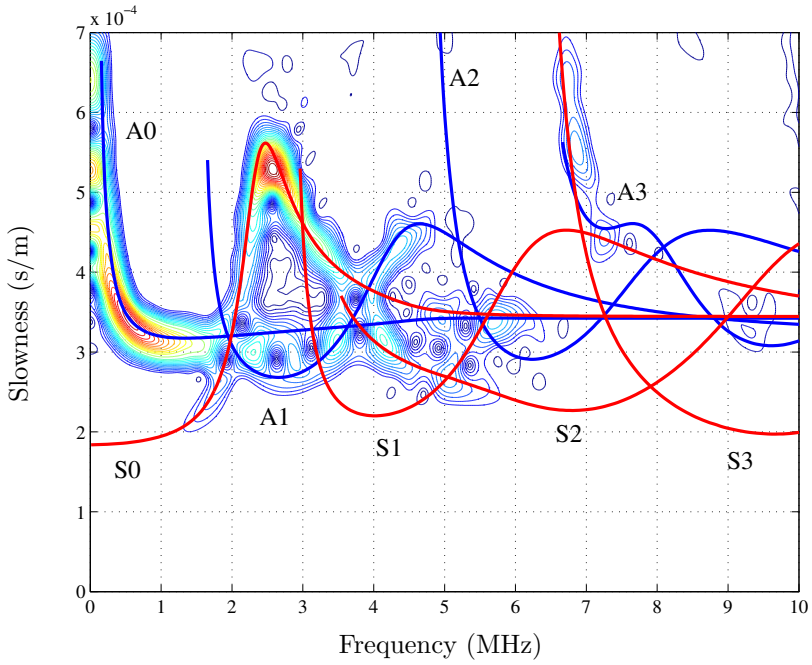

(b) A free-plate specimen.

Figure 5.21: The STFT's of the time-domain signals shown in Figure 5.20.

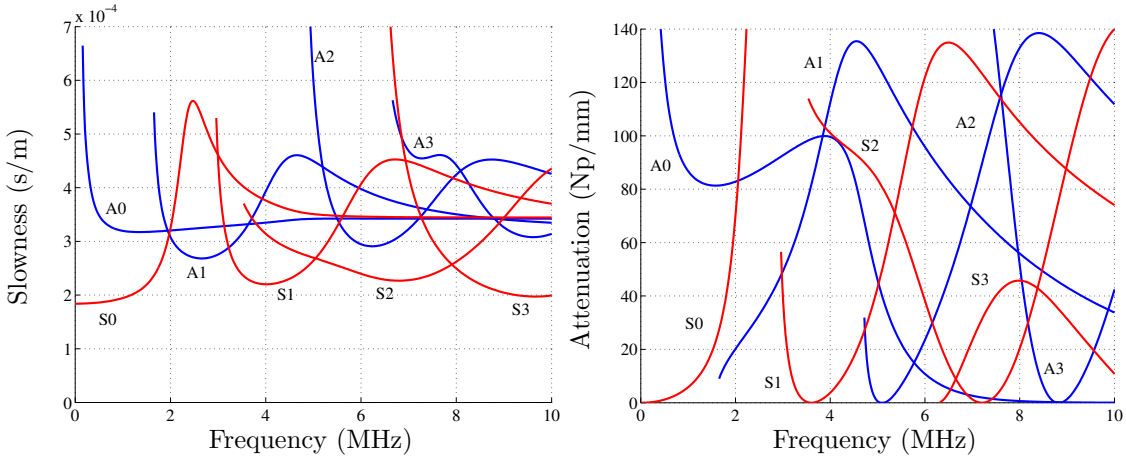

(a) Propagation part.

(b) Attenuation part.

Figure 5.22: Complete dispersion curves of Lamb waves propagating in a 1-mm-thick aluminum plate loaded with a water half-space.

in Figure 5.21(b)). The low-frequency component below 2 MHz of the pseudo-S0 mode is attenuated so little that it remains seen (area II). The higher-order modes at high frequency above 5 MHz experience high attenuation so that they are relatively much smaller than the same component of the pseudo-A0 mode (area III).

From the analysis, the part of measured time-domain signals which will be used in attenuation calculation will be in the frequency range of 0.5–2 MHz. The low-frequency components below 0.5 MHz of the pseudo-A0 mode are not of interest because they are slowly propagating and will be contaminated by reflections of the much faster pseudo-S0 mode from the sides of a specimen. The components of the pseudo-S0 mode below 0.5 MHz are not of interest either since their attenuation is so low that the results become too sensitive to experimental errors. Also, the half-bandwidth of the filters used in the processing is 0.5 MHz. The mid- and high-frequency components of signals contain more than two modes propagating with close slownesses in the same order of the limitation of the developed techniques (around 0.6×10^{-4} s/m), so they can be neglected for this set of propagation distances. Therefore, all unwanted components of measured time-domain signals are filtered out first in the pre-conditioning process. The bandpass filter with a passband of 0.5–2.5 MHz is digitally designed and applied to the measured signals. The

filtered signals, which will be used in the attenuation extraction algorithm, are shown in Figure 5.23. In this figure, only six of eleven signals are shown; the propagation distances selected are 40–60 mm, every 4 mm.

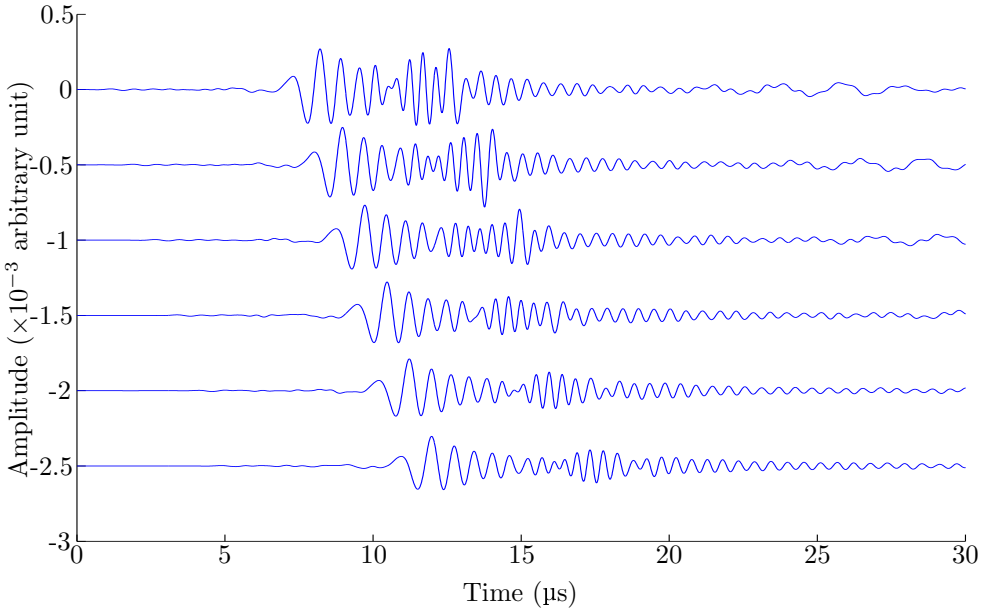

Figure 5.23: Pre-conditioned (filtered), experimental time-domain signals used as input for attenuation extraction algorithm. The plot shows six signals measured between 40–60 mm, every 4 mm.

The attenuation extraction algorithm in this subsection uses the MBF method. It is applied to all eleven filtered signals to obtain $|\tilde{U}|$'s at different frequencies. Intermediate results are shown in Figure 5.24 as $|\tilde{U}|$'s plotted versus slowness for the 1.2-MHz and 1.7-MHz components of the signals. At 1.2 MHz, both peaks representing the arrivals of the pseudo-S0 and pseudo-A0 modes are considered reliable since, for each mode, all peaks lie in the same slowness range. Then, attenuation is calculated at both slownesses (for both modes). However, at 1.7 MHz, whereas peaks of the pseudo-S0 modes are consistently located at the same slowness, the peaks of the pseudo-A0 mode, which are the smaller ones, are interfered by part of the pseudo-S0 mode. As a result, the peak of this pseudo-A0 mode is shifted differently at each different propagation distance. The developed algorithm considers this slowness location unreliable and rejects to calculate attenuation for this mode at this frequency. At each frequency, acceptable peaks or $|\tilde{U}|$'s at different propagation distances

are fitted to a exponentially-decaying model to obtain attenuation. In fact, the fitting is done in the semi-log domain in terms of the distances and $\ln|\tilde{U}|$'s. The attenuation results for these real experimental signals are shown as circles in Figure 5.25. Predicted values are shown for comparison purposes as solid lines.

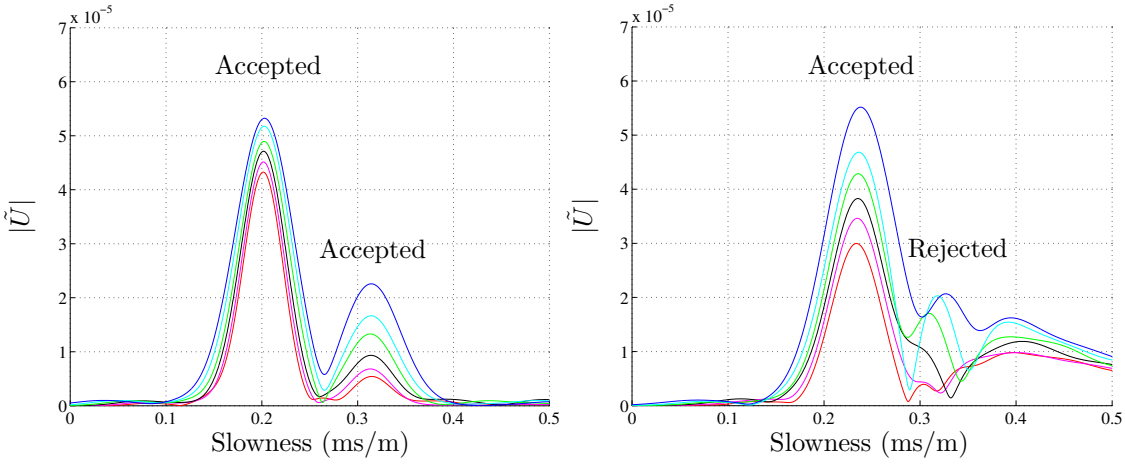

(a) 1.2 MHz. (b) 1.7 MHz.

Figure 5.24: Magnitudes of the 1.2-MHz and 1.7-MHz components of experimental time-domain signals by the MBF method. The figure also shows acceptance and rejection of peaks by the developed algorithm.

As in the previous subsection, one should consider the goodness of curve-fitting for each attenuation calculated although each value in Figure 5.25 is a result of a successful curve-fitting procedure. The parameter for the goodness of curve-fitting will be R_a^2 by the reason stated in the previous subsection. Using this parameter, one can reject some fitted attenuation values obtained from the measured data which vary too much from the model or could not be explained well by the model. Figure 5.26 shows the attenuation results from the measured data with $R_a^2 > 0.6$. This figure is in effect the plot in Figure 5.25 with some points from the large-variation data removed. Examples of the case where the attenuation model explains the extracted $|\tilde{U}|$'s well are shown in Figure 5.27 for attenuation calculation at 1.2 MHz of both pseudo-S0 and pseudo-A0 modes. Figure 5.28 shows eliminated attenuation points when the minimum value on R_a^2 of 0.6 is imposed. The figure shows two curve-fitting at 0.5 and 0.7 MHz. Notice that the calculated values which are eliminated by the criterion

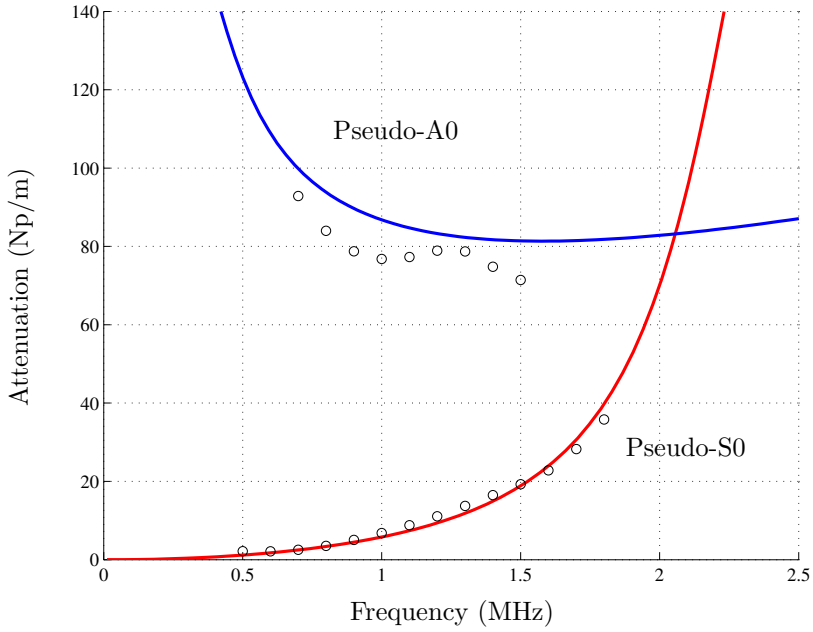

Figure 5.25: Calculated attenuation of broadband, experimental time-domain signals by the MBF method.

on R_a^2 belong to the pseudo-S0 mode at lower frequency. This is not surprising and can be explained in a similar fashion to the case of the pseudo-S0 mode of narrowband signals in the previous subsection. That is, at those frequencies, attenuation of the pseudo-S0 mode is very small (< 4 Np/m from the prediction) so that the magnitude $|\tilde{U}|$ does not decay much over a short distance ($< 8\%$ over 20 mm). Hence, the values of $|\tilde{U}|$'s, which include experimental errors and estimation in the signal processing, can be sensitive when a small change among them is to be detected. In other words, the *changes* in the measured $|\tilde{U}|$'s of the pseudo-S0 mode in those frequencies due to attenuation are too small, so they can be masked by errors in experiment and signal processing. However, as seen in Figure 5.28(b), although there is a large variation in the measured data, the developed attenuation extraction algorithm can still capture the decrease in magnitudes of the pseudo-S0 mode, especially when a large number of signals are used in the algorithm. Moreover from Figure 5.28(b), the fit with $R^2 \approx 0.3$ does look reasonable. The decreasing trend is obvious and the calculated attenuation value at that frequency perfectly fits the prediction.

For the pseudo-A0 mode, the extracted attenuation values underestimate the prediction

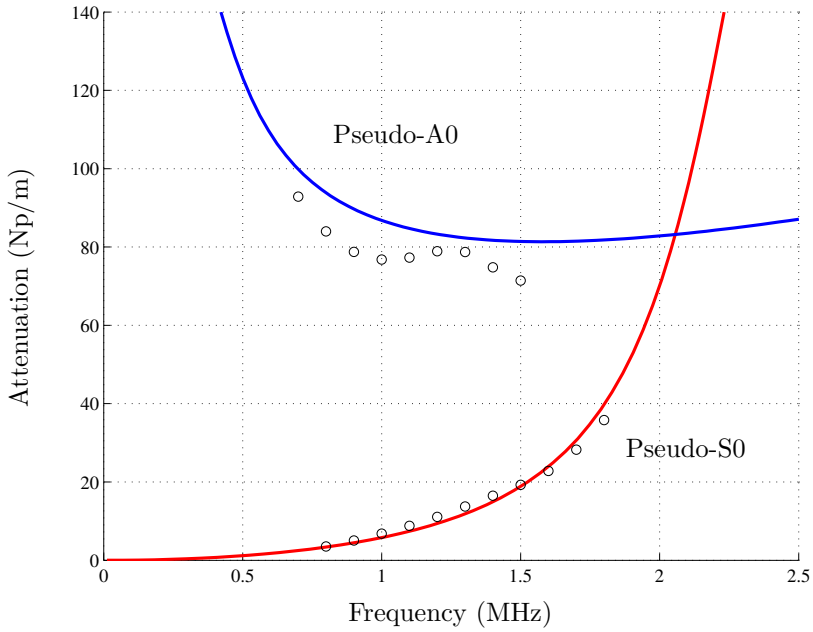

Figure 5.26: Calculated attenuation of real, experimental time-domain signals (by the MBF method) for the good model-fit of $R_a^2 > 0.6$.

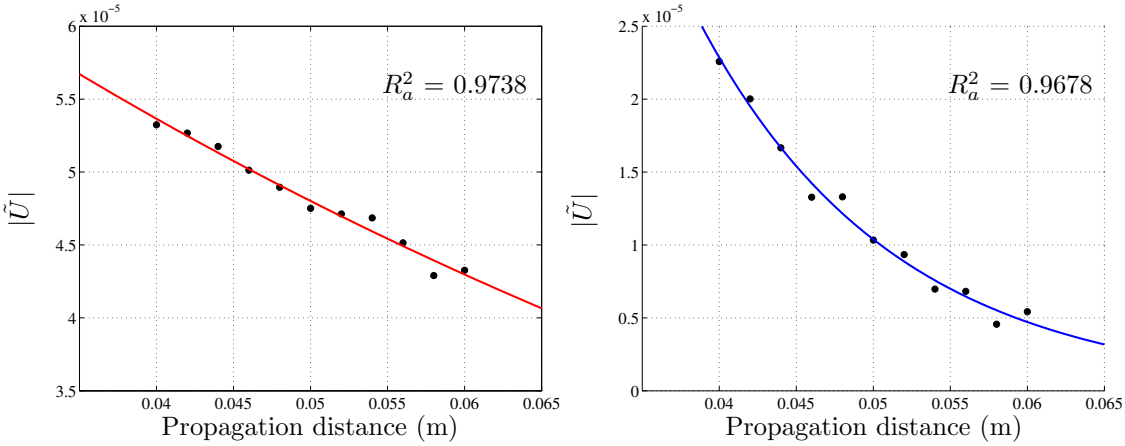

(a) Pseudo-S0 mode at 1.2 MHz.

(b) Pseudo-A0 mode at 1.2 MHz.

Figure 5.27: Attenuation extraction by the curve-fitting scheme with $R_a^2 > 0.6$.

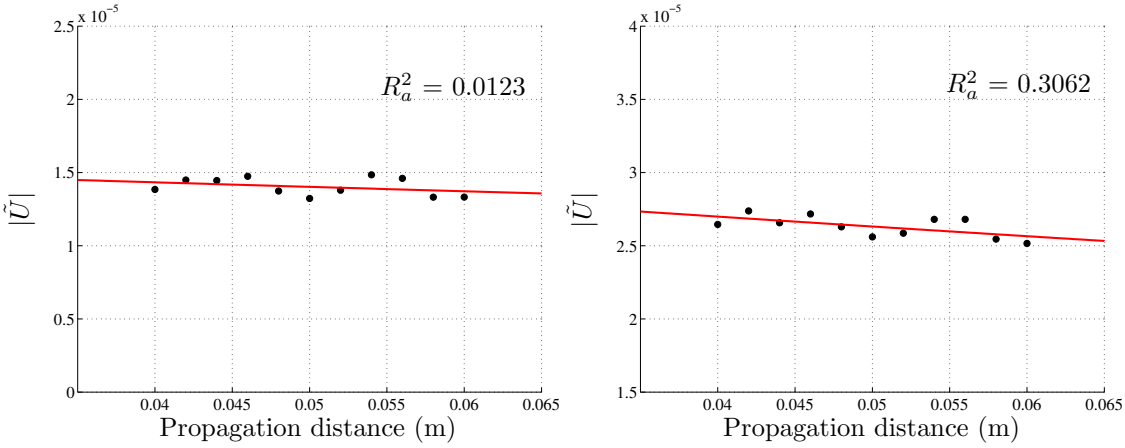

(a) Pseudo-S0 mode at 0.5 MHz.

(b) Pseudo-S0 mode at 0.7 MHz.

Figure 5.28: Attenuation extraction by the curve-fitting scheme with $R_a^2 < 0.6$.

in the range of 4–10 Np/m although all of measured $|\tilde{U}_i|$'s at those frequencies are explained well by the model. This discrepancy is due to the nature of accuracy of the measurement in the logarithmic scale. This kind of measurement is usually sensitive to the variations in the tests since the variations are magnified by the logarithm. Specifically for this attenuation measurement of the pseudo-A0 mode around 0.5–1.5 MHz, the calculated results suffer accuracy problem since the range of propagation distances used is not suitable for the attenuation of this level. This is depicted in Figure (5.29) for the 1-MHz component of the pseudo-A0 mode, of which the extracted attenuation is of the largest discrepancy ($\approx$ 10 Np/m). In this figure, two curves with different values of attenuation are fitted to the measured results. The solid curve is the best-fitted curve which results in the attenuation value shown in Figure 5.25 (76.80 Np/m) whereas the dotted curve is the best-fitted curve with a fixed predicted attenuation value (86.79 Np/m). Both curves show qualitatively good fits for the measurements in this range. The total sum-square error and the R_a^2-value of the dotted curve (0.1277 and 0.9523, respectively) are a little worse than those of the solid curve (0.0838 and 0.9652), which is the best fit in overall. The difference between those two fitting curves can be observed and distinguished at shorter propagation distance because the attenuation is high (the total attenuation is high so that the amplitude of the signal drop very quickly after a short distance).

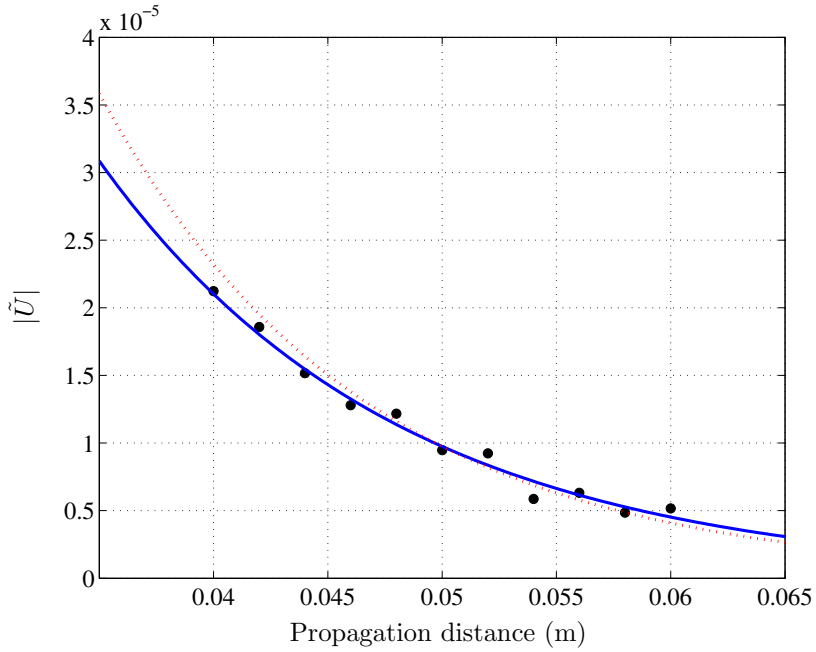

Figure 5.29: Two best-fitted curves for the pseudo-A0 at 1 MHz. The solid curve is the overall best fit, and the dotted curve is the best fit with the attenuation value from a numerical prediction.

In conclusion, from Figure 5.25 or 5.26, the developed algorithm can extract accurate attenuation information from the experimentally-measured broadband time-domain signals, provided that proper constraints are imposed to ensure reliability and consistency of the measured data. The attenuation of the pseudo-S0 mode agrees well with the prediction; the largest discrepancy is around 4 Np/m occurring when the pseudo-S0 mode is most dispersive and arrives very closely to the pseudo-A0 mode. The high dispersion affects the accuracy in the signal processing since the same time-frequency window might not capture the same portions of this mode for all signals. The close propagation velocities of the two mode also results in strong interference which can alter the peaks of both modes, and thus, cause the locations of peaks to be unreliable. The results for the pseudo-A0 mode present significant discrepancies because of the sensitivity of the measurements for very high attenuation. However, the extracted results can capture the trend of increase attenuation at lower frequency. Moreover, the average difference in attenuation for this mode at this frequency range is about 8 Np/m which is reasonably good. Attenuation over broader

frequency range can be achieved if the longer propagation distances are used.

5.4.3 Remarks on attenuation extraction of broadband signals

For broadband leaky Lamb wave signals, sometimes reference time-domain signals are available; a typical signal is shown in Figure 5.20(b). That is, for a system consisting of a solid plate loaded with a fluid half-space, if a time-domain signals can be measured in a dry condition or in a plate without a fluid as a reference signal, attenuation of Lamb waves in the corresponding leaky system can be extracted by the direct method using the time-domain signal measured at the same propagation distance as a reference signal. The relationship between the magnitudes of a particular Lamb mode and frequency of interest extracted from the two time-domain signals, $|U|$ and $|U_{\text{ref}}|$ for attenuated and reference signals, respectively, follows the equation

$$|U| = |U_{\text{ref}}|e^{-\alpha x}, \tag{5.21}$$

where x is the propagation distance. Hence, the attenuation is calculated by

$$\alpha = \frac{1}{x} \ln\left(\frac{|U_{\text{ref}}|}{|U|}\right). \tag{5.22}$$

For the fluid-plate and the free-plate specimens in the previous subsection, this approach requires only one measurement from each specimen. However, multiple measurements at a number of propagation distances will reduce the variations in the measurements and usually give better representative results. The final attenuation value at each frequency of each existing Lamb mode is taken to be the average value among the values calculated from all available pairs of time-domain signals. With the MBF method for the magnitude extraction, typical intermediate results are shown for the 1.4-MHz components in Figure 5.30(a) and for the 1.8-MHz components in Figure 5.30(b). The figure shows the calculated attenuation values for both pseudo-S0 and pseudo-A0 modes. The time-domain signals are measured at 52 mm. In Figure 5.30(b), the pseudo-A0 mode is masked by the pseudo-S0 mode for the fluid-plate specimen, while for the free-plate specimen, the S0 mode is masked by the A0 mode, so both magnitudes in Equation (5.22) cannot completely determined. As a result, attenuation of neither of those two modes is calculated. Lastly, the final attenuation

results are shown as squares in Figure 5.31. In this figure, predicted attenuation curves are shown in solid lines and the attenuation values extracted by the technique presented in Section 5.4.2 are also shown as circles for comparison.

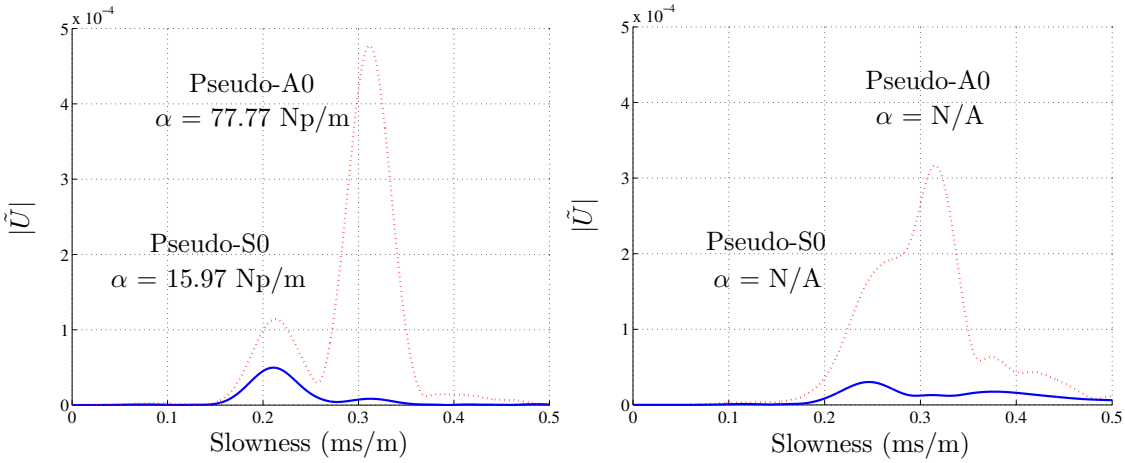

(a) 1.4-MHz components.

(b) 1.8-MHz components.

Figure 5.30: Direct attenuation measurements when reference time-domain signals in the dry condition are available. The reference signal and its leaky counterpart are plotted by dotted and solid lines, respectively. The plot shows the results from time-domain signals measured at 52 mm.

The results shown in Figure 5.31 show an improvement in accuracy, especially for the pseudo-A0 mode. The reason for this improvement is that one attenuation value is calculated from a pair of signals which have the same spreading in the slowness because the propagation distance is the same. This eliminates the variations in signal processing stage due to uncertainty. The drawback of this direct technique is that the calculated attenuation values also depend on the reference time-domain signals measured from the free-plate specimen, so the values at some frequencies cannot be calculated even though two Lamb modes are sufficiently separated and well-behaved in the time-domain signals from the fluid-plate specimen. This situation is seen in Figure 5.30(b) when, in the free-plate specimen, the arrival of the 1.8-MHz component of the S0 mode cannot be identified because of interference by the dominant A0 mode of the same frequency. At this same frequency (1.8 MHz), the technique presented in Section 5.4.2 still give a satisfactory value for the attenuation of the pseudo-S0 mode since the pseudo-A0 experiences large attenuation and its interference on

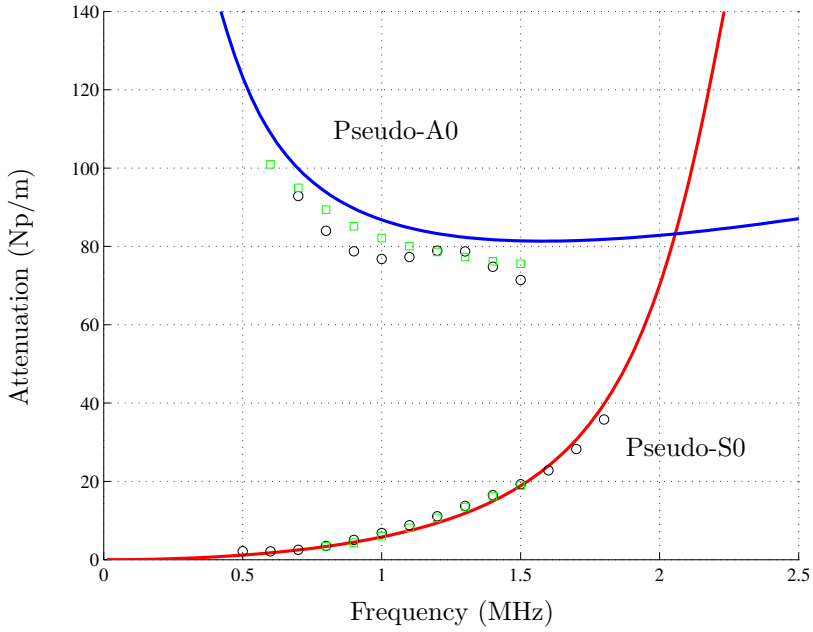

Figure 5.31: Direct attenuation extraction from eleven pairs of time-domain signals. Results are shown as squares. For comparison, the predicted attenuation curves and the results from Section 5.4.2 are shown as solid curves and circles, respectively.

the pseudo-S0 mode does not mask the arrival of the pseudo-S0 mode.

CHAPTER 6

REALISTIC APPLICATIONS

This chapter presents the uses of measured attenuation in realistic applications. Two examples are chosen here to be representative applications for material characterization and condition monitoring. The objective of this chapter is to present potential practical uses of measured attenuation values obtained in the previous chapter by the developed attenuation extraction techniques. Although the following examples might seem specific, they should present the essences of concepts of the real uses of attenuation data so that they can be modified to fit a vast variety of real applications.

The first section starts with the application for material characterization. Since material characterization usually involves the nonlinear inversion technique, a number of measured data are usually required for reliable results. Therefore, the measured attenuation of broadband Lamb wave signals over a frequency range from Section 5.4.2 will be used. The next section presents the application in the aspect of condition monitoring. This kind of applications can sometimes require nonlinear inversion. However, often times, a one-to-one measurement is sufficient, except only that the entire measurement process must be performed over a period of time or even at real time. This thesis presents such an application; therefore, attenuation only at one frequency or the measured data from Section 5.4.1 will be used.

6.1 Applications for material characterization

This section presents the use of measured Lamb wave attenuation over a range of frequencies for material characterization. As stated earlier, attenuation of broadband Lamb wave signals will be used since a large number of measured data, in comparison to the number of unknown properties, are usually required to increase the stability and robustness of a complicated inversion algorithm.

6.1.1 Problem statement and objective

This example considers a closed container with a fluid inside. Some properties of that fluid needs to be characterized. However, it is assumed that the container is accessible only from the outside, so direct property measurements are not possible. Therefore, the objective of this application is to determine the fluid properties from outside of the container. Note that this generic example can apply to a number of real applications. For example, in a chemical reactor, characterization of the properties of a chemical product inside that reactor might be needed from time to time for the product quality control. Moreover, the technique presented in this example can be extended to include the characterization of viscoelastic materials or polymers. Attenuation of Lamb waves in that kind of materials can be directly related to their viscoelastic properties as briefly explained in Section 3.2.

For the example in this section, the container is a 1-mm-thick aluminum box. The fluid inside is an ideal fluid with a known density. Therefore, only the sound wave velocity in that fluid, c_f (c'_L in Section 3.3.3) needs to be characterized. This example presents a simple but realistic application. It can also be extended to involve more unknown parameters and more complex structures. In those cases, the core concept is still the same, but the implementations might be much more involved, especially in the inversion part.

6.1.2 Approach

Due to the layered-like structure of a container, Lamb waves are generated to propagate along the container's wall. Multiple broadband time-domain signals are recorded at different propagation distances, and they are processed to obtain attenuation over a certain frequency range in which the calculated results are reliable and accurate. The technique to achieve this set of attenuation values is presented in Section 5.4.2. Typical measured attenuation data are circles in Figure 5.26. This set of data contains information of the properties of a fluid; therefore, they are used as an input to an inversion algorithm to obtain a sound wave velocity in a fluid.

Recall from the analytical model, presented in Section 3.3.3, that attenuation values of Lamb waves in a plate are parts of the roots of the dispersion equation of the system.

Specifically, they are imaginary parts of the wavenumber roots of Equation (3.46) at a fixed frequency ω. Since dispersion curves are unique characteristics of the system, in principle, given the dispersion curves and the known properties of the system, the unknown properties can be uniquely determined. The straightforward inversion scheme is the nonlinear curve-fitting technique. However, this technique is not efficient because it requires iterative solving of Equation (3.46), each of which contains numerous iterations in itself and can easily encounter numerical problem[1]. This research proposes the use of an artificial *neural network* for this inversion.

Another reason that this research employs a neural network in the inversion is the following. In a more complicated scenario, such as a more complex layered system or an inversion for multiple parameters, all available measured attenuation data may be required in the inversion step. However, available measured data might be system-dependent so that its structure changes from system to system. This makes a specific inversion scheme which works with one system difficult to be applied for a different system. Unlike other inversion techniques, a technique using a neural network, at one extent, does not require any structure of the relationship between the input and output so that it can be very flexible and applicable for universal applications. Therefore, besides a computational advantage, this research also aims to present the concept of this inversion technique to lay a fundamental foundation of using this technique for more general applications. It is important to note that the flexibility of a neural network can be considered its disadvantage. Since a neural network does not require any structure of the system of interest, it will be very difficult to verify that a particular designed and trained network will work well for a desired application. Moreover, a proper design and training requires some experience of a designer, and sometimes, requires trial and error.

An artificial neural network, or in short, a neural network, is a mathematical model

[1]Solving for complex roots of Equation (3.46) is many times more difficult than solving the dispersion equation of a free plate (Equations (2.26) and (2.28)) since, at a fixed ω, two real equations containing two real variables—the real and imaginary parts of the wavenumber—must be satisfied simultaneously. So, even solving for roots of Equation (3.46) at a single frequency becomes a formidable task which requires careful numerical treatments.

which is inspired by human being's biological neurons. Basically, this neural network contains combinations of algebraic operations and mathematical functions so that it calculates a certain output (sometimes called "target") from a certain input. The complication of a network can be of any levels. In an ideal concept, the designed mathematical model will "learn" to give an appropriate output, or respond properly, from a "training" process. A training process is referred to a process in which a large number of sets of known inputs and corresponding targets are run through a network so that parameters in that network can be adjusted to give a desired output in a general case. This training process is a part of the network design process; it will be finished when a desired goal is met. The goal of the training process is usually to achieve acceptable difference between the network outputs and the known exact outputs.

The concept of a neural network can be applied to a number of real applications; examples include function approximation, pattern recognition and classification, adaptive filtering and noise cancellation [37]. For this research, a neural network is used to approximate the relationship between measured attenuation data and the sound wave velocity in a fluid. It should be emphasized that this relationship is very complicated and not expressible so that common function-approximation techniques are not applicable.

This research proposes a simple feedforward, multi-layer neural network shown in Figure 6.1. This network has two layers with transfer functions f_1 and f_2 for the first and second layers, respectively. The first layer contains S_1 neurons and takes an input $\mathbf{p}$ of R elements. The output of the first layer, which has S_1 elements, is an input of the second layer of S_2 neurons. The output $\mathbf{t}$ of size $S_2 \times 1$ coming of the second layer is the target of the entire network. The weights and biases of both layers, $\mathbf{W}_i$'s and $\mathbf{b}_i$'s, for $i = 1$ or 2, respectively, with proper sizes, are parameters in the network, which will be adjusted to give the desired target in the learning process. This choice of a standard multi-layer feedforward network is proven to be able to approximate any Borel measurable function[2] from one finite dimensional space to another to any desired degree of accuracy, provided

[2]A thorough definition of a Borel measurable function requires detailed explanation and a long list of technical terms in real analysis. However, if the focus is only on continuous functions, this statement applies since any continuous function is Borel measurable [14].

that the network is properly designed and trained [43]. For the application at hand, the input **p** will be related to available measured attenuation values, and the output **t** will be the sound wave velocity in an unknown fluid.

In summary, the entire application consists of two stages. In the first stage, a neural network as described earlier is properly designed. The form of an network input, the number of neurons and the transfer function in each layer are carefully chosen. This stage ends after a training process is finished so that proper weights and biases in the network are obtained. The second stage is when the measured attenuation data from Section 5.4.2 are input into the designed network. The output, which is the sound velocity in a fluid, is compared with the expected value.

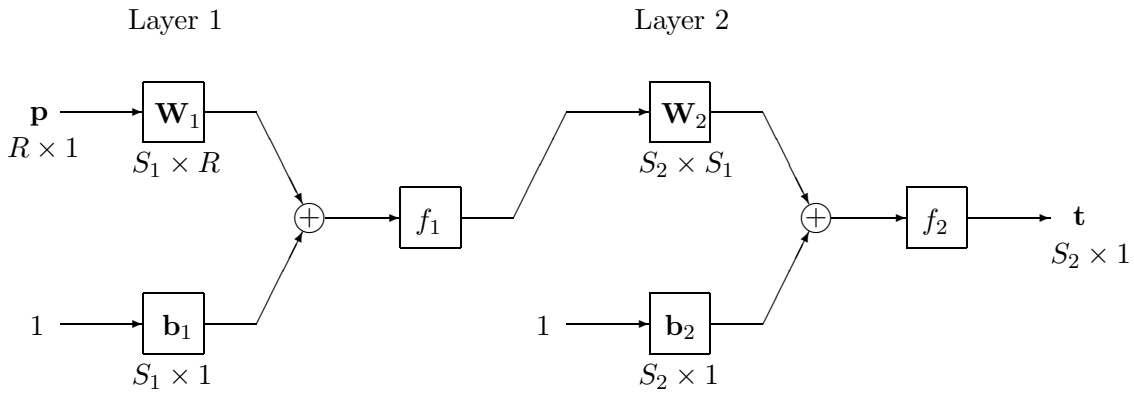

Figure 6.1: The designed 2-layer, feed-forward neural network.

6.1.3 Implementation and verification

To properly design the network, a numerical study of how the sound wave velocity affects the attenuation of Lamb waves is carried out. The frequency range of interest is focused to below 2 MHz for a given aluminum plate thickness of 1 mm. This frequency range represents the range where acceptably accurate attenuation can be measured reliably as presented in Section 5.4.2. Only the pseudo-S0 mode is considered since the measurement of its attenuation is robust for the current setup. Figure 6.2(a) shows the effect of the sound wave velocity, c_f, on attenuation of the pseudo-S0 mode while other problem's parameters

are fixed (1-mm-thick aluminum plate and a fluid density of 1000 kg/m^3). This variable c_f is varied from 0.5 km/s to 2.4 km/s, every 0.1 km/s (a set of 20 dispersion curves) to represent a reasonable range of the sound wave velocity in a fluid. This figure shows that the attenuation of the pseudo-S0 mode increases as c_f increases. This is expected since the larger c_f means that the bulk stiffness of the fluid increases. As a result, the impedances of a solid plate and a fluid half-space become better matched, and the wave energy is more easily transferred across the interface between those two domains. The numerical study also shows two important features of the attenuation dispersion curve of the pseudo-S0 mode in this frequency range, which will be used in this research. Figure 6.2(a) shows that, in this frequency range (below 2 MHz), for any reasonable c_f, the attenuation of the pseudo-S0 mode increases in an exponential-like fashion with frequency. Furthermore, the attenuation of this pseudo-S0 mode also vanishes in the limit at zero frequency. This observation is from the physical fact that, as the frequency approaches zero, the pseudo-S0 mode behaves like a plane wave propagating along the plate in one dimension. Its velocity converges to the extensional velocity (Equation (4.130)). Since the motion of this wave component is mainly in the plate direction (in-plane), the presence of a half-space has very little effect on it, especially when the half-space is an ideal fluid. From these two observations, instead of inputting the measured attenuation data directly to the neural network, this research chooses to represent the measured attenuation data by a proper parametric model and use the parameters in that model as an input $\mathbf{p}$ to the designed neural network. The idea will accommodate the variations in the frequency range of the measured data, which might be dependent of material properties and measurement setup.

From the mentioned observations, the parametric model for the attenuation dispersion curve of the pseudo-S0 mode in this problem is chosen to be

$$\alpha = a(e^{bf} - 1), \tag{6.1}$$

where α and f are attenuation in Np/m and frequency in Hz, respectively; a and b are two parameters. It is not difficult to see that this parametric model captures well, at least approximately, the characteristics of attenuation of the pseudo-S0 mode in this range of

frequency and geometry. Figure 6.2(b) shows the comparison between the best-fitted curve of the form (6.1) and the actual attenuation dispersion curve when $c_f = 1.5$ km/s and the frequency range is chosen to be 0.8–1.8 MHz (from the good measured data shown in Figure 5.26). The parameters a and b are also given in the figure. This comparison confirms that the parametric model in Equation (6.1) can represent the actual attenuation dispersion curve of the pseudo-S0 mode very well. The list of a's and b's for all 20 numerically-generated curves are summarized in Table 6.1. This choice of an input vector $\mathbf{p}$ results in the number of its element $R = 2$ in the network diagram. Note from Table 6.1 that the parameter b of the parametric model (6.1) changes very little with the target. This means that the output of the network is relatively insensitive to the input b, as compared to the input a. This observation suggests that the inversion might be successful with only one input a, which simplifies the entire design process. However, this research chooses to keep both inputs. The insensitivity of the output on b will result in the final weights and biases once the network is properly trained.

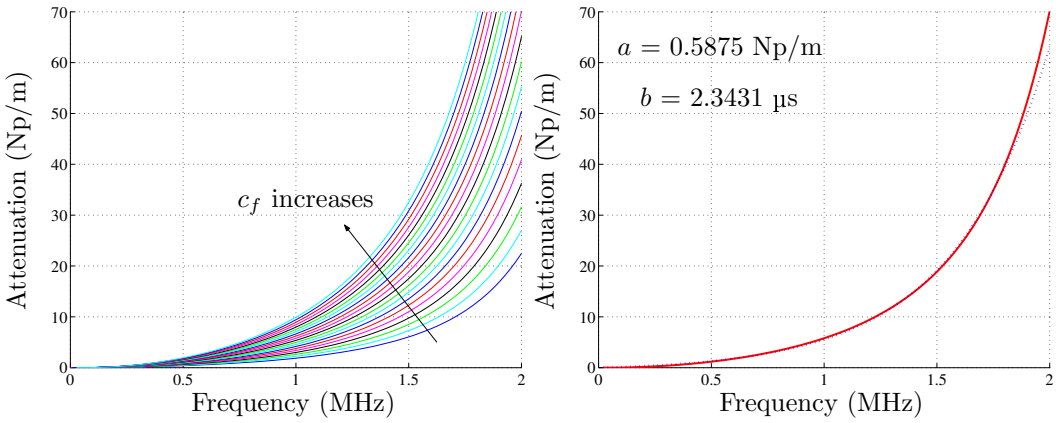

(a) Effect of c_f on the attenuation of the pseudo-S0 mode (c_f = 0.5–2.4 km/s, every 0.1 km/s).

(b) A parametric representation of the attenuation of the pseudo-S0 mode for c_f = 1.5 km/s.

Figure 6.2: Numerical study on the attenuation of the pseudo-S0 mode. Figure (a) shows the effect of c_f. Figure (b) shows an example of a parametric representation (dotted line) compared to the exact curve (solid line) when $c_f = 1.5$ km/s.

Since an output vector $\mathbf{t}$ contains only a single element representing the sound wave velocity in a fluid, c_f, the number of neurons in the second layer S_2 is 1, and the vector

Table 6.1: Parameters a's and b's of Equation (6.1) to represent the attenuation of the pseudo-S0 mode in the frequency range of 0.8–1.8 MHz.

c_f (km/s)	0.5	0.6	0.7	0.8	0.9	1.0	1.1	1.2
a (Np/m)	0.1895	0.2277	0.2663	0.3048	0.3445	0.3834	0.4239	0.4644
b (µs)	2.3397	2.3402	2.3403	2.3410	2.3400	2.3413	2.3406	2.3407
c_f (km/s)	1.3	1.4	1.5	1.6	1.7	1.8	1.9	2.0
a (Np/m)	0.5045	0.5455	0.5875	0.6313	0.6742	0.7196	0.7640	0.8108
b (µs)	2.3419	2.3427	2.3431	2.3422	2.3432	2.3426	2.3438	2.3437
c_f (km/s)	2.1	2.2	2.3	2.4				
a (Np/m)	0.8597	0.9088	0.9591	1.0131				
b (µs)	2.3430	2.3431	2.3433	2.3422				

$\mathbf{t}$ can be simply replaced by a scalar t. So, the only network parameters to be selected are the number of neurons in the first layer S_1, and two transfer functions in both layers f_1 and f_2. This research chooses $S_1 = 2$, the log-sigmoid and linear functions for the two transfer functions, f_1 and f_2, respectively. These choices of design parameters represent a simple set commonly used for function approximation applications. In the context of neural networks, the log-sigmoid and linear functions have special names as "logsig" and "purelin", respectively, and are defined as

$$\text{logsig}(x) = \frac{1}{1+e^{-x}}, \tag{6.2}$$

and

$$\text{purelin}(x) = x, \tag{6.3}$$

where these functions operate on each element of the input if the input is a vector. The plots of these functions are shown in Figure 6.3. So, from the diagram in Figure 6.1, the output of the entire network can be expressed as

$$\mathbf{t} \text{ or } t = F(\mathbf{p}) = \mathbf{W}_2\big[\,\text{logsig}(\mathbf{W}_1\mathbf{p} + \mathbf{b}_1)\big] + \mathbf{b}_2. \tag{6.4}$$

The weights and biases, $\mathbf{W}_i$'s and $\mathbf{b}_i$'s, will be obtained from training. The training starts with the performance index defined as the mean-square error of the known pairs of inputs and outputs

$$P(\boldsymbol{\theta}) = \frac{1}{N}\sum_{i=1}^{N} |t - F(\mathbf{p};\boldsymbol{\theta})|^2, \tag{6.5}$$

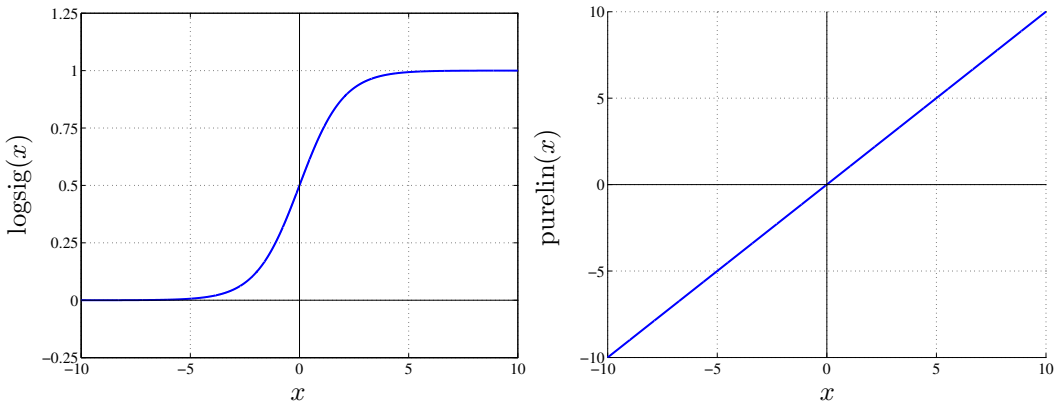

(a) logsig function.

(b) purelin function.

Figure 6.3: The transfer functions used for f_1 and f_2.

where N pairs of training data are available ($N = 20$ for this research), and the variable $\boldsymbol{\theta}$ represents a combination of all weights and biases. The goal of the training process is to minimize this performance index over a variable $\boldsymbol{\theta}$.

For this research, this training stage, which requires iteration, is achieved by the Levenberg-Marquardt "backpropagation" algorithm[3]. With a step of 0.001 and a performance goal of 1×10^{-8}, the training process is successful in 370 epochs, where 1 epoch is one round of training on all available training data (20 pairs of inputs and outputs). This training is considered very fast; this is due to a straightforward trend of the function to be approximated (although the function itself is complicated). The final weights and biases are shown in Figure 6.4. Note that the order of training data is not significant because in each epoch, the performance index is minimized for all training data (see Equation (6.5)).

This ready neural network is next applied for the real attenuation data from measurements. The attenuation data from Figure 5.26 is first represented by a parametric model of the form (6.1). The parameters a and b from this operation, which will be used in the

[3]Training a neural network requires optimization of a function—the performance index. In the optimization process, derivatives of transfer functions inside a network need be calculated. The term "backpropagation" is used to describe how the algorithm updates the derivatives of functions in each iteration of the training input. That is, with the backpropagation scheme, the derivatives are calculated from the last layer back to the first layer using some kind of recurrence formula. Among backpropagation neural networks, a number of different optimization techniques such as the steepest descent or conjugate gradient method, etc. can be used. The Levenberg-Marquardt algorithm is a common method which is modified from the Newton's method [27]. Implementation of this algorithm in a neural network is discussed in Reference [37].

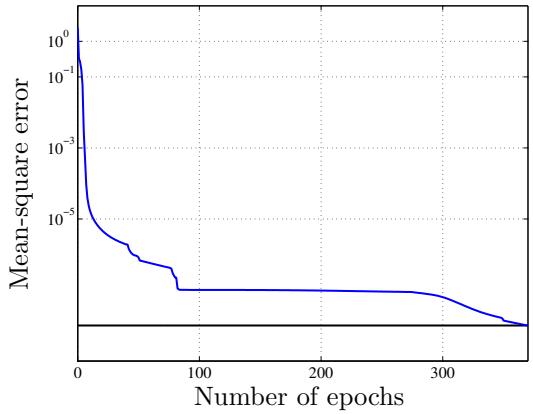

(a) Convergence of a training process.

$$\mathbf{W}_1 = \begin{bmatrix} 2.3239 & -0.9802 \\ 1.7984 & 3.2386 \end{bmatrix}$$

$$\mathbf{b}_1 = \begin{Bmatrix} 2.5570 \\ -9.1377 \end{Bmatrix}$$

$$\mathbf{W}_2 = \begin{bmatrix} 3.0952 & 3.2058 \end{bmatrix}$$

$$\mathbf{b}_2 = \begin{Bmatrix} -2.3019 \end{Bmatrix}$$

(b) Final weights and biases.

Figure 6.4: Final weights and biases, with a performance of a training process, for the designed neural network used for the current example.

elements of the input vector to the trained neural network, are 0.5659 Np/m and 2.3397 µs, respectively. With the weights and biases in Figure 6.4, the network output is calculated according to Equation (6.4) to be 1.442 km/s. Figure 6.5 summarizes the final results.

This final result of 1.442 km/s for the sound wave velocity in water is in good agreement with a referenced value[4] of 1.487 km/s (around 3% difference). Hence, the proposed neural network as an inversion technique is capable and efficient in this illustrated application, provided that the network is well-designed and well-trained. The entire processing time is very fast (< 5 s) on a regular personal computer.

6.2 Applications for condition monitoring

This section demonstrates the use of measured Lamb wave attenuation for condition monitoring. Since, the example presented here will not require an inversion procedure, attenuation at a single frequency of a single Lamb mode is sufficient. Therefore, narrowband

[4]The sound wave velocity c in distilled water when the temperature T and absolute pressure p of water are in the ranges of 0–20°C, and 10^5–10^7 Pa, respectively, follows the empirical formula [75]

$$c = 1447 + 4.0(T - 10) + (1.6 \times 10^{-6})p,$$

where c is in m/s; T and p are measured in °C and Pa, respectively. Hence, at 10^5 Pa (around 1 atm) and 20°C, the sound wave velocity in water is 1487 m/s.

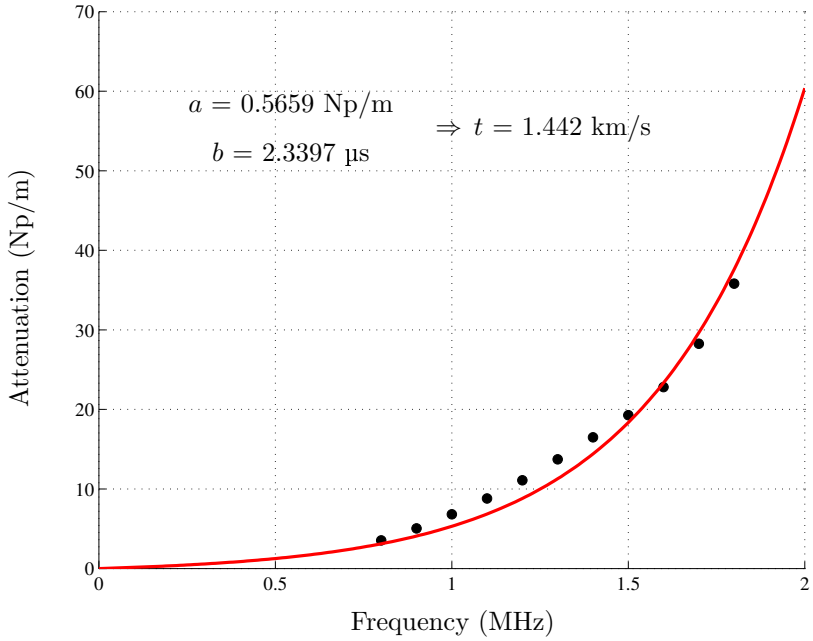

Figure 6.5: Inversion results from the real measured attenuation data. The figure shows the parametric representation of the measured data with the model's parameters a, b, and the output of the designed network.

signals will be considered.

6.2.1 Problem statement and objective

This example concerns a chemical reactor which cannot be monitored from the inside. This reactor is constantly fed with reactants from the outside supplier. During the chemical process, since reactants are continuously input, the elevation of the mixture inside the reactor is rising. This elevation is critical for safety purposes. The outside supplier must stop feeding reactants once the elevation of the product inside the reactor reaches a certain level, which is given. So, the goal of this application is to develop a technique to monitor the elevation of the chemical product inside the reactor from the outside.

6.2.2 Approach

Because of a layered structure of the reactor's wall, ultrasonic Lamb waves along the reactor's wall is proposed as a tool. Transducers will be used to generate and detect Lamb waves. The test setup is proposed to be as shown in Figure 5.13. From that figure, the

idea is that as the elevation of the chemical product increases from the receiving (lower) transducer, the amplitude of propagating Lamb waves will decrease because of larger total attenuation. The longer propagation path in contact with the chemical product will induce more leakage and lead to larger reduction in amplitudes of Lamb waves.

With all parameters defined according to Figure 5.13, assume that the reference level is set at the level of the lower transducer since a reference measurement can be made in the dry condition before the start of the chemical process; hence, the reference time-domain signal for the case when $y = 0$ is available. By using the first step of the developed attenuation extraction technique, one can extract the magnitude spectrum of the generated Lamb mode at a specific frequency, $|U_{\text{ref}}|$, from the reference time-domain signal. Now, during the chemical process, if the elevation of the chemical product is at y from the reference level, the magnitude spectrum $|U|$ extracted from the received signal is related to the elevation y by the expression of the form of Equation (5.18), i.e.

$$|U| = |U_{\text{ref}}|e^{-\alpha y}, \tag{6.6}$$

where α is the attenuation of a particular Lamb mode at a specific frequency under consideration. This form of expression is derived from the analytical study of Lamb wave propagation in a plate in contact with a half-space presented in Section 3.3. Then, the elevation y can be straightforwardly calculated as

$$y = \frac{1}{\alpha} \ln\left(\frac{|U_{\text{ref}}|}{|U|}\right), \tag{6.7}$$

provided that the attenuation α is known. The assumption that this attenuation is known or at least, can be approximated, is reasonable since the material properties of the reactor's wall can be measured and the properties of the chemical product inside the reactor can be predicted (if not measured). With known material properties of the system, the dispersion characteristics of Lamb waves along the reactor's wall both with and without attenuation can be numerically calculated. Note that, strictly speaking, the dispersion curves of Lamb waves with and without attenuation are different. However, since usually, the stiffness of the chemical product inside the reactor is much lower than the stiffness of the reactor's wall, especially when that product is fluid, the propagation dispersion curves of Lamb waves will

not be significantly changed. The presence of a chemical product half-space can be thought to only introduce attenuation to Lamb waves, but not alter their propagation characteristics. Figure 6.6 shows two sets of dispersion curves in the same plot for a free 0.76-mm-thick stainless-steel plate and the same plate loaded with a water half-space. Dispersion curves for a free plate are plotted as solid lines while dispersion curves for a plate loaded with a water half-space are plotted by dotted lines. Material properties used in the calculation are given in Section 5.4.1. This figure shows no difference between the two sets of dispersion curves and confirms that a water half-space does not induce any visible changes in the propagation dispersion curves of a free stainless-steel plate. In this case, Lamb waves are only attenuated by the half-space. The induced attenuation is presented through the attenuation dispersion curves as shown in Figure 6.7.

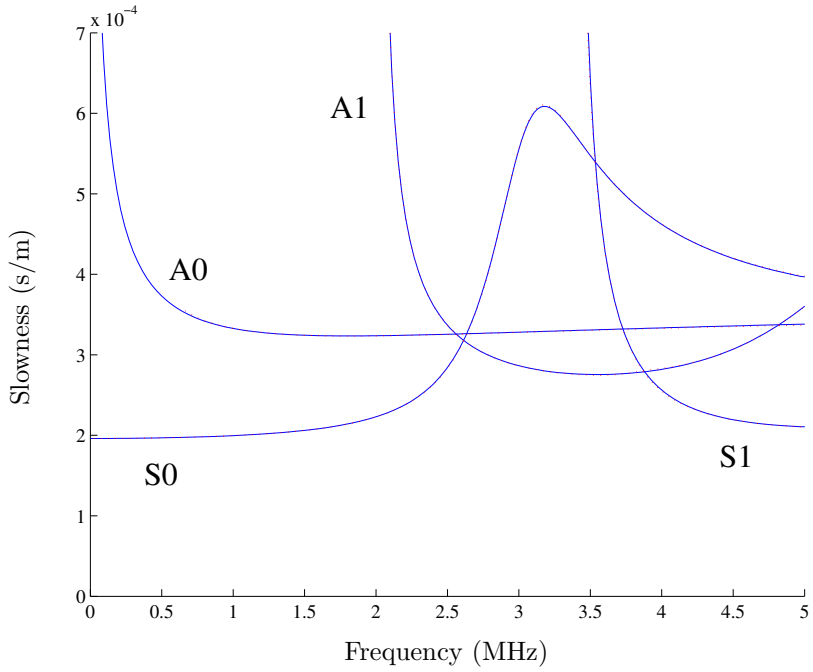

Figure 6.6: Calculated propagation dispersion curves of a 0.76-mm-thick stainless-steel plate for 2 conditions: a free plate (solid lines) and a plate loaded with a water half-space (dotted lines).

These attenuation characteristics are important since they govern the choice of frequency and Lamb mode to be used for a given resolution of the change in elevation y. To see this, consider two measurements at the elevation y_1 and y_2; let $y_2 > y_1$. Let the magnitude

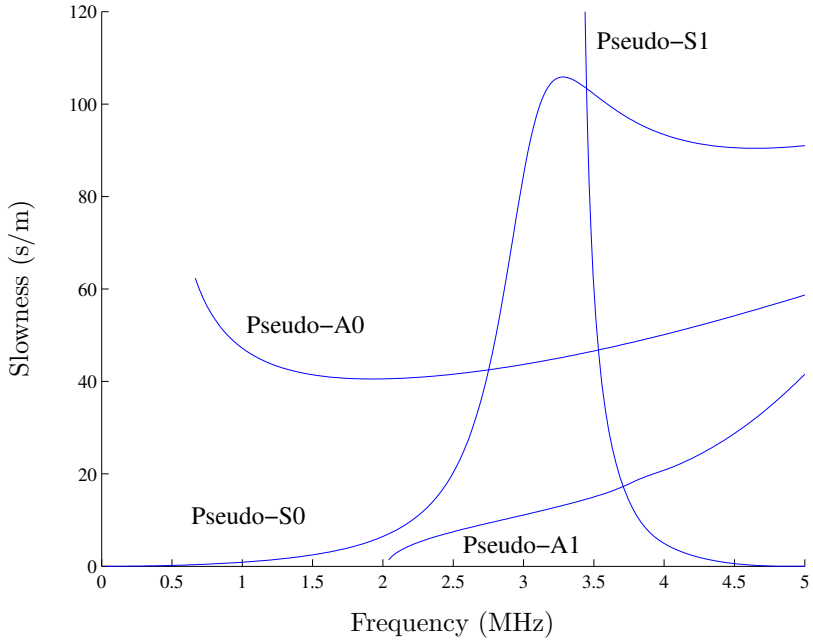

Figure 6.7: Calculated attenuation dispersion curves of a 0.76-mm-thick stainless-steel plate loaded with a water half-space.

spectra of the generated Lamb mode from those two measurements be $|U_1|$ and $|U_2|$. Then, the change in $|U|$ can be related to the change in y by the use of Equation (6.6). With $\Delta y = y_2 - y_1$ and $|U_2| = (1-\beta)|U_1|$, this relationship can be expressed as (see details in Appendix A.5.1)

$$\Delta y = \frac{1}{\alpha} \ln\left(\frac{1}{1-\beta}\right). \tag{6.8}$$

In the above equation, β represents the amplitude reduction from position 1 to 2 in the form of fraction. In the real application, usually, the resolution in y is set to the desired level, and the resolution in the amplitude measurement or the accuracy of β is governed by the noise level in the measurements. Therefore, in order for the change in $|U|$ to be large enough so that it can be accurately measured (i.e. $\beta \geq \beta_{\text{set}}$) over the change in the product elevation within Δy_{set}, the attenuation level of the selected Lamb mode must reach a certain level calculated by Equation (6.8) (see details in Appendix A.5.2) as

$$\alpha \geq \frac{1}{\Delta y_{\text{set}}} \ln\left(\frac{1}{1-\beta_{\text{set}}}\right). \tag{6.9}$$

This inequality indicates that a small change in the elevation of the chemical product can

be detected by using a Lamb wave mode with high attenuation. High attenuation will guarantee that the situation when the decrease in the magnitude spectrum of that Lamb mode cannot be reliably detected because it is in the same order as present noises (this is the case of the pseudo-S0 mode in Section 5.4.1), does not happen. Figure 6.8 shows the plot of required attenuation as a function of a desired level of elevation change detection at different resolutions in amplitude measurement. The plot is normalized by a thickness h of the reactor's wall so that all quantities are dimensionless. Note that, although higher attenuation gives a better detection resolution, a Lamb mode with very high attenuation is not preferred since it will decay too quickly and cannot cover a long-enough range. The entire implementation becomes impractical.

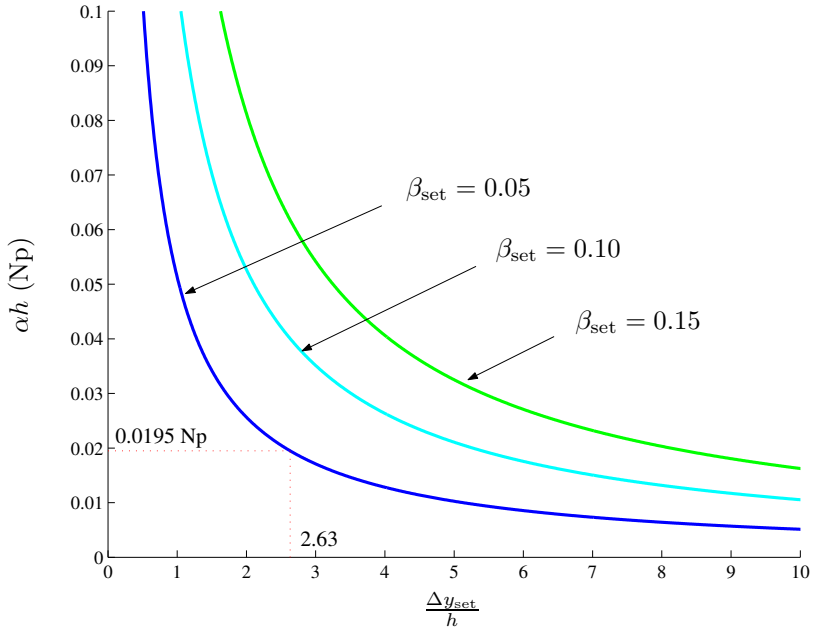

Figure 6.8: Attenuation required to achieve a given resolution Δy_{set} at different β_{set}'s.

In summary, the approach consists of three steps. The first step is to choose the proper Lamb wave mode and frequency for desired measurement resolutions and given test conditions. This step is based on analytical dispersion curves calculated from known properties of the test system. The second step is to measure the magnitude spectrum of the select Lamb mode in the dry condition ($y = 0$) as $|U_{\text{ref}}|$. The last step is in the application during the chemical process. The magnitude spectrum of the select Lamb mode, $|U|$, is monitored

as the elevation of the chemical product increases. That elevation at a specific time can be calculated from Equation (6.7).

6.2.3 Implementation and verification

This approach is verified by the experimental result from Section 5.4.1. A stainless-steel tank of thickness of 0.76 mm and water inside are viewed as a reactor and a chemical product, respectively. Dispersion curves of this system are generated by common material properties given in Figures 6.6 and 6.7 for the propagation and attenuation parts, respectively. To select a proper Lamb mode and frequency, Figure 6.6 is considered. From that figure, since two fundamental modes of Lamb waves are the most easily to be excited and detected from the test configuration, it is suggestive to select the exciting frequency lower than 2 MHz so that only two fundamental modes can propagate. Now, if the resolution of the change in the water elevation, Δy_{set}, is given to be 2 mm ($\frac{\Delta y_{\text{set}}}{h} = 2.63$), the total attenuation required for the select Lamb mode is obtained from Figure 6.8 to be 0.0195 Np, provided that the amplitude measurement can be made accurate within 5%. This total attenuation is equivalent to the attenuation of 25.65 Np/m for the wall thickness of 0.76 mm. It can be seen from Figure 6.7 that, below 2 MHz, only pseudo-A0 mode has sufficiently large attenuation required by the given resolutions. Hence, the pseudo-A0 mode is chosen; the frequency selected is 1.5 MHz since at this frequency, the pseudo-A0 mode will undergo relatively small attenuation and should be well separated from the pseudo-S0 mode in the time domain. The predicted attenuation of the pseudo-A0 mode at this frequency is 41.44 Np/m, which is well beyond the required value.

Next, the reference measurement is made when the water level is below the receiving transducer. The reference time-domain signal is shown as the first signal in Figure 5.16, and the corresponding spectrogram is shown in Figure 5.17(a). The magnitude spectrum of the pseudo-A0 mode is calculated from the square root of the volume under the spectrogram contour in the slowness-frequency region of 0.3–0.4 ms/m and 1–2 MHz. Within a constant multiplicative factor, the extracted $|U_{\text{ref}}|$ is calculated to be 0.3220. During the monitoring process, time-domain signals with different levels of water are recorded; some of them are

shown in Figure 5.16 (for $y \neq 0$). The same process to extract the magnitude spectrum of each time-domain signal is repeated to obtain $|U_i|$. Then, the elevation of water for each recorded signal, y_i is calculated by Equation (6.7). Figure 6.9 shows the calculated y_i's, resulting from all time-domain signals, as solid circles. In the figure, the exact water elevations for all measurements are shown as a solid line.

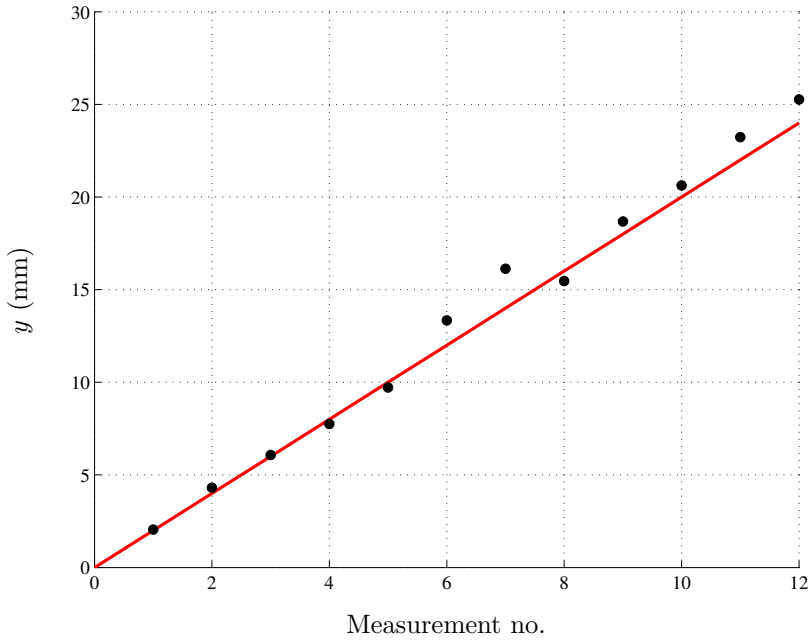

Figure 6.9: Water elevations calculated from attenuation of the pseudo-A0 mode (solid circles) in comparison with the exact values (solid line).

Figure 6.9 shows good agreement between the calculated elevations and their exact values. Small discrepancies are resulted from discrepancy in material properties used in the prediction and measurement errors both in obtaining the exact values and the measurements themselves. However, the overall quality of the results is more than sufficient for the real application because a significant tolerance must be imposed on the measured elevations for safety purposes. The performance of the proposed technique can be improved if the ultrasonic properties of all materials involved (the reactor's wall and the chemical product) can be measured or calibrated before real implementations.

CHAPTER 7

CONCLUSIONS AND RECOMMENDATIONS

This chapter concludes the research presented in this thesis. The chapter is divided into two parts. In the first part consisting of two sections, all work is summarized and concluded; comments and discussions are given. The second part presents related ongoing researches as recommendations for the improvements of the work.

7.1 Summary

This research has developed an entire procedure of Lamb wave attenuation measurement for real applications. Necessary background, including mechanics of wave phenomena, signal processing techniques and laser ultrasonic techniques used in this research, are given in Chapter 2. This research studies characteristics of Lamb waves with attenuation through the analytical model based on the fundamental principles of wave mechanics in Chapter 3. Attention is paid to the special case of leaky Lamb waves when the system is a solid plate loaded with a fluid half-space. Two sets of dispersion curves are successfully obtained through a numerical root-finding technique.

This research also develops a numerical simulation to generate synthetic signals representing transient Lamb waves' surface responses to a normal, point excitation. This simulation imitates the laser ultrasonic system used in the experiment, and provides realistic dispersive time-domain signals. The simulation employs the normal-mode expansion technique to solve the governing wave equations and resolve individual Lamb wave modal responses. The normal-mode expansion technique has twofold advantages. In one, this technique is very efficient, i.e. fast, since its nature is semi-analytical so that multiple repetitive calculations are not required. The current problem is solved analytically to the very end, and only integrations and summations need to be carried out afterwards for the final results. It is important to note that this technique is possible only when the geometry of

the problem is simple. The simple geometry allows for tractable mathematical operations and manipulations. However, this is the case considered in Chapter 4, and it suffices for this research. The second advantage of the normal-mode expansion technique is that it gives the final total response as a summation of individual modal responses of all existing normal modes. These normal modes when properly-chosen constitute a Lamb mode; therefore, a response of a particular Lamb mode can be obtained as a by-product. This benefits the development of attenuation extraction techniques in Chapter 5. Note that this research develops a numerical simulation for a simple case when leakage is not present or a *free-plate* response. Synthetic time-domain signals with attenuation are obtained by the proper additions of the attenuation terms in the solutions. The known attenuation values are obtained from the analytical model in Chapter 3.

The simulation of a free-plate response benefits its verification. A number of aspects of a simulated time-domain signal, such as the velocity of the first-arrival Lamb mode, and relative excitability and dispersive nature of each individual mode, are considered and verified. A simulated signal is finally compared to a real measured signal. In this last verification, the characteristic of a laser excitation is first obtained through a reference system, which is a solid half-space. This choice of a reference system is made since this system is not dispersive or multi-mode, and the analysis to derive its unit-impulse response is well-documented. The real measurement is made on that reference system, and the excitation characteristics of a laser source is calculated through the deconvolution between a measured signal and the unit-impulse response of the system. The calculated excitation characteristics are then used to produce a predicted response of a free plate, which can be compared with a real measurement signal. The comparison shows good agreement in the overall dispersive features and amplitudes, and hence, verifies the simulation.

This research develops attenuation extraction techniques in Chapter 5. The chapter presents the idea of extracting attenuation from two or more time-domain signals, and develops two methods for Lamb wave signals using a spectrogram and multiple bandpass filters. The first method, called the spectrogram method, considers a spectrogram of a time-domain signal to extract the energy of a particular Lamb mode at a specific frequency.

The study shows that a number of reasonable choices for a Lamb mode's magnitude can be used, and all of them lead to acceptable extracted attenuation values. A similar idea is applied in a reversed order in the second method which is called a multi-bandpass-filtering (MBF) method. The MBF method applies a series of simple bandpass filters to time-domain signals to obtain a bandlimited time-domain signal so that the arrivals of existing wave modes of that frequency are clearly seen in the time domain. The amplitude of each wave packet represents the magnitude of the Lamb wave mode at the filter's frequency, and hence, leads to the calculation of attenuation. Those two methods are developed and verified with synthetic single-mode and multi-mode time-domain signals, respectively. The verification results show that the developed techniques work reasonably well when existing modes are reasonably separated and proper constraints are imposed in the algorithm. These developed techniques are then verified with real measurement signals. The attenuation results are in good agreement with the predictions in both narrowband and broadband cases. Some discrepancies are observed when the attenuation values are too low and too high. When attenuation is very small, the change in the magnitude of the wave component of interest needs a long distance to develop. Over a small range used in this research, this attenuation effect is masked by experimental errors and noises. This variation is shown through the goodness of curve-fitting used in the algorithm since the attenuation model cannot explain well the regression of the measured wave magnitudes. On the other end when the attenuation is very large, the measured wave magnitudes are insensitive to attenuation over the propagation distance used in the research. In other words, the measured wave magnitudes over propagation distances can be fitted well with a wide range of attenuation values. So, the extracted value contains a large variation and cannot be regarded as very reliable. However, the discrepancies in both low- and high-attenuation cases are in the acceptable tolerances, and the overall result can be improved when a wider range of propagation distances are used.

Uses of extracted attenuation values in the realistic applications of material characterization and condition monitoring are presented in Chapter 6. This research gives two examples which are applicable in the real practice. The first example is a simple material

characterization of a fluid inside a closed container. This application quantifies the sound wave velocity, which can be related to the bulk stiffness of a fluid, through attenuation of Lamb waves propagating along the container's wall, provided that properties of the container's wall are known. The attenuation of the pseudo-S0 mode in the low frequency is used since it is reliable from the experimental setup in this study. The measured attenuation data are inverted to the sound wave velocity in a fluid by the use of an artificial neural network. This choice of the inversion scheme is made due to the complication of the relationship between attenuation and the sound wave velocity in a fluid, and the inefficiency of the direct curve-fitting scheme. In particular, a simple 2-layer, feedforward neural network is designed and trained to take two parameters from a parametric model representing the measured attenuation data and predict the desired sound wave velocity. The designed network is verified with the extracted attenuation of broadband time-domain signals from Chapter 5. The performance of the designed network is efficient and the network output is in good agreement with the predicted value.

The example of the real application for condition monitoring is given in the case when a fluid level in a closed chemical reactor needs to be monitored. Since the magnitude of a particular Lamb wave mode propagating along the reactor's wall can be measured in a dry condition as a reference, the real-time reduction in the magnitude or attenuation when a chemical product is present inside the reactor can be directly related to the elevation of that product. This example is verified with the narrowband attenuation result from Chapter 5 since only a single attenuation value is sufficient. The verification shows a good exponential decay of the magnitude of the select Lamb wave mode, which matches the analytical prediction, provided that the Lamb wave mode is properly selected for given desire measurement resolutions. A guideline for this selection is also given in the same section.

7.2 Conclusions

In conclusion, Lamb wave propagation with attenuation is studied extensively. A numerical simulation of Lamb wave transient signals measured by a point source/receiver laser system

is developed and verified in a number of aspects. With synthetic signals generated by a simulation, attenuation extraction procedures using the spectrogram and multi-banpass filtering are developed. These developed procedures are made systematic for real measured time-domain signals with critical considerations given. The final procedures are tested with real broadband signals. Finally, to complete a successful NDE process using attenuation of Lamb waves, this research demonstrates the uses of extracted attenuation for realistic applications of material characterization and condition monitoring.

Attenuation information is a critical value for complete material characterization. The success of this research establishes a standard procedure for accurate Lamb wave attenuation measurement and fulfills a need of such a procedure. The obvious improvements of the technique developed in this research over existing techniques are the following. First, the developed technique does not require full access to the test component; only one-sided accessibility is sufficient. Secondly, the developed technique applies to the most general broadband, multi-mode Lamb wave signals. Attenuation information over a reasonably large frequency bandwidth can be accurately measured. Together with the existing conventional techniques, the proposed procedure provides a complementary procedure for attenuation measurements depending system configuration and instrumentation.

7.3 Recommendations for future work

It is seen that the developed attenuation extraction techniques encounter difficulty when two existing Lamb modes propagate with close velocities. Thus, resolving this difficulty will improve the developed attenuation extraction techniques. The idea for such an improvement is to decompose the two existing Lamb modes before extracting attenuation. This decomposition is believed to be possible provided that propagation characteristics of Lamb waves in the system are known. This assumption is reasonable since these propagation characteristics can be obtained through propagation dispersion curves which can be measured effectively by a number of measurements and signal processing techniques as mentioned in Section 1.1. With the known propagation characteristics of existing Lamb waves, their interferences over different propagation distances can be tracked and compensated so that

two modes can be separated. The research on this modal decomposition has been started by the author [57, 58] for "double-mode" Lamb wave signals—time-domain signals containing only two Lamb modes—without attenuation. The details for that work are presented in Appendix E.

From the current state of the research, the future work consists of two directions. On one direction, the work focusing on the modal decomposition techniques should be continued. The already-developed techniques presented in Appendix E should be studied more in depth. For example, appropriate optimization schemes accounting for the phase differences from measurement to measurement should be more studied. The proper scheme suitable for experiments using the laser system should be found. Moreover, the extension of the developed techniques to cover experimental signals with attenuation should be carried out. This extension is thought to involve another level of nonlinear optimization, which will requires a careful treatment in the implementation.

The other direction of the future work should include improvements in the applications of the measured attenuation data. For example, the inversion algorithm which can give more unknown parameters, e.g. density and sound wave velocity of a fluid for the system in Section 6.1, should be developed to strengthen the usefulness of the idea of attenuation measurement. For this specific task, an artificial neural network is still believed to a potential inversion tool since the entire concept remains the same. For the more general applications, the designed network might need to be more complicated—for example, more layers or more neurons in hidden layers than the one used in Section 6.1; more training data and training time should be expected. It is also believed that attenuation of more than one modes must be included to provide a robust inversion for many unknowns. This is tied back to the future work in the other direction, which develops the improvements of modal decomposition techniques.

APPENDIX A

SUPPLEMENTAL DETAILS

This appendix provides mathematical details which are omitted inside the thesis' content. These details are presented in accordance with the chapters they appear in so that the readers should find no difficulty referring back to the contents.

A.1 Chapter 2

A.1.1

Substitution of Equation (2.1) into Equation (2.3) gives

$$\sigma_{ij} = \lambda u_{k,k}\delta_{ij} + \mu(u_{i,j} + u_{j,i}). \tag{A.1}$$

Further substitution of Equation (A.1) into Equation (2.5), together with the symmetry of σ_{ij}, results in

$$\begin{aligned}
[\lambda u_{k,k}\delta_{ij} + \mu(u_{i,j} + u_{j,i})]_{,j} + f_i &= \rho\ddot{u}_i \\
\lambda u_{k,kj}\delta_{ij} + \mu(u_{i,jj} + u_{j,ij}) + f_i &= \rho\ddot{u}_i \\
\lambda u_{k,ki} + \mu(u_{i,jj} + u_{j,ij}) + f_i &= \rho\ddot{u}_i \\
\lambda u_{j,ji} + \mu(u_{i,jj} + u_{j,ij}) + f_i &= \rho\ddot{u}_i \\
(\lambda + \mu)u_{j,ji} + \mu u_{i,jj} + f_i &= \rho\ddot{u}_i.
\end{aligned}$$

A.1.2

Equation (2.9) in the indicial notation is

$$u_i = f(ct - p_k x_k)d_i.$$

Then,

$$\begin{aligned}
\nabla(\nabla \cdot \mathbf{u}) &= u_{j,ji} \\
&= [f(ct - p_k x_k) d_j]_{,ji} \\
&= f''(ct - p_k x_k) d_j p_j p_i \\
&= f''(ct - \mathbf{p} \cdot \mathbf{x})(\mathbf{d} \cdot \mathbf{p})\mathbf{p}
\end{aligned}$$

$$\begin{aligned}
\nabla^2 \mathbf{u} &= u_{i,jj} \\
&= [f(ct - p_k x_k) d_i]_{,jj} \\
&= f''(ct - p_k x_k) d_i p_j p_j \\
&= f''(ct - \mathbf{p} \cdot \mathbf{x})\mathbf{d} \qquad (\mathbf{p} \cdot \mathbf{p} = 1) \\
\ddot{\mathbf{u}} &= c^2 f''(ct - \mathbf{p} \cdot \mathbf{x})\mathbf{d}.
\end{aligned}$$

Hence, Equation (2.7) becomes

$$[(\lambda + \mu)(\mathbf{d} \cdot \mathbf{p})\mathbf{p} + \mu\mathbf{d} - \rho c^2 \mathbf{d}] f''(ct - \mathbf{p} \cdot \mathbf{x}) = 0.$$

A.1.3

From Equation (2.3) with the plane-strain assumption in the y-direction,

$$\begin{aligned}
\sigma_{zz} &= \lambda(u_{x,x} + u_{z,z}) + 2\mu u_{z,z} \\
&= (\lambda + 2\mu)(u_{x,x} + u_{z,z}) - 2\mu u_{x,x} \\
&= \mu \frac{c_L^2}{c_T^2}(u_{x,x} + u_{z,z}) - 2\mu u_{x,x} \\
\sigma_{zx} &= \mu(u_{x,z} + u_{z,x}).
\end{aligned}$$

Then, with displacement fields in Equations (2.21) and (2.22),

Symmetric modes

$$\begin{aligned}
\sigma_{zz}^{(s)} &= \mu\Big\{\frac{c_L^2}{c_T^2}\Big(-jk\big[C_1k\cos(\alpha_Lz)+C_3\alpha_T\cos(\alpha_Tz)\big]+j\big[-C_1\alpha_L^2\cos(\alpha_Lz)+C_3k\alpha_T\cos(\alpha_Tz)\big]\Big)\\
&\qquad +2jk\big[C_1k\cos(\alpha_Lz)+C_3\alpha_T\cos(\alpha_Tz)\big]\Big\}F\\
&= \mu j\Big\{\Big[\frac{c_L^2}{c_T^2}(-k^2-\alpha_L^2)+2k^2\Big]C_1\cos(\alpha_Lz)+2k\alpha_TC_3\cos(\alpha_Tz)\Big\}F\\
&= \mu j\Big\{\Big[\frac{c_L^2}{c_T^2}\Big(-\frac{\omega^2}{c_L^2}\Big)+2k^2\Big]C_1\cos(\alpha_Lz)+2k\alpha_TC_3\cos(\alpha_Tz)\Big\}F\\
&= \mu j\big[-(\alpha_T^2-k^2)C_1\cos(\alpha_Lz)+2k\alpha_TC_3\cos(\alpha_Tz)\big]F.
\end{aligned}$$

$$\begin{aligned}
\sigma_{zx}^{(s)} &= \mu\Big\{\big[-C_1k\alpha_L\sin(\alpha_Lz)-C_3\alpha_T^2\sin(\alpha_Tz)\big]+k\big[-C_1\alpha_L\sin(\alpha_Lz)+C_3k\sin(\alpha_Tz)\big]\Big\}F\\
&= -\mu\big[2k\alpha_LC_1\sin(\alpha_Lz)+(\alpha_T^2-k^2)C_3\sin(\alpha_Tz)\big]F.
\end{aligned}$$

Anti-symmetric modes

$$\begin{aligned}
\sigma_{zz}^{(a)} &= \mu\Big\{\frac{c_L^2}{c_T^2}\Big(-k\big[C_2k\sin(\alpha_Lz)+C_4\alpha_T\sin(\alpha_Tz)\big]+\big[-C_2\alpha_L^2\sin(\alpha_Lz)+C_4k\alpha_T\sin(\alpha_Tz)\big]\Big)\\
&\qquad +2k\big[C_2k\sin(\alpha_Lz)+C_4\alpha_T\sin(\alpha_Tz)\big]\Big\}F\\
&= \mu\Big\{\Big[\frac{c_L^2}{c_T^2}(-k^2-\alpha_L^2)+2k^2\Big]C_2\sin(\alpha_Lz)+2k\alpha_TC_4\sin(\alpha_Tz)\Big\}F\\
&= \mu\Big\{\Big[\frac{c_L^2}{c_T^2}\Big(-\frac{\omega^2}{c_L^2}\Big)+2k^2\Big]C_2\sin(\alpha_Lz)+2k\alpha_TC_4\sin(\alpha_Tz)\Big\}F\\
&= \mu\big[-(\alpha_T^2-k^2)C_2\sin(\alpha_Lz)+2k\alpha_TC_4\sin(\alpha_Tz)\big]F.
\end{aligned}$$

$$\begin{aligned}
\sigma_{zx}^{(a)} &= -\mu j\Big\{\big[C_2k\alpha_L\cos(\alpha_Lz)+C_4\alpha_T^2\cos(\alpha_Tz)\big]+k\big[C_2\alpha_L\cos(\alpha_Lz)-C_4k\cos(\alpha_Tz)\big]\Big\}F\\
&= -\mu j\big[2k\alpha_L\cos(\alpha_Lz)+(\alpha_T^2-k^2)C_4\cos(\alpha_Tz)\big]F.
\end{aligned}$$

A.2 Chapter 3

A.2.1

In Equation (3.27), when all d_{ij}'s are zero, the matrix $\tilde{\mathbf{D}}$ becomes $\mathbf{D}$ such that

$$\mathbf{D}=\begin{bmatrix} D_{11} & D_{12} & D_{13} & D_{14}\\ D_{21} & D_{22} & D_{23} & D_{24}\\ D_{11} & -D_{12} & D_{13} & -D_{14}\\ D_{21} & -D_{22} & D_{23} & -D_{24}\end{bmatrix},$$

where all D_{ij}'s are given in Equation (3.28). By row and column operations,

$$
\begin{aligned}
|\mathbf{D}| &= \begin{vmatrix} 2D_{11} & 0 & 2D_{13} & 0 \\ 2D_{21} & 0 & 2D_{23} & 0 \\ D_{11} & -D_{12} & D_{13} & -D_{14} \\ D_{21} & -D_{22} & D_{23} & -D_{24} \end{vmatrix} \begin{matrix} R_1 + R_3 \\ R_2 + R_4 \\ \\ \end{matrix} \\
&= \begin{vmatrix} 2D_{11} & 0 & 2D_{13} & 0 \\ 2D_{21} & 0 & 2D_{23} & 0 \\ 0 & -D_{12} & 0 & -D_{14} \\ 0 & -D_{22} & 0 & -D_{24} \end{vmatrix} \begin{matrix} \\ \\ R_3 - \frac{R_1}{2} \\ R_4 - \frac{R_2}{2} \end{matrix} \\
&= 4 \begin{vmatrix} D_{11} & 0 & D_{13} & 0 \\ D_{21} & 0 & D_{23} & 0 \\ 0 & D_{12} & 0 & D_{14} \\ 0 & D_{22} & 0 & D_{24} \end{vmatrix} \begin{matrix} \frac{R_1}{2} \\ \frac{R_2}{2} \\ -R_3 \\ -R_4 \end{matrix} \\
&= -4 \begin{vmatrix} D_{11} & D_{13} \\ D_{21} & D_{23} \end{vmatrix} \begin{vmatrix} D_{12} & D_{14} \\ D_{22} & D_{24} \end{vmatrix} \quad \text{(Swap } C_2 \text{ and } C_3\text{)} \\
&= 4R_sR_a,
\end{aligned}
$$

where R_s and R_a are given in Equations (2.26) and (2.28) ($D_{11}D_{23} - D_{21}D_{13} = -jR_s$ and $D_{12}D_{24} - D_{24}D_{14} = -jR_a$).

A.2.2

Consider the quantity

$$
\begin{aligned}
\omega\sqrt{\frac{\rho_f}{\lambda_f + \frac{4}{3}j\omega\eta}} &= \omega\sqrt{\frac{1}{c_f^2 + \frac{4}{3}\frac{j\omega\eta}{\rho_f}}} \\
&= \frac{\omega}{c_f}\sqrt{\frac{1}{1 + \frac{4}{3}\frac{j\omega\eta}{\rho_f c_f^2}}}.
\end{aligned}
$$

By a series expansion

$$
\sqrt{\frac{1}{1+x}} = 1 - \frac{1}{2}x + \ldots,
$$

if the term $\frac{4}{3}\frac{\omega\eta}{\rho_f c_f^2}$ is small compared to unity, the above quantity can be approximated as

$$\omega\sqrt{\frac{\rho_f}{\lambda_f+\frac{4}{3}j\omega\eta}} \approx \frac{\omega}{c_f}\left(1-j\frac{2}{3}\frac{\omega\eta}{\rho_f c_f^2}\right).$$

Hence,

$$-\Im\left\{\omega\sqrt{\frac{\rho_f}{\lambda_f+\frac{4}{3}j\omega\eta}}\right\} \approx \frac{2\omega^2\eta}{3c_f^3\rho_f}.$$

A.2.3

Similar to the expressions in Appendix A.1.3, the stress components in a half-space are

$$\begin{aligned}
\sigma_{zz}^{(hs)} &= \mu'\frac{{c'_L}^2}{{c'_T}^2}(u_{x,x}^{(hs)}+u_{z,z}^{(hs)}) - 2\mu' u_{x,x}^{(hs)} \\
\sigma_{zx}^{(hs)} &= \mu'(u_{x,z}^{(hs)}+u_{z,x}^{(hs)}).
\end{aligned}$$

Hence, with the displacement components given in Equations (3.13) and (3.14), those stress components can be expressed explicitly as

$$\begin{aligned}
\sigma_{zz}^{(hs)} &= \mu'\Bigg\{\frac{{c'_L}^2}{{c'_T}^2}\Big[-jk(kC_5e^{j\alpha'_L z}+\alpha'_T C_6 e^{j\alpha'_T z}) + (-j{\alpha'_L}^2 C_5 e^{j\alpha'_L z} + jk\alpha'_T C_6 e^{j\alpha'_T z})\Big] \\
&\qquad -2(-jk)(kC_5e^{j\alpha'_L z}+\alpha'_T C_6 e^{j\alpha'_T z})\Bigg\}F \\
&= \mu'\Bigg\{j\Big[\frac{{c'_L}^2}{{c'_T}^2}(-k^2-{\alpha'_L}^2)+2k^2\Big]C_5e^{j\alpha'_L z} + j2k\alpha'_T C_6 e^{j\alpha'_T z}\Bigg\}F \\
&= \mu' j\Big[-({\alpha'_T}^2-k^2)C_5e^{j\alpha'_L z} + 2k\alpha'_T C_6 e^{j\alpha'_T z}\Big]F,
\end{aligned}$$

and

$$\begin{aligned}
\sigma_{zx}^{(hs)} &= \mu'\Big[(j\alpha'_L kC_5e^{j\alpha'_L z} + j{\alpha'_T}^2 C_6 e^{j\alpha'_T z}) - jk(-\alpha'_L C_5 e^{j\alpha'_L z} + kC_6 e^{j\alpha'_T z})\Big]F \\
&= \mu' j\Big[2k\alpha'_L C_5 e^{j\alpha'_L z} + ({\alpha'_T}^2-k^2)C_6 e^{jalpha'_T z}\Big]F.
\end{aligned}$$

A.2.4

For the special case when the half-space is an ideal (inviscid) fluid, μ' approaches zero. Consider first d_{31} in Equations (3.29). Rearrange it as

$$\begin{aligned} d_{31} &= \frac{\mu'}{\mu} j \Bigg\{ \frac{{\alpha'_T}^2 - k^2}{k^2 + \alpha'_L \alpha'_T} \big[k^2 \cos(\alpha_L h) - j\alpha_L \alpha'_T \sin(\alpha_L h) \big] \\ &\qquad - \frac{2k\alpha'_T}{k^2 + \alpha'_L \alpha'_T} \big[k\alpha'_L \cos(\alpha_L h) + j\alpha_L k \sin(\alpha_L h) \big] \Bigg\} \\ &= \frac{j}{\mu} \Bigg\{ \frac{\mu'({\alpha'_T}^2 - k^2)}{\frac{k^2}{\alpha'_T} + \alpha'_L} \Big[\frac{k^2}{\alpha'_T} \cos(alpha_L h) - j\alpha_L \sin(\alpha_L h) \Big] \\ &\qquad - \frac{2k\mu'}{\frac{k^2}{\alpha'_T} + \alpha'_L} \big[k\alpha'_L \cos(\alpha_L h) + j\alpha_L k \sin(\alpha_L h) \big] \Bigg\}. \end{aligned} \tag{A.2}$$

Then, from

$$\begin{aligned} \lim_{\mu' \to 0} \mu'({\alpha'_T}^2 - k^2) &= \mu' \Big(\frac{\omega^2}{{c'_T}^2} - 2k^2 \Big) \\ &= \rho'\omega^2 - 2\mu' k^2 \\ &= \rho'\omega^2, \end{aligned}$$

and the fact that $\alpha'_T \to \infty$ as $\mu' \to 0$,

$$\begin{aligned} \lim_{\mu' \to 0} d_{31} &= \lim_{\mu' \to 0} \frac{j}{\mu} \Bigg\{ \frac{\mu'({\alpha'_T}^2 - k^2)}{\frac{k^2}{\alpha'_T} + \alpha'_L} \Big[\frac{k^2}{\alpha'_T} \cos(\alpha_L h) - j\alpha_L \sin(\alpha_L h) \Big] \\ &\qquad - \frac{2k\mu'}{\frac{k^2}{\alpha'_T} + \alpha'_L} \big[k\alpha'_L \cos(\alpha_L h) + j\alpha_L k \sin(\alpha_L h) \big] \Bigg\}. \\ &= \lim_{\mu' \to 0} \frac{j}{\mu} \frac{\mu'({\alpha'_T}^2 - k^2)}{\frac{k^2}{\alpha'_T} + \alpha'_L} \Big[\frac{k^2}{\alpha'_T} \cos(\alpha_L h) - j\alpha_L \sin(\alpha_L h) \Big] \\ &= \frac{\rho'\omega^2}{\mu\alpha'_L} \alpha_L \sin(\alpha_L h). \end{aligned}$$

Similar rearrangements and limiting processes yield the similar results for d_{32}, d_{33} and d_{34}:

$$\begin{aligned} \lim_{\mu' \to 0} d_{32} &= -j \frac{\rho'\omega^2}{\mu\alpha'_L} \alpha_L \cos(\alpha_L h), \\ \lim_{\mu' \to 0} d_{33} &= -\frac{\rho'\omega^2}{\mu\alpha'_L} k \sin(\alpha_T h), \\ \lim_{\mu' \to 0} d_{34} &= j \frac{\rho'\omega^2}{\mu\alpha'_L} k \cos(\alpha_T h). \end{aligned}$$

The limits of d_{4j}'s are obviously zero as $\mu' \to 0$.

A.2.5

Start from the matrix

$$\tilde{\mathbf{D}} = \begin{bmatrix} D_{11} & D_{12} & D_{13} & D_{14} \\ D_{21} & D_{22} & D_{23} & D_{24} \\ D_{11}+d_{31} & -D_{12}+d_{32} & D_{13}+d_{33} & -D_{14}+d_{34} \\ D_{21} & -D_{22} & D_{23} & -D_{24} \end{bmatrix}.$$

Then, following the same row operations as in Appendix A.2.1, one obtains

$$\begin{aligned}
|\tilde{\mathbf{D}}| &= -4 \begin{vmatrix} D_{11}+\frac{d_{31}}{2} & D_{13}+\frac{d_{33}}{2} & \frac{d_{32}}{2} & \frac{d_{34}}{2} \\ D_{21} & D_{23} & 0 & 0 \\ -\frac{d_{31}}{2} & -\frac{d_{33}}{2} & D_{12}-\frac{d_{32}}{2} & D_{14}-\frac{d_{34}}{2} \\ 0 & 0 & D_{22} & D_{24} \end{vmatrix} \\
&= -4\Bigg\{ \Big(D_{11}+\frac{d_{31}}{2}\Big)\Big[D_{23}\Big(D_{12}-\frac{d_{32}}{2}\Big)D_{24} - D_{23}\Big(D_{14}-\frac{d_{34}}{2}\Big)D_{22}\Big] \\
&\quad -\Big(D_{13}+\frac{d_{33}}{2}\Big)\Big[D_{21}\Big(D_{12}-\frac{d_{32}}{2}\Big)D_{24} - D_{21}\Big(D_{14}-\frac{d_{34}}{2}\Big)D_{22}\Big] \\
&\quad +\frac{d_{32}}{2}\Big[D_{21}\Big(-\frac{d_{33}}{2}\Big)D_{24} - D_{23}\Big(-\frac{d_{31}}{2}\Big)D_{24}\Big] \\
&\quad -\frac{d_{34}}{2}\Big[D_{21}\Big(-\frac{d_{33}}{2}\Big)D_{22} - D_{23}\Big(-\frac{d_{31}}{2}\Big)D_{22}\Big]\Bigg\} \\
&= -4\Big[D_{11}D_{23}(D_{12}D_{24}-D_{22}D_{14}) - D_{21}D_{13}(D_{12}D_{24}-D_{22}D_{14}) \\
&\quad +\frac{d_{31}}{2}D_{23}(D_{12}D_{24}-D_{22}D_{14}) - \frac{d_{33}}{2}D_{21}(D_{12}D_{24}-D_{22}D_{14}) \\
&\quad -\frac{d_{32}}{2}D_{24}(D_{11}D_{23}-D_{21}D_{13}) + \frac{d_{34}}{2}D_{22}(D_{11}D_{23}-D_{21}D_{13})\Big] \\
&= -4(D_{11}D_{23}-D_{21}D_{13})(D_{12}D_{24}-D_{22}D_{14}) \\
&\quad -2(D_{12}D_{24}-D_{22}D_{14})(D_{23}d_{31}-D_{21}d_{33}) \\
&\quad -2(D_{11}D_{23}-D_{21}D_{13})(D_{22}d_{34}-D_{24}d_{32}).
\end{aligned}$$

From D_{ij}'s and d_{ij}'s given in Equations (3.28) and (3.45),

$$\begin{aligned}
D_{23}d_{31} - D_{21}d_{33} &= (\alpha_T^2 - k^2)\sin(\alpha_T h)\Big[\frac{\rho'}{\rho}\frac{\omega^2}{c_T^2}\frac{\alpha_L}{\alpha'_L}\sin(\alpha_L h)\Big] \\
&\qquad -2k\alpha_L \sin(\alpha_L h)\Big[-\frac{\rho'}{\rho}\frac{\omega^2}{c_T^2}\frac{k}{\alpha'_L}\sin(\alpha_T h)\Big] \\
&= \frac{\rho'}{\rho}\frac{\omega^4}{c_T^4}\frac{\alpha_L}{\alpha'_L}\sin(\alpha_L h)\sin(\alpha_T h) \\
D_{22}d_{34} - D_{24}d_{32} &= 2jk\alpha_L\cos(\alpha_L h)\Big[j\frac{\rho'}{\rho}\frac{\omega^2}{c_T^2}\frac{k}{\alpha'_L}\cos(\alpha_T h)\Big] \\
&\qquad -j(\alpha_T^2 - k^2)\cos(\alpha_T h)\Big[-j\frac{\rho'}{\rho}\frac{\omega^2}{c_T^2}\frac{\alpha_L}{\alpha'_L}\cos(\alpha_L h)\Big] \\
&= -\frac{\rho'}{\rho}\frac{\omega^4}{c_T^4}\frac{\alpha_L}{\alpha'_L}\cos(\alpha_L h)\cos(\alpha_T h).
\end{aligned}$$

With $D_{11}D_{23} - D_{21}D_{13} = -jR_s$, and $D_{12}D_{24} - D_{24}D_{14} = -jR_a$,

$$|\tilde{\mathbf{D}}| = 4R_sR_a - 2j\frac{\rho'}{\rho}\frac{\omega^4}{c_T^4}\frac{\alpha_L}{\alpha'_L}\big[R_s\cos(\alpha_L h)\cos(\alpha_T h) - R_a\sin(\alpha_L h)\sin(\alpha_T h)\big].$$

A.2.6

With Equations (3.48) and (3.49), Equation (3.46) can be written in terms of real quantities as

$$\begin{aligned}
D(\omega,k) &= R_sR_a - j\frac{1}{2}\frac{\rho'}{\rho}\frac{\omega^4}{c_T^4}\frac{\alpha_L}{\alpha'_L}\big[R_s\cos(\alpha_L h)\cos(\alpha_T h) - R_a\sin(\alpha_L h)\sin(\alpha_T h)\big] \\
&= -\bar{R}_s\bar{R}_a - j\frac{1}{2}\frac{\rho'}{\rho}\frac{\omega^4}{c_T^4}\frac{\bar{\alpha}_L}{\bar{\alpha}'_L}\Big\{-j\bar{R}_s\cosh(\bar{\alpha}_L h)\cosh(\bar{\alpha}_T h) \\
&\qquad -(-j\bar{R}_a)\big[-j\sinh(\bar{\alpha}_L h)\big]\big[-j\sinh(\bar{\alpha}_T h)\big]\Big\} \\
&= -\bar{R}_s\bar{R}_a - \frac{1}{2}\frac{\rho'}{\rho}\frac{\omega^4}{c_T^4}\frac{\bar{\alpha}_L}{\bar{\alpha}'_L}\big[\bar{R}_s\cosh(\bar{\alpha}_L h)\cosh(\bar{\alpha}_T h) + \bar{R}_a\sinh(\bar{\alpha}_L h)\sinh(\bar{\alpha}_T h)\big].
\end{aligned}$$

Then, defining $\bar{D}(\omega,k) = -D(\omega,k)$, one finds that the equation $D(\omega,k) = 0$ is equivalent to

$$\bar{D}(\omega,k) \equiv \bar{R}_s\bar{R}_a + \frac{1}{2}\frac{\rho'}{\rho}\frac{\omega^4}{c_T^4}\frac{\bar{\alpha}_L}{\bar{\alpha}'_L}\big[\bar{R}_s\cosh(\bar{\alpha}_L h)\cosh(\bar{\alpha}_T h) + \bar{R}_a\sinh(\bar{\alpha}_L h)\sinh(\bar{\alpha}_T h)\big] = 0.$$

A.3 Chapter 4

A.3.1

Consider the surface traction vector, $\mathbf{t}$. For an isotropic material, one can use Equations (2.1) and (2.3) to obtain this traction as

$$\begin{aligned} t_i &= \big(\lambda\varepsilon_{kk}\delta_{ij} + 2\mu\varepsilon_{ij}\big)n_j \\ &= \big[\lambda u_{k,k}\delta_{ij} + \mu(u_{i,j} + u_{j,i})\big]n_j \\ &= \lambda u_{k,k}n_i + \mu(u_{i,j} + u_{j,i})n_j. \end{aligned}$$

With the identities: $u_{k,k} = \nabla\mathbf{u}$ and $\big[\nabla\mathbf{u} + (\nabla\mathbf{u})^T\big]_{ij} = u_{j,i} + u_{i,j}$, the above equations for traction can be written in the vector format as

$$\mathbf{t} = \lambda(\nabla\cdot\mathbf{u})\mathbf{n} + \mu\big[\nabla\mathbf{u} + (\nabla\mathbf{u})^T\big]\mathbf{n}.$$

A.3.2

The Leibniz integral rule for differentiation under the integral sign states that

$$\frac{d}{dt}\int_{x=a(t)}^{b(t)} F(x,t)\,dx = \int_{a(t)}^{b(t)} \frac{\partial}{\partial t}F(x,t)\,dx + \frac{db(t)}{dt}F(b(t),t) - \frac{da(t)}{dt}F(a(t),t),$$

provided that both $F(x,t)$ and $\frac{\partial}{\partial t}F(x,t)$ are continuous over the domain of integration. When a and b are independent of t, this rule allows the differentiation and integration to be directly reordered:

$$\frac{d}{dt}\int_a^b F(x,t)\,dx = \int_a^b \frac{\partial}{\partial t}F(x,t)\,dx.$$

Now consider the inner-product defined in Equation (4.14). Assuming that the change in the domain V over time is negligible, one can apply the above Leibniz rule for constant a

and b to $\langle \ddot{\mathbf{w}}(\mathbf{x},\tau), \mathbf{u}_m(\mathbf{x})\rangle$ to obtain

$$\begin{aligned}
\langle \ddot{\mathbf{w}}(\mathbf{x},\tau), \mathbf{u}_m(\mathbf{x})\rangle &= \int_V \frac{\partial^2}{\partial\tau^2}\mathbf{w}(\mathbf{x},\tau)\cdot\mathbf{u}_m(\mathbf{x})\,dV \\
&= \int_V \left[\frac{\partial}{\partial\tau}\Big(\frac{\partial}{\partial\tau}\mathbf{w}(\mathbf{x},\tau)\cdot\mathbf{u}_m(\mathbf{x})\Big) - \frac{\partial}{\partial\tau}\mathbf{w}(\mathbf{x},\tau)\cdot\frac{\partial}{\partial\tau}\mathbf{u}_m(\mathbf{x})\right] dV \\
&= \int_V \frac{\partial}{\partial\tau}\Big(\frac{\partial}{\partial\tau}\mathbf{w}(\mathbf{x},\tau)\cdot\mathbf{u}_m(\mathbf{x})\Big)\,dV \\
&= \int_V \frac{\partial}{\partial\tau}\Big[\frac{\partial}{\partial\tau}\big(\mathbf{w}(\mathbf{x},\tau)\cdot\mathbf{u}_m(\mathbf{x})\big) - \mathbf{w}(\mathbf{x},\tau)\cdot\frac{\partial}{\partial\tau}\mathbf{u}_m(\mathbf{x})\Big]\,dV \\
&= \int_V \frac{\partial^2}{\partial\tau^2}\Big(\mathbf{w}(\mathbf{x},\tau)\cdot\mathbf{u}_m(\mathbf{x})\Big)\,dV \\
&= \frac{\partial^2}{\partial\tau^2}\int_V \mathbf{w}(\mathbf{x},\tau)\cdot\mathbf{u}_m(\mathbf{x})\,dV \\
&= \frac{\partial^2}{\partial\tau^2}\langle \mathbf{w}(\mathbf{x},\tau), \mathbf{u}_m(\mathbf{x})\rangle.
\end{aligned}$$

Note that the above derivation employs the property $\frac{\partial \mathbf{u}_m}{\partial\tau} = 0$ since $\mathbf{u}_m$ depends only on $\mathbf{x}$.

A.3.3

From Equation (4.32), integration by parts gives

$$\begin{aligned}
q'_m(t) &= -\frac{1}{\omega_m M_{mm}}\int_{\tau=0}^{\tau=t}\Big(\sin\big[\omega_m(t-\tau)\big]\Big)\,d\Big(\frac{\partial}{\partial\tau}\langle \mathbf{w}(\mathbf{x},\tau), \mathbf{u}_m(\mathbf{x})\rangle\Big) \\
&= -\frac{1}{\omega_m M_{mm}}\Big\{\frac{\partial}{\partial\tau}\langle \mathbf{w}(\mathbf{x},\tau), \mathbf{u}_m(\mathbf{x})\rangle \sin\big[\omega_m(t-\tau)\big]\Big|_0^t \\
&\qquad +\omega_m\int_0^t \frac{\partial}{\partial\tau}\langle \mathbf{w}(\mathbf{x},\tau), \mathbf{u}_m(\mathbf{x})\rangle \cos\big[\omega_m(t-\tau)\big]\,d\tau\Big\} \\
&= -\frac{1}{M_{mm}}\int_{\tau=0}^{\tau=t}\Big(\cos\big[\omega_m(t-\tau)\big]\Big)\,d\Big(\langle \mathbf{w}(\mathbf{x},\tau), \mathbf{u}_m(\mathbf{x})\rangle\Big),
\end{aligned}$$

where the zero initial condition $\dot{\mathbf{w}}(\mathbf{x},0) = 0$ is assumed. Integration by parts of the last equation, together with zero initial condition $\mathbf{w}(\mathbf{x},0) = 0$, results in

$$\begin{aligned}
q'_m(t) &= -\frac{1}{M_{mm}}\Big\{\langle \mathbf{w}(\mathbf{x},\tau), \mathbf{u}_m(\mathbf{x})\rangle \cos\big[\omega_m(t-\tau)\big]\Big|_0^t \\
&\qquad -\omega_m\int_0^t \langle \mathbf{w}(\mathbf{x},\tau), \mathbf{u}_m(\mathbf{x})\rangle \sin\big[\omega_m(t-\tau)\big]\,d\tau\Big\} \\
&= -\frac{\langle \mathbf{w}(\mathbf{x},t), \mathbf{u}_m(\mathbf{x})\rangle}{M_{mm}} + \frac{\omega_m}{M_{mm}}\int_0^t \langle \mathbf{w}(\mathbf{x},\tau), \mathbf{u}_m(\mathbf{x})\rangle \sin\big[\omega_m(t-\tau)\big]\,d\tau.
\end{aligned}$$

A.3.4

Start with the potentials ϕ_{mn} and ψ_{mn} in terms of f_{mn} and g_{mn} from Equations (4.64):

$$\begin{aligned}\phi(r,z) &= f(z)J_0(kr)\\ \psi(r,z) &= g(z)J_1(kr),\end{aligned}$$

where the indices mn are dropped for brevity. With the use of the identities in Equations (4.65), Equations (4.56) and (4.57) give the displacement

$$\begin{aligned}u &= \frac{\partial\phi}{\partial r}-\frac{\partial\psi}{\partial z}\\ &= kf(z)J_0'(kr)-g'(z)J_1(kr)\\ &= -\big[kf(z)+g'(z)\big]J_1(kr)\\ w &= \frac{\partial\phi}{\partial z}+\frac{\partial\psi}{\partial r}+\frac{\psi}{r}\\ &= f'(z)J_0(kr)+kg(z)J_1'(kr)+\frac{g(z)J_1(kr)}{r}\\ &= f'(z)J_0(kr)+kg(z)\Big[J_0(kr)-\frac{J_1(kr)}{kr}\Big]+\frac{g(z)J_1(kr)}{r}\\ &= \big[f'(z)+kg(z)\big]J_0(k\,r).\end{aligned}$$

These u and w are substituted into Equations (4.61) and (4.62) to obtain

$$\begin{aligned}\sigma_{zz} &= \mu\Big[\frac{c_L^2}{c_T^2}\Big(\frac{\partial u}{\partial r}+\frac{u}{r}+\frac{\partial w}{\partial z}\Big)-2\Big(\frac{\partial u}{\partial r}+\frac{u}{r}\Big)\Big]\\ &= \mu\Big\{\frac{c_L^2}{c_T^2}\Big(-\big[kf(z)+g'(z)\big]k\Big[J_0(kr)-\frac{J_1(kr)}{kr}\Big]-\frac{\big[kf(z)+g'(z)\big]J_1(kr)}{r}\\ &\qquad +\big[f''(z)+kg'(z)\big]J_0(kr)\Big)-2\Big(-\big[kf(z)+g'(z)\big]k\Big[J_0(kr)-\frac{J_1(kr)}{kr}\Big]\\ &\qquad -\frac{\big[kf(z)+g'(z)\big]J_1(k\,r)}{r}\Big)\Big\}\\ &= \mu\Big(\frac{c_L^2}{c_T^2}\big[-k^2f(z)+f''(z)\big]J_0(kr)+2\big[k^2f(z)+kg'(z)\big]J_0(kr)\Big)\\ &= \mu\big[-(\alpha_T^2-k^2)f(z)+2kg'(z)\big]J_0(kr)\\ \sigma_{zr} &= \mu\Big(\frac{\partial u}{\partial z}+\frac{\partial w}{\partial r}\Big)\\ &= \mu\Big(-\big[kf'(z)+g''(z)\big]J_1(kr)-\big[f'(z)+kg(z)\big]kJ_1(kr)\Big)\\ &= -\mu\Big(2kf'(z)+\big[g''(z)+k^2g(z)\big]\Big)J_1(kr)\\ &= \mu\big[-2kf'(z)+(\alpha_T^2-k^2)g(z)\big]J_1(kr),\end{aligned}$$

where the properties $f''(z) = -\alpha_L^2 f(z)$ and $g''(z) = -\alpha_T^2 g(z)$ are employed. Note that the first property results in the identity:

$$\frac{c_L^2}{c_T^2}\big[-k^2 f(z) + f''(z)\big] = -\frac{\omega^2}{c_T^2} f(z).$$

A.3.5

Define a parameter t (not a time variable) as

$$t = \frac{r}{R}.$$

Then,

$$\begin{aligned}\int_0^R J_\nu^2(k_{mn}r) r\, dr &= R^2 \int_0^1 t J_\nu^2(k_{mn}Rt)\, dt \\ &= R^2 \int_0^1 t J_\nu^2(\alpha_n t)\, dt,\end{aligned}$$

where the parameter $\alpha_n = k_{mn}R$ satisfies the equation

$$J_1(\alpha_n) = 0.$$

Equivalently, with the identity in Equations (4.65), this parameter α_n satisfies the equation

$$J_0'(\alpha_n) = 0,$$

where the prime $'$ represents the derivative with respect to the argument.

Using the formula in Section 11.4.5 of Reference [1]:

$$\int_0^1 J_\nu(\alpha_m t) J_\nu(\alpha_n t) = \begin{cases} 0 & \text{for } m \neq n \text{ and } \nu > -1 \\ \frac{1}{2}\big[J_\nu'(\alpha_n)\big]^2 & \text{for } m = n,\ b = 0 \text{ and } \nu > -1 \\ \frac{1}{2\alpha_n^2}\left(\frac{a^2}{b^2} + \alpha_n^2 - \nu^2\right)\big[J_\nu'(\alpha_n)\big]^2 & \text{for } m = n,\ b \neq 0 \text{ and } \nu \geq -1, \end{cases}$$

where α_1, α_2, ... are the positive zeros of the equation $aJ_\nu(x) + bx\, J_\nu'(x) = 0$; a and b are real constants, one can obtain the results for the original integrals:

- $(a = 1,\ b = 0,\ \nu = 1)$

$$R^2 \int_0^1 t J_1^2(\alpha_n t)\, dt = \frac{R^2}{2}\big[J_1'(\alpha_n)\big]^2 = \frac{R^2}{2}\big[J_1'(k_{mn}R)\big]^2.$$

- $(a = 0,\ b = 1,\ \nu = 0)$

$$R^2 \int_0^1 t J_0^2(\alpha_n t)\, dt = \frac{R^2}{2}\big[J_0(\alpha_n)\big]^2 = \frac{R^2}{2}\big[J_0(k_{mn}R)\big]^2.$$

A.3.6

Consider the sum-square error

$$\mathcal{E} = \sum_{n=0}^{N+M-2} \Big(y[n] - \sum_{m=0}^{M-1} a[n,m]x[m] \Big)^2.$$

Differentiation of $\mathcal{E}$ with respect to each of $x[l]$'s gives

$$-2 \sum_{n=0}^{N+M-2} \Big[\Big(y[n] - \sum_{m=0}^{M-1} a[n,m]x[m] \Big) a[n,l] \Big].$$

Hence, the equation $\frac{\partial \mathcal{E}}{\partial x[l]} = 0$ leads to

$$\begin{aligned}
\sum_{n=0}^{N+M-2} \Big[\Big(y[n] - \sum_{m=0}^{M-1} a[n,m]x[m] \Big) a[n,l] \Big] &= 0 \\
\sum_{n=0}^{N+M-2} y[n]a[n,l] - \sum_{n=0}^{N+M-2} \sum_{m=0}^{M-1} a[n,m]x[m]a[n,l] &= 0 \\
\sum_{n=0}^{N+M-2} y[n]a[n,l] - \sum_{m=0}^{M-1} \Big(x[m] \sum_{n=0}^{N+M-2} a[n,m]a[n,l] \Big) &= 0,
\end{aligned}$$

for $l = 0, 1, \ldots, M-1$.

A.4 Chapter 5

A.4.1

Equations (5.4) can be written explicitly as

$$\begin{aligned}
|U_1(x_1,\omega)| &= |F_1(x_1,\omega)||Q(\omega)|e^{-\alpha(\omega)x_1} \\
|U_2(x_2,\omega)| &= |F_2(x_2,\omega)||Q(\omega)|e^{-\alpha(\omega)x_2}.
\end{aligned}$$

The division of these two equations gives

$$\begin{aligned}
\frac{|U_1(x_1,\omega)|}{|U_2(x_2,\omega)|} &= \frac{|F_1(x_1,\omega)|}{|F_2(x_2,\omega)|} e^{\alpha(\omega)(x_2-x_1)} \\
\frac{|U_1(x_1,\omega)|}{|U_2(x_2,\omega)|} \frac{|F_2(x_2,\omega)|}{|F_1(x_1,\omega)|} &= e^{\alpha(\omega)(x_2-x_1)}.
\end{aligned}$$

Thus, by taking the natural logarithm on both sides of the above equation, one can obtain

$$\alpha(\omega) = \frac{1}{x_2 - x_1} \ln \left(\frac{|U_1(x_1,\omega)|}{|U_2(x_2,\omega)|} \frac{|F_2(x_2,\omega)|}{|F_1(x_1,\omega)|} \right).$$

A.4.2

Let y_i and $\hat{y}_i$ be the measured and the estimated values of $\ln|\tilde{U}_i|$, respectively. Also, let b_1 and b_0 be $-\alpha$ and $\ln|Q|$, respectively. Then, Equation (5.12) suggests the linear relationship

$$\hat{y}_i = b_1 x_i + b_0,$$

and the sum-square error in Equation (5.12) can be written as

$$\hat{\mathcal{E}} = \sum_{i=1}^{N} (y_i - \hat{y}_i)^2.$$

The function $\hat{\mathcal{E}}$ can be minimized with respect to b_1 and b_0 by setting both of its partial derivatives to zero, i.e.

$$\begin{aligned} \frac{\partial \hat{\mathcal{E}}}{\partial b_1} = -2 \sum (y_i - \hat{y}_i) x_i &= 0 \\ \frac{\partial \hat{\mathcal{E}}}{\partial b_0} = -2 \sum (y_i - \hat{y}_i) &= 0, \end{aligned}$$

where the summation is taken from $i = 1$ to N. With a linear model presented at the beginning of this section, the above two equations give a linear system of two equations governing b_1 and b_0 as

$$\begin{aligned} \sum x_i y_i - b_1 \sum x_i^2 - b_0 \sum x_i &= 0 \\ \sum y_i - b_1 \sum x_i - b_0 N &= 0. \end{aligned}$$

In the matrix form, this system of equations can be written as

$$\begin{bmatrix} \sum x_i^2 & \sum x_i \\ \sum x_i & N \end{bmatrix} \begin{Bmatrix} b_1 \\ b_0 \end{Bmatrix} = \begin{Bmatrix} \sum x_i y_i \\ \sum y_i \end{Bmatrix}. \tag{A.3}$$

Then, the parameters b_1 and b_0 can be determined by the direct inversion

$$\begin{Bmatrix} b_1 \\ b_0 \end{Bmatrix} = \begin{bmatrix} \sum x_i^2 & \sum x_i \\ \sum x_i & N \end{bmatrix}^{-1} \begin{Bmatrix} \sum x_i y_i \\ \sum y_i \end{Bmatrix}.$$

A.5 Chapter 6

A.5.1

For two measurements at y_1 and y_2, Equation (6.7) gives two relationships:

$$\begin{aligned} y_1 &= \frac{1}{\alpha}\ln\left(\frac{|U_{\text{ref}}|}{|U_1|}\right) \\ y_2 &= \frac{1}{\alpha}\ln\left(\frac{|U_{\text{ref}}|}{|U_2|}\right). \end{aligned}$$

Subtraction of these two equations eliminates $|U_{\text{ref}}|$; the remaining gives the relationship between the change in y and the change in $|U|$ as

$$y_2 - y_1 = \frac{1}{\alpha}\ln\left(\frac{|U_1|}{|U_2|}\right).$$

For $y_2 > y_1$, let $\Delta y = y_2 - y_1$ and let $|U_2|$ be written in terms of the reduction of $|U_1|$ as $|U_2| = (1-\beta)|U_1|$; then the above equation becomes

$$\Delta y = \frac{1}{\alpha}\ln\left(\frac{1}{1-\beta}\right).$$

A.5.2

From Equation (6.8),

$$\begin{aligned} e^{\alpha\Delta y} &= \frac{1}{1-\beta} \\ \beta &= 1 - e^{-\alpha\Delta y}. \end{aligned}$$

If Δy is set to Δy_{set} and β is greater than β_{set}, the above equation requires the condition

$$\begin{aligned} 1 - e^{-\alpha\Delta y_{\text{set}}} &\geq \beta_{\text{set}} \\ e^{-\alpha\Delta y_{\text{set}}} &\leq 1 - \beta_{\text{set}} \\ e^{\alpha\Delta y_{\text{set}}} &\geq \frac{1}{1-\beta_{\text{set}}} \\ \alpha &\geq \frac{1}{\Delta y_{\text{set}}}\ln\left(\frac{1}{1-\beta_{\text{set}}}\right). \end{aligned}$$

A.6 Appendix D

A.6.1

Consider the integral

$$I = \int_0^\infty r\left[\frac{d^2 f(r)}{dr^2} + \frac{1}{r}\frac{df(r)}{dr}\right] J_\nu(kr)\, dr.$$

Integration by parts of the first term with $U = rJ_\nu(kr)$ and $dV = \frac{d^2f(r)}{dr^2}\,dr$ gives

$$\begin{aligned} I &= rJ_\nu(kr)\frac{df(r)}{dr}\bigg|_0^\infty - \int_0^\infty \frac{df(r)}{dr}\big[J_\nu(kr) + krJ'_\nu(kr)\big]\,dr \\ &\quad + \int_0^\infty \frac{df(r)}{dr}J_\nu(kr)\,dr \\ &= -k\int_0^\infty r\frac{df(r)}{dr}J'_\nu(kr)\,dr, \end{aligned}$$

where the condition $rJ_\nu(kr)\frac{df(r)}{dr} \to 0$ as $r \to \infty$ is assumed, the $'$ denotes the derivative with the entire argument. Another integration by parts of the above equation with $U = rJ'_\nu(kr)$ and $dV = \frac{df(r)}{dr}\,dr$ results in

$$\begin{aligned} I &= -krJ'_\nu(kr)f(r)\bigg|_0^\infty + k\int_0^\infty f(r)\big[J'_\nu(kr) + krJ''_\nu(kr)\big]\,dr \\ &= \frac{1}{r}\int_0^\infty f(r)\big[(kr)J'_\nu(kr) + (kr)^2J''_\nu(kr)\big]\,dr \\ &= -\frac{1}{r}\int_0^\infty f(r)[(kr)^2 - \nu^2]J_\nu(kr)\,dr, \end{aligned}$$

where, again, the condition $rJ'_\nu(kr)f(r) \to 0$ as $r \to \infty$ is assumed, and the property of the Bessel function that $x^2J''_\nu(x) + xJ'_\nu(x) + (x^2 - \nu^2)J_\nu(x) = 0$ is used.

Hence,

$$\begin{aligned} \int_0^\infty r\left[\frac{d^2f(r)}{dr^2} + \frac{1}{r}\frac{df(r)}{dr} - \frac{\nu^2}{r^2}f(r)\right]J_\nu(kr)\,dr &= -\frac{1}{r}\int_0^\infty f(r)[(kr)^2 - \nu^2]J_\nu(kr)\,dr \\ &\quad - \int_0^\infty \frac{\nu^2}{r}f(r)J_\nu(kr)\,dr \\ &= -k^2\tilde{f}^{(\nu)}(k). \end{aligned}$$

A.6.2

Let a function $f(r)$ have its Hankel transform of order 0 and a function $g(r)$ have its Hankel transform of order 1.

Then, by integration by parts with vanishing property at $r \to \infty$ of f,

$$\begin{aligned}
\mathcal{H}_1\{f'(r)\} &= \int_0^\infty r f'(r) J_1(kr)\, dr \\
&= -\int_0^\infty f(r) \frac{d}{dr}\big[r J_1(kr)\big]\, dr \\
&= -\int_0^\infty f(r) \frac{d}{d(kr)}\big[(kr) J_1(kr)\big]\, dr \\
&= -\int_0^\infty f(r)\, k\, r\, J_0(k\, r)\, dr \\
&= -k\tilde{f}^{(0)}(k).
\end{aligned}$$

Similarly for g,

$$\begin{aligned}
\mathcal{H}_0\Big\{g'(r) + \frac{g(r)}{r}\Big\} &= \int_0^\infty r\Big[g'(r) + \frac{g(r)}{r}\Big] J_0(kr)\, dr \\
&= -\int_0^\infty g(r) \frac{d}{dr}\big[r J_0(kr)\big]\, dr + \int_0^\infty g(r) J_0(kr)\, dr \\
&= k\int_0^\infty g(r) r J_1(kr)\, dr \\
&= k\tilde{g}^{(1)}(k).
\end{aligned}$$

A.6.3

Consider the function

$$f(r) = \begin{cases} 1, & r \le a \\ 0, & r > a. \end{cases} \tag{A.4}$$

Its Hankel transform of order 0 is

$$\begin{aligned}
\tilde{f}^{(0)}(k) &= \int_0^\infty r f(r) J_0(kr)\, dr \\
&= \int_0^a r J_0(kr)\, dr.
\end{aligned}$$

Let $x = kr$. With the use of the identity in the second of Equations (4.65):

$$\frac{d}{dx}\big[x J_1(x)\big] = x J_0(x),$$

the Hankel transform of $f(r)$ is

$$\begin{aligned}
\tilde{f}^{(0)}(k) &= \int_0^a rJ_0(kr)\,dr \\
&= \int_0^{ka} \frac{x}{k}\frac{1}{x}\frac{d}{dx}\Big[xJ_1(x)\Big]\frac{1}{k}\,dx \\
&= \frac{1}{k^2}\int_0^{ka} \frac{d}{dx}\Big[xJ_1(x)\Big]\,dx \\
&= \frac{1}{k^2}xJ_1(x)\Big|_0^{ka} \\
&= \frac{aJ_1(ka)}{k}.
\end{aligned}$$

A.6.4

Consider the matrix equation of the form

$$\begin{bmatrix} D_{11} & D_{12} & D_{13} & D_{14} \\ D_{21} & D_{22} & D_{23} & D_{24} \\ D_{11} & D_{12} & -D_{13} & -D_{14} \\ -D_{21} & -D_{22} & D_{23} & D_{24} \end{bmatrix} \begin{Bmatrix} A_1 \\ B_2 \\ A_2 \\ B_1 \end{Bmatrix} = \begin{Bmatrix} 1 \\ 0 \\ 0 \\ 0 \end{Bmatrix}.$$

This equation can be split into two sub-equations by the combination of addition and subtraction between the first and third rows (R_1 and R_3, respectively) and the second and fourth rows (R_2 and R_4, respectively). The combination of $R_1 + R_3$ and $R_2 - R_4$ results in

$$\begin{bmatrix} 2D_{11} & 2D_{12} \\ 2D_{21} & 2D_{22} \end{bmatrix} \begin{Bmatrix} A_1 \\ B_2 \end{Bmatrix} = \begin{Bmatrix} 1 \\ 0 \end{Bmatrix}.$$

Similarly, the combination of $R_1 - R_3$ and $R_2 + R_4$ gives

$$\begin{bmatrix} 2D_{13} & 2D_{14} \\ 2D_{23} & 2D_{24} \end{bmatrix} \begin{Bmatrix} A_2 \\ B_1 \end{Bmatrix} = \begin{Bmatrix} 1 \\ 0 \end{Bmatrix}.$$

Solving these two matrix equations are straightforward; the results are

$$\begin{aligned}
\begin{Bmatrix} A_1 \\ B_2 \end{Bmatrix} &= \frac{1}{2(D_{11}D_{22} - D_{12}D_{21})} \begin{bmatrix} D_{22} & -D_{12} \\ -D_{21} & D_{11} \end{bmatrix} \begin{Bmatrix} 1 \\ 0 \end{Bmatrix} \\
&= \frac{1}{2(D_{11}D_{22} - D_{12}D_{21})} \begin{Bmatrix} D_{22} \\ -D_{21} \end{Bmatrix},
\end{aligned}$$

and

$$\begin{Bmatrix} A_2 \\ B_1 \end{Bmatrix} = \frac{1}{2(D_{13}D_{24} - D_{14}D_{23})} \begin{bmatrix} D_{24} & -D_{13} \\ -D_{23} & D_{13} \end{bmatrix} \begin{Bmatrix} 1 \\ 0 \end{Bmatrix}$$
$$= \frac{1}{2(D_{13}D_{24} - D_{14}D_{23})} \begin{Bmatrix} D_{24} \\ -D_{23} \end{Bmatrix}.$$

Comparing the considered matrix equation at the beginning of this section and Equation (D.14) in Appendix D, one can find that

$$\begin{aligned} D_{11}D_{22} - D_{12}D_{21} &= -R_s \\ D_{13}D_{24} - D_{14}D_{23} &= -R_a. \end{aligned} \tag{A.5}$$

This result, together with the derived forms of roots of the current matrix equation leads to Equations (D.15) and (D.16).

APPENDIX B

OPERATIONS IN THE CYLINDRICAL COORDINATES

A point in the cylindrical coordinates is given by (r, θ, z). These three independent variables can be related to x, y, and z in the Cartesian coordinates by the following relationships:

$$\begin{aligned} x &= r\cos\theta \\ y &= r\sin\theta \\ z &= z. \end{aligned} \tag{B.1}$$

B.1 Transformation

A vector $\mathbf{v}$ in the Cartesian coordinates can be expressed in the cylindrical coordinates, $\mathbf{v}'$ by the transformation matrix

$$\mathbf{A} = \begin{bmatrix} \cos\theta & \sin\theta & 0 \\ -\sin\theta & \cos\theta & 0 \\ 0 & 0 & 1 \end{bmatrix}. \tag{B.2}$$

That is, $\mathbf{v}'$ can be obtained from the matrix multiplication

$$\mathbf{v}' = \mathbf{A}\mathbf{v}. \tag{B.3}$$

In the indicial notation, Equation (B.3) can be written as

$$v_i' = A_{ij}v_j, \tag{B.4}$$

where the summation is assumed over the index j as usual. This transformation concept can be extended to the second- and higher-order tensors by successive transformations, i.e.

$$\begin{aligned} G_{ij}' &= A_{ia}A_{jb}G_{ab} \\ H_{ijk}' &= A_{ia}A_{jb}A_{kc}H_{abc}, \end{aligned} \tag{B.5}$$

and so on. Let the vector $\mathbf{e}_i$ denote a base unit vector in the i direction. Explicitly, by the transformation given by Equation (B.4), using the transformation matrix in Equations (B.2), one can express the components of a vector field $\mathbf{v} = v_r\,\mathbf{e}_r + v_\theta\,\mathbf{e}_\theta + v_z\,\mathbf{e}_z$ in the cylindrical coordinates in terms of itself in the cartesian coordinates $\mathbf{v} = v_x\,\mathbf{e}_x + v_y\,\mathbf{e}_y + v_z\,\mathbf{e}_z$ as

$$\begin{aligned} v_r &= v_x \cos\theta + v_y \sin\theta \\ v_\theta &= -v_x \sin\theta + v_y \cos\theta \\ v_z &= v_z. \end{aligned} \tag{B.6}$$

Conversely, similar to Equation (B.6), one can obtain

$$\begin{aligned} v_x &= v_r \cos\theta - v_\theta \sin\theta \\ v_y &= v_r \sin\theta + v_\theta \cos\theta \\ v_z &= v_z. \end{aligned} \tag{B.7}$$

B.2 Operations in calculus

From Equation (B.1), the inverse relationships are

$$\begin{aligned} r &= \sqrt{x^2 + y^2} \\ \theta &= \arctan\left(\frac{y}{x}\right) \\ z &= z. \end{aligned} \tag{B.8}$$

Then, by the chain rule, for some scalar function Q,

$$\begin{aligned} \frac{\partial Q}{\partial x} &= \frac{\partial Q}{\partial r}\frac{\partial r}{\partial x} + \frac{\partial Q}{\partial \theta}\frac{\partial \theta}{\partial x} \\ &= \frac{x}{\sqrt{x^2+y^2}}\frac{\partial Q}{\partial r} - \frac{y}{x^2+y^2}\frac{\partial Q}{\partial \theta} \\ &= \cos\theta\frac{\partial Q}{\partial r} - \frac{\sin\theta}{r}\frac{\partial Q}{\partial \theta} \end{aligned} \tag{B.9}$$

$$\begin{aligned} \frac{\partial Q}{\partial y} &= \frac{\partial Q}{\partial r}\frac{\partial r}{\partial y} + \frac{\partial Q}{\partial \theta}\frac{\partial \theta}{\partial y} \\ &= \frac{y}{\sqrt{x^2+y^2}}\frac{\partial Q}{\partial r} + \frac{x}{x^2+y^2}\frac{\partial Q}{\partial \theta} \\ &= \sin\theta\frac{\partial Q}{\partial r} + \frac{\cos\theta}{r}\frac{\partial Q}{\partial \theta}. \end{aligned} \tag{B.10}$$

The *grad* of a scalar function Q becomes

$$\begin{aligned}
\nabla Q &= \frac{\partial Q}{\partial x}\,\mathbf{e}_x + \frac{\partial Q}{\partial y}\,\mathbf{e}_y + \frac{\partial Q}{\partial z}\,\mathbf{e}_z \\
&= \Big(\cos\theta\frac{\partial Q}{\partial r} - \frac{\sin\theta}{r}\frac{\partial Q}{\partial \theta}\Big)(\mathbf{e}_r\cos\theta - \mathbf{e}_\theta\sin\theta) \\
&\quad + \Big(\sin\theta\frac{\partial Q}{\partial r} + \frac{\cos\theta}{r}\frac{\partial Q}{\partial \theta}\Big)(\mathbf{e}_r\sin\theta + \mathbf{e}_\theta\cos\theta) + \frac{\partial Q}{\partial z}\,\mathbf{e}_z \\
&= \frac{\partial Q}{\partial r}\,\mathbf{e}_r + \frac{1}{r}\frac{\partial Q}{\partial \theta}\,\mathbf{e}_\theta + \frac{\partial Q}{\partial z}\,\mathbf{e}_z. \qquad \text{(B.11)}
\end{aligned}$$

The *divergence* of a vector function $\mathbf{v}$ is

$$\begin{aligned}
\nabla\cdot\mathbf{v} &= \frac{\partial v_x}{\partial x} + \frac{\partial v_y}{\partial y} + \frac{\partial v_z}{\partial z} \\
&= \cos\theta\frac{\partial}{\partial r}(v_r\cos\theta - v_\theta\sin\theta) - \frac{\sin\theta}{r}\frac{\partial}{\partial\theta}(v_r\cos\theta - v_\theta\sin\theta) \\
&\quad + \sin\theta\frac{\partial}{\partial r}(v_r\sin\theta + v_\theta\cos\theta) + \frac{\cos\theta}{r}\frac{\partial}{\partial\theta}(v_r\sin\theta + v_\theta\cos\theta) + \frac{\partial v_z}{\partial z} \\
&= \frac{\partial v_r}{\partial r} + \frac{v_r}{r} + \frac{1}{r}\frac{\partial v_\theta}{\partial\theta} + \frac{\partial v_z}{\partial z}. \qquad \text{(B.12)}
\end{aligned}$$

Lastly, the *curl* of a vector function $\mathbf{v}$ can be found as

$$\begin{aligned}
\nabla\times\mathbf{v} &= \Big(\frac{\partial v_z}{\partial y} - \frac{\partial v_y}{\partial z}\Big)\,\mathbf{e}_x + \Big(\frac{\partial v_x}{\partial z} - \frac{\partial v_z}{\partial x}\Big)\,\mathbf{e}_y + \Big(\frac{\partial v_y}{\partial x} - \frac{\partial v_x}{\partial y}\Big)\,\mathbf{e}_z \\
&= \Big(\sin\theta\frac{\partial v_z}{\partial r} + \frac{\cos\theta}{r}\frac{\partial v_z}{\partial\theta} - \frac{\partial}{\partial z}(v_r\sin\theta + v_\theta\cos\theta)\Big)(\mathbf{e}_r\cos\theta - \mathbf{e}_\theta\sin\theta) \\
&\quad + \Big(\frac{\partial}{\partial z}(v_r\cos\theta - v_\theta\sin\theta) - \cos\theta\frac{\partial v_z}{\partial r} + \frac{\sin\theta}{r}\frac{\partial v_z}{\partial\theta}\Big)(\mathbf{e}_r\sin\theta + \mathbf{e}_\theta\cos\theta) \\
&\quad + \Big(\cos\theta\frac{\partial}{\partial r}(v_r\sin\theta + v_\theta\cos\theta) - \frac{\sin\theta}{r}\frac{\partial}{\partial\theta}(v_r\sin\theta + v_\theta\cos\theta) \\
&\quad - \sin\theta\frac{\partial}{\partial r}(v_r\cos\theta - v_\theta\sin\theta) - \frac{\cos\theta}{r}\frac{\partial}{\partial\theta}(v_r\cos\theta - v_\theta\sin\theta)\Big)\,\mathbf{e}_z \\
&= \Big(\frac{1}{r}\frac{\partial v_z}{\partial\theta} - \frac{\partial v_\theta}{\partial z}\Big)\,\mathbf{e}_r + \Big(\frac{\partial v_r}{\partial z} - \frac{\partial v_z}{\partial r}\Big)\,\mathbf{e}_\theta + \Big(\frac{\partial v_\theta}{\partial r} + \frac{v_\theta}{r} - \frac{1}{r}\frac{\partial v_r}{\partial\theta}\Big)\,\mathbf{e}_z. \qquad \text{(B.13)}
\end{aligned}$$

Now, consider the *Laplacian*. First, let Q be a scalar function, the Laplacian of Q can be obtained with the use of Equations (B.11) and (B.12),

$$\begin{aligned}
\nabla^2 Q &= \nabla\cdot(\nabla Q) \\
&= \frac{\partial}{\partial r}\Big(\frac{\partial Q}{\partial r}\Big) + \frac{1}{r}\frac{\partial Q}{\partial r} + \frac{1}{r}\frac{\partial}{\partial\theta}\Big(\frac{1}{r}\frac{\partial Q}{\partial\theta}\Big) + \frac{\partial}{\partial z}\Big(\frac{\partial Q}{\partial z}\Big) \\
&= \frac{\partial^2 Q}{\partial r^2} + \frac{1}{r}\frac{\partial Q}{\partial r} + \frac{1}{r^2}\frac{\partial^2 Q}{\partial\theta^2} + \frac{\partial^2 Q}{\partial z^2}. \qquad \text{(B.14)}
\end{aligned}$$

For a vector function $\mathbf{v}$, its Laplacian is

$$\begin{aligned}
\nabla^2\mathbf{v} &= \nabla^2 v_x\,\mathbf{e}_x + \nabla^2 v_y\,\mathbf{e}_y + \nabla^2 v_z\,\mathbf{e}_z \\
&= \Big[\frac{\partial^2}{\partial r^2}(v_r\cos\theta - v_\theta\sin\theta) + \frac{1}{r}\frac{\partial}{\partial r}(v_r\cos\theta - v_\theta\sin\theta) + \frac{1}{r^2}\frac{\partial^2}{\partial\theta^2}(v_r\cos\theta - v_\theta\sin\theta) \\
&\quad + \frac{\partial^2}{\partial z^2}(v_r\cos\theta - v_\theta\sin\theta)\Big](\mathbf{e}_r\cos\theta - \mathbf{e}_\theta\sin\theta) + \Big[\frac{\partial^2}{\partial r^2}(v_r\sin\theta + v_\theta\cos\theta) \\
&\quad + \frac{1}{r}\frac{\partial}{\partial r}(v_r\sin\theta + v_\theta\cos\theta) + \frac{1}{r^2}\frac{\partial^2}{\partial\theta^2}(v_r\sin\theta + v_\theta\cos\theta) + \\
&\quad + \frac{\partial^2}{\partial z^2}(v_r\sin\theta + v_\theta\cos\theta)\Big](\mathbf{e}_r\sin\theta + \mathbf{e}_\theta\cos\theta) \\
&\quad + \Big(\frac{\partial^2 v_z}{\partial r^2} + \frac{1}{r}\frac{\partial v_z}{\partial r} + \frac{1}{r^2}\frac{\partial^2 v_z}{\partial\theta^2} + \frac{\partial^2 v_z}{\partial z^2}\Big)\mathbf{e}_z \\
&= \Big(\frac{\partial^2 v_r}{\partial r^2} + \frac{1}{r}\frac{\partial v_r}{\partial r} + \frac{1}{r^2}\frac{\partial^2 v_r}{\partial\theta^2} - \frac{v_r}{r^2} - \frac{2}{r^2}\frac{\partial v_\theta}{\partial\theta} + \frac{\partial^2 v_r}{\partial z^2}\Big)\mathbf{e}_r \\
&\quad + \Big(\frac{\partial^2 v_\theta}{\partial r^2} + \frac{1}{r}\frac{\partial v_\theta}{\partial r} + \frac{2}{r^2}\frac{\partial v_r}{\partial\theta} + \frac{1}{r^2}\frac{\partial^2 v_\theta}{\partial\theta^2} - \frac{v_\theta}{r^2} + \frac{\partial^2 v_\theta}{\partial z^2}\Big)\mathbf{e}_\theta \\
&\quad + \Big(\frac{\partial^2 v_z}{\partial r^2} + \frac{1}{r}\frac{\partial v_z}{\partial r} + \frac{1}{r^2}\frac{\partial^2 v_z}{\partial\theta^2} + \frac{\partial^2 v_z}{\partial z^2}\Big)\mathbf{e}_z \\
&= \Big(\nabla^2 v_r - \frac{v_r}{r^2} - \frac{2}{r^2}\frac{\partial v_\theta}{\partial\theta}\Big)\mathbf{e}_r + \Big(\nabla^2 v_\theta + \frac{2}{r^2}\frac{\partial v_r}{\partial\theta} - \frac{v_\theta}{r^2}\Big)\mathbf{e}_\theta + \nabla^2 v_z\,\mathbf{e}_z. \qquad \text{(B.15)}
\end{aligned}$$

B.3 Quantities and equations in elasticity

This section will apply the expressions developed in the previous sections to displacement and stress fields and equations of motion in elasticity.

B.3.1 Displacement components by Helmholtz decomposition

Recall the Helmholtz decomposition of the displacement:

$$\mathbf{u} = \nabla\phi + \nabla\times\boldsymbol{\psi}. \qquad \text{(B.16)}$$

From Equations (B.11) and (B.13), the components of $\mathbf{u}$ in the above equation can be written explicitly as

$$\begin{aligned}
u_r &= \frac{\partial\phi}{\partial r} + \frac{1}{r}\frac{\partial\psi_z}{\partial\theta} - \frac{\partial\psi_\theta}{\partial z} \\
u_\theta &= \frac{1}{r}\frac{\partial\phi}{\partial\theta} + \frac{\partial\psi_r}{\partial z} - \frac{\partial\psi_z}{\partial r} \\
u_z &= \frac{\partial\phi}{\partial z} + \frac{\partial\psi_\theta}{\partial r} + \frac{\psi_\theta}{r} - \frac{1}{r}\frac{\partial\psi_r}{\partial\theta}. \qquad \text{(B.17)}
\end{aligned}$$

B.3.2 Governing wave equations

Regardless of the coordinate system, substitution of $\mathbf{u}$ in terms of potentials ϕ and $\boldsymbol{\psi}$, into the displacement equations of motion without body forces,

$$(\lambda + \mu)\nabla(\nabla \cdot \mathbf{u}) + \mu\nabla^2\mathbf{u} = \rho\ddot{\mathbf{u}}, \tag{B.18}$$

results in two wave equations governing the two potentials:

$$\begin{aligned} \nabla^2\phi &= \frac{1}{c_L^2}\ddot{\phi} \\ \nabla^2\boldsymbol{\psi} &= \frac{1}{c_T^2}\ddot{\boldsymbol{\psi}}, \end{aligned} \tag{B.19}$$

where c_L and c_T are longitudinal and shear wave velocities, respectively. Using the results from Equations (B.14) and (B.15), one can expand Equation (B.19) into four scalar equations:

$$\begin{aligned} \nabla^2\phi &= \frac{1}{c_L^2}\ddot{\phi} \\ \nabla^2\psi_r - \frac{\psi_r}{r^2} - \frac{2}{r^2}\frac{\partial\psi_\theta}{\partial\theta} &= \frac{1}{c_T^2}\ddot{\psi}_r \\ \nabla^2\psi_\theta + \frac{2}{r^2}\frac{\partial\psi_r}{\partial\theta} - \frac{\psi_\theta}{r^2} &= \frac{1}{c_T^2}\ddot{\psi}_\theta \\ \nabla^2\psi_z &= \frac{1}{c_T^2}\ddot{\psi}_z, \end{aligned} \tag{B.20}$$

where the operator ∇^2 is given by $\frac{\partial^2}{\partial r^2} + \frac{1}{r}\frac{\partial}{\partial r} + \frac{1}{r^2}\frac{\partial^2}{\partial\theta^2} + \frac{\partial^2}{\partial z^2}$.

B.3.3 Stress-displacement relations

The stress-displacement relations can be obtained via the transformation stated in Section B.1. Starting with Equations (B.5), the stress components in the cylindrical coordinates

can be written explicitly in terms of the stress in the Cartesian coordinates as

$$\begin{bmatrix} \sigma_{rr} & \sigma_{r\theta} & \sigma_{rz} \\ \sigma_{\theta r} & \sigma_{\theta\theta} & \sigma_{\theta z} \\ \sigma_{zr} & \sigma_{z\theta} & \sigma_{zz} \end{bmatrix} = \begin{bmatrix} \cos\theta & \sin\theta & 0 \\ -\sin\theta & \cos\theta & 0 \\ 0 & 0 & 1 \end{bmatrix} \begin{bmatrix} \sigma_{xx} & \sigma_{xy} & \sigma_{xz} \\ \sigma_{yx} & \sigma_{yy} & \sigma_{yz} \\ \sigma_{zx} & \sigma_{zy} & \sigma_{zz} \end{bmatrix} \begin{bmatrix} \cos\theta & -\sin\theta & 0 \\ \sin\theta & \cos\theta & 0 \\ 0 & 0 & 1 \end{bmatrix}$$

$$= \begin{bmatrix} \cos\theta & \sin\theta & 0 \\ -\sin\theta & \cos\theta & 0 \\ 0 & 0 & 1 \end{bmatrix}$$

$$\times \begin{bmatrix} \sigma_{xx}\cos\theta + \sigma_{xy}\sin\theta & -\sigma_{xx}\sin\theta + \sigma_{xy}\cos\theta & \sigma_{xz} \\ \sigma_{yx}\cos\theta + \sigma_{yy}\sin\theta & -\sigma_{yx}\sin\theta + \sigma_{yy}\cos\theta & \sigma_{yz} \\ \sigma_{zx}\cos\theta + \sigma_{zy}\sin\theta & -\sigma_{zx}\sin\theta + \sigma_{yz}\cos\theta & \sigma_{zz} \end{bmatrix}. \quad \text{(B.21)}$$

From this equation, one can obtain expressions for six distinct stress components:

$$\begin{aligned} \sigma_{rr} &= \sigma_{xx}\cos^2\theta + \sigma_{yy}\sin^2\theta + 2\sigma_{xy}\sin\theta\cos\theta \\ \sigma_{\theta\theta} &= \sigma_{xx}\sin^2\theta + \sigma_{yy}\cos^2\theta - 2\sigma_{xy}\sin\theta\cos\theta \\ \sigma_{zz} &= \sigma_{zz} \\ \sigma_{r\theta} &= -\sigma_{xx}\sin\theta\cos\theta + \sigma_{xy}(\cos^2\theta - \sin^2\theta) + \sigma_{yy}\sin\theta\cos\theta \\ \sigma_{rz} &= \sigma_{xz}\cos\theta + \sigma_{yz}\sin\theta \\ \sigma_{\theta z} &= -\sigma_{xz}\sin\theta + \sigma_{yz}\cos\theta. \end{aligned} \quad \text{(B.22)}$$

To obtain the expressions for the stress in the Cartesian coordinates in terms of displacement in the cylindrical coordinates, one first obtain the first strain invariant

$$\begin{aligned} \Theta &= \varepsilon_{xx} + \varepsilon_{yy} + \varepsilon_{zz} \\ &= \frac{\partial u_x}{\partial x} + \frac{\partial u_y}{\partial y} + \frac{\partial u_z}{\partial z} \\ &= \nabla \cdot \mathbf{u} \\ &= \frac{\partial u_r}{\partial r} + \frac{u_r}{r} + \frac{1}{r}\frac{\partial u_\theta}{\partial \theta} + \frac{\partial u_z}{\partial z}. \end{aligned} \quad \text{(B.23)}$$

With the use of Equations (B.7), (B.9)–(B.10) and (B.23) in the definition of stress and Equation (B.22), the stress components in the cylindrical coordinates are

$$
\begin{aligned}
\sigma_{rr} &= \cos^2\theta\Big(\lambda\Theta + 2\mu\frac{\partial u_x}{\partial x}\Big) + \sin^2\theta\Big(\lambda\Theta + 2\mu\frac{\partial u_y}{\partial y}\Big) + 2\sin\theta\cos\theta\mu\Big(\frac{\partial u_x}{\partial y} + \frac{\partial u_y}{\partial x}\Big) \\
&= \lambda\Theta + 2\mu\Big\{\cos^2\theta\Big[\cos\theta\frac{\partial}{\partial r}(u_r\cos\theta - u_\theta\sin\theta) - \frac{\sin\theta}{r}\frac{\partial}{\partial\theta}(u_r\cos\theta - u_\theta\sin\theta)\Big] \\
&\quad + \sin^2\theta\Big[\sin\theta\frac{\partial}{\partial r}(u_r\sin\theta + u_\theta\cos\theta) + \frac{\cos\theta}{r}\frac{\partial}{\partial\theta}(u_r\sin\theta + u_\theta\cos\theta)\Big] \\
&\quad + \sin\theta\cos\theta\Big[\sin\theta\frac{\partial}{\partial r}(u_r\cos\theta - u_\theta\sin\theta) + \frac{\cos\theta}{r}\frac{\partial}{\partial\theta}(u_r\cos\theta - u_\theta\sin\theta) \\
&\quad + \cos\theta\frac{\partial}{\partial r}(u_r\sin\theta + u_\theta\cos\theta) - \frac{\sin\theta}{r}\frac{\partial}{\partial\theta}(u_r\sin\theta + u_\theta\cos\theta)\Big]\Big\} \\
&= \lambda\Theta + 2\mu\frac{\partial u_r}{\partial r} \\
&= \lambda\Big(\frac{\partial u_r}{\partial r} + \frac{u_r}{r} + \frac{1}{r}\frac{\partial u_\theta}{\partial\theta} + \frac{\partial u_z}{\partial z}\Big) + 2\mu\frac{\partial u_r}{\partial r} \qquad \text{(B.24)} \\
\sigma_{\theta\theta} &= \sin^2\theta\Big(\lambda\Theta + 2\mu\frac{\partial u_x}{\partial x}\Big) + \cos^2\theta\Big(\lambda\Theta + 2\mu\frac{\partial u_y}{\partial y}\Big) - 2\sin\theta\cos\theta\mu\Big(\frac{\partial u_x}{\partial y} + \frac{\partial u_y}{\partial x}\Big) \\
&= \lambda\Theta + 2\mu\Big\{\sin^2\theta\Big[\cos\theta\frac{\partial}{\partial r}(u_r\cos\theta - u_\theta\sin\theta) - \frac{\sin\theta}{r}\frac{\partial}{\partial\theta}(u_r\cos\theta - u_\theta\sin\theta)\Big] \\
&\quad + \cos^2\theta\Big[\sin\theta\frac{\partial}{\partial r}(u_r\sin\theta + u_\theta\cos\theta) + \frac{\cos\theta}{r}\frac{\partial}{\partial\theta}(u_r\sin\theta + u_\theta\cos\theta)\Big] \\
&\quad - \sin\theta\cos\theta\Big[\sin\theta\frac{\partial}{\partial r}(u_r\cos\theta - u_\theta\sin\theta) + \frac{\cos\theta}{r}\frac{\partial}{\partial\theta}(u_r\cos\theta - u_\theta\sin\theta) \\
&\quad + \cos\theta\frac{\partial}{\partial r}(u_r\sin\theta + u_\theta\cos\theta) - \frac{\sin\theta}{r}\frac{\partial}{\partial\theta}(u_r\sin\theta + u_\theta\cos\theta)\Big]\Big\} \\
&= \lambda\Theta + 2\mu\Big(\frac{u_r}{r} + \frac{1}{r}\frac{\partial u_\theta}{\partial\theta}\Big) \\
&= \lambda\Big(\frac{\partial u_r}{\partial r} + \frac{u_r}{r} + \frac{1}{r}\frac{\partial u_\theta}{\partial\theta} + \frac{\partial u_z}{\partial z}\Big) + 2\mu\Big(\frac{u_r}{r} + \frac{1}{r}\frac{\partial u_\theta}{\partial\theta}\Big) \qquad \text{(B.25)} \\
\sigma_{zz} &= \lambda\Theta + 2\mu\frac{\partial u_z}{\partial z} \\
&= \lambda\Big(\frac{\partial u_r}{\partial r} + \frac{u_r}{r} + \frac{1}{r}\frac{\partial u_\theta}{\partial\theta} + \frac{\partial u_z}{\partial z}\Big) + 2\mu\frac{\partial u_z}{\partial z} \qquad \text{(B.26)} \\
\sigma_{r\theta} &= \sin\theta\cos\theta\Big(\lambda\Theta + 2\mu\frac{\partial u_y}{\partial y} - \lambda\Theta - 2\mu\frac{\partial u_x}{\partial x}\Big) + \mu(\cos^2\theta - \sin^2\theta)\Big(\frac{\partial u_x}{\partial y} + \frac{\partial u_y}{\partial x}\Big) \\
&= \mu\Big\{2\sin\theta\cos\theta\Big[\sin\theta\frac{\partial}{\partial r}(u_r\sin\theta + u_\theta\cos\theta) + \frac{\cos\theta}{r}\frac{\partial}{\partial\theta}(u_r\sin\theta + u_\theta\cos\theta) \\
&\quad - \cos\theta\frac{\partial}{\partial r}(u_r\cos\theta - u_\theta\sin\theta) + \frac{\sin\theta}{r}\frac{\partial}{\partial\theta}(u_r\cos\theta - u_\theta\sin\theta)\Big] \\
&\quad + (\cos^2\theta - \sin^2\theta)\Big[\sin\theta\frac{\partial}{\partial r}(u_r\cos\theta - u_\theta\sin\theta) + \frac{\cos\theta}{r}\frac{\partial}{\partial\theta}(u_r\cos\theta - u_\theta\sin\theta) \\
&\quad + \cos\theta\frac{\partial}{\partial r}(u_r\sin\theta + u_\theta\cos\theta) - \frac{\sin\theta}{r}\frac{\partial}{\partial\theta}(u_r\sin\theta + u_\theta\cos\theta)\Big]\Big\} \\
&= \mu\Big(\frac{\partial u_\theta}{\partial r} + \frac{1}{r}\frac{\partial u_r}{\partial\theta} - \frac{u_\theta}{r}\Big) \qquad \text{(B.27)}
\end{aligned}
$$

$$
\begin{aligned}
\sigma_{rz} &= \cos\theta\mu\Big(\frac{\partial u_x}{\partial z}+\frac{\partial u_z}{\partial x}\Big)+\sin\theta\mu\Big(\frac{\partial u_y}{\partial z}+\frac{\partial u_z}{\partial y}\Big) \\
&= \mu\Big\{\cos\theta\Big[\frac{\partial}{\partial z}(u_r\cos\theta-u_\theta\sin\theta)+\cos\theta\frac{\partial u_z}{\partial r}-\frac{\sin\theta}{r}\frac{\partial u_z}{\partial\theta}\Big] \\
&\quad +\sin\theta\Big[\frac{\partial}{\partial z}(u_r\sin\theta+u_\theta\cos\theta)+\sin\theta\frac{\partial u_z}{\partial r}+\frac{\cos\theta}{r}\frac{\partial u_z}{\partial\theta}\Big]\Big\} \\
&= \mu\Big(\frac{\partial u_r}{\partial z}+\frac{\partial u_z}{\partial r}\Big) \qquad \text{(B.28)} \\
\sigma_{\theta z} &= -\sin\theta\mu\Big(\frac{\partial u_x}{\partial z}+\frac{\partial u_z}{\partial x}\Big)+\cos\theta\mu\Big(\frac{\partial u_y}{\partial z}+\frac{\partial u_z}{\partial y}\Big) \\
&= \mu\Big\{-\sin\theta\Big[\frac{\partial}{\partial z}(u_r\cos\theta-u_\theta\sin\theta)+\cos\theta\frac{\partial u_z}{\partial r}-\frac{\sin\theta}{r}\frac{\partial u_z}{\partial\theta}\Big] \\
&\quad +\cos\theta\Big[\frac{\partial}{\partial z}(u_r\sin\theta+u_\theta\cos\theta)+\sin\theta\frac{\partial u_z}{\partial r}+\frac{\cos\theta}{r}\frac{\partial u_z}{\partial\theta}\Big]\Big\} \\
&= \mu\Big(\frac{\partial u_\theta}{\partial z}+\frac{1}{r}\frac{\partial u_z}{\partial\theta}\Big). \qquad \text{(B.29)}
\end{aligned}
$$

Note that the expressions in Equations (B.24)–(B.29) can also be derived directly from geometry by applying the proper definitions of stress and strain to the deformed infinitesimal element of a material.

B.3.4 Axial symmetry

For an axisymmetric problem, the dependence of θ and u_θ vanish. From Equations (B.17), ψ_r and ψ_z are forced to be identically zero. Therefore, the vector potential $\boldsymbol{\psi}$ has only one nonzero component in the θ-direction, ψ_θ. This nonzero component can be replaced by a scalar function ψ. Then, Equations (B.17) reduce to

$$
\begin{aligned}
u_r &= \frac{\partial\phi}{\partial r}-\frac{\partial\psi}{\partial z} \\
u_z &= \frac{\partial\phi}{\partial z}+\frac{\partial\psi}{\partial r}+\frac{\psi}{r}. \qquad \text{(B.30)}
\end{aligned}
$$

Also, the four coupled governing equations (B.20) reduce to two uncoupled equations:

$$
\begin{aligned}
\nabla^2\phi &= \frac{1}{c_L^2}\ddot{\phi} \\
\nabla^2\psi-\frac{\psi}{r^2} &= \frac{1}{c_T^2}\ddot{\psi}. \qquad \text{(B.31)}
\end{aligned}
$$

Lastly, the expressions for the stress components given by Equations (B.24)–(B.29) reduce to

$$\begin{aligned}
\sigma_{rr} &= \lambda\Big(\frac{\partial u_r}{\partial r} + \frac{u_r}{r} + \frac{\partial u_z}{\partial z}\Big) + 2\mu\frac{\partial u_r}{\partial r} \\
\sigma_{\theta\theta} &= \lambda\Big(\frac{\partial u_r}{\partial r} + \frac{u_r}{r} + \frac{\partial u_z}{\partial z}\Big) + 2\mu\frac{u_r}{r} \\
\sigma_{zz} &= \lambda\Big(\frac{\partial u_r}{\partial r} + \frac{u_r}{r} + \frac{\partial u_z}{\partial z}\Big) + 2\mu\frac{\partial u_z}{\partial z} \\
\sigma_{r\theta} &= 0 \\
\sigma_{rz} &= \mu\Big(\frac{\partial u_r}{\partial z} + \frac{\partial u_z}{\partial r}\Big) \\
\sigma_{\theta z} &= 0. \qquad \text{(B.32)}
\end{aligned}$$

APPENDIX C

SOME DEFINITE INTEGRAL FORMULAS

Using fundamental trigonometric identities, one can derive:

$$\begin{aligned}
\int \cos(az)\cos(bz)\,dz &= \int \frac{1}{2}\big(\cos[(a-b)z] + \cos[(a+b)z]\big)\,dz \\
&= \frac{1}{2}\Big(\frac{\sin[(a-b)z]}{a-b} + \frac{\sin[(a+b)z]}{a+b}\Big) \qquad \text{(C.1)} \\
\int \sin(az)\sin(bz)\,dz &= \int \frac{1}{2}\big(\cos[(a-b)z] - \cos[(a+b)z]\big)\,dz \\
&= \frac{1}{2}\Big(\frac{\sin[(a-b)z]}{a-b} - \frac{\sin[(a+b)z]}{a+b}\Big) \qquad \text{(C.2)}
\end{aligned}$$

If $a = b$, the above equations still apply in the limit $a \to b$, i.e.

$$\begin{aligned}
\int \cos^2(az)\,dz &= \frac{1}{2}\Big(z + \frac{\sin[(a+b)z]}{a+b}\Big) \qquad \text{(C.3)} \\
\int \sin^2(az)\,dz &= \frac{1}{2}\Big(z - \frac{\sin[(a+b)z]}{a+b}\Big). \qquad \text{(C.4)}
\end{aligned}$$

Hence,

$$\begin{aligned}
\int_{-h}^{h} \cos^2(az)\,dz &= \frac{1}{2}\Big(z + \frac{\sin(2az)}{2a}\Big)\Big|_{-h}^{h} \\
&= h + \frac{\sin(2ah)}{2a} \qquad \text{(C.5)} \\
\int_{-h}^{h} \cos(az)\cos(bz)\,dz &= \frac{1}{2}\Big(\frac{\sin[(a-b)z]}{a-b} + \frac{\sin[(a+b)z]}{a+b}\Big)\Big|_{-h}^{h} \\
&= \frac{\sin[(a-b)h]}{a-b} + \frac{\sin[(a+b)h]}{a+b} \\
&= \frac{2}{a^2-b^2}\Big[a\sin(ah)\cos(bh) - b\cos(ah)\sin(bh)\Big] \qquad \text{(C.6)}
\end{aligned}$$

$$\begin{aligned}
\int_{-h}^{h} \sin^2(az)\,dz &= \frac{1}{2}\Big(x - \frac{\sin(2az)}{2a}\Big)\Big|_{-h}^{h} \\
&= h - \frac{\sin(2ah)}{2a} \qquad \text{(C.7)} \\
\int_{-h}^{h} \sin(az)\sin(bz)\,dz &= \frac{1}{2}\Big(\frac{\sin[(a-b)z]}{a-b} - \frac{\sin[(a+b)z]}{a+b}\Big)\Big|_{-h}^{h} \\
&= \frac{\sin[(a-b)h]}{a-b} - \frac{\sin[(a+b)h]}{a+b} \\
&= \frac{2}{a^2-b^2}\Big[-a\cos(ah)\sin(bh) + b\sin(ah)\cos(bh)\Big]. \qquad \text{(C.8)}
\end{aligned}$$

Equations (C.5)–(C.8) are still applicable even when one or both of a and b are pure imaginary by employing the identities: $\cos(jx) = \cosh(x)$ and $\sin(jx) = j\sinh(x)$, where x is real. Then, the following formulas can be derived:

$$\begin{aligned}
\int_{-h}^{h} \cosh^2(az)\,dz &= \int_{-h}^{h} \cos^2(jaz)\,dz \\
&= h + \frac{\sin(2jah)}{2ja} \\
&= h + \frac{\sinh(2ah)}{2a} \qquad \text{(C.9)} \\
\int_{-h}^{h} \cosh(az)\cos(bz)\,dz &= \int_{-h}^{h} \cos(jaz)\cos(bz)\,dz \\
&= \frac{2}{-a^2-b^2}\Big[ja\sin(jah)\cos(bh) - b\cos(jah)\sin(bh)\Big] \\
&= \frac{2}{a^2+b^2}\Big[a\sinh(ah)\cos(bh) + b\cosh(ah)\sin(bh)\Big] \qquad \text{(C.10)} \\
\int_{-h}^{h} \sinh^2(az)\,dz &= -\int_{-h}^{h} \sin^2(jaz)\,dz \\
&= -h + \frac{\sin(2jah)}{2ja} \\
&= -h + \frac{\sinh(2ah)}{2a} \qquad \text{(C.11)} \\
\int_{-h}^{h} \sinh(az)\sin(bz)\,dz &= -j\int_{-h}^{h} \sin(jaz)\sin(bz)\,dz \\
&= -j\frac{2}{-a^2-b^2}\Big[-ja\cos(jah)\sin(bh) + b\sin(jah)\cos(bh)\Big] \\
&= \frac{2}{a^2+b^2}\Big[a\cosh(ah)\sin(bh) - b\sinh(ah)\cos(bh)\Big]. \qquad \text{(C.12)}
\end{aligned}$$

APPENDIX D

EXCITABILITY OF LAMB WAVE MODES DUE TO A NORMAL POINT EXCITATION

This appendix presents the derivation of excitability of Lamb wave modes. The analysis is presented in detail by the conventional method of integral transform outlined in References [77] and [24].

Consider an infinite plate (isotropic, linearly elastic) with an axisymmetric normal excitation on the top surface as shown in Figure D.1. The stress distribution of the excitation is assumed uniform with the amplitude $\bar{Q}$ over a circular region of radius a, so the stress boundary conditions of this plate can be expressed as

$$\begin{cases} \sigma_{zz}(z=h,r) = \begin{cases} \bar{Q}e^{j\omega t} & \text{if } r<a \\ 0 & \text{if } r>a \end{cases} \\ \sigma_{zz}(z=-h,r)=0 \\ \sigma_{zr}(z=\pm h,r)=0. \end{cases} \tag{D.1}$$

The positive sign of $\bar{Q}$ indicates the upward $(+z)$ direction. Note that the total normal force can be easily calculated as $Q=\bar{Q}\pi a^2$. Since the excitation is time-harmonic, all field quantities are also time-harmonic. With the time-harmonic factor $e^{j\omega t}$ dropped throughout, in terms of displacement potentials ϕ and $\boldsymbol{\psi}=\psi\,\mathbf{e}_\theta$ in the cylindrical coordinates, the governing equations of the problem can be derived by substituting $\mathbf{u}=\nabla\phi+\nabla\times\boldsymbol{\psi}$ into Equation (2.8). Similarly to what had been done for the free-vibration analysis in Section 4.2.1, the equations governing two scalar potentials with no body forces are (see derivation of Equations (4.58))

$$\begin{aligned} \nabla^2\phi+\frac{\omega^2}{c_L^2}\phi &= 0 \\ \nabla^2\psi-\frac{\psi}{r^2}+\frac{\omega^2}{c_T^2}\psi &= 0, \end{aligned} \tag{D.2}$$

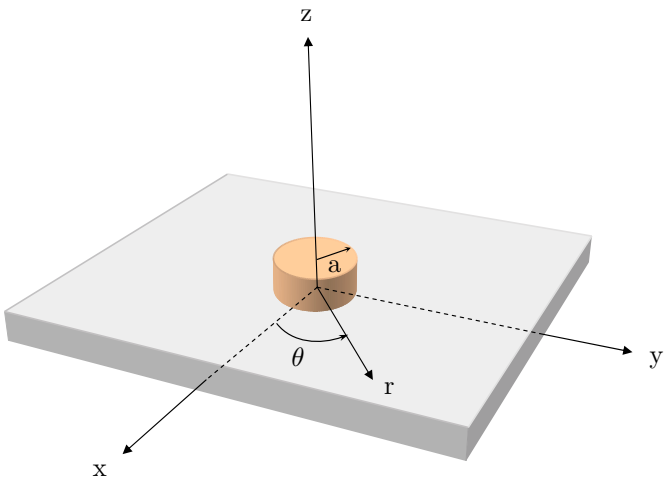

Figure D.1: An axisymmetric normal excitation on an infinite plate.

where c_L and c_T are longitudinal and shear wave velocities in the plate, respectively.

Recall the Hankel transform of order ν of a function $f(r)$ and its corresponding inverse transform, which are, respectively, defined as

$$\mathcal{H}_\nu\{f(r)\} = \tilde{f}^{(\nu)}(k) = \int_0^\infty r f(r) J_\nu(kr)\, dr, \tag{D.3}$$

and

$$\mathcal{H}_\nu^{-1}\{\tilde{f}^{(\nu)}(k)\} = f(r) = \int_0^\infty k \tilde{f}^{(\nu)}(k) J_\nu(kr)\, dk, \tag{D.4}$$

where $J_\nu(x)$ is the Bessel function of the first kind of order ν with $\nu \geq -\frac{1}{2}$. The function f is assumed to be piecewise continuous and of bounded variation[1]. The condition that guarantees the integrability of the integral in Equation (D.3) is

$$\int_0^\infty \sqrt{r}|f(r)|\, dr < \infty.$$

Such a condition can be easily satisfied by, for example, $f \to 0$ as $r \to \infty$ (note that f is already assumed to be piecewise continuous and of bounded variation). With the above

[1]The function $f : [a, b] \to \mathbf{R}$ is of *bounded variation* if the variations of f over a partition $P = \{a = t_0 < t_1 < \cdots < t_n = b\}$, $V(f, P)$, defined by

$$V(f, P) = \sum_{i=1}^{n} |f(t_i) - f(t_{i-1})|,$$

are bounded above, independent of the partition P [14].

definition, one can establish the relation (see details in Appendix A.6.1)

$$\int_0^\infty r\left[\frac{d^2f(r)}{dr^2}+\frac{1}{r}\frac{df(r)}{dr}-\frac{\nu^2}{r^2}f(r)\right]J_\nu(kr)\,dr=-k^2\tilde{f}^{(\nu)}(k), \tag{D.5}$$

where, in this relation, all Hankel transforms of f and its first and second derivatives are assumed to exist.

Application of the Hankel transforms of order 0 and 1 to the variable r in the two equations of (D.2), respectively, with the use of the relation (D.5), reduces two partial differential equations to two ordinary differential equations

$$\begin{aligned}\frac{d^2\tilde{\phi}^{(0)}}{dz^2}+\alpha_L^2\tilde{\phi}^{(0)} &= 0\\ \frac{d^2\tilde{\psi}^{(1)}}{dz^2}+\alpha_T^2\tilde{\psi}^{(0)} &= 0,\end{aligned} \tag{D.6}$$

where the parameters α_L and α_T are defined earlier in Section 2.1.4 or in Equations (4.60) (without the indices mn).

The general solutions in the transformed domain of the two equations in (D.6) are

$$\begin{aligned}\tilde{\phi}^{(0)} &= A_1\cos(\alpha_L z)+A_2\sin(\alpha_L z)\\ \tilde{\psi}^{(1)} &= B_1\cos(\alpha_T z)+B_2\sin(\alpha_T z),\end{aligned} \tag{D.7}$$

where the constants (each of which can depend on the parameter k) are to be determined from the boundary conditions. Subsequently, following the relationships (4.56), (4.57), (4.61) and (4.62) (without the indices mn), together with the identities (see details in Appendix A.6.2):

$$\begin{aligned}\mathcal{H}_1\{f'(r)\} &= -k\tilde{f}^{(0)}(k)\\ \mathcal{H}_0\Big\{g'(r)+\frac{g(r)}{r}\Big\} &= k\tilde{g}^{(1)}(k),\end{aligned} \tag{D.8}$$

the displacement and stress components in the proper transformed domain can be derived

as

$$\begin{aligned}
\tilde{u}_r^{(1)} &= -k\tilde{\phi}^{(0)} - \frac{d\tilde{\psi}^{(1)}}{dz} \\
&= -\Big[kA_1\cos(\alpha_L z) + \alpha_T B_2\cos(\alpha_T z)\Big] - \Big[kA_2\sin(\alpha_L z) - \alpha_T B_1\sin(\alpha_T z)\Big] \quad \text{(D.9)} \\
\tilde{u}_z^{(0)} &= \frac{d\tilde{\phi}^{(0)}}{dz} + k\tilde{\psi}^{(1)} \\
&= \Big[-\alpha_L A_1\sin(\alpha_L z) + kB_2\sin(\alpha_T z)\Big] + \Big[\alpha_L A_2\cos(\alpha_L z) + kB_1\cos(\alpha_T z)\Big] \\
& \qquad \text{(D.10)} \\
\tilde{\sigma}_{zz}^{(0)} &= \mu\frac{c_L^2}{c_T^2}\Big(k\tilde{u}_r^{(1)} + \frac{d\tilde{u}_z^{(0)}}{dz}\Big) - 2\mu k\tilde{u}_r^{(1)} \\
&= -\mu\Big\{\Big[(\alpha_T^2 - k^2)A_1\cos(\alpha_L z) - 2k\alpha_T B_2\cos(\alpha_T z)\Big] \\
&\qquad + \Big[(\alpha_T^2 - k^2)A_2\sin(\alpha_L z) + 2k\alpha_T B_1\sin(\alpha_T z)\Big]\Big\} \quad \text{(D.11)} \\
\tilde{\sigma}_{zr}^{(1)} &= \mu\Big(\frac{d\tilde{u}_r^{(1)}}{dz} - k\tilde{u}_z^{(0)}\Big) \\
&= \mu\Big\{\Big[2k\alpha_L A_1\sin(\alpha_L z) + (\alpha_T^2 - k^2)B_2\sin(\alpha_T z)\Big] \\
&\qquad + \Big[-2k\alpha_L A_2\cos(\alpha_L z) + (\alpha_T^2 - k^2)B_1\cos(\alpha_T z)\Big]\Big\}. \quad \text{(D.12)}
\end{aligned}$$

These field quantities must satisfy the boundary conditions and then all constants become specified. Before the boundary conditions are imposed, they have to be also transformed into the same domain as the field quantities (z-k domain). The proper Hankel transform of the conditions in (D.1) are (see details in Appendix A.6.3)

$$\begin{cases}
\tilde{\sigma}_{zz}^{(0)}(z=h) = \frac{aJ_1(ka)\bar{Q}}{k} \\
\tilde{\sigma}_{zz}^{(0)}(z=-h) = 0 \\
\tilde{\sigma}_{zr}^{(1)}(z=\pm h) = 0.
\end{cases} \quad \text{(D.13)}$$

Satisfying the boundary conditions results in a system of linear equations[2] which can

[2]Unlike in the free-vibration analysis, this system is non-homogeneous due to the non-homogeneous boundary conditions.

be written in a matrix form as

$$\begin{bmatrix} -(\alpha_T^2-k^2)\cos(\alpha_L h) & 2k\alpha_T\cos(\alpha_T h) & -(\alpha_T^2-k^2)\sin(\alpha_L h) & -2k\alpha_T\sin(\alpha_T h) \\ 2k\alpha_L\sin(\alpha_L h) & (\alpha_T^2-k^2)\sin(\alpha_T h) & -2k\alpha_L\cos(\alpha_L h) & (\alpha_T^2-k^2)\cos(\alpha_T h) \\ -(\alpha_T^2-k^2)\cos(\alpha_L h) & 2k\alpha_T\cos(\alpha_T h) & (\alpha_T^2-k^2)\sin(\alpha_L h) & 2k\alpha_T\sin(\alpha_T h) \\ -2k\alpha_L\sin(\alpha_L h) & -(\alpha_T^2-k^2)\sin(\alpha_T h) & -2k\alpha_L\cos(\alpha_L h) & (\alpha_T^2-k^2)\cos(\alpha_T h) \end{bmatrix}$$

$$\times \begin{Bmatrix} A_1 \\ B_2 \\ A_2 \\ B_1 \end{Bmatrix} = \frac{aJ_1(ka)\bar{Q}}{\mu k} \begin{Bmatrix} 1 \\ 0 \\ 0 \\ 0 \end{Bmatrix}. \quad \text{(D.14)}$$

Inversion of the above equations gives the values of constants (see details in Appendix A.6.4):

$$\begin{Bmatrix} A_1 \\ B_2 \end{Bmatrix} = \frac{aJ_1(ka)}{2\mu k}\frac{\bar{Q}}{R_s} \begin{Bmatrix} -(\alpha_T^2-k^2)\sin(\alpha_T h) \\ 2k\alpha_L\sin(\alpha_L h) \end{Bmatrix}, \quad \text{(D.15)}$$

$$\begin{Bmatrix} A_2 \\ B_1 \end{Bmatrix} = \frac{aJ_1(ka)}{2\mu k}\frac{\bar{Q}}{R_a} \begin{Bmatrix} -(\alpha_T^2-k^2)\cos(\alpha_T h) \\ -2k\alpha_L\cos(\alpha_L h) \end{Bmatrix}, \quad \text{(D.16)}$$

(D.17)

where the functions R_s and R_a are the dispersion relations of symmetric and anti-symmetric Lamb wave modes, respectively; both functions are given by Equations (2.26) and (2.28). The frequency ω is understood as a given parameter in the excitation, so R_s and R_a are functions of k only.

For a normal point excitation of magnitude Q, the radius a of the excitation is taken to be approaching zero while the total magnitude $\bar{Q}\pi a^2$ is kept fixed to Q. From the limiting form of $J_1(x)$ when the argument x is small (Section 9.1.7 of Reference [1]):

$$J_\nu(x) \sim \left(\frac{x}{2}\right)^\nu \frac{1}{\Gamma(\nu+1)}, \qquad (\nu \neq -1, -2, -3, \ldots),$$

where $\Gamma(n)$ is the Gamma function, i.e. $\Gamma(n) = (n-1)!$ for an integer n, the following limit

can be obtained

$$\begin{aligned}\lim_{a\to 0}\frac{aJ_1(ka)\bar{Q}}{k} &= \lim_{a\to 0}\frac{aJ_1(ka)}{k}\frac{Q}{\pi a^2}\\ &= \frac{a}{k}\frac{ka}{2}\frac{Q}{\pi a^2}\\ &= \frac{Q}{2\pi}.\end{aligned} \tag{D.18}$$

In fact, Equation (D.18) can be obtained directly if the normal stress on the top surface of a plate in (D.1) is prescribed as $\sigma_{zz}(z=h,r)=\frac{\delta(r)}{2\pi r}Q$ to represent a normal point excitation (see Equation (4.85)). In this case, it is not difficult to see that the Hankel transform of order 0 of this normal point excitation function becomes a constant in Equation (D.18). Hence, due to the point excitation, the displacement components in the transformed domain, separated into symmetric and anti-symmetric parts (the total displacement is the summation of both parts) in the same manner as in Section 2.1.4 (the symmetric modes involve the constants in Equation (D.15) and the anti-symmetric modes involve the constants in Equation (D.16)), are given by

Symmetric modes

$$\begin{aligned}\tilde{u}_r^{(1)}(z) &= \frac{Q}{4\pi\mu}\frac{k(\alpha_T^2-k^2)\sin(\alpha_T h)\cos(\alpha_L z)-2k\alpha_L\alpha_T\sin(\alpha_L h)\cos(\alpha_T z)}{R_s(k)}\\ \tilde{u}_z^{(0)}(z) &= \frac{Q}{4\pi\mu}\frac{\alpha_L(\alpha_T^2-k^2)\sin(\alpha_T h)\sin(\alpha_L z)+2k^2\alpha_L\sin(\alpha_L h)\sin(\alpha_T z)}{R_s(k)}.\end{aligned} \tag{D.19}$$

Anti-symmetric modes

$$\begin{aligned}\tilde{u}_r^{(1)}(z) &= \frac{Q}{4\pi\mu}\frac{k(\alpha_T^2-k^2)\cos(\alpha_T h)\sin(\alpha_L z)-2k\alpha_L\alpha_T\cos(\alpha_L h)\sin(\alpha_T z)}{R_a(k)}\\ \tilde{u}_z^{(0)}(z) &= -\frac{Q}{4\pi\mu}\frac{\alpha_L(\alpha_T^2-k^2)\cos(\alpha_T h)\cos(\alpha_L z)+2k^2\alpha_L\cos(\alpha_L h)\cos(\alpha_T z)}{R_a(k)}.\end{aligned} \tag{D.20}$$

Then, the displacement in the original r-domain can be analytically obtained through the inverse Hankel transform defined in Equation (D.4). According to the excitability defined in Section 4.3.2, of the most interest in this research is the out-of-plane component of the displacement at the surface of the plate ($z=h$). Let the subscripts s and a indicate the symmetric and anti-symmetric modes, respectively; from Equations (D.19) and (D.20),

the normal component of the displacement can be expressed in an integral form as

$$u_{z;s}(r,h) = \frac{Q}{4\pi\mu}\frac{\omega^2}{c_T^2}\int_0^\infty k\alpha_L \sin(\alpha_T h)\sin(\alpha_L h)\frac{J_0(kr)}{R_s}\,dk \tag{D.21}$$

$$u_{z;a}(r,h) = -\frac{Q}{4\pi\mu}\frac{\omega^2}{c_T^2}\int_0^\infty k\alpha_L \cos(\alpha_T h)\cos(\alpha_L h)\frac{J_0(kr)}{R_a}\,dk. \tag{D.22}$$

The integrals in the above equations will be done in the complex k-plane. By the natures of all functions involved in these two integrals, one will need to evaluate the integral of a generic form

$$I = \int_0^\infty \frac{G(k)}{R(k)}J_0(kr)\,dk = \int_0^\infty G_o(k)J_0(kr)\,dk, \tag{D.23}$$

where the functions $G(k)$ and $R(k)$ are odd and even functions of k, respectively, and thus, the net function $G_o(k) = \frac{G(k)}{R(k)}$ becomes an odd function of k. A usual trick is to extend the limit of the integration to cover the entire real line (or sometimes imaginary line) in order to create a closed semicircular contour to which the residue theorem can be applied. To do this, first, start from the identities in Sections 9.1.35 and 9.1.36 of Reference [1] ($m = 1$ and $\nu = 0$):

$$\begin{aligned} J_\nu(-z) &= J_\nu(z) \\ Y_\nu(-z) &= Y_\nu(z) + 2jJ_0(z), \end{aligned} \tag{D.24}$$

where $Y_\nu(z)$ is the Bessel function of the second kind of order ν. By the definition of the Hankel function of the first kind,

$$H_\nu^{(1)}(z) = J_\nu(z) + jY_\nu(z), \tag{D.25}$$

with the identities in Equations (D.24), one can obtain

$$\begin{aligned} H_0^{(1)}(z) &= J_0(z) + jY_0(z) \\ H_0^{(1)}(-z) &= J_0(-z) + jY_0(-z) \\ &= -J_0(z) + jY_0(z). \end{aligned}$$

Subtraction of the two equations above results in the identity

$$J_0(z) = \frac{1}{2}\big[H_0^{(1)}(z) - H_0^{(1)}(-z)\big]. \tag{D.26}$$

Thus, substitution of this identity into Equation (D.23) gives

$$\begin{aligned} I &= \frac{1}{2}\int_0^\infty G_o(k)\big[H_0^{(1)}(kr) - H_0^{(1)}(-kr)\big]\,dk \\ &= \frac{1}{2}\bigg[\int_0^\infty G_o(k)H_0^{(1)}(kr)\,dk - \int_0^\infty G_o(k)H_0^{(1)}(-kr)\,dk\bigg]. \end{aligned}$$

Replacing the integration variable in the second integral by $\tilde{k} = -k$ and using the property: $G_o(-k) = -G_o(k)$, one can obtain the integral in the above equation as

$$\begin{aligned} I &= \frac{1}{2}\bigg[\int_0^\infty G_o(k)H_0^{(1)}(kr)\,dk - \int_0^{-\infty}\big[-G_o(\tilde{k})\big]H_0^{(1)}(\tilde{k}r)\,(-d\tilde{k})\bigg] \\ &= \frac{1}{2}\int_{-\infty}^{\infty} G_o(k)H_0^{(1)}(kr)\,dk. \end{aligned} \tag{D.27}$$

In Equation (D.27), the principal value of this integral is implicitly assumed.

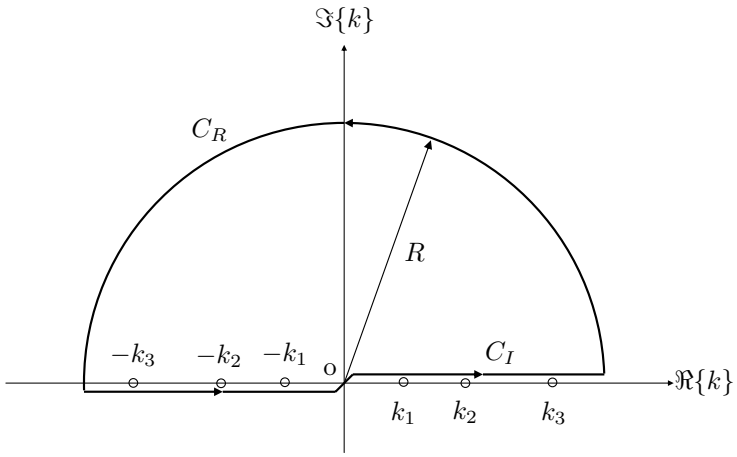

Figure D.2: A closed contour in the complex k-plane used to evaluate the integral I in Equation (D.27).

Consider the contour along the real axis. For the purpose of mathematical analysis, the material is assumed to have some dissipation. Then, to ensure waves propagating away from the origin with non-growing amplitudes, the complex wavenumbers k with a positive real part must have the negative imaginary part for a time-harmonic factor of $e^{j\omega t}$ (see Section 3.1). This statement implies that, in general, the roots of the function $R(k)$ or the poles of the function $G_o(k)$ are in quadrant 4. Since the function $R(k)$ is even with respect

to k, there are also roots in quadrant 2 as mirror images (with respect to the origin) to those roots in quadrant 4. In the limiting case of no dissipation, those roots in quadrants 4 and 2 approach the real axis from below and above, respectively. Therefore, the contour of the integration along the real axis is indeed below quadrant 2 and above quadrant 4 (see Figure D.2) to ensure inclusion of all proper poles. The contour of integration is closed by a semicircular arc of radius R (not to be confused with the function $R(k)$) in the upper half-plane. The choice is made from the fact that $|H_0^{(1)}(kr)| \to 0$ as $|k| \to \infty$. This fact allows the application of Jordan's lemma[3] with the use of the asymptotic expression of $H_0^{(1)}(z)$ for large $|z|$. Another consideration concerns branch points since function $G_o(k)$ involves radicals $\alpha_L = \sqrt{\frac{\omega^2}{c_L^2} - k^2}$ and $\alpha_T = \sqrt{\frac{\omega^2}{c_T^2} - k^2}$. However, since $G_o(k)$ is an even function of both α_L and α_T, $G_o(k)$ becomes a single-valued function of k and thus, the integrand in Equation (D.27) does not possess branch points (this statement is true for both symmetric and anti-symmetric cases). Hence, the final closed contour is shown in Figure D.2 with real poles on the real axis.

Jordan's lemma implies that

$$\lim_{R\to\infty} \int_{C_R} G_o(k) H_0^{(1)}(kr)\, dk = 0.$$

Then, by the residue theorem[4], with only negative zeros of $R(k)$, $-k_1$, $-k_2$, ..., $-k_{N_M}$

[3]Jordan's lemma [79] states that, for a function $f(z)$ of a complex variable z, if (i) $f(z)$ is analytic in the upper half-plane except for a finite number of poles, (ii) the maximum of $|f(z)| \to 0$ as $|z| \to \infty$ in the upper half-plane, and (iii) $m > 0$, then

$$I_{C_R} = \int_{C_R} e^{jmz} f(z)\, dz \to 0 \text{ as } R \to \infty,$$

where C_R is the semicircular contour shown in Figure D.2.

[4]The residue theorem [11] states that, if $f(z)$ is analytic inside and on a positively-oriented simple closed contour C, except for a finite number of poles z_n, $n = 1, 2, \ldots, N$ inside C, then

$$\int_C f(z)\, dz = 2\pi j \sum_{n=1}^{N} \operatorname*{Res}_{z=z_n} f(z),$$

where $\text{Res}_{z=z_n} f(z)$ is the residues of $f(z)$ at its pole z_n.

included in the closed contour $C_I \cup C_R$, the integral

$$\begin{aligned} I &= \frac{1}{2} \lim_{R\to\infty} \int_{C_I \cup C_R} G_o(k) H_0^{(1)}(kr)\, dk \\ &= \pi j \sum_{n=1}^{N_M} \operatorname*{Res}_{k=-k_n} \frac{G(k)}{R(k)} H_0^{(1)}(kr), \end{aligned} \tag{D.28}$$

where N_M is the number of zeros of $R(k)$ for a given frequency ω. This number is the number of Lamb mode existing at that frequency, which is finite (and in fact, not smaller than two).

By analysis, almost all poles of the integrand (zeros of $R(k)$) on the real axis are simple poles [94]. Therefore, if the contributions of higher-order poles are neglected, the integral I from the above equation is evaluated as

$$I = \pi j \sum_{n=1}^{N_M} \frac{G(-k_n)}{R'(-k_n)} H_0^{(1)}(-k_n r), \tag{D.29}$$

where the formula [11]

$$\operatorname*{Res}_{z=z_n} \frac{p(z)}{q(z)} = \frac{p(z_n)}{q'(z_n)} \tag{D.30}$$

is used, and $'$ denotes the derivative with the argument.

With the properties: $G(-k) = -G(k)$, $R'(-k) = -R'(k)$ (since $R(k)$ is an even function) and the identity $H_0^{(1)}(-z) = -H_0^{(2)}(z)$, where $H_0^{(2)}(z)$ is the Hankel function of the second kind of order 0 defined by

$$H_\nu^{(2)}(z) = J_\nu(z) - jY_\nu(z), \tag{D.31}$$

the value of I in Equation (D.29) can be written in terms of a function of positive real roots k_n of $R(k)$ as

$$I = -\pi j \sum_{n=1}^{N_M} \frac{G(k_n)}{R'(k_n)} H_0^{(2)}(k_n r). \tag{D.32}$$

Application of Equation (D.32) to Equations (D.21) and (D.22) gives the out-of-plane displacement of symmetric and anti-symmetric Lamb modes at the surface of the plate as

$$u_{z;s}(r,h) = -j \frac{Q}{4\mu} \frac{\omega^2}{c_T^2} \sum_{n=1}^{N_s} \frac{k_n \alpha_{L;n} \sin(\alpha_{T;n} h) \sin(\alpha_{L;n} h)}{R_s'(k_n)} H_0^{(2)}(k_n r) \tag{D.33}$$

$$u_{z;a}(r,h) = j \frac{Q}{4\mu} \frac{\omega^2}{c_T^2} \sum_{n=1}^{N_a} \frac{k_n \alpha_{L;n} \cos(\alpha_{T;n} h) \cos(\alpha_{L;n} h)}{R_a'(k_n)} H_0^{(2)}(k_n r), \tag{D.34}$$

where N_s and N_a are numbers of existing symmetric and anti-symmetric Lamb modes at a given frequency ω, respectively ($N_s + N_a = N_M$); $\alpha_{L;n}$ and $\alpha_{T;n}$ are α_L and α_T evaluated at k_n. The individual term in the series of either (D.33) or (D.34) represents the contribution of that individual Lamb mode. In other words, the contribution of a symmetric Lamb mode n, to the out-of-plane displacement at the surface of the plate, $u_{z;s;n}(r,h)$ is

$$u_{z;s;n}(r,h) = -j\frac{Q}{4\mu}\frac{\omega^2}{c_T^2}\frac{k_n\alpha_{L;n}\sin(\alpha_{T;n}h)\sin(\alpha_{L;n}h)}{R_s'(k_n)}H_0^{(2)}(k_n r), \tag{D.35}$$

and, similarly, the contribution of an anti-symmetric Lamb mode n, $u_{z;a;n}(r,h)$, is

$$u_{z;a;n}(r,h) = j\frac{Q}{4\mu}\frac{\omega^2}{c_T^2}\frac{k_n\alpha_{L;n}\cos(\alpha_{T;n}h)\cos(\alpha_{L;n}h)}{R_a'(k_n)}H_0^{(2)}(k_n r). \tag{D.36}$$

Hence, by the definition defined in Reference [99], the excitability of symmetric or anti-symmetric Lamb mode n, $E_{s;n}$ or $E_{a;n}$, respectively, as a function of frequency, in this case is the coefficient of the Hankel function normalized by the strength of the excitation, Q, i.e.

$$\begin{aligned} E_{s;n}(\omega) &= -\frac{j}{4\mu}\frac{\omega^2}{c_T^2}\frac{k_n\alpha_{L;n}\sin(\alpha_{T;n}h)\sin(\alpha_{L;n}h)}{R_s'(k_n)} \\ E_{a;n}(\omega) &= \frac{j}{4\mu}\frac{\omega^2}{c_T^2}\frac{k_n\alpha_{L;n}\cos(\alpha_{T;n}h)\cos(\alpha_{L;n}h)}{R_a'(k_n)}. \end{aligned} \tag{D.37}$$

The magnitudes of E_s and E_a for a 1-mm-thick aluminum plate with the properties given in Section 4.3.1 are plotted in Figure D.3. In the figure, E_s's are plotted as solid lines while E_a's are plotted as dashed lines.

It is important to note that, in fact, besides a *finite* number of real zeros, the function $R(k)$ also possesses *infinitely many* complex and imaginary zeros even in the case of no dissipation. The existence of these zeros leads to additional poles in the complex k-plane which, strictly speaking, must be included in the summation in Equation (D.32). However, compared to those of the real poles, the contributions of these complex and imaginary poles are very small after a distance far enough from the excitation [94]. At a radial distance of 30–40 times of the plate thickness as studied in the experiment in this research, the contributions of those complex poles can be ignored. This behavior can be physically explained as the following. For a non-absorbing plate (or a plate with no dissipation), those complex and imaginary zeros of $R(k)$ correspond to attenuated and non-propagating

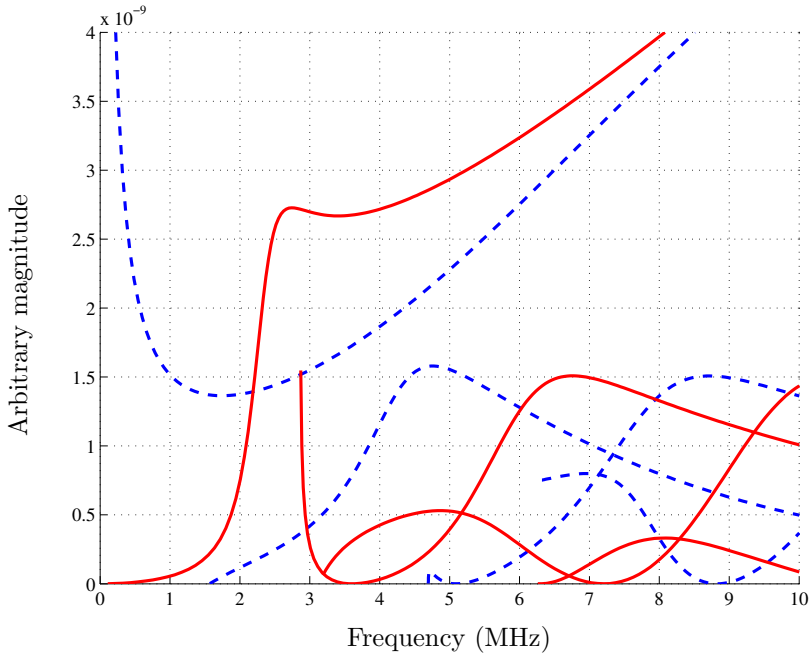

Figure D.3: Excitability of symmetric (solid lines) and anti-symmetric (dashed lines) modes of the circularly-spreading Lamb waves in an 1-mm-aluminum plate (Equations (D.37)).

Lamb modes, respectively, which characterize only local vibration near the excitation and do not carry energy along the plate. Therefore, at far away from the excitation, their contributions to the vibration (thus displacement) vanish. However, this is not true if the plate is absorbing because those non-propagating modes become propagating modes [88]. In this latter case, all of those zeros or at least some of them must be included in the calculation of the total displacement.

APPENDIX E

MODAL DECOMPOSITION OF DOUBLE-MODE LAMB WAVE SIGNALS

This appendix carries out the idea of "modal" decomposition of Lamb wave signal introduced in Section 7.3. This development considers general broadband time-domain signals, but attenuation is excluded for simplicity. That is, this section attempts to develop the modal decomposition technique for Lamb waves in a free elastic plate. The time-domain signals used in the development are double-mode signals. This consideration suffices since the scenario when more than two Lamb modes exist is just an extension of this development. Thus, the same concept can be extended with another level of complication but no new issues.

E.1 Modal decomposition by mode cancellation

This research starts with the technique, which will be called the "mode-cancellation" technique. The idea of this technique is to measure time-domain signals at two different propagation distances (for double-mode decomposition) and use one signal to cancel one mode in the other signal. This cancellation can be done since the propagation characteristics of the mode to be eliminated are known. The remaining signal will contain only one mode, but its amplitude is modified. The modification factor can be calculated from the propagation characteristics of both modes; hence, the strength of the present mode can also be calculated. Then, the strength of the eliminated mode follows from the known relative excitability between the two modes. Finally, the phase of the excitation is calculated and the decomposition is achieved.

E.1.1 Theoretical derivation

Consider Lamb waves in an infinite, elastic plate. Let the excitation be a normally-applied point force so that Lamb waves are propagating axisymetrically. Assume that only two of the Lamb wave modes are excited or measured; those two modes are referred to as modes 1 and 2. If the excitation is harmonic, i.e. $f(t) = Qe^{j\omega t}$, the response of interest—such as the out-of-plane displacement at the surface of the plate—of an individual Lamb mode at any point r away from the excitation in cylindrical coordinates (t, r) $(z = 0)$, can be expressed by Equation (4.134). This equation suggests that the total measured double-mode signal, $s(t, r)$ is of the form

$$s(t,r) = E_1(\omega)\tilde{A}(\omega)H_0^{(2)}(k_1 r)e^{j\omega t} + E_2(\omega)\tilde{A}(\omega)H_0^{(2)}(k_2 r)e^{j\omega t}, \tag{E.1}$$

where $\tilde{A}(\omega)$ is, in general, complex-valued ($\tilde{}$ in this section will indicate a complex quantity); E_1 and E_2 are "real-valued" excitabilities of modes 1 and 2, respectively[1]; $H_0^{(2)}$ is the second Hankel function of order 0.

As seen in Appendix D, E_1 and E_2 depend on the propagation characteristics of the corresponding Lamb modes, frequency ω, and the quantity field which is measured. In the far-field (large kr), following the same approximation leading to Equation (4.137) in Section 4.3.2, the spreading-normalized ($\sqrt{r}$-normalized) signal can be expressed as

$$\begin{aligned} \hat{s}(t,r) &= \sqrt{r}s(t,r) \\ &= \hat{E}_1\tilde{B}e^{j(\omega t - k_1 r)} + \hat{E}_2\tilde{B}e^{j(\omega t - k_2 r)}, \end{aligned} \tag{E.2}$$

where $\hat{E}_1 = \frac{E_1}{\sqrt{k_1}}$ and $\hat{E}_2 = \frac{E_1}{\sqrt{k_1}}$ are net (real) excitabilities of modes 1 and 2, respectively, and $\tilde{B} = \tilde{A}\sqrt{\frac{2}{\pi}}e^{j\frac{\pi}{4}}$ is the net source strength (complex-valued).

Now, let two time-domain signals be recorded at two propagation distances, say r_1 and

[1]The two excitabilities can be made real-valued by associating any of their present imaginary units into the complex amplitude $\tilde{A}$.

r_2 with $r_1 < r_2$. According to the aforementioned derivation and notation, the spreading-normalized, double-mode signals at those two locations, r_1 and r_2, are

$$\begin{aligned}\hat{s}_1(t) &= \hat{E}_1\tilde{B}e^{j(\omega t-k_1r_1)} + \hat{E}_2\tilde{B}e^{j(\omega t-k_2r_1)} \\ \hat{s}_2(t) &= \hat{E}_1\tilde{B}e^{j(\omega t-k_1r_2)} + \hat{E}_2\tilde{B}e^{j(\omega t-k_2r_2)}.\end{aligned}$$

If mode 2 is the mode to be eliminated, the combined signal at one location, say r_2, is manually propagated back to the location r_1 using the propagation characteristics of mode 2, and also phase-shifted by 180 degrees. This signal is called the "cancelling" signal; it is defined by

$$\begin{aligned}\hat{s}_{2\to1}(t) &= e^{-j\left[k_2(r_1-r_2)+\pi\right]}\hat{s}_2(t) \\ &= -\hat{E}_1\tilde{B}e^{j\left[\omega t-k_1r_2+k_2(r_2-r_1)\right]} - \hat{E}_2\tilde{B}e^{j(\omega t-k_2r_1)}. \qquad \text{(E.3)}\end{aligned}$$

This modified signal is then added to the signal originally recorded at the propagation distance r_1. The resulting signal will be a single-mode signal with both phase and magnitude modified (called a modified single-mode signal):

$$\begin{aligned}\hat{s}_{1,t}(t) &= \hat{s}_1(t) + \hat{s}_{2\to1}(t) \\ &= \hat{E}_1\tilde{B}e^{j(\omega t-k_1r_1)}\left(1 - e^{-j\left[k_1(r_2-r_1)-k_2(r_2-r_1)\right]}\right) \\ &= \hat{E}_1\tilde{B}\tilde{G}e^{j(\omega t-k_1r_1)}, \qquad \text{(E.4)}\end{aligned}$$

where $\tilde{G} = 1 - e^{-j\left[k_1(r_2-r_1)-k_2(r_2-r_1)\right]} = 1 - e^{j(k_2-k_1)(r_2-r_1)}$ is the complex modification factor. Consider the magnitude of the Fourier transform of a single-mode signal $\hat{s}_{1,t}(t)$:

$$\begin{aligned}\hat{S}_{1,t} &= \mathrm{FT}\{\hat{s}_{1,t}(t)\} \\ &= \hat{E}_1\tilde{B}\tilde{G}e^{-jk_1r_1} \qquad \text{(E.5)} \\ |\hat{S}_{1,t}| &= \hat{E}_1|\tilde{B}||\tilde{G}|. \qquad \text{(E.6)}\end{aligned}$$

The combined effect of source strength and excitability which represents the total strength of mode 1 can be calculated by

$$\begin{aligned}C_1 &= \hat{E}_1|\tilde{B}| \\ &= \frac{|\hat{S}_{1,t}|}{|\tilde{G}|} \qquad \text{(E.7)}\end{aligned}$$

Once C_1 is calculated, with the known excitability ratio between two modes, the total strength of mode 2, C_2 easily follows as

$$\begin{aligned} C_2 &= \hat{E}_2|\tilde{B}| \\ &= \gamma C_1, \end{aligned} \tag{E.8}$$

where $\gamma = \frac{\hat{E}_2}{\hat{E}_1}$ is the excitability ratio between two modes at this specific frequency.

Let $\tilde{S}_1 = \mathrm{FT}\{(\hat{s}_1(t)\}$ be the Fourier transform of the recorded double-mode signal $\hat{s}_1(t)$. Writing $\tilde{B} = |\tilde{B}|e^{j\phi}$ gives

$$\begin{aligned} \tilde{S}_1 &= \hat{E}_1\tilde{B}e^{-jk_1r_1} + \hat{E}_2\tilde{B}e^{-jk_2r_1} \\ &= \hat{E}_1|\tilde{B}|e^{j(\phi-k_1r_1)} + \hat{E}_2|\tilde{B}|e^{j(\phi-k_2r_1)} \\ &= C_1e^{j(\phi-k_1r_1)} + C_2e^{j(\phi-k_2r_1)}. \end{aligned} \tag{E.9}$$

At each frequency, the net phase of an excitation, ϕ, can be calculated using the above relation. For a general case when the excitation function has an arbitrary spectrum, the Fourier integral theorem extends the proposed derivation, provided that the Fourier transform of a signal exists. Explicitly, the decomposed, spreading-normalized, single-mode signals of modes 1 and 2, recorded at the distance r_1 from the source, are given by

$$\begin{aligned} \hat{s}_{1,1}(t) &= \Re\Big\{\mathrm{FT}^{-1}\{C_1(\omega)e^{j[\phi(\omega)-k_1(\omega)r_1]}\}\Big\} \\ \hat{s}_{1,2}(t) &= \Re\Big\{\mathrm{FT}^{-1}\{C_2(\omega)e^{j[\phi(\omega)-k_2(\omega)r_1]}\}\Big\}, \end{aligned} \tag{E.10}$$

where FT^{-1} denotes an inverse Fourier transform operator and $\Re\{\,\}$ represents the real part of the argument.

E.1.2 Verification with synthetic signals

This proposed idea is verified with synthetic double-mode signals developed in Chapter 4 (a 1-mm-thick aluminum plate is a medium). The test signals are bandlimited double-mode signals consisting of the S0 and A0 modes. The propagation distances chosen are 36 and 46 mm. Those test signals are shown as spreading-normalized versions ($\hat{s}$) in Figure E.1. These time-domain signals represent typical pre-conditioned signals as presented in Section 5.4.2.

In Figure E.1, the frequency bandwidth of consideration is 0.3–1.8 MHz (this is the passband of a bandpass filter including the transition zones). From the dispersion curves of this system shown in Figure 2.3 or 6.6, this filtering guarantees that only two Lamb wave modes exist; thus, double-mode signals are obtained as desired. Four individual Lamb modes are shown in Figure E.2.

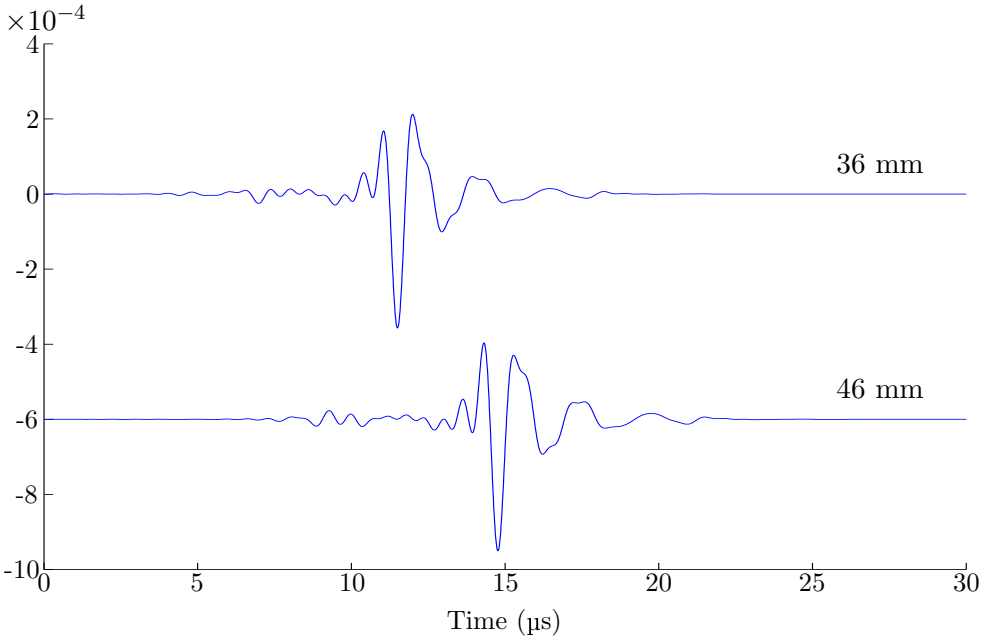

Figure E.1: Two synthetic double-mode signals consisting of the S0 and A0 modes in the frequency range of 0.3–1.8 MHz. The propagation distances are 36 and 46 mm.

From the theory, either mode can be eliminated, but for practical purposes, the larger mode should be retained. Since the retained mode will be used as a basis to calculate every parameter later in the procedure (e.g. the total strengths of itself and the eliminated mode), the larger mode is preferred to minimize numerical problems and reduce the effects of noises in real measurements. Therefore, the A0 mode will be retained in this case.

Let the signal recorded at 36 mm be decomposed. The signal recorded at 46 mm is propagated back to 36 mm and used as a cancelling signal according to Equations (E.3) and (E.4). Operations in these equations are done in the frequency domain. The magnitude spectra of $\hat{s}_{2\rightarrow1}(t)$ and $\hat{s}_{1,t}(t)$ are shown in Figure E.3(a) and (b), respectively. Note that,

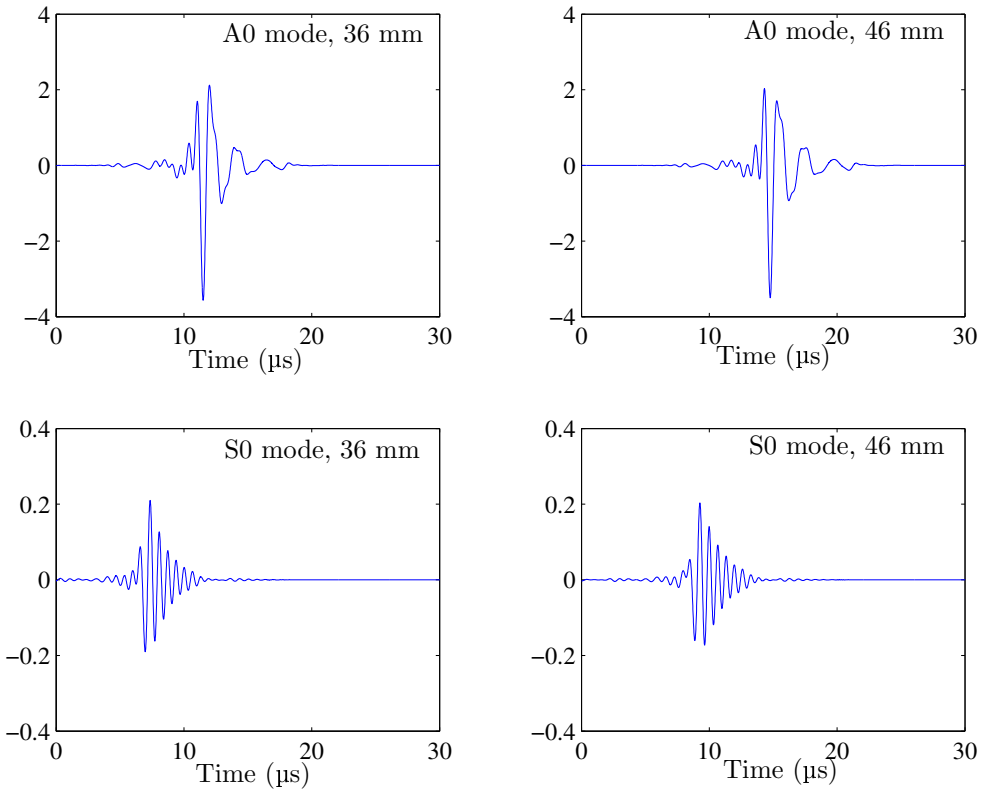

Figure E.2: Individual modal responses of synthetic double-mode signals shown in Figure E.1.

since the spectrum of $\hat{s}_{2\to1}(t)$ is derived from the spectrum of a combined signal at r_2 by nonlinear phase delays, both spectra are the same in magnitude. The complex modification factor $\tilde{G}$ is shown in the same plot as the spectrum of $\hat{s}_{1,t}(t)$ to emphasize that the zeros of both spectra coincide. This fact validates the operation in Equation (E.7), where the limiting process applies if $|\tilde{G}|$ approaches zero. The spectrum of $\hat{s}_{1,t}(t)$ is magnified by 100 times so that it can be shown in the same plot as $|\tilde{G}|$. Note that, since the signals are bandlimited to 0.3–1.8 MHz, the modification factor only in this frequency range needs be calculated.

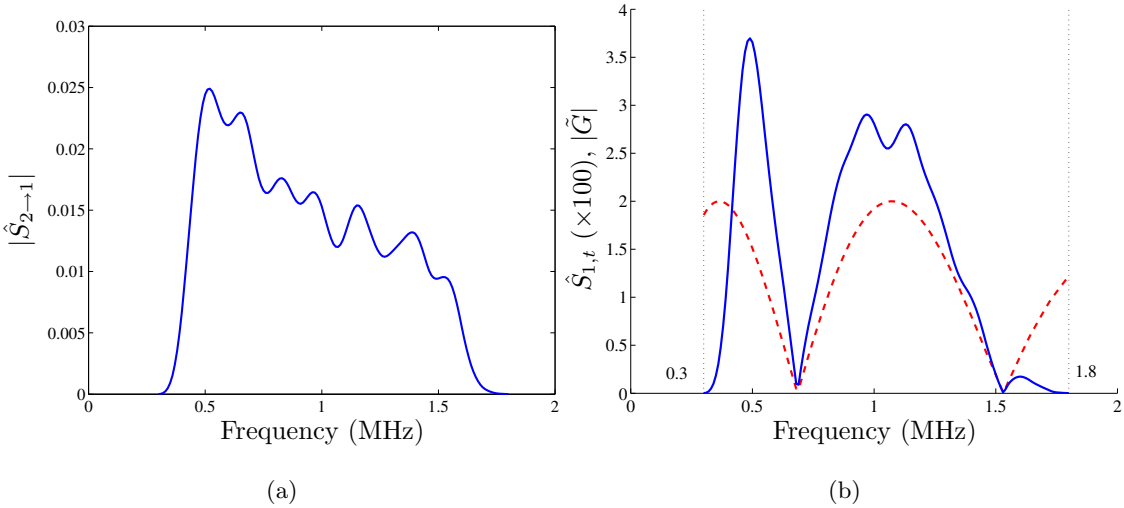

Figure E.3: Intermediate results for the mode cancellation of the S0 mode in the synthetic double-mode signals. Part (a) shows the magnitude spectrum of the cancelling signal, $\hat{s}_{2\to1}(t)$. Part (b) shows the magnitude spectrum of the remaining but modified single-mode signal $\hat{s}_{1,t}(t)$ (solid line) together with the magnitude of the modification factor $\tilde{G}$ (dashed line).

The division of two spectra in Figure E.3 gives the total strength of the A0 mode. The total strength of the S0 mode is then calculated from the relative excitability ratio which can be obtained from the formulas (D.37). Those two total strengths are plotted in Figure E.4 as dots. In the same figure, the exact curves, which are derived from the magnitude spectra of individual responses[2], are also plotted as solid lines for comparison.

Finally, the phase of the net excitation is calculated by solving Equation E.9 for ϕ,

[2]These exact curves are available since each response is separately simulated.

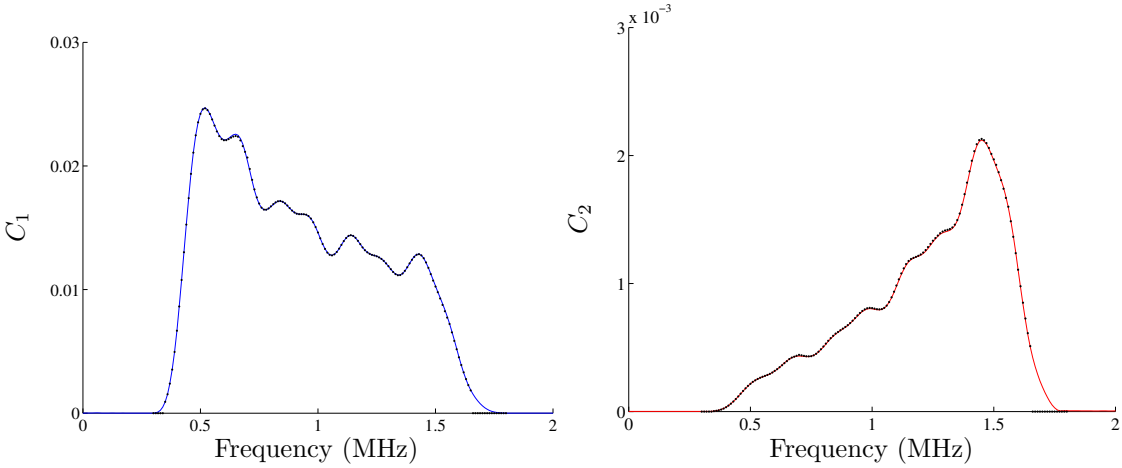

(a) The A0 mode.

(b) The S0 mode.

Figure E.4: Total strengths of the A0 and S0 modes for the signal measured at 36 mm. The plots show the calculated results C_1 and C_2 as dots, for the A0 and S0 modes, respectively. The exact curves, obtained from the magnitude spectra of individual modal responses, are shown by solid lines.

and the double-mode signal is decomposed. Figure E.5 shows the comparison between the decomposed signals and the exact modal responses. This figure shows very good agreement between the decomposed modal signals and simulated individual modal responses. Hence, it can be concluded that this mode-cancellation technique is capable of decomposing a double-mode Lamb wave signal very well, provided that accurate measurements can be achieved.

E.1.3 Implementation with experimental signals

The real performance of the mode-cancellation technique is studied through its implementation with real, experimentally measured signals. Two time-domain signals of Lamb waves in a free plate, measured at 36 and 46 mm are shown in Figure E.6. These signals are made double-mode by bandpass filtering with the filter of passband between 0.3 and 1.8 MHz (the same pre-conditioning process as the one used for synthetic signals). The resulting double-mode Lamb wave signals, which are to be decomposed, are shown in Figure E.7.

The implementation follows the steps described in Section E.1.2. The intermediate results are shown in Figure E.8 when the signal measured at 36 mm is decomposed and

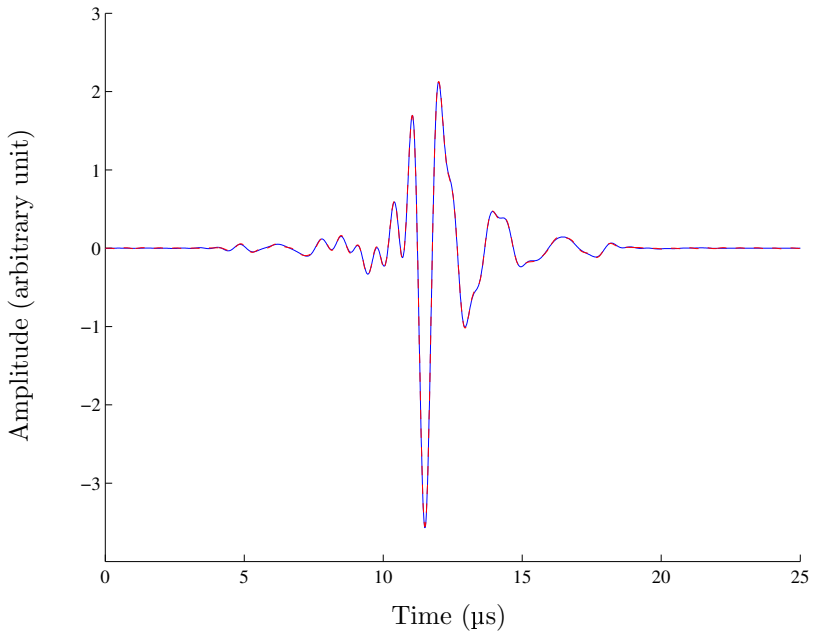

(a) The decomposed A0 mode.

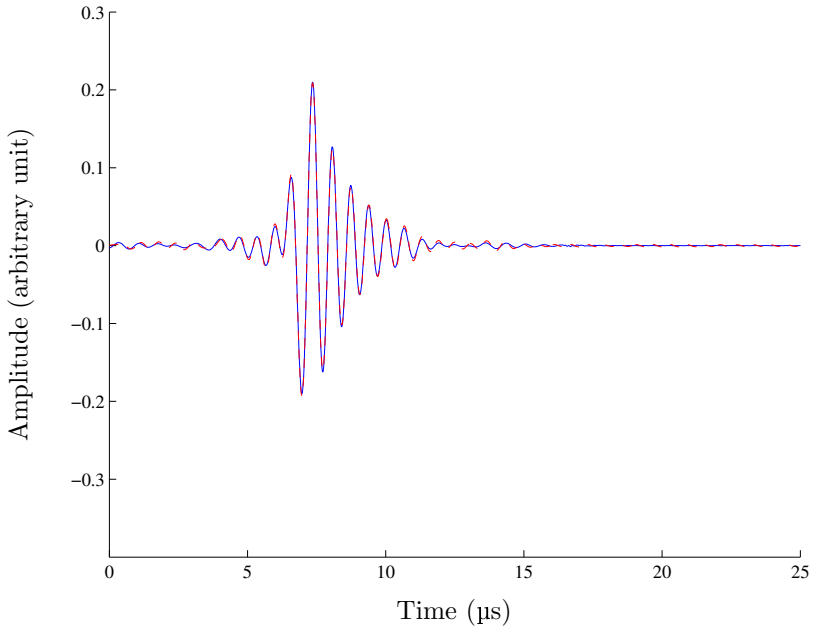

(b) The decomposed S0 mode.

Figure E.5: Final decomposed A0 and S0 modes (dashed lines) by the mode-cancellation technique. Exact modal responses obtained from the simulation are shown in solid lines.

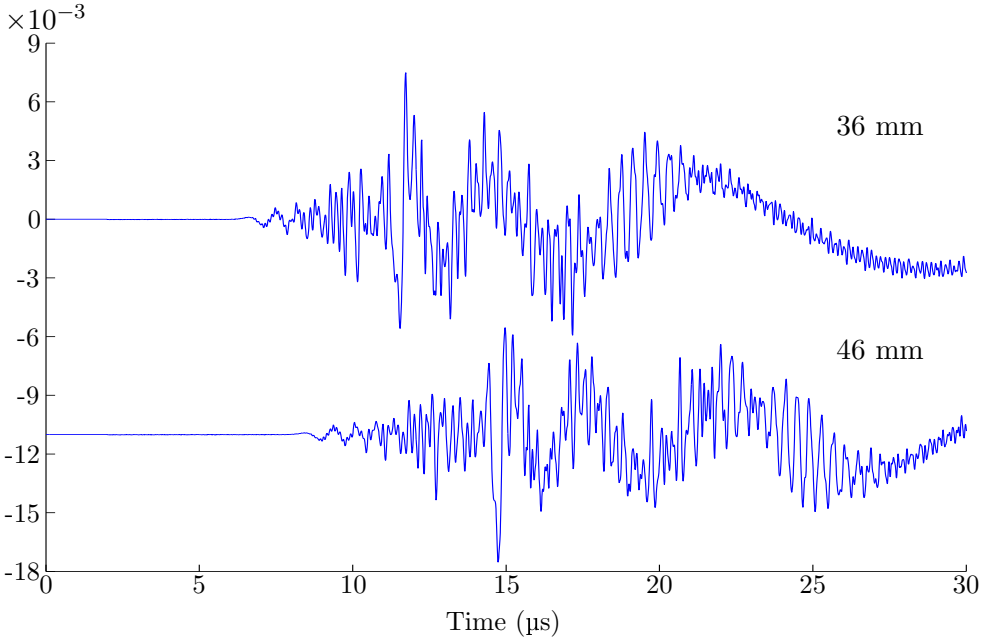

Figure E.6: Two experimental time-domain signals from a free plate, measured at 36 and 46 mm.

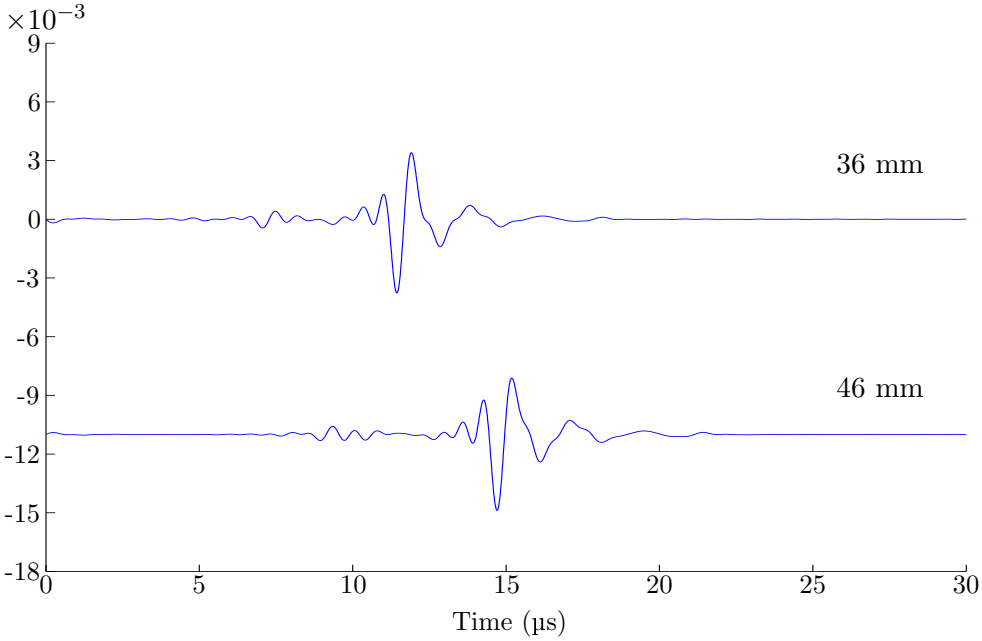

Figure E.7: Two experimental double-mode signals consisting of the S0 and A0 modes between 0.3–1.8 MHz. These signals are the filtered versions of the signals in Figure E.6.

the S0 mode is eliminated. Figure E.8(a) shows the magnitude spectrum of the modified single-mode signal $\hat{s}_{1,t}$ plotted together with the magnitude of the modification factor $\tilde{G}$; Figure E.8(b) shows the calculated total strengths of the two existing modes, where C_1 and C_2 correspond to the total strengths of the A0 and S0 modes, respectively. The final result which are the two decomposed modes of the signal measured at 36 mm are shown in Figure E.9.

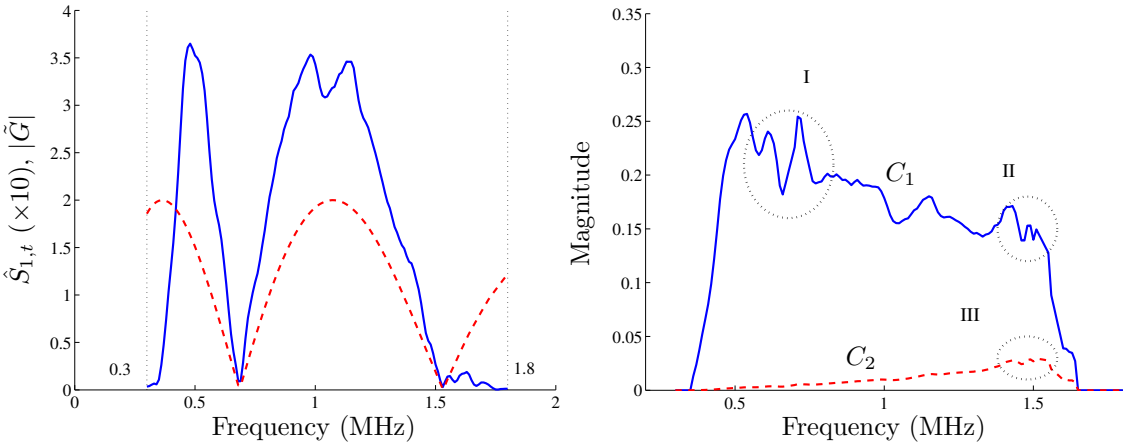

(a) The magnitude spectra of $\hat{s}_{1,t}$ and $\tilde{G}$.

(b) The total strength of decomposed modes.

Figure E.8: Intermediate results for the implementation of the mode-cancellation technique with real time-domain signals.

To verify the results, the reconstructed signal, which is the sum of the two decomposed signals, is compared with the real measured signal (from Figure E.6). This comparison is shown in Figure E.10.

It is seen in the Figure E.10 that the mode-cancellation technique does not work well with the real measured signals although it can capture the dominant part of the signal. Two major discrepancies occur at the beginning and the end of the measured signal. At the beginning of the signal, the decomposition technique gives the component which arrives before the actual first arrival time[3] as a part of the S0 mode. Also, around the end of the

[3]The first arrival time can be seen from the recorded signal shown in Figure E.6. This first arrival time, which is the arrival of the extensional wave, can also be estimated by using the estimated extensional wave velocity—5428 m/s for aluminum (see Section 4.3.1). For the propagation distance of 36 mm, the estimated first arrival time is 6.6 µs.

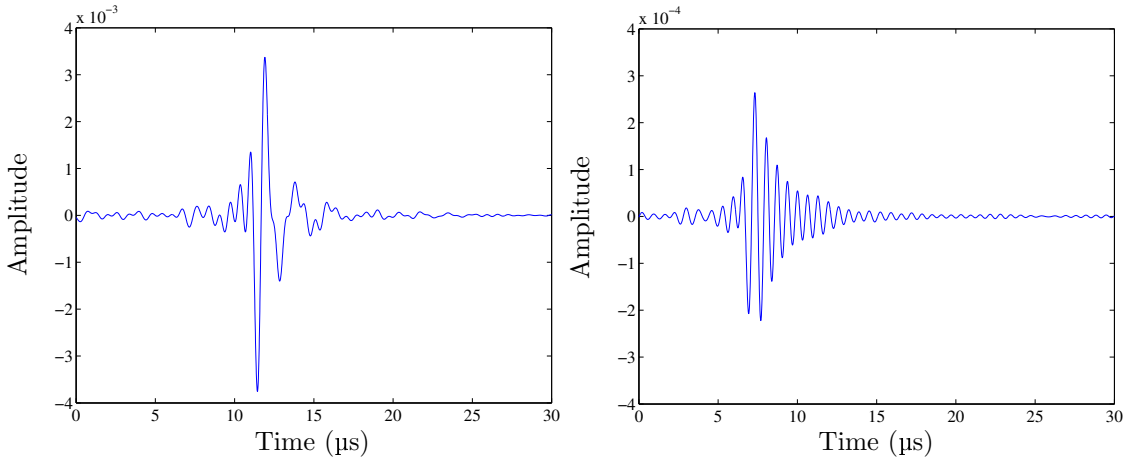

(a) The decomposed A0 mode.

(b) The decomposed S0 mode.

Figure E.9: Final decomposed A0 and S0 modes (by the mode-cancellation technique) of the experimental signal measured at 36 mm.

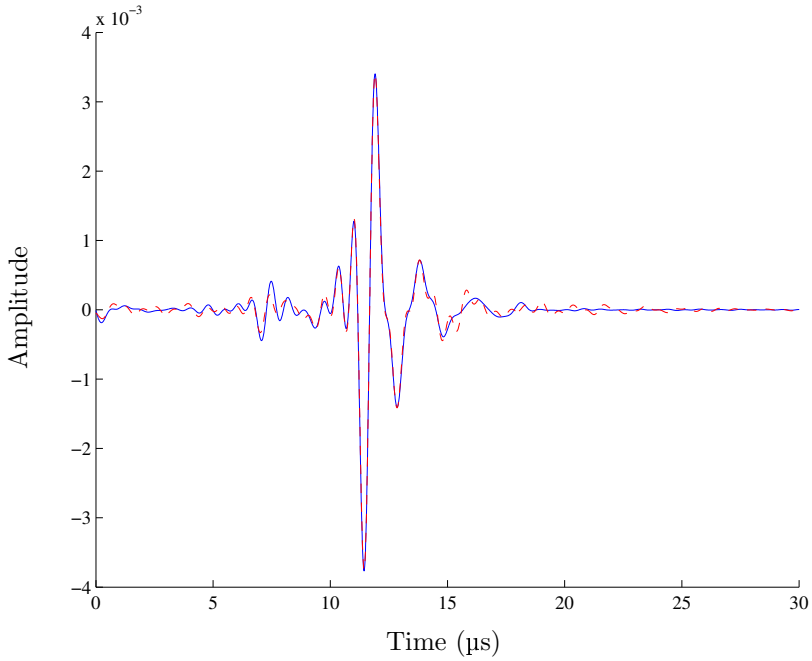

Figure E.10: Comparison between the reconstructed (dashed line) and measured (solid line) signals. The propagation distance is 36 mm.

signal, there is a spurious high-frequency component existing as a part of the A0 mode. These two discrepancies are basically from the same root cause which is the sensitiveness of this technique due to the division of spectra. Recall that the total strength of the retained mode, C_1, is obtained from Equation (E.7), which is effectively the division between two magnitude spectra. Although, in the theoretical development, this division is well-defined even at the zeros of $|\tilde{G}|$, this step becomes very sensitive to errors in the real implementation. Errors in the propagation characteristics of the two modes, represented as errors in k_1 and k_2, cause shifts in the zeros of $|\tilde{G}|$, and thus, differences in locations between zeros of $|\tilde{G}|$ and $|\hat{S}_{1,t}|$ so that the divisions around those zero points become unreliable. This result can be seen in the calculated total strengths where there are spurious peaks or dips around those zero points. These peaks and dips are circled in Figure E.8(b). These errors will propagate throughout the rest of the algorithm to the final decomposed results as evident in Figure E.10. To be specific for this present case, the spurious component of the S0 mode which arrives before the first arrival time, although small, is resulted from the spurious peak in area III, whereas, the high-frequency variation at the end of the A0 mode are caused by the spurious peaks in area I and II. Note that, this problem can be reduced by using thresholds for $|\tilde{G}|$ and $|\hat{S}_{1,t}|$ before the division. However, this improvement will not dramatically give a much better result because the sensitiveness is very strong and those thresholds cannot be set too high so that other parts of the signal are thrown away. In fact, the plots presented in Figures E.8–E.5 are obtained with the thresholds set to 5% on both $|\tilde{G}|$ and $|\hat{S}_{1,t}|$.

E.2 Modal decomposition by direct determination

This technique is developed with the objective to overcome the drawback of the previous technique. Basically, divisions of two spectra, which can be sensitive to errors of known parameters, are avoided. This technique also assumes the knowledge of propagation characteristics of existing modes, and uses the same setup as in Section E.1. Instead of eliminating or decomposing one mode at a time, this technique decomposes all existing modes at the

same time through the determination of the excitation. This technique is called the "direct-determination" technique since it decomposes modes based on the direct formulation.

E.2.1 Theoretical derivation

With the same setup as in Section E.1, this development starts with the spreading-normalized time-domain signal recorded at the distance r in the far-field. The expression for this signal is given in Equation (E.2). The Fourier transform of this signal can be expressed as

$$\hat{S}(\omega, r) = \hat{E}_1(\omega)\tilde{B}(\omega)e^{-jk_1(\omega)r} + \hat{E}_2(\omega)\tilde{B}(\omega)e^{-jk_2(\omega)r}, \tag{E.11}$$

where the dependency on ω and r are explicitly emphasized; $\hat{E}_1$, $\hat{E}_2$ and $\tilde{B}$ are defined in the referred section. Taking the magnitude on both sides of Equation (E.11), one can derive the relationship

$$|\hat{S}(\omega, r)| = |\tilde{B}(\omega)|\left|\hat{E}_1(\omega)e^{-jk_1(\omega)r} + \hat{E}_2(\omega)e^{-jk_2(\omega)r}\right|. \tag{E.12}$$

This equation leads to the calculation of the magnitude of the net source strength

$$|\tilde{B}(\omega)| = \frac{|\hat{S}(\omega, x)|}{\left|\hat{E}_1(\omega)\ e^{-jk_1(\omega)r} + \hat{E}_2(\omega)\ e^{-jk_2(\omega)r}\right|}. \tag{E.13}$$

Although this step involves division between two spectra, this operation is practically fine because frequency points where $\hat{E}_1 = \hat{E}_2$, which can cause the denominator to vanish, can be easily excluded from the calculation. Once the magnitude of $\tilde{B}(\omega)$ is calculated, its phase can be obtained by the use of Equation (E.11). That is, with $\tilde{B}(\omega) = |\tilde{B}(\omega)|e^{j\phi(\omega)}$, Equation (E.11) becomes

$$\hat{S}(\omega, r) = \left(\hat{E}_1(\omega)|\tilde{B}(\omega)|e^{-jk_1(\omega)r} + \hat{E}_2(\omega)|\tilde{B}(\omega)|e^{-jk_2(\omega)r}\right)e^{j\phi(\omega)};$$

hence, the phase of the net source strength can be calculated from

$$\phi(\omega) = -j \ln\left(\frac{\hat{S}(\omega, r)}{[\hat{E}_1(\omega)e^{-jk_1(\omega)r} + \hat{E}_2(\omega)e^{-jk_2(\omega)r}]|\tilde{B}(\omega)|}\right). \tag{E.14}$$

Then, the spectrum $\hat{S}(\omega, r)$ can be decomposed into two parts, each of which represents a spectrum of a single-mode response, i.e.

$$\hat{S}(\omega, r) = \hat{S}_1(\omega, r) + \hat{S}_2(\omega, r),$$

where

$$\hat{S}_i(\omega, x) = |\tilde{B}(\omega)|\hat{E}_i(\omega)e^{j[\phi(\omega)-k_i(\omega)r]}, \qquad i = 1,\, 2. \tag{E.15}$$

The corresponding single-mode responses in the time domain can be easily calculated by the applying of the inverse Fourier transform to the spectra in Equations (E.15). Explicitly, the decomposed time-domain signals are given by

$$\hat{s}_i(t, r) = \Re\Big\{\mathrm{FT}^{-1}\{\hat{S}_i(\omega, r)\}\Big\}, \qquad i = 1,\, 2. \tag{E.16}$$

E.2.2 Verification with synthetic signals

This improved technique will be verified with the same synthetic signals used in Section E.1.2. Since this technique requires only one time-domain signal, the synthetic double-mode signal recorded at 36 mm away from the excitation will be used. Figure E.11 shows the calculated spectrum of the net source strength $\tilde{B}$, which is obtained from the operations in Equations (E.13) and (E.14). The final decomposed modes are shown in Figure E.12 as dashed lines. In the same figure, each exact single-mode response is plotted together by a solid line for direct comparison.

Good agreement in Figure E.12 shows that, similar to the mode-cancellation technique, this technique works very well with the accurate time-domain signal. This situation also includes accurate propagation characteristics.

E.2.3 Implementation with experimental signals

As seen for the mode-cancellation technique, good performance with synthetic signals cannot be translated into good performance in practice. Then, the true performance of this direct-determination technique is studied with the real experimentally measured signals. However, since the development of the direct-determination technique does not involve any other signals from different locations, exact decomposition will always be achieved. Unlike in the verification with synthetic signals, the resulting decomposed modes for a real experimental signal cannot be verified with any independent sources. Therefore, it is advisable to develop the implementation of this direct-determination technique which employs more than one experimental signals. Note that this concept is also desirable because, in a much less

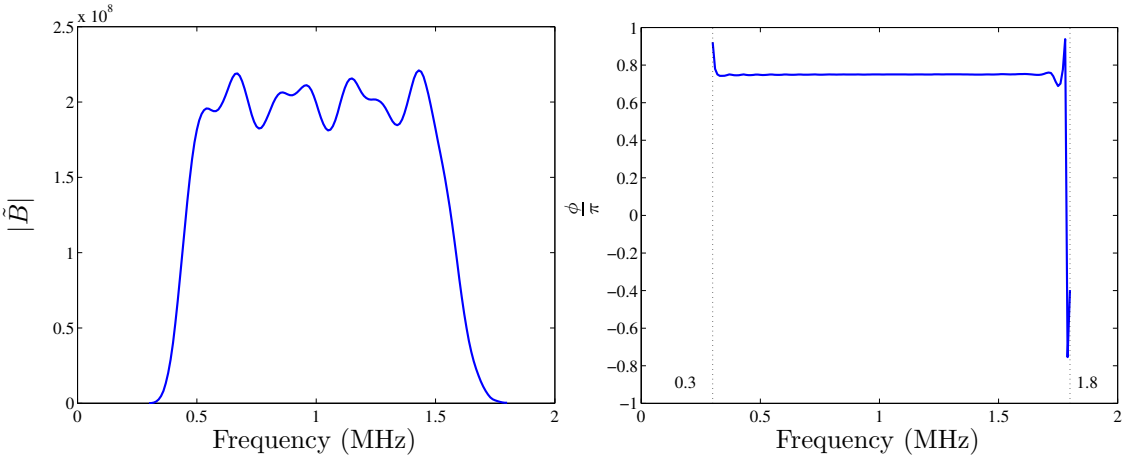

(a) Magnitude.

(b) Phase.

Figure E.11: Calculated spectrum of the net source strength, $\tilde{B}$ by the direct-determination technique. The time-domain signal used is a synthetic double-mode signal recorded at 36 mm (shown in Figure E.1).

controlled situation as in the real practice, problem's parameters cannot be obtained with high accuracy. Inclusion of several signals will contain the errors and variations, and improve the final results.

The incorporation of more signals should be inserted in the calculation of the net source strength. Ideally, a signal model represented by Equation (E.2) must be fitted onto all experimental signals. The unknowns are the source characteristics (magnitude and phase of $\tilde{B}(\omega)$—$|\tilde{B}|$ and $\angle\tilde{B}$, respectively). With measured signals as references, the square-error optimization problem can be naturally setup. However, the described procedure is not practical since $|\tilde{B}|$ and $\angle\tilde{B}$ are usually long vectors over frequency. This kind of optimization requires special cares in numerical processes and is very time-consuming (if not impossible).

In this study, for a practical purpose, a special optimization process is proposed to incorporate more experimental signals. Consider two measurements with different propagation distances, r_1 and r_2. Since the magnitude of a laser source is acceptably constant from measurement to measurement [56], it can be assumed that the difference between the laser sources in two measurements appears only in the phase but not in the magnitude. Explicitly, with the use of Equation (E.11), the Fourier transforms of signals from two measurements

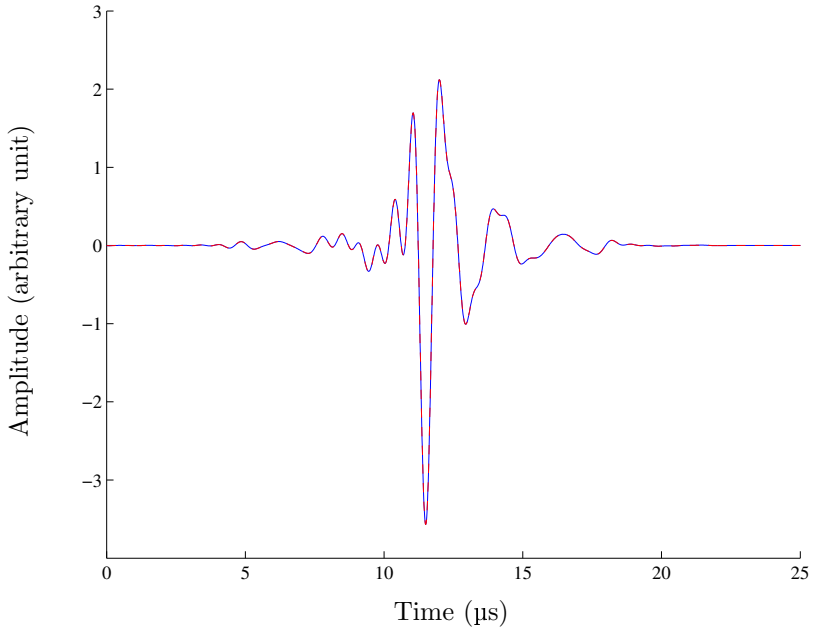

(a) The decomposed A0 mode.

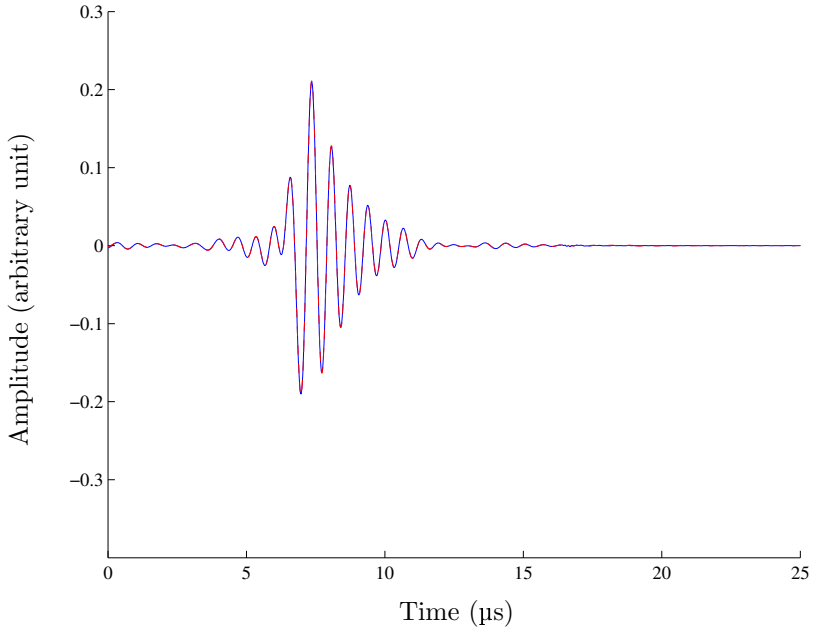

(b) The decomposed S0 mode.

Figure E.12: Final decomposed A0 and S0 modes (dashed lines) by the direct-determination technique. Exact modal responses obtained from the simulation are shown in solid lines.

can be written as

$$\hat{S}(\omega, r_i) = \left[\hat{E}_1(\omega)e^{-jk_1(\omega)r_i} + \hat{E}_2(\omega)e^{-jk_2(\omega)r_i}\right]|\tilde{B}(\omega)|e^{j\phi_i}, \qquad i = 1,\, 2, \tag{E.17}$$

where $\phi_2 = \phi_1 + \Delta_\phi$. In this study, since there is no obvious choice, the phase difference Δ_ϕ is assumed constant over the entire frequency range of interest.

The net source strength can be determined from each signal independently of the other signal by the use of Equation (E.13). Then, for two time-domain signals, the magnitude of this net source strength can be taken as an average between two independent values,

$$|\tilde{B}(\omega)|_{\text{avg}} = \frac{1}{2}\left(\frac{|\hat{S}(\omega, r_1)|}{|\hat{E}_1(\omega)e^{-jk_1(\omega)r_1} + \hat{E}_2(\omega)e^{-jk_2(\omega)r_1}|} + \frac{|\hat{S}(\omega, r_2)|}{|\hat{E}_1(\omega)e^{-jk_1(\omega)r_2} + \hat{E}_2(\omega)e^{-jk_2(\omega)r_2}|}\right). \tag{E.18}$$

As for the phase of the net source strength, since each of ϕ_1 and ϕ_2 can be calculated directly from the spectrum of each signal itself using Equation (E.14) and indirectly from one another through Δ_ϕ, the used value for each ϕ will be the average between values from the two calculations. The parameter Δ_ϕ is obtained by minimizing the square-error defined as a square-difference between a measured signal and a predicted signal given one signal as a fixed reference. More specifically, the square-error to be minimized is the average of the square-difference between measured and predicted signals at r_2 given a fixed signal at r_1 and the square-difference between measured and predicted signals at r_1 given a fixed signal at r_2, i.e.

$$\epsilon_{\text{avg}} = \frac{\epsilon_{2|1} + \epsilon_{1|2}}{2}, \tag{E.19}$$

where, in the continuous domain, with m, n replaced by 1 or 2, and $\hat{S}_1(\omega, r_m)$, $\hat{S}_2(\omega, r_m)$ being spectra of decomposed single-mode signals calculated from the signal measured at r_m alone, the one-sided square-error of the signal at r_n given the signal at r_m, $\epsilon_{n|m}$, is defined as

$$\epsilon_{n|m} = \int [\hat{s}(t, r_n) - \hat{s}_{n|m}(t)]^2 dt. \tag{E.20}$$

In the above equation, the reconstructed signal at r_n with respect to the signal at r_m, $\hat{s}_{n|m}(t)$, can be obtained from

$$\hat{s}_{n|m}(t) = \Re\left\{\text{FT}^{-1}\left\{\left[\hat{S}_1(\omega, r_m)e^{-jk_1(\omega)(r_n - r_m)} + \hat{S}_2(\omega, r_m)e^{-jk_2(\omega)(r_n - r_m)}\right]e^{j\Delta_\phi}\right\}\right\}. \tag{E.21}$$

Note that, from Equations (E.19)–(E.21), the only independent variable in the expression for ϵ_{avg} is Δ_ϕ, which is a vector of a constant value (over the entire frequency range of interest) by the assumption of constant phase difference. If $\Delta_{\phi,c}$ is a minimizer of ϵ_{avg}, then the phase of the net source strength in each measurement can be obtained as

$$\begin{aligned} \phi_{1,\text{avg}} &= \frac{\phi_1 + (\phi_2 - \Delta_{\phi,c})}{2} \\ \phi_{2,\text{avg}} &= \frac{\phi_2 + (\phi_1 + \Delta_{\phi,c})}{2}. \end{aligned} \tag{E.22}$$

After the average values for magnitude and phases of the net source strength are determined, the decomposed signals can be obtained by Equations (E.15) and (E.16), where the average values replace the corresponding values in those equations.

For comparison purposes, this section uses the same experimental time-domain signals as in Section E.1.3. They are filtered versions of signals in a free plate measured at 36 and 46 mm. Those double-mode signals are shown in Figure E.7.

Following the steps described above, one can calculate the average values for $\tilde{B}$, ϕ_1 and ϕ_2. Figures E.13(a)–(c) show those average values (solid lines) with two bounds (dotted lines) as functions of frequency. Finally, the decomposed signals which are calculated from the average values are shown in Figure E.14. To demonstrate the efficiency of this proposed technique, the reconstructed double-mode signal which is obtained by superposing two corresponding decomposed single-mode signals are plotted with the real measured signal for each propagation distance in Figure E.15.

The comparison results in Figure E.15 show reasonable performance of this direct-determination technique and the evident overall improvement from using the mode-cancellation technique (Figure E.10). There are still small components of both A0 and S0 modes arriving before the actual first arrival time. These components are results of signal processing. However, the spurious high-frequency component of the A0 mode around the end of the signal disappears at both propagation distances. This part of signals emphasizes a better performance over the mode-cancellation technique. Besides the efficiency of the proposed technique, the comparison results in Figure E.15 also highlight the robustness of the experimental system using laser ultrasonic techniques and the strategy of representing all the

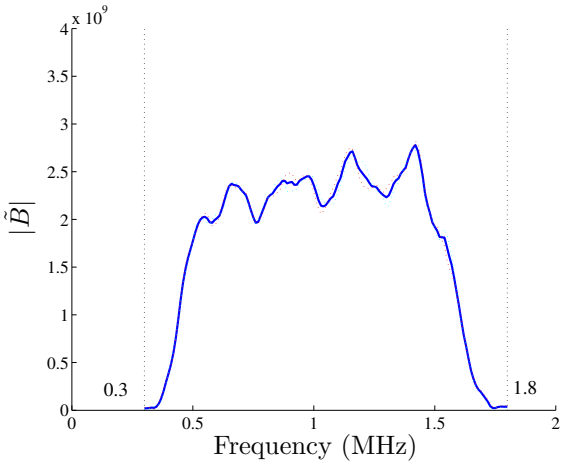

(a) Magnitude.

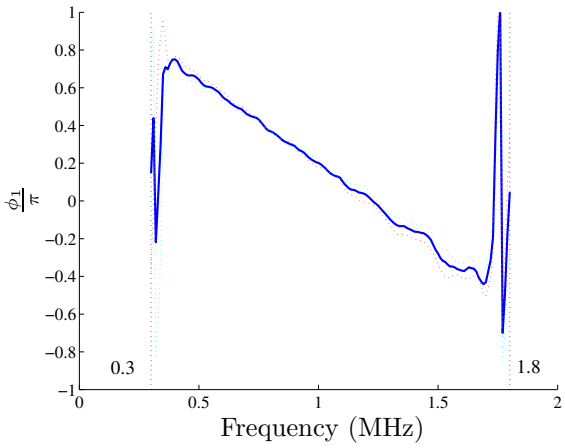

(b) Phase, $r = 36$ mm.

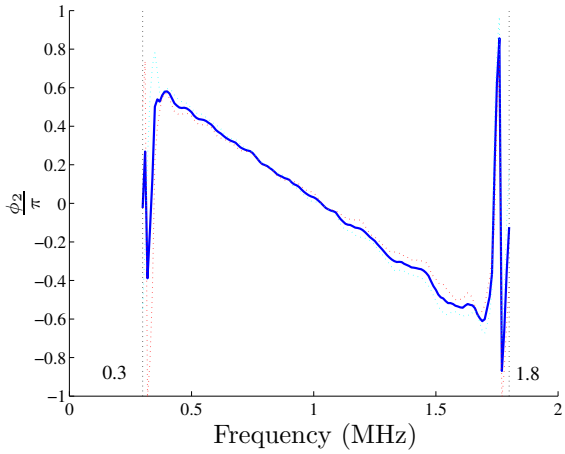

(c) Phase, $r = 46$ mm.

Figure E.13: Calculated spectrum of the net source strength assuming a constant phase-shift between two measurements. The time-domain signal used are experimental double-mode signals recorded at 36 and 46 mm. Solid lines show the average values while dotted lines show bounded values.

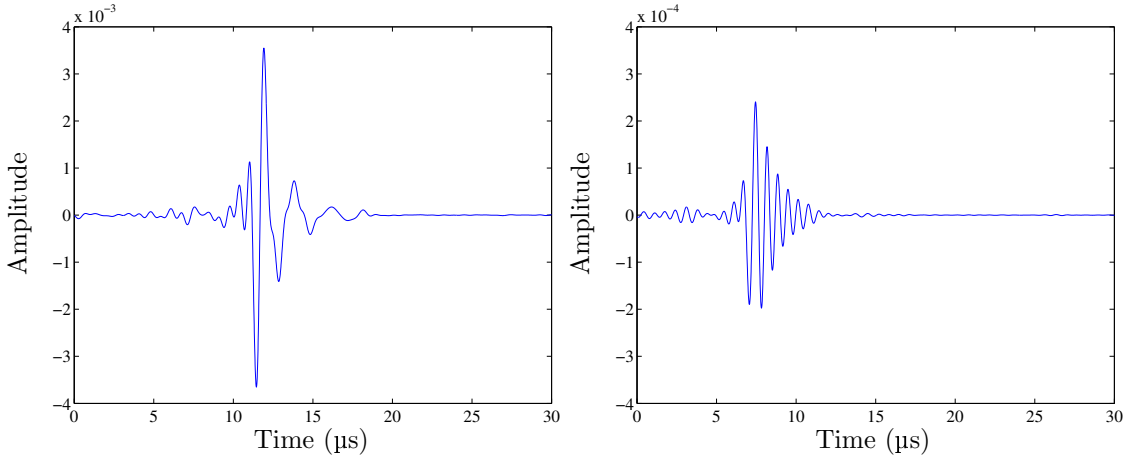

(a) The decomposed A0 mode, $r = 36$ mm.

(b) The decomposed S0 mode, $r = 36$ mm.

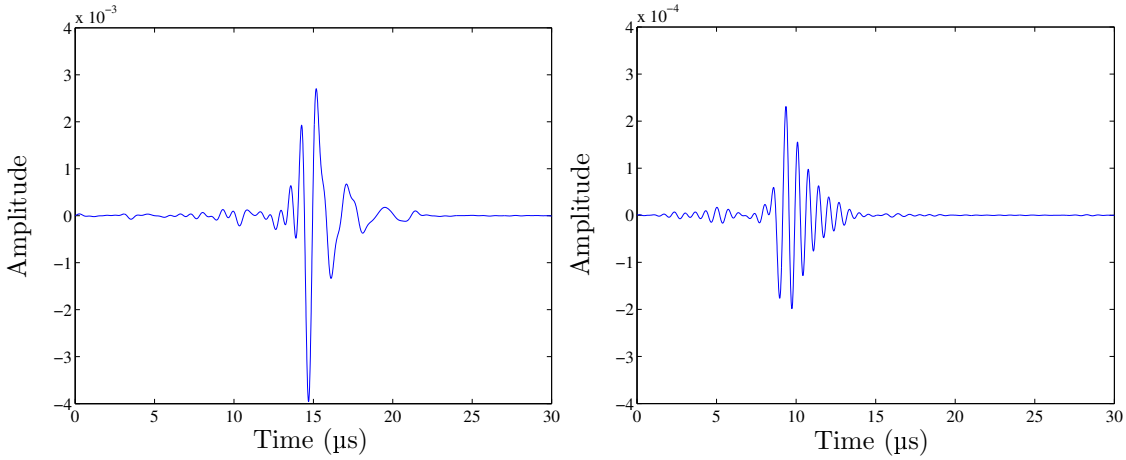

(c) The decomposed A0 mode, $r = 46$ mm.

(d) The decomposed S0 mode, $r = 46$ mm.

Figure E.14: Final decomposed A0 and S0 modes of experimental signals by the direct-determination technique.

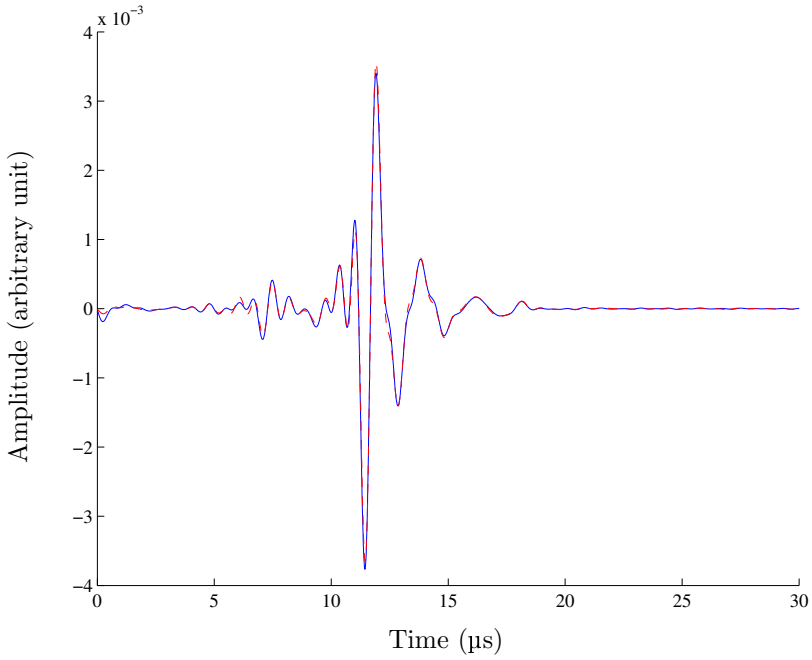

(a) $r = 36$ mm.

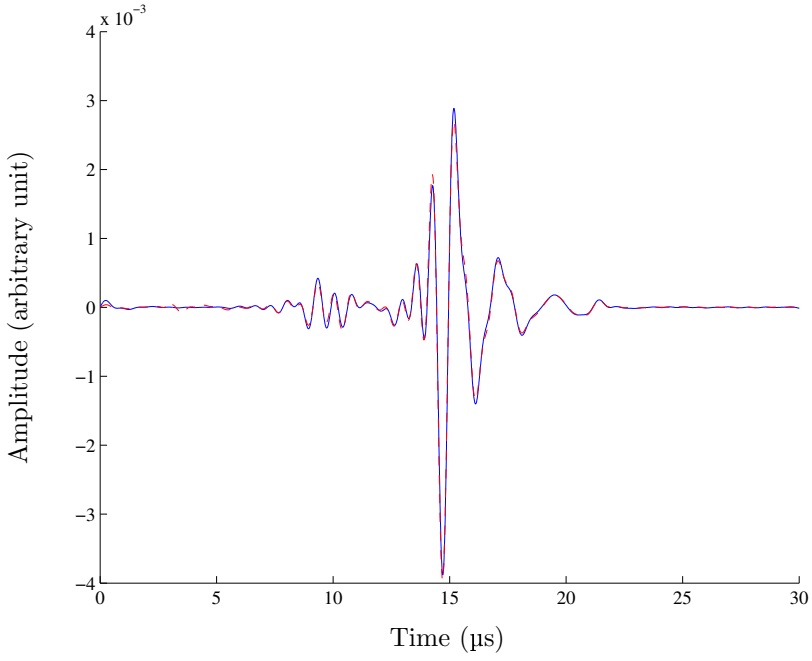

(b) $r = 46$ mm.

Figure E.15: Comparison between the reconstructed (dashed lines) and measured (solid lines) signals.

errors in terms of source's phase difference (Δ_ϕ). The more relaxed and flexible scheme, where other parameters are included in the optimization process, can be chosen, but it will result in additional computing costs. Discrepancy observed in this study is already small considering the fact that textbook values are used for material properties to derive the propagation dispersion curves.

REFERENCES

[1] Abramowitz, M. and Stegun, I. A., *Handbook of Mathematical Functions with Formulas, Graphs, and Mathematical Tables*. New York: Dover Publications, 1965.

[2] Achenbach, J. D., *Wave Propagation in Elastic Solids*. Amsterdam: North-Holland, 1973.

[3] Aindow, A. M., Dewhurst, R. J., Hutchins, D. A., and Palmer, S. B., "Laser-generated ultrasonic pulses at free metal surfaces," *Journal of the Acoustical Society of America*, vol. 69, no. 2, pp. 449–455, 1981.

[4] Alleyne, D. and Cawley, P., "A two-dimensional Fourier transform method for the measurement of propagating multimode signals," *Journal of the Acoustical Society of America*, vol. 89, no. 3, pp. 1159–1168, 1991.

[5] Auger, F. and Flandrin, P., "Improving the readability of time-frequency and time-scale representations by the reassignment method," *IEEE Transactions on Signal Processing*, vol. 43, no. 5, pp. 1068–1089, 1995.

[6] Auld, B. A., *Acoustics Fields and Waves in Solids*, vol. 2. Florida: Robert E. Krieger Publishing Company, second ed., 1990.

[7] Aussel, J.-D. and Monchalin, J.-P., "Measurement of ultrasound attenuation by laser ultrasonics," *Journal of Applied Physics*, vol. 65, no. 8, pp. 2918–2922, 1989.

[8] Benz, R., "Localization of notches with lamb waves," Master's thesis, Georgia Institute of Technology, 2003.

[9] Bernard, A., Lowe, M. J. S., and Deschamps, M., "Guided waves energy velocity in absorbing and non-absorbing plates," *Journal of the Acoustical Society of America*, vol. 110, no. 1, pp. 186–196, 2001.

[10] Braunisch, H., Habashy, T. M., Sinha, B. K., Pabon, J., and Kong, J. A., "Inversion of guided-wave dispersion data with application to borehole acoustics," *Journal of the Acoustical Society of America*, vol. 115, no. 1, pp. 269–279, 2004.

[11] Brown, J. W. and Churchill, R. V., *Complex Variables and Applications*. New York: McGraw-Hill, sixth ed., 1996.

[12] Brutomesso, D. A., *Laser Ultrasonic Techniques to Determine the Influence of Geometric Features on Rayleigh Waves*. PhD thesis, Georgia Institute of Technology, 1995.

[13] Bruttomesso, D. A., Jacobs, L. J., and Costley, R. D., "Development of an interferometer for acoustic emission testing," *Journal of Engineering Mechanics*, vol. 119, no. 11, pp. 2303–2316, 1993.

[14] Carothers, N. L., *Real Analysis*. UK: Cambridge University Press, 2000.

[15] Castaings, M. and Cawley, P., "Generation, propagation, and detection of Lamb waves in plates using air-coupled ultrasonic transducers," *Journal of the Acoustical Society of America*, vol. 100, no. 5, pp. 3070–3077, 1996.

[16] Castaings, M. and Hosten, B., "Use of electrostatic, ultrasonic, air-coupled transducers to generate and receive Lamb waves in anisotropic, viscoelastic plates," *Ultrasonics*, vol. 36, pp. 361–365, 1998.

[17] Chimenti, D. E., "Guided waves in plates and their use in materials characterization," *Applied Mechanics Reviews*, vol. 50, no. 5, pp. 247–284, 1997.

[18] Chimenti, D. E. and Nayfeh, A. H., "Ultrasonic leaky waves in a solid plate separating a fluid and vacuum," *Journal of the Acoustical Society of America*, vol. 85, no. 2, pp. 555–560, 1989.

[19] Chopra, A. K., *Dynamics of Structures: Theory and Applications to Earthquake Engineering*. New Jersey: Prentice Hall, second ed., 2001.

[20] Christensen, R. M., *Theory of Viscoelasticity: An Introduction*. New York: Academic Press, 1971.

[21] Cohen, L., *Time-frequency Analysis*. New Jersey: Prentice Hall, 1995.

[22] Coquin, G. A., "Attenuation of guided waves in isotropic viscoelastic materials," *Journal of the Acoustical Society of America*, vol. 36, no. 6, pp. 1074–1080, 1964.

[23] Deutsch, W. A. K., Cheng, A., and Achenbach, J. D., "Self-focusing of Rayleigh waves and Lamb waves with a linear phased array," *Research in Nondestructive Evaluation*, vol. 9, no. 2, pp. 81–95, 1997.

[24] Ditri, J. J., Pilarski, A., Pavlakovic, B., , and Rose, J. L., "Generation of guided waves in a plate by axisymmetric normal surface loading," in *Review of Progress in Quantitative Nondestructive Evaluation* (Thompson, D. O. and Chimenti, D. E., eds.), vol. 13A, (New York), pp. 133–140, Plenum Press, 1994.

[25] Dixon, S. and Palmer, S. B., "Wideband low frequency generation and detection of Lamb and Rayleigh waves using electromagnetic acoustic transducers (EMATs)," *Ultrasonics*, vol. 42, pp. 1129–1136, 2004.

[26] Eringen, A. C. and Suhubi, E. S., *Elastodynamics: Linear Theory*, vol. 2. New York: Academic Press, 1975.

[27] Fletcher, R., *Practical Methods of Optimization*, vol. 1. New York: John Wiley & Sons, 1980.

[28] Fung, Y. C., *Foundations of Solid Mechanics*. New Jersey: Prentice Hall, 1965.

[29] Gilchrist, M. D., "Attenuation of ultrasonic Rayleigh-Lamb waves by small horizontal defects in thin aluminum plates," *International Journal of Mechanical Sciences*, vol. 41, pp. 581–594, 1999.

[30] Gould, P. L., *Introduction to Linear Elasticity*. New York: Springer, second ed., 1994.

[31] Graff, K. F., *Wave Motion in Elastic Solids*. New York: Dover Publications, 1975.

[32] Gröchenig, K., *Foundations of time-frequency analysis*. Boston: Birkhauser, 2000.

[33] Guo, N. and Cawley, P., "The interaction of Lamb waves with delaminations in composite laminates," *Journal of the Acoustical Society of America*, vol. 94, no. 4, pp. 2240–2246, 1993.

[34] Guo, N. and Cawley, P., "Lamb wave propagation in composite laminates and its relationship with acousto-ultrasonics," *NDT&E International*, vol. 26, pp. 75–84, 1993.

[35] Guo, Z., Achenbach, J. D., and Krishnaswamy, S., "EMAT generation and laser detection of single Lamb wave modes," *Ultrasonics*, vol. 35, pp. 423–429, 1997.

[36] Gurtin, M. E. and Sternberg, E., "On the linear theory of viscoelasticity," *Archive of Rational Mechanics and Analysis*, vol. 11, pp. 291–356, 1962.

[37] Hagan, M. T., Demuth, H. B., and Beale, M., *Neural Network Design*. Boston: PWS Publishing Company, 1996.

[38] Hartmann, B. and Jarzynski, J., "Ultrasonic hysteresis absorption in polymers," *Journal of Applied Physics*, vol. 43, no. 11, pp. 4304–4312, 1972.

[39] Hayes, M. H., *Statistical Digital Signal Processing and Modeling*. New York: John Wiley & Sons, 1996.

[40] He, P. and Zheng, J., "Acoustic dispersion and attenuation measurement using both transmitted and reflected pulses," *Ultrasonics*, vol. 39, pp. 27–32, 2001.

[41] Heller, K., Jacobs, L. J., and Qu, J., "Characterization of adhesive bond properties using Lamb waves," *NDT&E International*, vol. 33, pp. 555–563, 2000.

[42] Holland, S. D., Teles, S. V., and Chimenti, D. E., "Air-coupled, focused ultrasonic dispersion spectrum reconstruction in plates," *Journal of the Acoustical Society of America*, vol. 115, no. 6, pp. 2866–2872, 2004.

[43] Hornik, K., Stinchcombe, M., and White, H., "Multilayer feedforward networks are universal approximators," *Neural Networks*, vol. 2, pp. 359–366, 1989.

[44] Hurlebaus, S., *A Contribution to Structural Health Monitoring Using Elastic Waves*. PhD thesis, University of Stuttgart, 2002.

[45] Hutchins, D. A., "Ultrasonic generation by pulsed laser," in *Physical Acoustics* (Mason, W. P. and Thurston, R. N., eds.), vol. 18, pp. 21–123, New York: Academic Press, 1988.

[46] Kinra, V. K. and Iyer, V. R., "Ultrasonic measurement of the thickness, phase velocity, density or attenuation of a thin-viscoelastic plate. part I: the forward problem," *Ultrasonics*, vol. 33, no. 2, pp. 95–109, 1995.

[47] Kinsler, L. E., Frey, A. R., Coppens, A. B., and Sanders, J. V., *Fundamentals of Acoustics*. New York: John Wiley & Sons, third ed., 1982.

[48] Kotte, O., Niethammer, M., and Jacobs, L. J., "Lamb wave characterization by differential reassignment and nonlinear anisotropic diffusion," *NDT&E International*, vol. 39, pp. 96–105, 2006.

[49] Kreuzinger, T., "Digital signal processing methods for source function extraction of piezoelectric elements," Master's thesis, Georgia Institute of Technology, 2004.

[50] Kutner, M. H., Nachtsheim, C. J., Neter, J., and Li, W., *Applied Linear Statistical Models*. Singapore: McGraw-Hill, fifth ed., 2005.

[51] Lamb, H., "On waves in an elastic plate," *Proceedings of the Royal Society of London. Series A*, vol. 93, pp. 114–128, 1917.

[52] Long, C. F., "On the completeness of the Lamé potentials," *Acta Mechanica*, vol. 3, pp. 371–375, 1967.

[53] Lowe, M. J. S., "Matrix techniques for modeling ultrasonic waves in multilayered media," *IEEE Transactions on Ultrasonics, Ferroelectrics, and Frequency Control*, vol. 42, no. 4, pp. 525–542, 1995.

[54] Lowe, M. J. S. and Cawley, P., "The applicability of plate wave techniques for the inspection of adhesive and diffusion bondded joints," *Journal of Nondestructive Evaluation*, vol. 13, no. 4, pp. 185–594, 1994.

[55] Lowe, M. J. S., Challis, R. E., and Chan, C. W., "The transmission of Lamb waves across adhesively bonded lap joints," *Journal of the Acoustical Society of America*, vol. 107, no. 3, pp. 1333–1345, 2000.

[56] Luangvilai, K. and Jacobs, L. J., "Repeatability of an ablation source using a time-frequency representation," in *Review of Progress in Quantitative Nondestructive Evaluation* (Thompson, D. O. and Chimenti, D. E., eds.), vol. 22B, (New York), pp. 1509–1515, AIP, 2003.

[57] Luangvilai, K., Jacobs, L. J., and Qu, J., "Modal decomposition of double-mode Lamb waves: Numerical verification and discussion on extension to general multi-mode leaky Lamb waves," in *Proceedings of SPIE: Health Monitoring and Smart Nondestructive Evaluation of Structural and Biological Systems IV 2005* (Kundu, T., ed.), vol. 5768, (Washington), pp. 304–3121, SPIE, 2005.

[58] Luangvilai, K., Jacobs, L. J., and Qu, J., "An improved technique for modal decomposition of a double-mode Lamb wave signal," in *Proceedings of SPIE: Nondestructive Evaluation and Health Monitoring of Aerospace Materials, Composites, and Civil Infrastructure V 2006* (Mufti, A. A., Gyekenyesi, A. L., and Shull, P. J., eds.), vol. 6176, (Washington), pp. 145–154, SPIE, 2006.

[59] Luangvilai, K., Punurai, W., and Jacobs, L. J., "Guided Lamb wave propagation in composite plate/concrete component," *Journal of Engineering Mechanics*, vol. 128, no. 12, pp. 1337–1341, 2002.

[60] Mal, A. K., Xu, P. C., and Bar-Cohen, Y., "Analysis of leaky Lamb waves in bonded plates," *International Journal of Engineering Sciences*, vol. 27, pp. 779–791, 1989.

[61] Mallat, S., *A Wavelet Tour of Signal Processing*. UK: Academic Press, second ed., 1998.

[62] McDonald, P. H., *Continuum Mechanics*. Boston: PWS Publishing Company, 1996.

[63] McSkimin, H. J., "Ultrasonic methods for measuring the mechanical properties of liquids and solids," in *Physical Acoustics: Principles and Methods* (Mason, W. P., ed.), vol. 1A, pp. 271–334, New York: Academic Press, 1964.

[64] Mindlin, R. D., "Waves and vibrations in isotropic, elastic plates," in *Proceedings of the First Symposium on Naval Structural Mechanics* (Goodier, J. N. and Hoff, N. J., eds.), (New York), pp. 199–232, Pergamon Press, 1960.

[65] Moon, T. K. and Stirling, W. C., *Mathematical Methods and Algorithms for Signal Processing*. New Jersey: Prentice Hall, 1999.

[66] Nagy, P. B. and Adler, L., "Nondestructive evaluation of adhesive joints by guided waves," *Journal of Applied Physics*, vol. 66, pp. 4658–4663, 1989.

[67] Nakamura, S., *Applied Numerical Methods with Software*. New Jersey: Prentice Hall, 1991.

[68] Nayfeh, A. H. and Nagy, P. B., "Excess attenuation of leaky Lamb waves due to viscous fluid loading," *Journal of the Acoustical Society of America*, vol. 101, no. 5, pp. 2649–2658, 1997.

[69] Niethammer, M., Jacobs, L. J., Qu, J., and Jarzynski, J., "Time-frequency representations of Lamb waves," *Journal of the Acoustical Society of America*, vol. 109, no. 5, pp. 1841–1847, 2001.

[70] Oppenheim, A. V., Schafer, R. W., and Buck, J. R., *Discrete-time Signal Processing*. New Jersey: Prentice Hall, second ed., 1999.

[71] Pavlakovic, B., Lowe, M., Alleyne, D., and Cawley, P., "Disperse: A general purpose program for creating dispersion curves," in *Review of Progress in Quantitative*

Nondestructive Evaluation (THOMPSON, D. O. and CHIMENTI, D. E., eds.), vol. 16A, (New York), pp. 185–192, Plenum Press, 1997.

[72] PEKERIS, C. L., "The seismic surface pulse," *Proceedings of the National Academy of Sciences of the U.S.A.*, vol. 41, pp. 469–480, 1955.

[73] PETERS, F. and PETIT, L., "A broad band spectroscopy method for ultrasound wave velocity and attenuation measurement in dispersive media," *Ultrasonics*, vol. 41, pp. 357–363, 2003.

[74] PIALUCHA, T., GUYOTT, C. C. H., and CAWLEY, P., "Amplitude spectrum method for the measurement of phase velocity," *Ultrasonics*, vol. 27, no. 5, pp. 270–279, 1989.

[75] PIERCE, A. D., *Acoustics: An Introduction to Its Physical Principles and Applications*. New York: AIP, 1981.

[76] POUET, B. F. and RASOLOFOSAON, N. J. P., "Measurement of broadband intrinsic ultrasonic attenuation and dispersion in solids with laser techniques," *Journal of the Acoustical Society of America*, vol. 93, no. 3, pp. 1286–1292, 1993.

[77] PURSEY, H., "The launching and propagation of elastic waves in plates," *Quarterly Journal of Mechanics and Applied Mathematics*, vol. 10, pp. 45–62, 1957.

[78] RAYLEIGH, J. W. S., "On the free vibrations of an infinite plate of homogeneous isotropic elastic matter," *Proceedings of the London Mathematical Society*, vol. 20, pp. 225–234, 1888.

[79] RILEY, K. F., HOBSON, M. P., and BENCE, S. J., *Mathematical Methods for Physics and Engineering*. UK: Cambridge University Press, 1997.

[80] ROGERS, P. H. and BUREN, A. L. V., "An exact expression for the Lommel diffraction correction integral," *Journal of the Acoustical Society of America*, vol. 55, no. 4, pp. 724–728, 1974.

[81] Rokhlin, S. I., "Lamb wave interaction with lap-shear adhesive joints: Theory and experiment," *Journal of the Acoustical Society of America*, vol. 89, no. 6, pp. 2758–2765, 1991.

[82] Rose, J. L. and Ditri, J. J., "Pulse-echo and through transmission Lamb wave techniques for adhesive bond inspection," *British Journal of NDT*, vol. 34, no. 12, pp. 591–594, 1992.

[83] Ruiz, M. A. and Nagy, P. B., "Diffraction correction for precision surface acoustic wave velocity measurements," *Journal of the Acoustical Society of America*, vol. 112, no. 3, pp. 835–842, 2002.

[84] Sachse, W. and Pao, Y.-H., "On the determination of phase and group velocities of dispersive waves in solids," *Journal of Applied Physics*, vol. 49, no. 8, pp. 4320–4327, 1978.

[85] Schumacher, N. A., Burger, C. P., and Gien, P. H., "A laser-based investigation of higher-order modes in transient Lamb waves," *Journal of the Acoustical Society of America*, vol. 69, no. 2, pp. 449–455, 1981.

[86] Scruby, C. B. and Drain, L. E., *Laser Ultrasonics: Techniques and Applications*. New York: Adam Hilger, 1990.

[87] Selfridge, A. R., "Approximate material properties in isotropic materials," *IEEE Transactions on Sonics and Ultrasonics*, vol. 32, no. 3, pp. 381–394, 1985.

[88] Simonetti, F. and Lowe, M. J. S., "On the meaning of Lamb mode nonpropagating branches," *Journal of the Acoustical Society of America*, vol. 118, no. 1, pp. 186–192, 2005.

[89] Sneddon, I. N., *Fourier Transforms*. New York: McGraw-Hill, 1951.

[90] Tan, K. S., Guo, N., Wong, B. S., and Tui, C. G., "Experimental evaluation of delaminations in composite plates by the use of Lamb waves," *Composites Science and Technology*, vol. 53, pp. 77–84, 1995.

[91] Timoshenko, S. P. and Goodier, J. N., *Theory of Elasticity*. New York: McGraw-Hill, third ed., 1970.

[92] Ting, C. S. and Sachse, W., "Measurement of ultrasonic dispersion by phase comparison of continuous harmonic waves," *Journal of the Acoustical Society of America*, vol. 64, no. 3, pp. 852–857, 1978.

[93] Valle, C., Niethammer, M., Qu, J., and Jacobs, L. J., "Crack characterization using guided circumferential waves," *Journal of the Acoustical Society of America*, vol. 110, no. 3, pp. 1282–1290, 2001.

[94] Vasudevan, N. and Mal, A. K., "Response of an elastic plate to localized transient sources," *Journal of Applied Mechanics*, vol. 52, pp. 356–362, 1985.

[95] Viktorov, I. A., *Rayleigh and Lamb Waves: Physical Theory and Applications*. New York: Plenum Press, 1967.

[96] Watson, T. H., "A real frequency complex wave-number analysis of leaking modes," *Bulletin of the Seismological Society of America*, vol. 62, pp. 369–384, 1972.

[97] Weaver, R. L. and Pao, Y.-H., "Axisymmetric elastic waves excited by a point source in a plate," *Journal of Applied Mechanics*, vol. 49, no. 1, pp. 821–836, 1982.

[98] Weaver, R. L., Sachse, W., and Niu, L., "Transient ultrasonic waves in a viscoelastic plate: Theory," *Journal of the Acoustical Society of America*, vol. 85, no. 6, pp. 2255–2261, 1989.

[99] Wilcox, P., "Modeling the excitation of Lamb and SH waves by point and line sources," in *Review of Progress in Quantitative Nondestructive Evaluation* (Thompson, D. O. and Chimenti, D. E., eds.), vol. 23A, (New York), pp. 206–213, AIP, 2004.

[100] Wilcox, P., Lowe, M., and Cawley, P., "The effect of dispersion on long-range inspection using ultrasonic guided waves," *NDT&E International*, vol. 34, pp. 1–9, 2001.

[101] Wilcox, P. D., Dalton, R. P., Lowe, M. J. S., and Cawley, P., "Mode and transducer selection for long range Lamb wave inspection," *Key Engineering Materials: Damage Assessment*, vol. 126, no. 7, pp. 152–161, 1999.

[102] Williams, Jr, A. O., "The piston source at high frequencies," *Journal of the Acoustical Society of America*, vol. 23, no. 1, pp. 1–6, 1951.

[103] Zhu, W. and Rose, J. L., "Lamb wave generation and reception with time-delay periodic linear arrays: a BEM simulation and experimental study," *IEEE Transactions on Ultrasonics, Ferroelectrics, and Frequency Control*, vol. 46, no. 3, pp. 654–664, 1999.